Optoelectronic Control of the Phase and Frequency of Semiconductor Lasers

Thesis by

Naresh Satyan

In Partial Fulfillment of the Requirements
for the Degree of
Doctor of Philosophy

California Institute of Technology
Pasadena, California

2011
(Defended May 16, 2011)

In loving memory of Dilip

Acknowledgements

I am grateful for the support, encouragement, and friendship of a large number of people who have made my stay at Caltech productive and enjoyable.

I am thankful to Prof. Amnon Yariv for the opportunity to be a member of his research group, and the freedom to grow as a researcher. He has always been a source of inspiration with his intuition and insight, and being part of his group has allowed me to interact with, and learn from, a number of knowledgeable and talented individuals.

A large part of this work has been collaborative, and I thank the number of researchers with whom I have benefited from working. Dr. Wei Liang was instrumental in helping me develop a good understanding of the theoretical and experimental aspects of optical phase-locked loops. I have enjoyed numerous brainstorming sessions with Dr. George Rakuljic, discussing new ideas and their feasibility and relevance to the real world. I have learned much about experimental system design from Dr. Anthony Kewitsch. More recently, I have enjoyed exploring various facets of optoelectronic control with Arseny Vasilyev, Jacob Sendowski, and Yasha Vilenchik. I have also had the pleasure of collaborating with other groups on some aspects of this work: Firooz Aflatouni and Prof. Hossein Hashemi at the University of Southern California designed custom integrated circuits to phase-lock semiconductor lasers; and Jason Gamba and Prof. Richard Flagan at Caltech helped us demonstrate the feasibility of using our laser sources for biomolecular sensing.

I thank the many current and past members of the research group with whom I have had fruitful interactions. Dr. John Choi and I spent too many hours together in the office, and he taught me how to be an experimentalist. Dr. Reginald Lee has provided stimulating conversations and expert advice every week. I have enjoyed technical and other discussions with Prof. Bruno Crosignani, Prof. Joyce Poon, Prof. Lin Zhu, Dr. Philip Chak, Prof. Avi Zadok, Dr. Xiankai Sun, Hsi-Chun Liu, Christos Santis, Scott Steger, James Raftery and Sinan Zhao. I owe special thanks to Connie Rodriguez for her thoughtfulness and hard work in looking after us. I also thank Alireza Ghaffari, Kevin Cooper and Mabel Chik for their support.

I thank Profs. Bruno Crosignani, Ali Hajimiri, Kerry Vahala, and Changhuei Yang for serving on my candidacy and thesis committees.

I am fortunate to have formed many friendships at Caltech that have helped me explore my interests outside work. Phanish Suryanarayana, Pinkesh Patel, Setu Mohta, and Devdutt Marathe have been wonderful roommates. I have greatly enjoyed the Carnatic music sessions with Shankar Kalyanaraman, Prabha Mandayam and Chithra Krishnamurthy. John Choi and Philip Tsao have introduced me to bad movies and good food. I have enjoyed many great times—on and off the cricket field—with the large Indian contingent at Caltech: Tejaswi Navilarekallu, Abhishek Tiwari, Vijay Natraj, Sowmya Chandrasekar, Krish Subramaniam, Swaminathan Krishnan, Shaunak Sen, Vikram Deshpande, Vikram Gavini, Abhishek Saha, Anu and Ashish Mahabal, Sonali and Vaibhav Gadre, Mayank Bakshi, Mansi Kasliwal, Zeeshan Ahmed, Uday Khankhoje, Ravi Teja Sukhavasi, Bharat Penmecha, Varun Bhalerao, Shriharsh Tendulkar and Srivatsan Hulikal. Thanks to all my regular hiking partners over the years: the Caltech Y, members of my research group, Shankar Kalyanaraman, Mayank Bakshi, Gautham Jayaram, and especially to Tejaswi Navilarekallu, Pinkesh Patel and Shriharsh Tendulkar. Thanks also to Saurabh Vyawahare and Shankar Kalyanaraman for their company on the long bike rides. I made the decision to live in the Los Angeles area without a car, and I owe many thanks (and apologies) to friends inconvenienced by this on occasion.

Finally, I am deeply thankful for the love, support, and understanding of my parents and my family.

Abstract

This thesis explores the precise control of the phase and frequency of the output of semiconductor lasers (SCLs), which are the basic building blocks of most modern optical communication networks. Phase and frequency control is achieved by purely electronic means, using SCLs in optoelectronic feedback systems, such as optical phase-locked loops (OPLLs) and optoelectronic swept-frequency laser (SFL) sources. Architectures and applications of these systems are studied.

OPLLs with single-section SCLs have limited bandwidths due to the nonuniform SCL frequency modulation (FM) response. To overcome this limitation, two novel OPLL architectures are designed and demonstrated, viz. (i) the sideband-locked OPLL, where the feedback into the SCL is shifted to a frequency range where the FM response is uniform, and (ii) composite OPLL systems, where an external optical phase modulator corrects excess phase noise. It is shown, theoretically and experimentally, and in the time and frequency domains, that the coherence of the master laser is "cloned" onto the slave SCL in an OPLL. An array of SCLs, phase-locked to a common master, therefore forms a coherent aperture, where the phase of each emitter is electronically controlled by the OPLL. Applications of phase-controlled apertures in coherent power-combining and all-electronic beam-steering are demonstrated.

An optoelectronic SFL source that generates precisely linear, broadband, and rapid frequency chirps (several 100 GHz in 0.1 ms) is developed and demonstrated using a novel OPLL-like feedback system, where the frequency chirp characteristics are determined solely by a reference electronic oscillator. Results from high-sensitivity biomolecular sensing experiments utilizing the precise frequency control are reported. Techniques are developed to increase the tuning range of SFLs, which is the primary

requirement in high-resolution three-dimensional imaging applications. These include (i) the synthesis of a larger effective bandwidth for imaging by "stitching" measurements taken using SFLs chirping over different regions of the optical spectrum; and (ii) the generation of a chirped wave with twice the chirp bandwidth and the same chirp characteristics by nonlinear four-wave mixing of the SFL output and a reference monochromatic wave. A quasi-phase-matching scheme to overcome dispersion in the nonlinear medium is described and implemented.

Contents

List of Figures

List of Tables

Glossary of Acronyms

CBC Coherent beam-combining

CCO Current-controlled oscillator

DFB Distributed feedback

EDFA Erbium-doped fiber amplifier

FM Frequency modulation

FMCW Frequency modulated continuous wave

FWHM Full width at half maximum

FWM Four-wave mixing

GVD Group velocity dispersion

HNLF Highly nonlinear fiber

LIDAR Light detection and ranging

MOPA Master oscillator power amplifier

MS-FMCW Multiple source-frequency modulated continuous wave

MZI Mach-Zehnder interferometer

OCT Optical coherence tomography

OPLL Optical phase-locked loop

PD Photodetector

PLL Phase-locked loop

RIN Relative intensity noise

RF Radio frequency

SCL Semiconductor laser

SFL Swept-frequency laser

SS-OCT Swept source-optical coherence tomography

VCO Voltage-controlled oscillator

VCSEL Vertical cavity surface-emitting laser

VECSEL Vertical external cavity surface-emitting laser

Chapter 1

Overview

1.1 Introduction

The modulation of the intensity of optical waves has been extensively studied over the past few decades and forms the basis of almost all of the information applications of lasers to date. This is in contrast to the field of radio frequency (RF) electronics where the phase of the carrier wave plays a key role. Specifically, phase-locked loop (PLL) systems [1, 2] are the main enablers of many applications such as wireless communications, clock delivery, and clock recovery, and find use in most modern electronic appliances including cellphones, televisions, pagers, radios, etc.

The semiconductor laser (SCL) is the basic building block of most optical communication networks, and has a number of unique properties, such as its very large current-frequency sensitivity, fast response, small volume, very low cost, robustness, and compatibility with electronic circuits. This work focuses on utilizing these unique properties of an SCL not only to import to optics and optical communication many of the important applications of the RF field, but also to harness the wide bandwidth inherent to optical waves to enable a new generation of photonic and RF systems. We demonstrate novel uses of optoelectronic phase and frequency control in the fields of sensor networks, high power electronically steerable optical beams, arbitrary waveform synthesis, and wideband precisely controlled swept-frequency laser sources for three-dimensional imaging, chemical sensing and spectroscopy. Phase control is achieved using the current-frequency modulation property of the SCL in

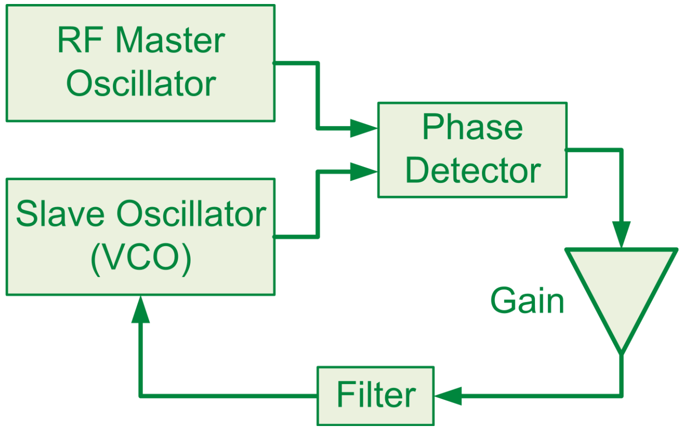

Figure 1.1. Schematic diagram of a generic phase-locked loop.

two optoelectronic feedback systems: the optical phase-locked loop (OPLL) and the optoelectronic swept-frequency laser (SFL).

1.2 Optical Phase-Locked Loops (OPLLs) and Applications

A PLL is a negative-feedback control system where the phase and frequency of a "slave" oscillator is made to track that of a reference or "master" oscillator. As shown in figure 1.1, a generic PLL has two important parts: a voltage-controlled oscillator (VCO), and a phase detector that compares the phases of the slave and master oscillators. The optical analogs of these electronic components are listed in table 1.1. A photodetector acts as a mixer since the photocurrent is proportional to the intensity of the incident optical signal; two optical fields incident on the detector result in a current that includes a term proportional to the product of the two fields. The SCL is a current-controlled oscillator (CCO) whose frequency is controlled via its injection current, thereby acting as the optical analog of an electronic VCO.

Ever since the first demonstration of a laser PLL [3] only five years after the first demonstration of the laser [4], OPLLs using a variety of lasers oscillators have been investigated by various researchers [5–24]. One of the basic requirements of an OPLL is that the summed linewidths of the master and slave lasers should be smaller than

Table 1.1. Comparison between electronic PLLs and OPLLs

	Electronic PLL	Optical PLL (OPLL)
Master oscillator	Electronic oscillator	High-quality laser
Slave oscillator	Voltage-controlled oscillator	Semiconductor laser (current-controlled oscillator)
Phase detector	Electronic mixer	Photodetector

the loop bandwidth, as shown in chapter 2. SCLs tend to have large linewidths (in the megahertz range) due to their small size and the linewidth broadening effect due to phase-amplitude coupling [25–28]. Therefore, OPLL demonstrations have typically been performed using specialized lasers such as solid-state lasers [5–9], gas lasers [10], external cavity lasers [11–16] or specialized multisection SCLs [17–23] which have narrow linewdths and desirable modulation properties. In this work, we explore OPLLs based on different commercially available SCLs, taking advantage of recent advances in laser fabrication that have led to the development of narrow-linewidth distributed feedback (DFB) and other types of SCLs. Further, we develop new phase-locking architectures that eliminate the need for specialized SCL design and enable the phase-locking of standard single-section DFB SCLs.

Research into OPLLs was mainly driven by interest in robust coherent optical communication links for long-distance communications in the 1980s and early 1990s, but the advent of the erbium doped fiber amplifier (EDFA) [29, 30] and difficulties in OPLL implementation made coherent modulation formats unattractive. Interest in OPLL research has been renewed recently, for specialized applications such as free-space and intersatellite optical communication links, extremely high bandwidth optical communication, clock distribution etc. It is no surprise, then, that the majority of OPLL research has focused on applications in phase-modulated coherent optical communication links [5, 6, 17, 18, 31–36], clock generation and transmission [14, 19, 37–39], synchronization and recovery [21, 40]. More recent work has investigated applications of OPLLs in intersatellite communications [9], optical frequency standards [41–43]

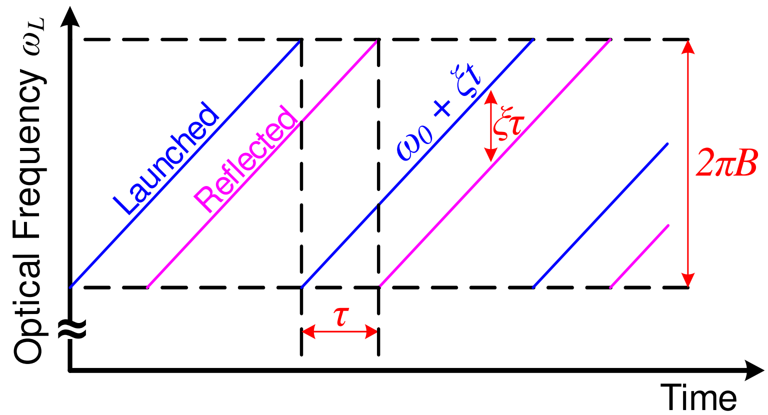

Figure 1.2. A frequency-modulated continuous wave (FMCW) experiment.

and phase-sensitive amplification [15, 44], to name a few.

In this work, we instead look at novel applications that focus on arrays of phase-locked lasers that form phase-controlled apertures with electronic control over the shape of the optical wavefront. We first show that the coherence properties of the master laser are "cloned" onto the slave laser, by direct measurements of the phase noise of the lasers in the frequency and time domains. This coherence cloning enables an array of lasers which effectively behaves as one coherent aperture, but with electronic control over the individual phases. We study applications of these phase-controlled apertures in coherent power-combining and electronic beam-steering.

1.3 Optoelectronic Swept-Frequency Lasers (SFLs)

Swept-frequency lasers have an important application in the field of three-dimensional (3-D) imaging, since axial distance can be encoded onto the frequency of the optical waveform. In particular, consider an imaging experiment with an SFL source whose frequency varies linearly with time, with a known slope ξ, as shown in figure 1.2. When the reflected signal with a total time delay τ is mixed with the SFL output, a beat term with frequency $\xi\tau$ is generated, and the time delay τ can by calculated by measuring the frequency of the beat note. This is the principle of frequency modulated continuous wave (FMCW) reflectometry, also known as optical frequency domain imaging (OFDI). Due to the method's high dynamic range and data acquisition that does not require high-speed electronics [45], FMCW reflectometry finds applications in light detection and ranging (LIDAR) [46–49] and in biomedical imaging [50, 51], where the experiment described above is known, for historical reasons, as swept source optical coherence tomography (SS-OCT). In fact, SS-OCT is now the preferred form of biomedical imaging using OCT, and represents the biggest potential application for SFL sources. Other applications include noncontact profilometry [52], biometrics [53], sensing and spectroscopy. The key metrics for an SFL are the total chirp (or "chirp bandwidth") B—the axial range resolution of the SFL is inversely proportional to B [54, 55]—and the chirp speed ξ, which determines the rate of image acquisition. It is desirable for the SFL to sweep rapidly across a very large bandwidth B.

State-of-the-art SFL sources for biomedical and other imaging applications are typically mechanically tuned external cavity lasers where a rotating grating tunes the lasing frequency [50, 56, 57]. Fourier-domain mode locking [58] and quasi-phase continuous tuning [59] have been developed to further improve the tuning speed and lasing properties of these sources. However, all these approaches suffer from complex mechanical embodiments that limit their speed, linearity, coherence, reliability and ease of use and manufacture. In this work, we develop a solid-state optoelectronic SFL source based on an SCL in a feedback loop. The starting frequency and slope of the optical chirp are locked to, and determined solely by, an electronic reference oscillator. By tuning this oscillator, we demonstrate the generation of arbitrary optical waveforms. The use of this precisely controlled optoelectronic SFL in a high-sensitivity label-free biomolecular sensing experiment is demonstrated.

While single-mode SCLs enable optoelectronic control and eliminate the need for mechanical tuning elements, they suffer from a serious drawback: their tuning range is limited to <1 THz. High resolution biomedical imaging applications require bandwidths of ≥10 THz to resolve features tens of microns in size. We therefore develop and demonstrate two techniques to increase the chirp bandwidth of SFLs, namely four-wave mixing (FWM) and algorithmic "stitching" or multiple source- (MS-) FMCW reflectometry. When the chirped output from an SFL is mixed with a monochromatic optical wave in a nonlinear medium, a new optical wave with twice the optical chirp is generated by the process of FWM. We show that this wave retains the chirp characteristics of the original chirped wave, and is therefore useful for imaging and sensing applications. As do all nonlinear distributed optical interactions, the efficiency of the above scheme suffers from lack of phase-matching. We develop a quasi-phase-matching technique to overcome this limitation. On the other hand, the MS-FMCW technique helps to generate high resolution images using distinct measurements taken using lasers that sweep over different regions of the optical spectrum, in an experiment similar to synthetic aperture radio imaging [60].

1.4 Organization of the Thesis

This thesis is organized as follows. SCL-OPLLs are described in chapter 2, including theoretical analyses and experimental characterizations. The limitations imposed by the FM response of a single-section SCL are described, and two techniques developed to overcome these limitations are described, viz. sideband locking [61] and composite OPLLs [62].

OPLL applications are described in chapters 3 and 4. The cloning of the coherence of the master laser in an OPLL onto the slave SCL [63] is thoroughly characterized, theoretically and experimentally, in chapter 3. Frequency domain (spectrum of the laser frequency noise) and time domain (Allan variance) measurements are performed and are shown to match theoretical predictions. The effect of coherence cloning on interferometric sensing experiments is analyzed. Applications of arrays of phase-locked SCLs are studied in chapter 4. These include coherent power-combining [64–67] and electronic beam-steering [68].

The optoelectronic SFL developed in this work [69] is described in chapter 5, and the generation of precisely controlled arbitrary swept-frequency waveforms is demonstrated. An application of the SFL to biomolecular sensing is studied. The extension of the bandwidth of swept-frequency waveforms for high resolution imaging applications is the focus of chapter 6. Two methods to achieve this: FWM [70] and MS-FMCW reflectometry [71] are analyzed and demonstrated.

A summary of the work and a number of possible directions to further develop this field are presented in chapter 7.

Chapter 2

Semiconductor Laser Optical Phase-Locked Loops

2.1 OPLL Basics

The SCL-OPLL, shown in figure 2.1, is a feedback system that enables electronic control of the phase of the output of an SCL. The fields of the master laser and the slave SCL are mixed in a photodetector PD. A part of the detected photocurrent is monitored using an electronic spectrum analyzer. The detected output is amplified, mixed down with an "offset" radio frequency (RF) signal, filtered and fed back to the SCL to complete the loop.

A schematic model of the OPLL is shown in figure 2.2(a). We will assume that the free-running SCL has an output $a_s \cos\left(\omega_s^{fr} t + \phi_s^{fr}(t)\right)$, where the "phase noise" $\phi_s^{fr}(t)$ is assumed to have zero mean. When the loop is in lock, we drop the superscript fr from the laser phase and frequency variables. Similarly, the master laser output is given by $a_m \cos(\omega_m t + \phi_m(t))$. The detected photocurrent is then

$$i_{PD}(t) = \rho\left(a_m^2 + a_s^2 + 2a_s a_m \cos\left[(\omega_m - \omega_s)\, t + (\phi_m(t) - \phi_s(t))\right]\right), \tag{2.1}$$

where ρ is the responsivity of the PD. The last term above shows that the PD acts as a frequency mixer in the OPLL. Let us further define a photodetector gain $K_{PD} \doteq 2\rho \langle a_s a_m \rangle$, where $\langle . \rangle$ denotes the average value. The detected photocurrent is then mixed down with a radio frequency (RF) signal, whose output is taken to

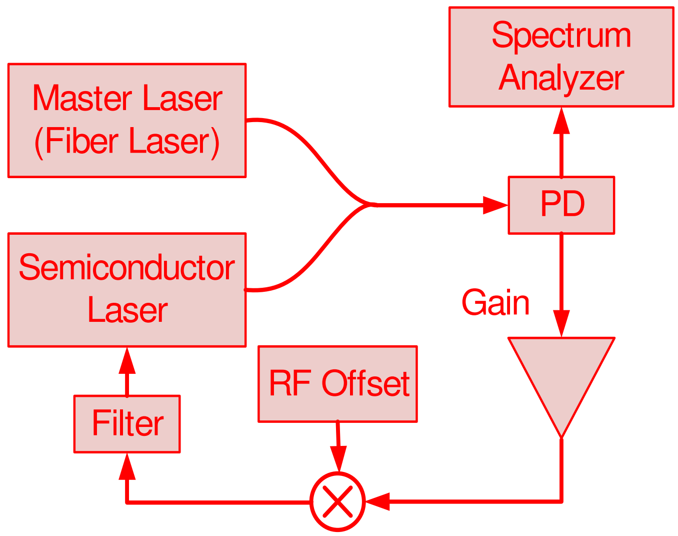

Figure 2.1. A heterodyne semiconductor laser optical phase-locked loop. PD: photodetector.

be $a_{RF} \sin(\omega_{RF} t + \phi_{RF}(t))$. The choice of trigonometric functions ensures a mixer output of the form

$$i_M(t) = \pm K_M K_{PD} a_{RF} \sin\left[(\omega_m - \omega_s \pm \omega_{RF})\, t + (\phi_m(t) - \phi_s(t) \pm \phi_{RF}(t))\right]. \qquad (2.2)$$

Without loss of generality, we will consider only the "+" sign in the rest of this thesis. This mixer output is amplified with gain K_{amp}, filtered and fed into the SCL, which acts as a current-controlled oscillator whose frequency shift is proportional to the input current, i.e.,

$$\delta\omega_s = -K_s i_s(t) = -K_s K_{amp} i_M(t) \qquad (2.3)$$

The minus sign indicates that the frequency of the SCL decreases with increasing current. A propagation delay τ_L is included in the analysis. We will assume that the filter has a unity gain at DC, i.e., the area under its impulse response is zero. We lump together the DC gains of the various elements in the loop, and denote it by K_{dc}, i.e., $K_{dc} = a_{RF} K_M K_{PD} K_{amp} K_s$. This parameter will shortly be defined in a more rigorous manner. When in lock, the frequency shift of the SCL is given by

$$\delta\omega_s = -K_{dc} \sin\left[(\omega_m - \omega_s \pm \omega_{RF})\, t + (\phi_m(t) - \phi_s(t) \pm \phi_{RF}(t))\right]. \qquad (2.4)$$

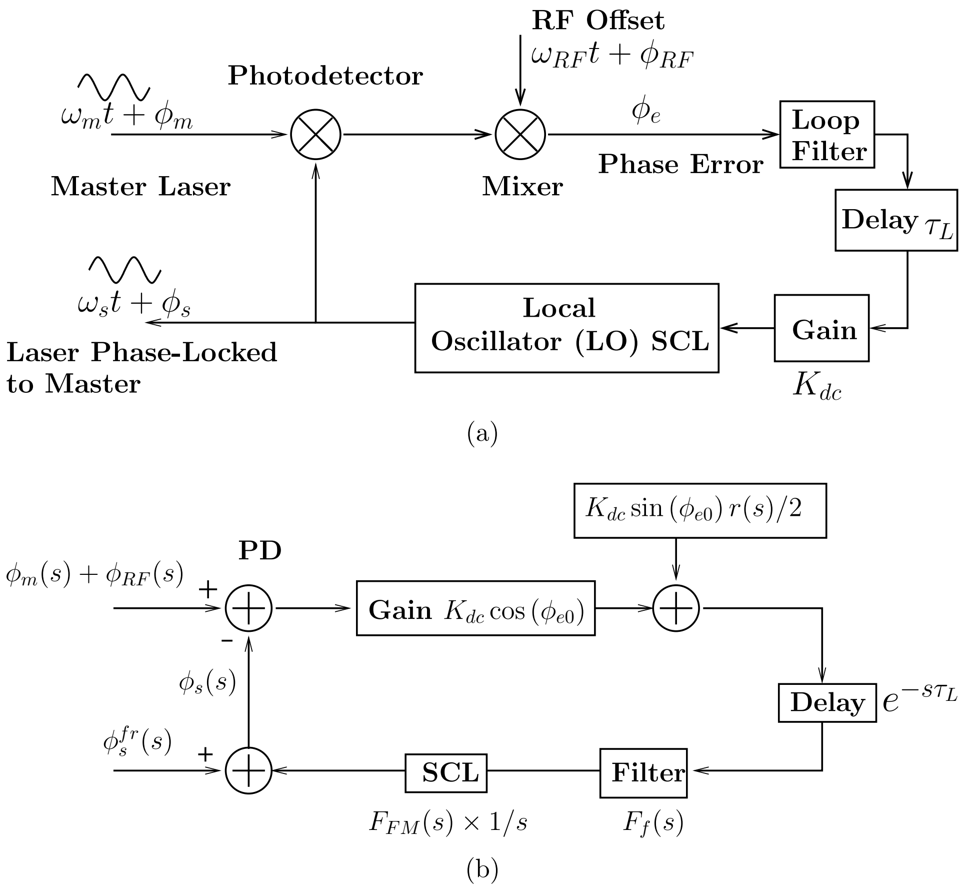

Figure 2.2. (a) Schematic diagram of an OPLL. (b) Linearized small-signal model for phase noise propagation in the OPLL.

The frequency of the slave laser is the sum of the free-running frequency and the correction from the feedback loop, i.e.,

$$\omega_s = \omega_s^{fr} + \delta\omega_s. \tag{2.5}$$

The free-running frequency difference between the slave and master lasers (offset by the RF frequency) is defined as

$$\Delta\omega_{fr} \doteq \omega_m - \omega_s^{fr} + \omega_{RF}. \tag{2.6}$$

We now derive the the steady-state operating point of this laser [2]. In steady state, the error signal at the output of the mixer (equation (2.2)) does not change with time, which yields

$$\begin{aligned} \omega_s &= \omega_m + \omega_{RF}, \\ \bar{\phi}_s &= \bar{\phi}_m + \bar{\phi}_{RF} + \phi_{e0}. \end{aligned} \tag{2.7}$$

The bars in the second part of equation (2.7) denote that this equation is valid for the steady-state values of the phase. The parameter ϕ_{e0} is the steady-state phase error in the loop. This phase error is a consequence of the feedback current keeping the loop in lock, which can be understood by substituting equation (2.7) into equation (2.4) and using equations (2.5) and (2.6) to obtain

$$\delta\omega_s = \Delta\omega_{fr} = K_{dc} \sin \phi_{e0}. \tag{2.8}$$

The frequency shift induced by the feedback loop, $\delta\omega_s$, compensates for the free-running frequency difference between the slave and master lasers, and its maximum value is limited by the DC gain of the loop. The maximum value of the free-running frequency difference that the loop can tolerate in lock is called the "hold-in range," and is defined in section 2.1.2. The steady-state phase error is given by

$$\phi_{e0} = \sin^{-1}\left(\frac{\Delta\omega_{fr}}{K_{dc}}\right). \tag{2.9}$$

It is important that the DC gain K_{dc} be as large as possible and the laser free-running frequency fluctuations be minimized, so that ϕ_{e0} is small. Indeed, this is the case in most well-designed OPLLs, and we will ignore this steady state phase error in large parts of this thesis. In the absence of ϕ_{e0}, the phase of the locked slave SCL exactly follows that of the master laser, offset by the RF phase.

The heterodyne OPLL of figure 2.1 differs from the homodyne PLL shown in figure 1.1 in the addition of an extra reference ("offset") RF oscillator. This results in some powerful advantages: as is clear from equation (2.7), *the optical phase can be controlled in a degree for degree manner by adjusting the electronic phase of the offset signal.* Further, heterodyne locking ensures that the beat note at the photodetector is at an intermediate frequency, where it is away from low-frequency noise sources and can easily be separated from the low frequency ("DC") terms.

2.1.1 Small-Signal Analysis

The OPLL is next linearized about the steady-state operating point given in equation (2.7) and the propagation of the phase around the loop is analyzed in the Laplace domain [2], as shown in figure 2.2(b). The variables in the loop are the Laplace transforms of the phases of the lasers and the RF signal.[1] Fourier transforms are also useful to understand some loop properties, and will be used in parts of the thesis. The Fourier transform $X(f)$ is the Laplace transform $X(s)$ evaluated along the imaginary axis, $s = j2\pi f$. The notation $X(\omega)$ is also used in literature to denote the Fourier transform, with the angular Fourier frequency, ω, given by $\omega = 2\pi f$; we will use $X(f)$ in this thesis to avoid confusion. It is to be understood that the steady-state values of the phase in equation (2.7) are subtracted from the phases before the Laplace (or Fourier) transform is computed. The free-running phase fluctuation of the slave SCL ("phase noise") is denoted by the additive term $\phi_s^{fr}(s)$.[2] The summed relative intensity noises of the lasers $r(s)$ are also incorporated into the model.[3]

The SCL acts as a current-controlled oscillator and, in the ideal case, produces an output phase equal to the integral of the input current for all modulation frequencies, i.e. it has a transfer function $1/s$. However, the response of a practical SCL is not ideal, and the change in output optical frequency is a function of the frequency components of the input current modulation. This dependence is modeled by a frequency-dependent FM response $F_{FM}(s)$. The shape of the FM response and

[1]Notation: the Laplace transform of the variable $x(t)$ is denoted by $X(s)$. For Greek letters, the Fourier transform of $\phi(t)$ is just denoted by $\phi(s)$. The argument s is sometimes dropped when the usage is clear from the context.

[2]Strictly speaking, the Laplace or Fourier transform of the phase noise cannot be defined—it is a random process, and we can only describe its spectral density. However, the use of Laplace transforms provides valuable insight—for this purpose, we can regard the observed phase noise as a particular instance of the underlying random process. The spectral density will be used in all calculations involving the phase noise, e.g., see chapter 3.

[3]The model of figure 2.2(b) is easily derived by noting that the expansion of the phase detector output $K_{dc}\,(1 + r(t)/2)\sin(\phi_{e0} + \phi_e(t))$ about the steady state value $K_{dc}\sin\phi_{e0}$ is $K_{dc}\sin\phi_{e0}$ + $(K_{dc}\sin\phi_{e0})\,r(t)/2$ + $(K_{dc}\cos\phi_{e0})\,\phi_e(t)$. The relative amplitude noise is one-half the relative intensity noise.

its effects are discussed in section 2.3. The filter response and the FM response of the SCL are assumed to be normalized to have unit gain at DC, i.e., $F_f(0) = 1$,[4] $F_{FM}(0) = 1$. For simplicity, we have also assumed that the photodetector and mixer have flat frequency responses—this is true if wideband detectors and mixers are used in the loop, as is the case in this work. It is straightforward to include nonuniform detector and mixer responses in the analysis.

Let us define the open-loop transfer function of the loop as the product of the transfer functions of all the elements in the loop for the ideal case $\phi_{e0} = 0$:

$$G_{op}(s) = \frac{K_{dc} F_f(s) F_{FM}(s) e^{-s\tau_L}}{s}. \tag{2.10}$$

This allows us to define the DC gain in a more rigorous manner:

$$K_{dc} \doteq \lim_{s \to 0} s G_{op}(s). \tag{2.11}$$

The phase of the locked SCL is then given by

$$\phi_s(s) = (\phi_m(s) + \phi_{RF}(s)) \frac{G_{op} \cos \phi_{e0}}{1 + G_{op} \cos \phi_{e0}} + \frac{\phi_s^{fr}(s)}{1 + G_{op} \cos \phi_{e0}} + \frac{r(s)}{2} \frac{G_{op} \sin \phi_{e0}}{1 + G_{op} \cos \phi_{e0}}, \tag{2.12}$$

where we have omitted the argument s in $G_{op}(s)$. Phase noise, $\phi_s^{fr}(s)$, represents the largest source of noise in an SCL-OPLL due to the relatively large linewidth of an SCL, and the contribution of the last term on the right-hand side can usually be neglected, especially if $\phi_{e0} \approx 0$. We will therefore ignore the laser relative intensity noise in the rest of this thesis. For similar reasons, we also neglect the effects of shot noise and detector noise on the phase of the SCL in this thesis. It will also be assumed, unless stated otherwise, that $\phi_{e0} = 0$.

[4]For some filter transfer functions, e.g., integrators, this normalization is not feasible. In such cases, we simply let $K_{dc} \to \infty$.

2.1.2 OPLL Performance Metrics

We now define the important OPLL performance metrics that will be used in this work.

Loop bandwidth is the largest Fourier frequency for which the open loop transfer function $G_{op}(f)$ is larger than unity. From equation (2.12), this means that *the phase of the locked SCL follows that of the master and the RF offset within the loop bandwidth, and reverts to the free-running value at higher frequencies.* The loop bandwidth is usually limited by the stability of the loop—in particular, we will use the Bode stability criterion [2], which states that the magnitude of the complex valued function $G_{op}(f)$ should be lesser than unity when its phase is lesser than or equal to $-\pi$. The frequency at which the phase response equals $-\pi$ is referred to as the "phase-crossover frequency" and represents the maximum possible value of the loop bandwidth.

Hold-in range is defined as the largest change in the free-running frequency of the slave SCL over which the loop still remains in lock. This can be evaluated from equation (2.8), where the sine function takes a maximum value of unity. Using equation (2.11), we write the hold-in range as

$$f_{hold} = \frac{1}{2\pi} \lim_{s \to 0} sG_{op}(s). \tag{2.13}$$

Clearly, a large hold-in range is desired so that the loop is insensitive to environmental fluctuations.

Residual phase error in the loop is one of the most important metrics to evaluate the performance of the loop. It is defined as the variance in the deviation of the phase of the locked SCL from the ideal case where it follows the master laser, i.e.,

$$\sigma_\phi^2 = \left\langle \left(\phi_s(t) - \phi_m(t) - \phi_{RF}(t)\right)^2 \right\rangle , \tag{2.14}$$

where $\langle . \rangle$ denotes averaging over all time.[5] Using the Wiener-Khintchine theorem, equation (2.14) can be written in the frequency domain as

$$\sigma_\phi^2 = \int_{-\infty}^{\infty} S_\phi^e(f)\, df, \tag{2.15}$$

where $S_\phi^e(f)$ is the spectral density of the random variable $\phi_s(t) - \phi_m(t) - \phi_{RF}(t)$, i.e., the spectrum of the phase error. Using equation (2.12), and assuming $\phi_{e0} = 0$, we have

$$S_\phi^e(f) = \left| \frac{1}{1 + G_{op}(f)} \right|^2 \left(S_\phi^m(f) + S_\phi^{s,fr}(f) \right), \tag{2.16}$$

where we have used the fact that the phase noise of the master laser and free-running slave laser are uncorrelated. $S_\phi^m(f)$ and $S_\phi^{s,fr}(f)$ are the spectra of the phase noise of the master and free-running slave SCL respectively, and the phase noise of the RF source is assumed to be negligible. Under the assumption of a Lorenzian lineshape for the lasers, these spectral densities are related to their 3 dB linewidths $\Delta\nu$ by [72]

$$\begin{aligned} S_\phi^m(f) &= \frac{\Delta\nu_m}{2\pi f^2}, \\ S_\phi^{s,fr}(f) &= \frac{\Delta\nu_s}{2\pi f^2}. \end{aligned} \tag{2.17}$$

Using (2.16) and (2.17) in (2.15), we obtain the result for the variance of the residual phase error of the OPLL:

$$\sigma_\phi^2 = \frac{\Delta\nu_m + \Delta\nu_s}{2\pi} \int_{-\infty}^{\infty} \frac{1}{f^2} \left| \frac{1}{1 + G_{op}(f)} \right|^2 df. \tag{2.18}$$

For a stable OPLL, we require that $\sigma_\phi^2 \ll 1$ rad^2. σ_ϕ is the standard deviation of the residual phase error, measured in radians.

Settling time is defined as the time taken by the error signal in the loop to relax back to its steady-state value, within 1%, when a step phase input $\Delta\phi$ is applied.

[5]For simplicity, we make the common assumption that the phase noise is a stationary process.

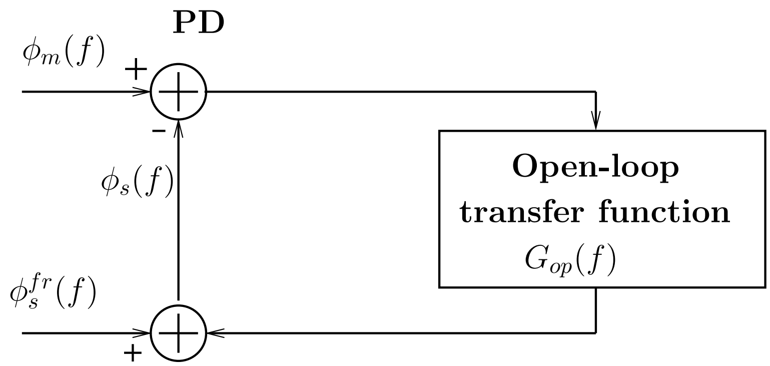

Figure 2.3. Simplified schematic diagram of an OPLL.

If the step is applied at $t = 0$, the phase error goes from $(\phi_{e0} + \Delta\phi)$ to $(\phi_{e0} + 0.01\Delta\phi)$ at time $t = \tau_s$. Alternatively, this is the time taken by the laser phase to change by $0.99\Delta\phi$. The settling time is of interest in applications where the laser phase is changed using an RF phase input.

The response of the loop error signal to a step input is given by

$$\phi_e(t) - \phi_{e0} = \mathcal{L}^{-1}\left[\Delta\phi\frac{1}{s\left(1 + G_{op}(s)\right)}\right], \tag{2.19}$$

where $\mathcal{L}^{-1}$ is the inverse Laplace transform operator.

Other OPLL metrics such as acquisition range, mean time between cycle-slips etc. are not central to this work and will not be considered here. Some of these metrics are discussed in references [2, 73].

2.2 Performance of Different OPLL Architectures

We now evaluate the performance metrics listed above for three different OPLL architectures that are relevant to this work. In this section, we assume that the FM response of the SCL is flat, i.e., $F_{FM}(f) = 1$. The "type" of an OPLL is the number of poles[6] at $s = 0$, and its "order" is the total number of poles. The RF source is assumed to have no noise, which allows the OPLL to be simplified as in figure 2.3.

[6]A pole is a root of the equation $D(s) = 0$, where $D(s)$ is the denominator of the open-loop transfer function $G_{op}(s)$.

As a concrete example, let us assume that the summed linewidth of the master and slave lasers is 0.5 MHz, which is representative of (good) DFB SCLs.

2.2.1 Type I OPLL

This OPLL has a transfer function

$$G_{op}(f) = \frac{K}{j2\pi f}, \tag{2.20}$$

where the pole at $f = 0$ denotes that the optical phase at the output of the SCL is obtained by integrating the input control signal. The magnitude and phase of $G_{op}(f)$ are plotted in a "Bode plot" in figure 2.4(a). Since the phase of $G_{op}(f)$ never goes to $-\pi$, this OPLL is unconditionally stable, with bandwidth and hold-in range $K/2\pi$. Practical OPLLs are always bandwidth-limited; let us therefore arbitrarily assume that the bandwidth of this loop is 2 MHz, i.e., $K = 1.26 \times 10^7$ rad/s.

The laser frequency drifts due to fluctuations in the laser bias current and temperature. Assuming that a low noise current source is used to bias the laser, the primary source of *free-running* frequency variations is environmental temperature fluctuations. The thermal frequency tuning coefficient of InP-based lasers is typically 10 GHz/°C. A hold-in range of 2 MHz therefore means that the loop loses lock if the SCL temperature fluctuates by only $\sim 2 \times 10^{-4}$ °C.

The residual phase error of this loop is given by

$$\sigma_\phi^2 = \frac{\pi(\Delta\nu_m + \Delta\nu_s)}{K}, \tag{2.21}$$

which, with the assumed values of laser linewidth and loop bandwidth, yields $\sigma_\phi^2 = 0.4$ rad^2. Equation (2.21) leads us to an important general result: *it is necessary that the summed linewidths of the two lasers be much smaller than the loop bandwidth for good OPLL performance.*

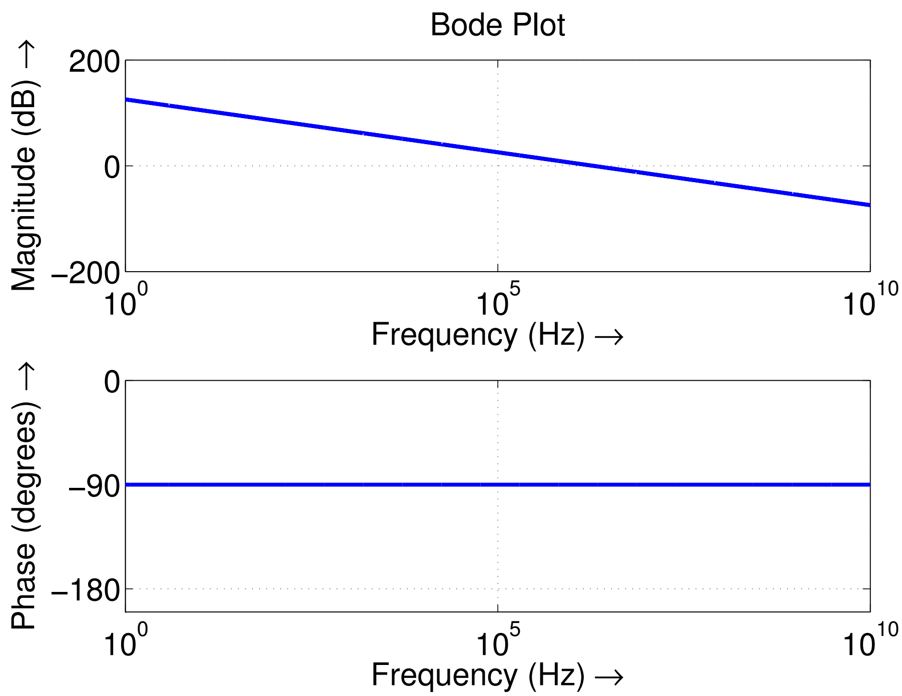

(a)

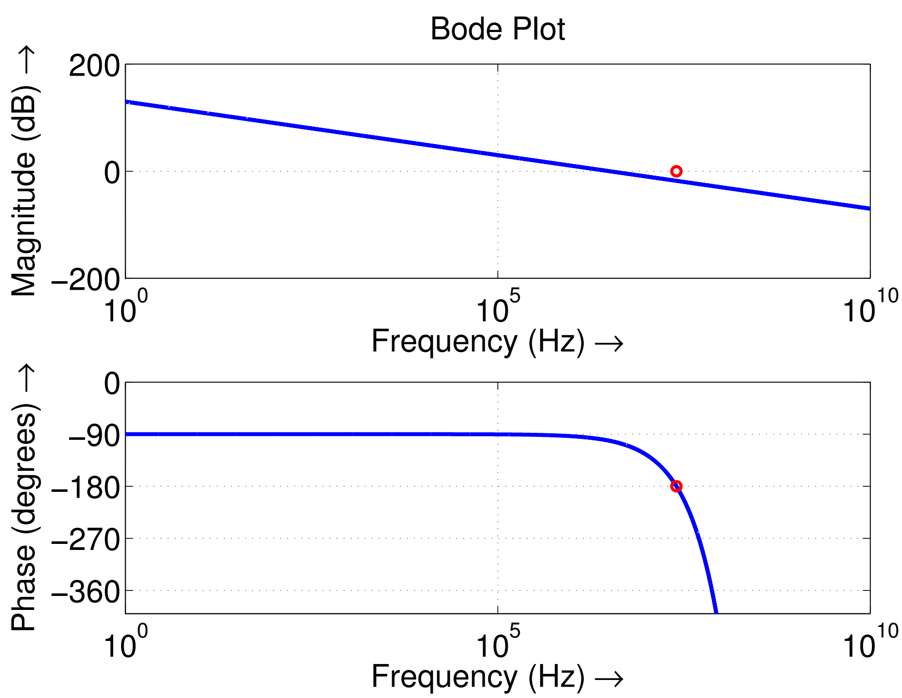

(b)

Figure 2.4. Bode plots for (a) a Type I OPLL and (b) a Type I OPLL with a propagation delay of 10 ns. The phase-crossover frequency is indicated by the marker in (b).

The response of the phase error to a step response is

$$\phi_e(t) - \phi_{e0} = \Delta\phi \exp(-Kt), \tag{2.22}$$

which gives a 99% settling time of $\tau_s \simeq 4.6/K \simeq 4 \times 10^{-7}$ s.

The high sensitivity of this loop to temperature fluctuations is due to the arbitrary bandwidth limit assumed; however other factors such as the SCL FM response and loop propagation delay, discussed later, do impose such a restriction. It is therefore important to design loop filters to increase the DC gain and loop bandwidth.

2.2.2 Type I, Second-Order OPLL

The extremely high sensitivity of the basic Type I OPLL to temperature fluctuations can be overcome using a filter $F_f(f) = (1 + j2\pi f\tau_0)/(1 + j2\pi f\tau_1)$, with $\tau_0 < \tau_1$. This filter is called a lag filter or lag compensator [74][7] since its response has a phase lag (phase response is <0). The value of τ_0 is chosen so that τ_0^{-1} is much smaller than the loop bandwidth, which ensures that the filter response does not affect the phase-crossover frequency. To maintain the same value of the loop bandwidth as the Type I OPLL, the loop gain has to be increased by a factor τ_1/τ_0, so that the loop transfer function is

$$G_{op}(f) = \frac{K}{j2\pi f} \times \frac{\tau_1}{\tau_0} \times \frac{1 + j2\pi f\tau_0}{1 + j2\pi f\tau_1}. \tag{2.23}$$

In the limit of $\tau_1 \to \infty$, this loop is a Type-II control system.

The bandwidth of this loop is $K/2\pi = 2$ MHz, while the hold-in range is $K\tau_1/2\pi\tau_0$. By proper choice of τ_1 and τ_0, a hold-in range of several gigahertz can be achieved. A hold-in range of 1 GHz corresponds to a temperature change of 0.1 °C, and the SCL temperature is easily controlled to much smaller than this value.

The addition of the lag filter at low frequencies does not affect the residual phase error σ_ϕ^2, since most of the contribution to the integral in equation (2.18) is from frequencies of the order of the loop bandwidth.

[7]Some authors, e.g., [2], refer to this filter as a lag-lead filter.

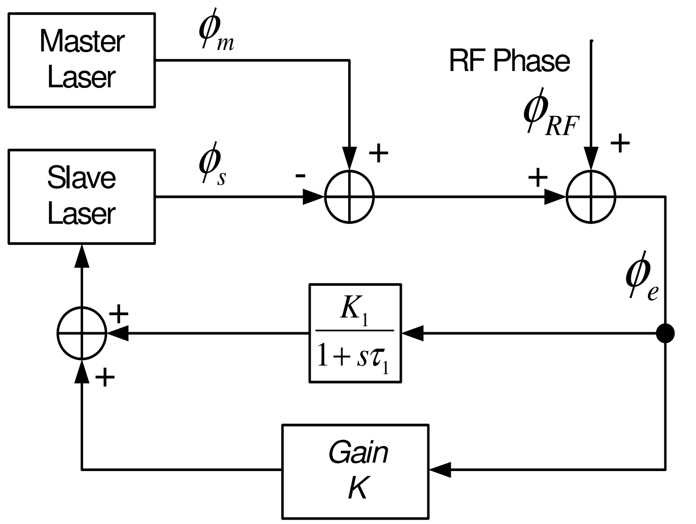

Figure 2.5. Type I, second-order OPLL using an active filter.

When a step input $\Delta\phi$ is applied, the phase error in the loop varies as

$$\phi_e(t) - \phi_{e0} = \mathcal{L}^{-1}\left(\Delta\phi\frac{s + 1/\tau_1}{s^2 + s(\frac{1}{\tau_1} + K) + \frac{K}{\tau_0}}\right). \tag{2.24}$$

Using the approximation $\tau_0^{-1} \ll \tau_1^{-1} \ll K$, this is an overdamped system, and the final solution for the phase error transient is

$$\phi_e(t) - \phi_{e0} = \Delta\phi \exp(-Kt), \tag{2.25}$$

which is identical to the simple Type I OPLL. The settling time of the loop is therefore unaffected, and the OPLL settles to (99% of) the new set-point in a time $\tau_s \simeq 4.6/K = 4 \times 10^{-7}$ s.

The loop filter described above is easily realized using passive R-C circuits [66]. The drawback of a passive filter is that additional gain has to be provided by the amplifier in the loop, which is not always feasible due to amplifier saturation. This can be overcome using an active low-pass filter in a parallel arm [66] as shown in figure 2.5. The additional branch has high DC gain ($K_1 \gg K$), and the pole is located at low frequencies so that it does not affect the loop bandwidth ($K_1/K\tau_1 \ll 1$). The transfer function of this loop is

$$G_{op}(f) = \frac{1}{j2\pi f}\left(K + \frac{K_1}{1 + j2\pi f\tau_1}\right), \tag{2.26}$$

which is identical to equation (2.23) with $\tau_0/\tau_1 = K/K_1$.

2.2.3 Type I OPLL with Delay

We now study an OPLL in the presence of propagation delay. It must be emphasized that *all* negative feedback systems suffer from delay limitations, but the wide linewidth of SCLs makes the delay a very important factor in OPLLs, and has been studied by different authors [75, 76]. The transfer function of a delay element is given by $\exp(-j2\pi f\tau_L)$ where τ_L is the delay time. We write the open loop transfer function of a first-order loop with delay τ_L as

$$\begin{aligned} G(f) &= \frac{K_L}{jf}\exp(-j2\pi f\tau_L) \\ &= \frac{\bar{K}_L}{j\bar{f}}\exp\left(-j2\pi\bar{f}\right), \end{aligned} \tag{2.27}$$

where the normalized variables are defined as

$$\begin{aligned} \bar{f} &\doteq f\tau_L, \\ \bar{K}_L &\doteq K_L\tau_L. \end{aligned} \tag{2.28}$$

We identify the π-crossover frequency and the maximum stable gain by $\angle G(f_\pi) = -\pi$ and $|G(f_\pi)| = 1$:

$$\begin{aligned} \bar{f}_\pi &= 1/4\,, \\ \bar{K}_{L,max} &= 1/4\,. \end{aligned} \tag{2.29}$$

The loop bandwidth is therefore limited to $1/(4\tau_L)$, which is equal to the maximum hold-in range. The Bode plot for this transfer function is calculated and plotted

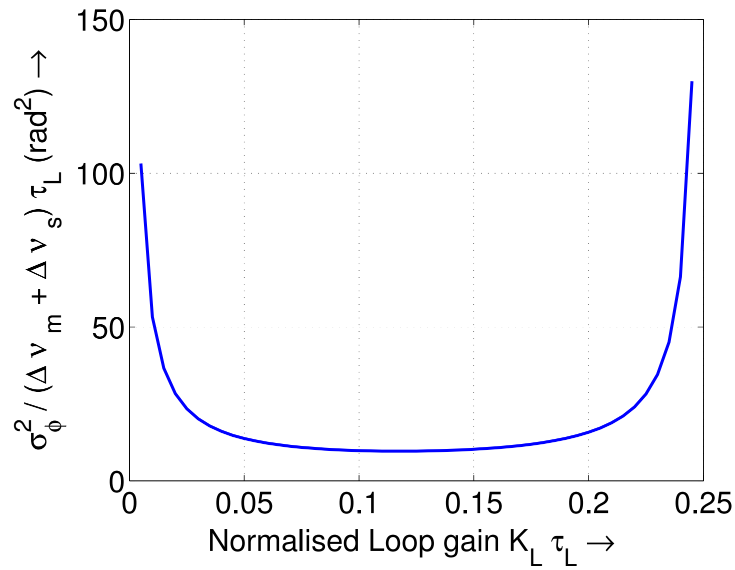

Figure 2.6. Variation of the minimum variance of the phase error as a function of the normalized gain for a Type I OPLL in the presence of propagation delay.

in figure 2.4(b), assuming a delay $\tau_L = 10$ ns, which is a typical value for optical fiber-based OPLLs. The phase crossover frequency is then equal to 25 MHz.

The variance of the residual phase error is calculated using equation (2.27) in equation (2.18) to obtain

$$\sigma_\phi^2 = \tau_L \frac{\Delta\nu_m + \Delta\nu_s}{2\pi} \int_{-\infty}^{\infty} \frac{d\bar{f}}{\bar{K}_L^2 + \bar{f}^2 - 2\bar{K}_L \bar{f} \sin(2\pi \bar{f})}. \tag{2.30}$$

The calculated value of the variance of the phase error as a function of the normalized gain is shown in figure 2.6. As expected, the phase error is very large at $\bar{K}_L = 0$ (no PLL correction) and $\bar{K}_L = 1/4$ (borderline instability). The phase error is minimum when $\bar{K}_L = \bar{K}_{L,opt} = 0.118$, and the minimum value is given by

$$\sigma_{\phi,min}^2 = 9.62\ \tau_L(\Delta\nu_m + \Delta\nu_s). \tag{2.31}$$

For a delay of 10 ns, the minimum achievable phase error is 0.05 rad^2.

2.2.4 Type II Loop with Delay

The limited hold-in range of the Type I loop of the previous loop can be improved using a lag filter design similar to section 2.2.2. Here, we consider the limiting case ($\tau_1 \to \infty$) of a Type II OPLL. In the presence of a propagation delay τ_L, the open loop transfer function is given by

$$\begin{aligned} G(f) &= -\frac{K_L(1+j2\pi f\tau_0)}{f^2}\exp(-j2\pi f\tau_L) \\ &= -\frac{\bar{K}_L(1+j2\pi\bar{f}\bar{\tau}_0)}{\bar{f}^2}\exp\left(-j2\pi\bar{f}\right), \end{aligned} \tag{2.32}$$

where the normalized variables are defined as

$$\begin{aligned} \bar{f} &\doteq f\tau_L, \\ \bar{K}_L &\doteq K_L\tau_L^2, \\ \bar{\tau}_0 &\doteq \tau_0/\tau_L. \end{aligned} \tag{2.33}$$

The π-crossover frequency is identified by setting $\angle G(f_\pi) = -\pi$, to obtain

$$\tan(2\pi\bar{f}_\pi) = 2\pi\bar{f}_\pi\bar{\tau}_0. \tag{2.34}$$

A solution to this equation exists only if $\bar{\tau}_0 > 1$, or $\tau_0 > \tau_L$. In other words, the loop is stable only if, at low frequencies, the phase lead introduced by the zero is larger than the phase lag introduced by the delay. The maximum stable loop gain is given by

$$\bar{K}_{L,max} = \frac{\bar{f}_\pi^2}{\sqrt{1+(2\pi\bar{f}_\pi\bar{\tau}_0)^2}}. \tag{2.35}$$

The variation of $\bar{f}_\pi$ and $\bar{K}_{L,max}$ as a function of the position of the loop zero $\bar{\tau}_0$ are plotted in figure 2.7, from which it is clear that the loop bandwidth approaches the limit $1/(4\tau_L)$ as $\bar{\tau}_0$ increases. *The hold-in range of this loop is infinite, owing to the presence of the pole at* $f = 0$.

We next calculate the variance of the residual phase error by plugging equation

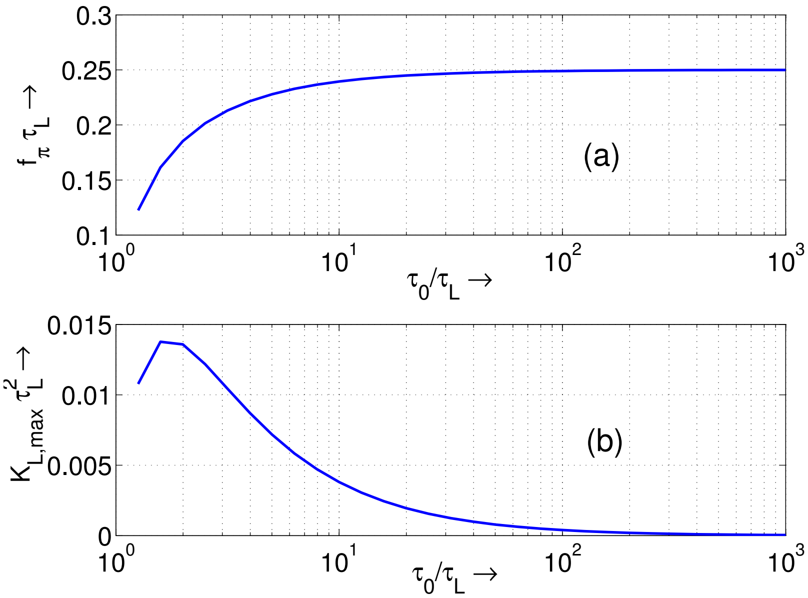

Figure 2.7. Variation of (a) the π-crossover frequency $\bar{f}_\pi$ and (b) the maximum stable loop gain $\bar{K}_{L,max}$ as a function of the position of the loop zero $\bar{\tau}_0$, for a Type II OPLL in the presence of a delay τ_L.

(2.32) into equation (2.18) to obtain

$$\sigma_\phi^2 = \tau_L \frac{\Delta\nu_m + \Delta\nu_s}{2\pi} \times \int_{-\infty}^{\infty} \frac{\bar{f}^2\, d\bar{f}}{\bar{K}_L^2 + \bar{f}^4 + 4\pi^2 \bar{K}_L^2 \bar{\tau}_1^2 \bar{f}^2 - 2\bar{K}_L \bar{f}^2 \cos(2\pi\bar{f}) - 4\pi \bar{K}_L \bar{\tau}_0 \bar{f}^3 \sin(2\pi\bar{f})}, \tag{2.36}$$

which is a function of both $\bar{\tau}_0$ and $\bar{K}_L$. As seen in the previous section, for a given value of $\bar{\tau}_0$, there is an optimum value of $\bar{K}_L$ that minimizes the variance of the phase error. For this OPLL architecture, the optimum gain is related to the maximum stable loop gain by

$$\frac{K_{L,opt}}{K_{L,max}} = 0.47\,. \tag{2.37}$$

The value of the *minimum* of the variance of the phase error as a function of $\bar{\tau}_0$ is shown in figure 2.8. As $\bar{\tau}_0$ is increased, the minimum variance of the phase error

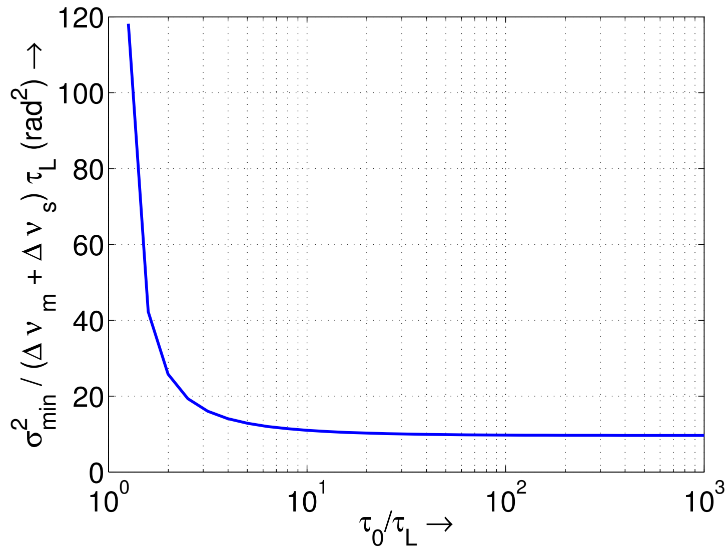

Figure 2.8. Variation of the minimum variance of the phase error as a function of the parameter $\bar{\tau}_0$, for a Type II OPLL with delay τ_L.

asymptotically reaches the value

$$\lim_{\bar{\tau}_0 \to \infty} \sigma^2_{min} = 9.62\ \tau_L(\Delta\nu_m + \Delta\nu_s). \tag{2.38}$$

This result is identical to the result obtained for a first-order loop with delay in (2.31). We therefore arrive at the conclusion that in the presence of propagation delay, the performance of a second-order loop is not superior to that of a first-order loop in terms of the residual phase error. The advantage is the increased hold-in range which makes the loop insensitive to environmental fluctuations.

The settling time of OPLLs with propagation delay cannot be calculated in closed form, but is of the order of the propagation delay in the loop. It is important to minimize the loop delay in order to reduce the variance of the phase error and the settling time, and OPLLs constructed using microoptics [20] and recent efforts toward integrated OPLLs [22, 23, 77] are steps toward high-performance OPLL systems.

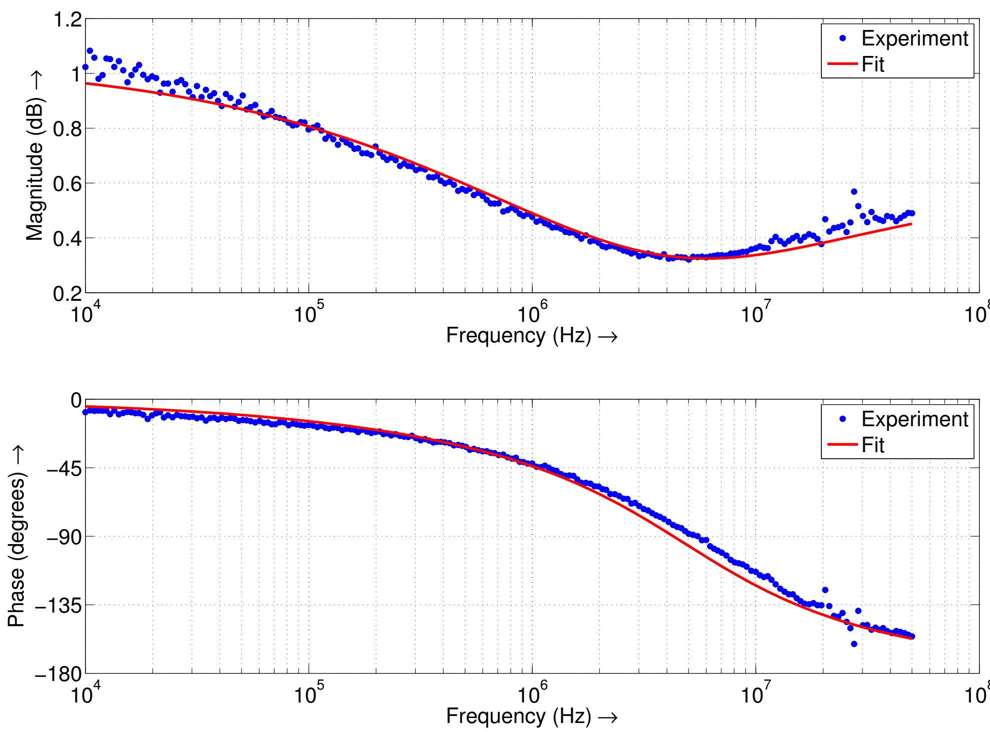

Figure 2.9. Experimentally measured FM response of a commercial DFB laser (JDS-Uniphase) with a theoretical fit using a low-pass filter model [32].

2.3 FM Response of Single-Section SCLs

We have shown that the loop propagation delay ultimately limits the achievable bandwidth and residual phase error in an OPLL, and reducing the delay is ultimately very important to achieve high-speed OPLLs. However, this discussion ignored the nonuniform frequency modulation response of the slave SCL. In practice, the biggest challenge in constructing stable OPLLs is not the propagation delay, but the SCL FM response, which limits the achievable bandwidth. The FM response of single-section SCLs is characterized by a thermal redshift with increasing current at low modulation frequencies, and an electronic blueshift at higher frequencies. This implies that at low modulation frequencies, the variation of the output optical frequency is out of phase with the input modulation, whereas the optical frequency changes in phase with the input modulation at high modulation frequencies. The FM response of the SCL therefore has a "phase reversal," which occurs at a Fourier frequency in the range of 0.1–10 MHz.

Different theoretical models have been used in literature to explain the thermal FM response of a single section SCL, including an empirical low-pass filter (LPF) response [32] and a more "physical" model based on the dynamics of heat transfer within the laser [78], [79]. In this work, we will use the empirical LPF model since it better fits the experimentally measured response of various DFB lasers, an example of which is shown in figure 2.9 for a commercially available DFB laser (JDS-Uniphase) at a wavelength of 1539 nm. The SCL FM response was measured by modulating the laser with a sinusoidal modulating current and using a Mach-Zehnder interferometer (MZI) biased in quadrature as a frequency discriminator [80]. The measurement system is calibrated using the amplitude modulation response as the baseline.

The LPF model for the FM response takes the form

$$F_{FM}(f) = K_{el} - \frac{K_{th}}{1 + \sqrt{jf/f_c}}, \tag{2.39}$$

where the first term denotes the broadband electronic response and the second term denotes the thermal response. Note the opposite signs of the two effects—this implies that the phase of the FM response goes through a change of π radians (a "phase-reversal") as shown in figure 2.9. It is also important to note that this is a relatively "low-frequency" behavior, as opposed to high-speed free-carrier effects near the relaxation resonance frequency which have been studied more extensively [81,82]. Equation (2.39) can be rewritten in the form

$$F_{FM}(f) = \frac{1}{b}\left(\frac{b - \sqrt{jf/f_c}}{1 + \sqrt{jf/f_c}}\right), \tag{2.40}$$

where f_c denotes the corner frequency of the thermal response and depends on the device material and structure, and $b = K_{th}/K_{el} - 1$ denotes the relative strength of the thermal and electronic responses. For typical SCLs, $b > 0$, and f_c lies in the range of 0.1–10 MHz. The fit to the experimental data in figure 2.9 was obtained with $b = 1.64$ and $f_c = 1.8$ MHz.[8] A similar phase reversal was measured in a variety of single-section SCLs characterized in our lab. We will only consider $b > 0$ in this analysis, since it is the most typical case. If $b < 0$, the electronic response always dominates, and there is no phase reversal.

2.4 OPLL Filter Design

When the FM response of the SCL is included, the open-loop transfer function takes the form

$$G_{op}(f) = \frac{K}{j2\pi f}\frac{1}{b}\left(\frac{b - \sqrt{jf/f_c}}{1 + \sqrt{jf/f_c}}\right), \tag{2.41}$$

whose Bode plot is shown in figure 2.10(a) for the fitting parameters $b = 1.64$ and $f_c = 1.8$ MHz. It is clear that the FM response severely limits the phase-crossover frequency, limiting the loop bandwidth and increasing the residual phase error. This FM response limitation justifies the omission of the propagation delay in the above

[8] The fit is not very sensitive to the parameters b and f_c, and allowing for errors in experimental measurement, reasonably good fits are obtained for b in the range 1.5 to 3 and f_c between 0.7 and 2 MHz. In section 2.7, we use the values $b = 2.7$ and $f_c = 2.76$ MHz and the two curves are virtually indistinguishable.

equation; in fact, it is not possible to achieve delay-limited performance with single-section SCLs in standard OPLLs. For these fitting parameters, the minimum variance of the residual phase error can be calculated to be equal to (see appendix A)

$$\sigma^2_{min} = 8 \times 10^{-7} \left(\Delta\nu_m + \Delta\nu_s\right), \tag{2.42}$$

which yields a value of 0.4 rad^2 for a summed linewidth of 0.5 MHz.

The effect of the FM response can be somewhat mitigated using loop filters. We have developed a number of techniques to improve loop performance, and these are described in detail in reference [73]. We will here describe the salient features of our filter design. Firstly, a lead filter is used to push the phase-crossover frequency to higher frequencies, as shown in the Bode plot in figure 2.10(b). Such a filter has the form

$$F_f(f) = \frac{1 + j2\pi f\tau_2}{1 + j2\pi f\tau_3}, \tag{2.43}$$

with $\tau_2 > \tau_3$, and the values $\tau_2 = 10^{-7}$s and $\tau_3 = 10^{-9}$s were used in the calculation. The use of the lead filter reduces the minimum variance of the phase error from ∼0.4 to ∼0.2 rad^2. This value is in reasonable agreement with the experimentally measured residual phase error of 0.12 rad^2 for an optimized OPLL with this SCL (see section 2.5).[9]

An OPLL using a single-section SCL therefore requires that the SCL linewidth should be very narrow (<1 MHz), and a lead filter is necessary to improve the loop bandwidth. The hold-in range of the OPLL is still limited by the low DC gain of a Type I OPLL, and we therefore add a lag filter at low frequencies to increase the hold-in range, as analyzed in section 2.2.2. A practical SCL-OPLL configuration is therefore described in figure 2.11, and we have experimentally demonstrated an increase in the hold-in range from ∼10 MHz to ∼3.5 GHz using this configuration.

[9]An important cause of the discrepancy between theory and experiment is the assumption of a Lorenzian lineshape for the laser—it is shown in chapter 3 that this slave SCL has a significant amount of $1/f$ noise at low frequencies, which contributes to the measured free-running linewidth, but is very well corrected by the OPLL leading to a smaller residual phase error.

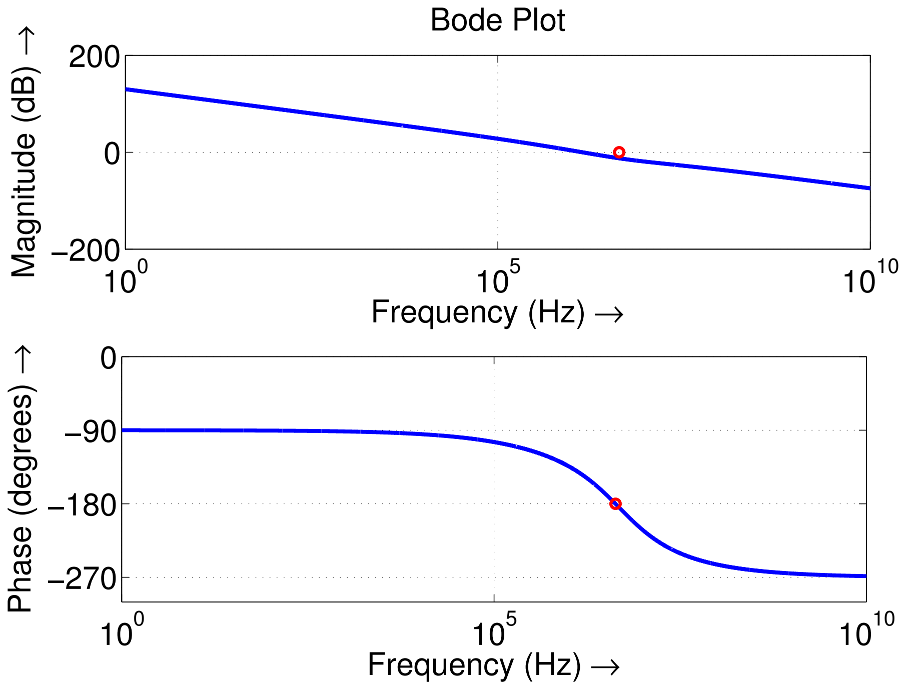

(a)

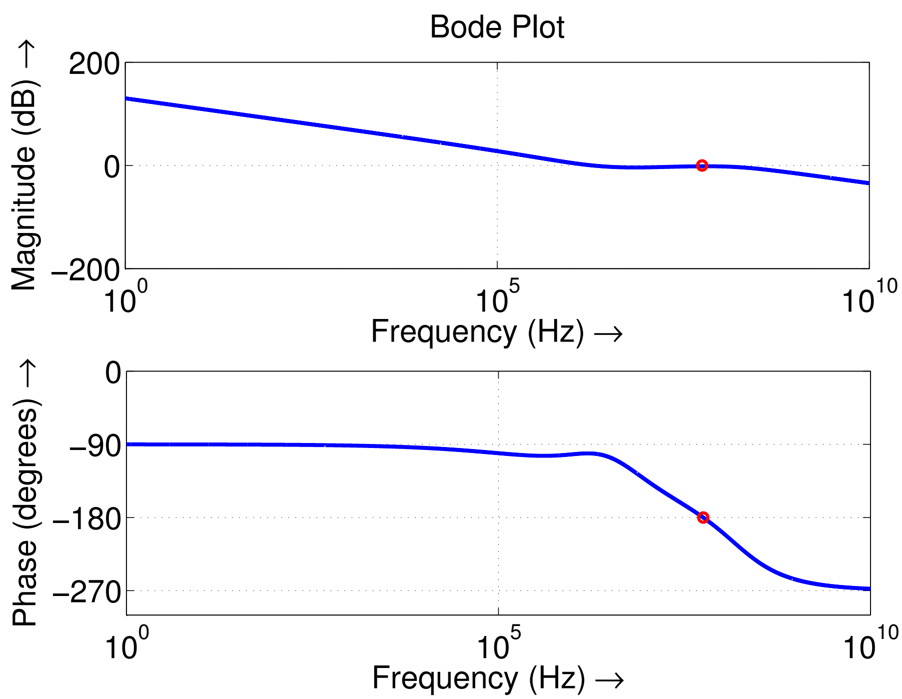

(b)

Figure 2.10. Bode plots for (a) a Type I OPLL including the SCL FM response, and (b) the same response with an additional lead filter. The lead filter pushes the phase-crossover frequency (indicated by the marker) to higher frequencies, enabling a larger loop bandwidth.

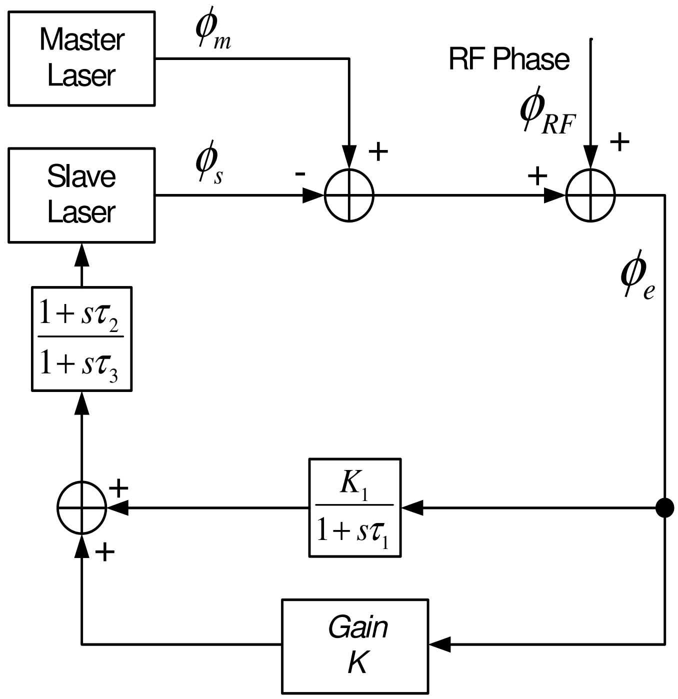

Figure 2.11. Practical OPLL configuration, including a lead filter to increase the phase-crossover frequency and a low frequency active lag filter (implemented by the parallel arm) to increase the hold-in range.

2.5 Phase-Locking of Commercial SCLs

We phase-locked a number of commercially available SCLs of different types and operating wavelengths in the heterodyne OPLL configuration shown in figure 2.1. We present phase-locking results of five different SCLs in table 2.1: a DFB laser at 1539 nm (JDS-Uniphase Corp., Milpitas, CA), an external cavity SCL at 1064 nm (Innovative Photonic Solutions, Monmouth Junction, NJ), a high power master-oscillator power amplifier (MOPA) SCL at 1548 nm (QPC Lasers, Sylmar, CA), a vertical external cavity surface-emitting laser (VECSEL) at 1040 nm (Novalux, Sunnyvale, CA, with a home-built external cavity) and a DFB laser at 1310 nm (Archcom Tech., Azusa, CA). The temperature of the slave SCLs was controlled to within 0.01 °C using a thermoelectric cooler. Different master lasers were used in the experiments. The outputs of the fiber-coupled slave and master lasers were combined using a fiber coupler, and a high speed PD (NewFocus 1544-B) was used to detect the beat note between the lasers. A tunable RF oscillator with linewidth $\ll$ 10 kHz was used as

Table 2.1. Parameters of OPLLs demonstrated using commercially available SCLs

Slave SCL	λ (nm)	SCL power	SCL 3 dB linewidth	Master Laser	σ_ϕ^2 (rad^2)
DFB[a]	1539	60 mW	0.5 MHz	Fiber Laser[h]	0.11
Ext. cavity[b]	1064	100 mW	0.2 MHz	Fiber Laser[h]	0.014
MOPA[c]	1548	1000 mW	0.5 MHz	Tunable Laser[i]	0.08
VECSEL[d]	1040	40 mW	<0.01 MHz[f]	VECSEL[d]	0.007
DFB[e]	1310	5 mW	∼0.5 MHz[g]	DFB SCL[e]	0.2

[a] JDS-Uniphase Corp.
[b] Innovative Photonic Solutions.
[c] QPC Lasers.
[d] Novalux, with home-built cavity.
[e] Archcom Tech.
[f] This is an estimate, the actual linewidth was too low to be measured by the self-heterodyne technique.
[g] Measured by beating two similar DFB lasers.
[h] NP Photonics, Tucson, AZ, linewidth ∼30 kHz.
[i] Agilent, linewidth ∼50 kHz.

the offset signal. Discrete RF amplifiers and mixers (MiniCircuits, Brooklyn, NY) were used to provide gain and mix the RF signals. The DC current and the temperature of the slave SCL were adjusted to bring the free-running frequency difference between the master and slave SCLs to within the loop acquisition range. The total propagation delay in the loop was estimated to be of the order of 10 ns. Filters were used to increase the loop hold-in range and bandwidth as described in the previous section, and stable phase-locking for at least 30 minutes was observed.

The phase-locking performance was characterized by measuring a part of the loop PD output using a high speed spectrum analyzer, and the results are shown in figure 2.12. The offset RF frequency, which ranged from 0.8 to 1.7 GHz in these experiments, is subtracted from the x-axis. If the phase-locking is perfect, this signal is a pure tone at the frequency $\omega_s - \omega_m = \omega_{RF}$ (zero in the figure). However, imperfect phase-locking leads to a residual phase error which shows up as wings in the spectrum. This beat signal is given by

$$V_{beat} \propto \cos(\omega_{RF}t + \phi_{RF}(t) + \phi_e(t)). \tag{2.44}$$

Since the phase noise of the RF source is negligible and the variance of the phase error ϕ_e is much smaller than 1 rad^2 in lock, the spectrum of the beat signal is directly proportional to the spectral density of the phase error, offset by the RF frequency, i.e.

$$V_{beat} \propto \cos(\omega_{RF}t) - \sin(\omega_{RF}t) \times \phi_e(t). \tag{2.45}$$

The first term is the ideal result with no phase error, leading to a delta function in the spectrum, while the spectrum of the second term is the spectral density of the phase error. The variance of the phase error, which is the integral of the spectral density, is therefore calculated by integrating the "noise" spectrum of the beat signal. Defining the "phase-locking efficiency" η as the ratio of coherent power (area under the delta function) to the total power (coherent power + noise power), we can write down

$$\eta = \frac{1}{1 + \langle \phi_e^2(t) \rangle} = \frac{1}{1 + \sigma_\phi^2}, \tag{2.46}$$

so that

$$\sigma_\phi^2 = \frac{1}{\eta} - 1. \tag{2.47}$$

The calculated standard deviations of the phase error for the different OPLLs are indicated in figure 2.12, and the variances are listed in table 2.1.

The linewidths of the slave SCLs were measured, wherever possible, using a delayed self-heterodyne interferometer with interferometer delay time much larger than the laser coherence time [83]. The laser output was split into two parts, and one arm was phase modulated using an external optical phase modulator to generate sidebands. The other arm was delayed by a delay time longer than the laser coherence time. The beat between this delayed signal and one of the phase-modulated sidebands yields a lineshape with linewidth equal to twice the linewidth of the SCL. The phase-locking results in figure 2.12 and table 2.1 show, unsurprisingly, that SCLs with narrower linewidths have lower residual phase errors in their OPLLs.

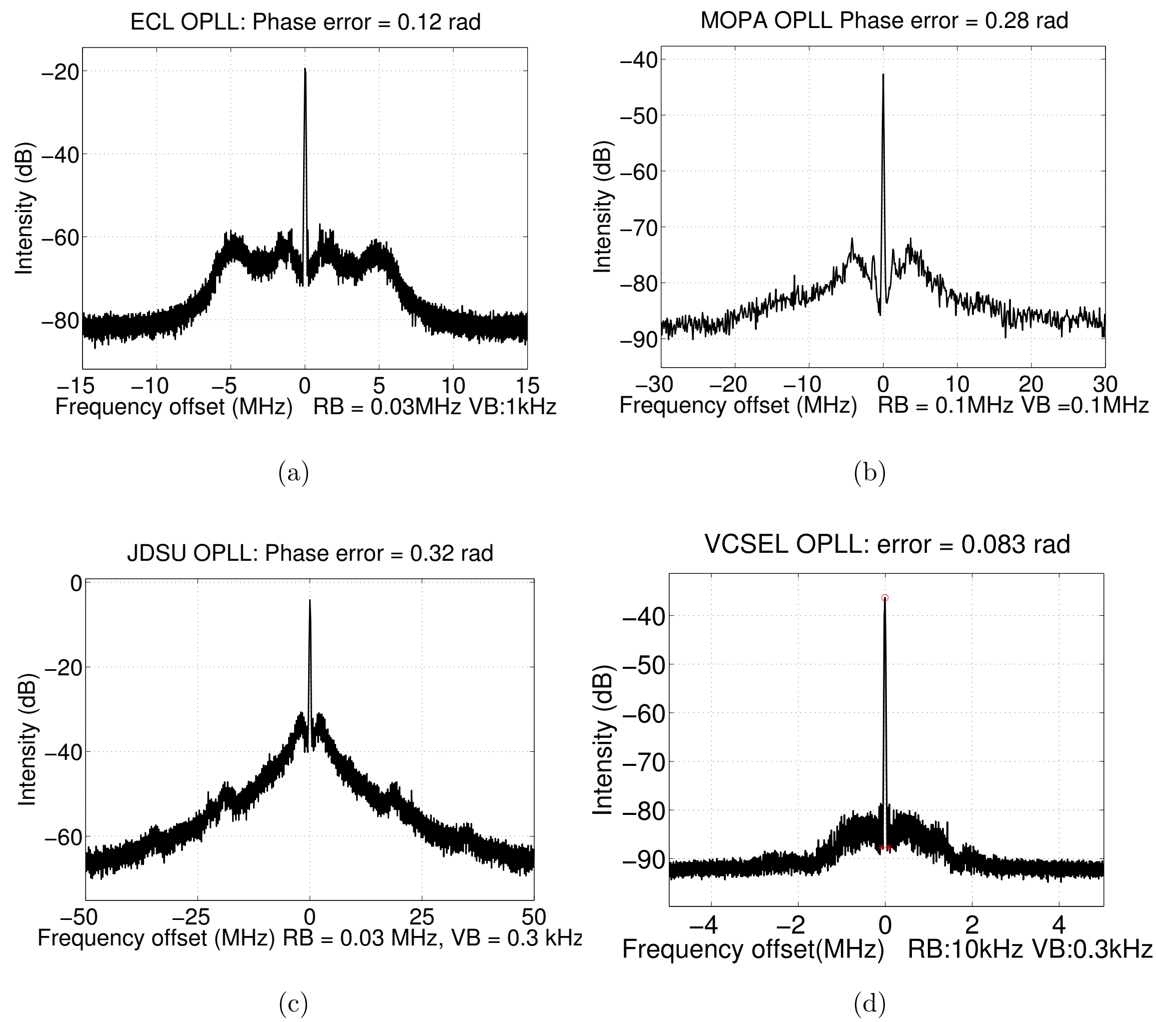

Figure 2.12. Phase-locking results using various commercially available SCLs. The standard deviation of the residual phase error in each OPLL is indicated, along with the resolution and video bandwidths of the measurement. (a) External cavity SCL (Innovative Photonic Solutions), (b) MOPA SCL (QPC Lasers), (c) DFB SCL (JDS-Uniphase Corp.), (d) VECSEL (Novalux, home-built). Other OPLL parameters are given in table 2.1.

In addition to the discrete-electronics-based SCL-OPLLs demonstrated in this section, integrated electronic circuits were developed by our collaborators at the University of Southern California for phase-locking [84]. This circuit also included an aided acquisition module which enables the automatic tuning of the SCL bias current in order to bring its free-running frequency to within the acquisition range of the OPLL.

While we have succeeded in phase-locking a number of commercial OPLLs, the standard OPLL architectures described above still impose stringent requirements on the SCL linewidth. We would like to reduce the residual phase error to even smaller numbers than reported in table 2.1. Further, it was not possible to phase-lock a number of other commercially available SCLs, and we would like to develop techniques to enable phase-locking of *any* SCL. Two such techniques have been developed as part of this work, and are described in the next two sections, namely, sideband locking (section 2.6) and composite OPLLs (section 2.7).

2.6 Novel Phase-Lock Architectures I: Sideband Locking

We have shown in the previous sections that for stable loop operation, it is necessary that the loop bandwidth be much larger than the summed linewidths of the two lasers. The maximum achievable bandwidth of an OPLL is ultimately limited by the loop propagation delay, but a more stringent limitation on the loop bandwidth is imposed by the phase reversal in the FM response $F_{FM}(f)$ of single section SCLs. The traditional solution to this problem has been the use of multielectrode SCLs [17–20], but they do not offer the robustness and simplicity of operation of single-section DFB SCLs. Other approaches to overcome the thermal-induced bandwidth limitation have included the use of external cavity SCLs with narrow linewidths [11–16] or the use of an additional optical injection locking loop [85–87] or external optical modulators for phase-locking [34, 35]. Most of these methods require the use of very specialized

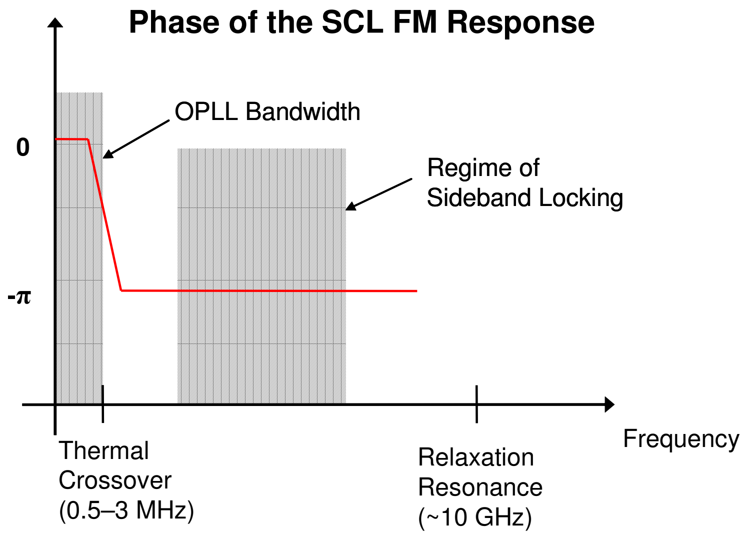

Figure 2.13. Cartoon representation of the phase response of a single-section SCL showing the regimes of operation of a conventional OPLL and a sideband-locked OPLL.

lasers or complicated optical feedback systems. In this section, we demonstrate that the limitation imposed by the phase reversal of the FM response of a single-section SCL can be eliminated using a sideband-locked heterodyne OPLL, which reduces system complexity when compared to other approaches, and *enables delay-limited SCL-OPLLs using most readily available SCLs.*

2.6.1 Principle of Operation

The FM response of a single section SCL is determined by a thermal redshift at low frequencies and an electronic blueshift at higher frequencies, leading to a dip in the amplitude response and a phase reversal at a few megahertz [78]. At frequencies between this crossover frequency and the relaxation resonance frequency of the laser ($\sim$10 GHz), the amplitude and phase of the FM response are constant. If the feedback current into the SCL is upshifted into this frequency range, a much wider frequency range is opened up for phase-locking, and loop bandwidths of up to a few GHz are achievable. This is depicted pictorially in figure 2.13.

Consider the heterodyne sideband-locked OPLL system shown in figure 2.14. A part of the SCL output is combined with the master laser using a 2×1 fiber coupler,

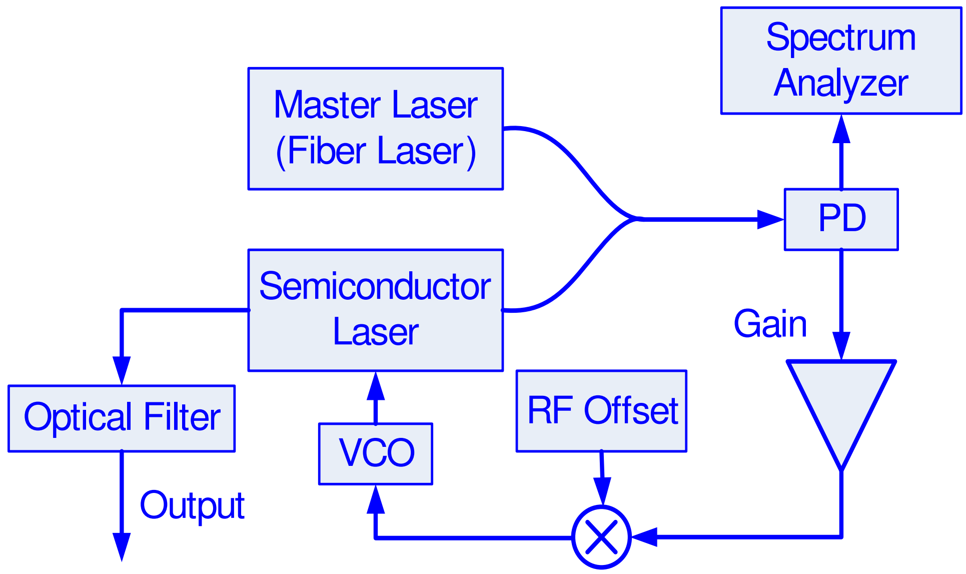

Figure 2.14. Schematic diagram of a heterodyne sideband-locked OPLL.

and mixed in a high speed PD. The error signal at the output of the PD is mixed with an RF offset signal, filtered, and fed into a voltage-controlled oscillator (VCO). The phase and frequency of the VCO are denoted by ω_v and ϕ_v respectively. The VCO output is in turn fed into the SCL, creating multiple FM sidebands whose frequency and phase in the free-running condition are given by

$$\begin{aligned} \omega_{s,k} &= \omega_s^{fr} + k\omega_v, \\ \phi_{s,k} &= \phi_s^{fr} + k\phi_v, \end{aligned} \tag{2.48}$$

with $k = 0, \pm1, \pm2, \ldots$. Any one of these sidebands can now be locked to the master laser. Assume the nth sideband is phase-locked to the master laser. The frequency and phase of this locked sideband are given by

$$\begin{aligned} \omega_{s,n}^{\text{lock}} &= \omega_m + \omega_{RF}, \\ \phi_{s,n}^{\text{lock}} &= \phi_m + \phi_{RF}. \end{aligned} \tag{2.49}$$

It is important to note that while the locked nth sideband is coherent with the master laser, the other sidebands are necessarily incoherent. This is clear from equation (2.48), where the phase correction provided by the VCO is different for different sideband orders. The other sidebands therefore have to be optically filtered out, as shown in figure 2.14. The power in the nth sideband (normalized to the total optical power) is given by

$$P_n = \left| J_n \left(\frac{|F_{FM}(\omega_v/2\pi)| \, A_v}{\omega_v} \right) \right|^2, \tag{2.50}$$

where J_n is the n^{th} order Bessel function of the first kind, and A_v is the amplitude of the modulating current at the VCO output. In order to maximize the total coherent power, the $n = 1$ sideband is phase-locked, and the amplitude A_v is chosen so as to maximize the power in the first sideband. From equation (2.50), at the optimal value of A_v, 33.6% of the total power is in the first sideband. This power penalty introduced by the filtering of the incoherent sidebands is acceptable in most applications of OPLLs owing to the high output power of the SCLs.

The open-loop transfer function of the system shown in figure 2.14, with respect to the phase of the first optical FM sideband is given by

$$G_1(f) = \frac{K_1 F_{FM}^{VCO}(f) F_f(f) e^{-j2\pi f \tau_L}}{j2\pi f}, \tag{2.51}$$

where K_1 is the open-loop DC gain and $F_{FM}^{VCO}(f)$ is the normalized FM response of the VCO. Equation (2.51) is valid whenever the nominal VCO frequency is chosen to be in the frequency range where the FM response of the SCL is constant. The loop bandwidth is therefore constrained by the FM bandwidth of the VCO and the loop propagation delay, *and is independent of the thermal FM response of the laser.* If a high-bandwidth VCO is used, the loop bandwidth is limited primarily by the propagation delay in the loop, which is what we set out to achieve in this section.

2.6.2 Experimental Demonstration

The sideband locking experiment was demonstrated using a commercially available fiber coupled DFB SCL (Archcom Tech.) with an output power of 40 mW at 1550 nm, and a tunable master laser with a linewidth of ~50 kHz. The loop PD had a bandwidth of 12 GHz. The measured FM response of the SCL, shown in figure 2.15,

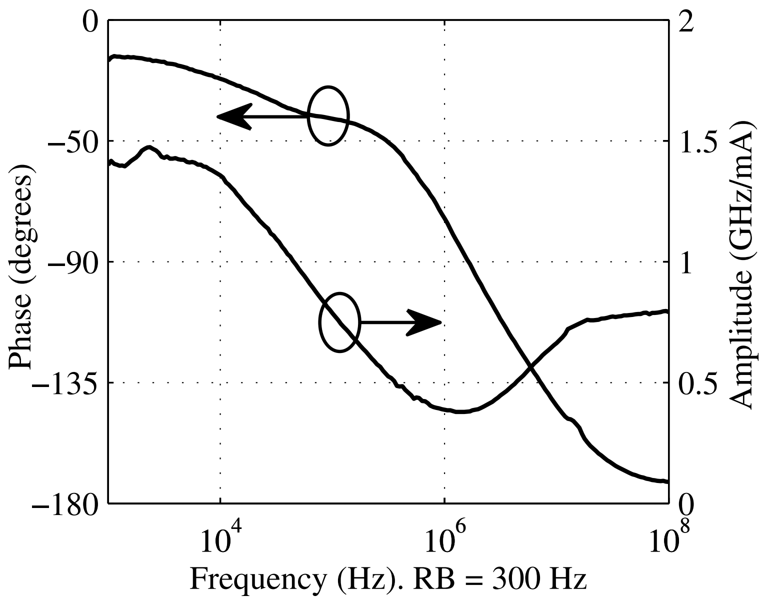

Figure 2.15. Measured FM response of the DFB SCL used in the sideband locking experiment.

exhibits a $\pi/2$ phase-crossover at a frequency of 1.6 MHz, which is lesser than its 3 dB linewidth of 5 MHz; and *the SCL therefore could not be phase-locked in the simple heterodyne OPLL of figure 2.1.* However, using the sideband-locking technique presented in this section, the first FM sideband of this SCL was successfully phase-locked to the master laser in a fiber-based OPLL using discrete RF electronic components. The frequencies of the VCO and the RF offset signal were chosen to be 4 GHz and 1.5 GHz respectively. The locked FM sideband was optically filtered using a Fiber Bragg Grating with a narrow 20 dB bandwidth of 10 GHz (Orbits Lightwave, Pasadena, CA). A suppression ratio of >25 dB to the carrier and the $n = 2$ sideband was achieved in the filtered output.

The bandwidth of the fiber-based OPLL without a loop filter was about 20 MHz, corresponding to a total loop propagation delay of 12.5 ns. By varying the fiber delay in the loop, it was verified that the bandwidth was limited by the loop delay. A

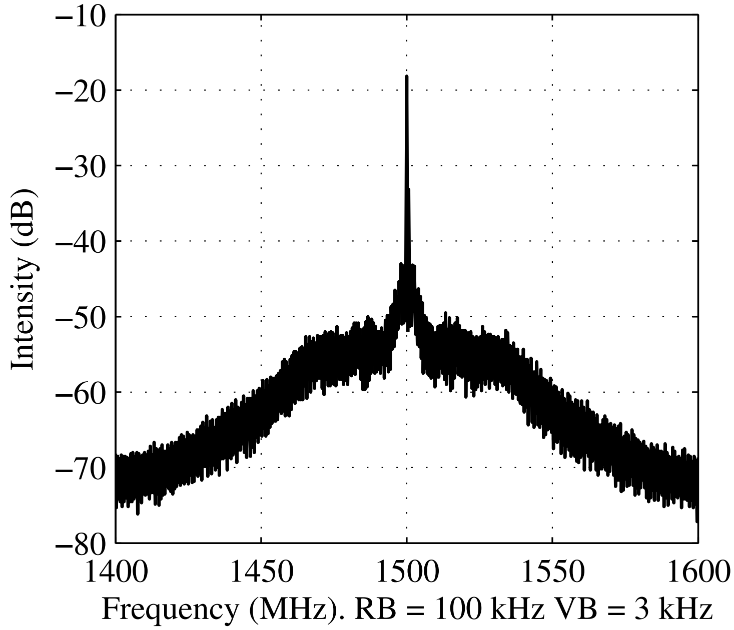

Figure 2.16. Beat spectrum between the locked sideband of the slave SCL and the master laser.

passive R-C filter with the transfer function

$$F_f(f) = \frac{(1 + j2\pi f \tau_{z1})(1 + j2\pi f \tau_{z2})}{(1 + j2\pi f \tau_{p1})(1 + j2\pi f \tau_{p2})} \tag{2.52}$$

was used in the loop to improve the bandwidth, with $\tau_{z1} = 53.6$ ns, $\tau_{z2} = 1.41$ µs, $\tau_{p1} = 4.34$ ns and $\tau_{p2} = 8.71$ µs. The resultant loop bandwidth was measured to be 35 MHz and the hold-in range was ± 90 MHz. The measured spectrum of the beat signal between the phase-locked FM sideband and the master laser is shown in figure 2.16. The locking efficiency η is calculated from the spectrum to be 80%. This corresponds to a residual phase error variance of $\sigma_\phi^2 = 0.25\ \mathrm{rad}^2$. The loop bandwidth and the residual phase error can be further improved by reducing the loop propagation delay.

The lineshape of the master laser and that of the filtered $n = 1$ sideband of the slave SCL, measured using the delayed self-heterodyne interferometer technique, are shown in figure 2.17. The lineshape of the locked SCL sideband follows that of the master laser for frequencies within the loop bandwidth, and reverts to the unlocked

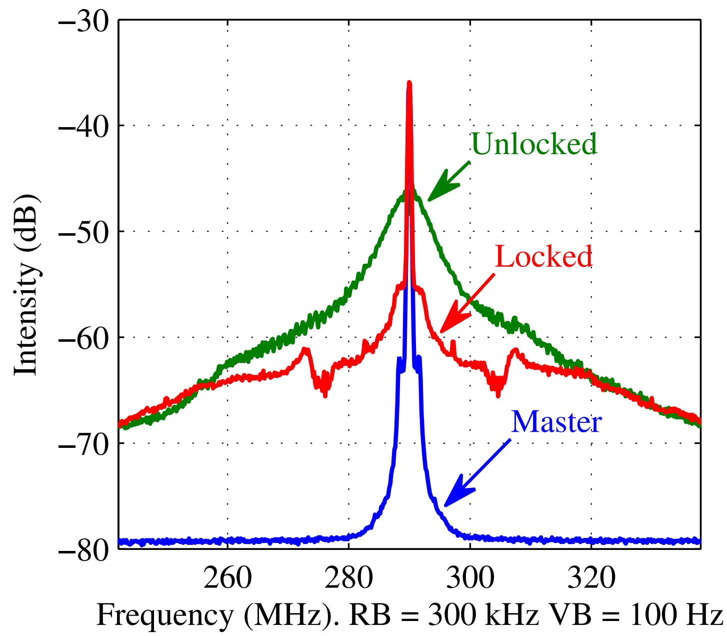

Figure 2.17. Lineshape measurements of the master laser, free-running and phase-locked optical sideband of the slave SCL, using a delayed self-heterodyne interferometer with a frequency shift of 290 MHz.

lineshape outside the loop bandwidth.

In summary, the limitation imposed on the loop bandwidth of an OPLL using a single section DFB SCL by the phase reversal of the laser FM response can be overcome by locking an FM sideband of the SCL to the master laser. Using this technique, the sideband locking of a DFB laser, which could not be locked in a simple heterodyne OPLL, was demonstrated. A delay-limited bandwidth of 35 MHz was achieved, which can be increased to a few hundreds of megahertz using miniature or integrated optics and integrated RF electronic circuits. The phase-locked sideband was optically filtered, and it was shown that the phase noise of the filtered locked sideband was determined by that of the master laser for frequencies within the loop bandwidth. The demonstrated approach to phase-locking SCLs facilitates the phase-locking of standard single section DFB SCLs with moderately large linewidths, with very little increase in system complexity.

2.7 Novel Phase-Lock Architectures II: Composite OPLLs

The sideband locking approach developed in section 2.6 can be used to phase-lock SCLs with large linewidths, but it comes with two drawbacks: (i) only a third of the SCL output power is useful coherent power, and (ii) a narrow-band optical filter is necessary to filter out the coherent optical sideband. While these restrictions are acceptable in most applications, there are some others, such as OPLLs where the frequency of the slave SCL needs to be tuned, where the use of the optical filter is undesirable. In this section, we demonstrate an alternative solution that involves the use of an optical phase modulator to extend the bandwidth of the loop and reduce the residual phase error. The basic idea behind the approach is to use the phase modulator to provide correction at higher frequencies where the thermal response of the SCL is negligible. We demonstrate theoretically and experimentally the improvement of loop bandwidth using two different loop configurations. The use of discrete optical and electronic components in our proof-of-principle experiment results in a reduction of the residual phase noise by about a factor of two; however, the use of integrated optical phase modulators in photonic integrated circuits [22, 77] can lead to very efficient OPLL systems.

2.7.1 System Description

2.7.1.1 Double-Loop Configuration

Consider the schematic diagram of the control system shown in figure 2.18(a). The SCL is first phase-locked to the master laser in a heterodyne OPLL; this loop is shown with the photodetector PD1 in the figure. The output of the phase-locked SCL is phase modulated and mixed with the master laser in a second photodetector PD2. The resultant error signal is down-converted, filtered, and input to the phase modulator. The output of the phase modulator serves as the useful optical output. The linearized small-signal model for the propagation of the optical phase in the

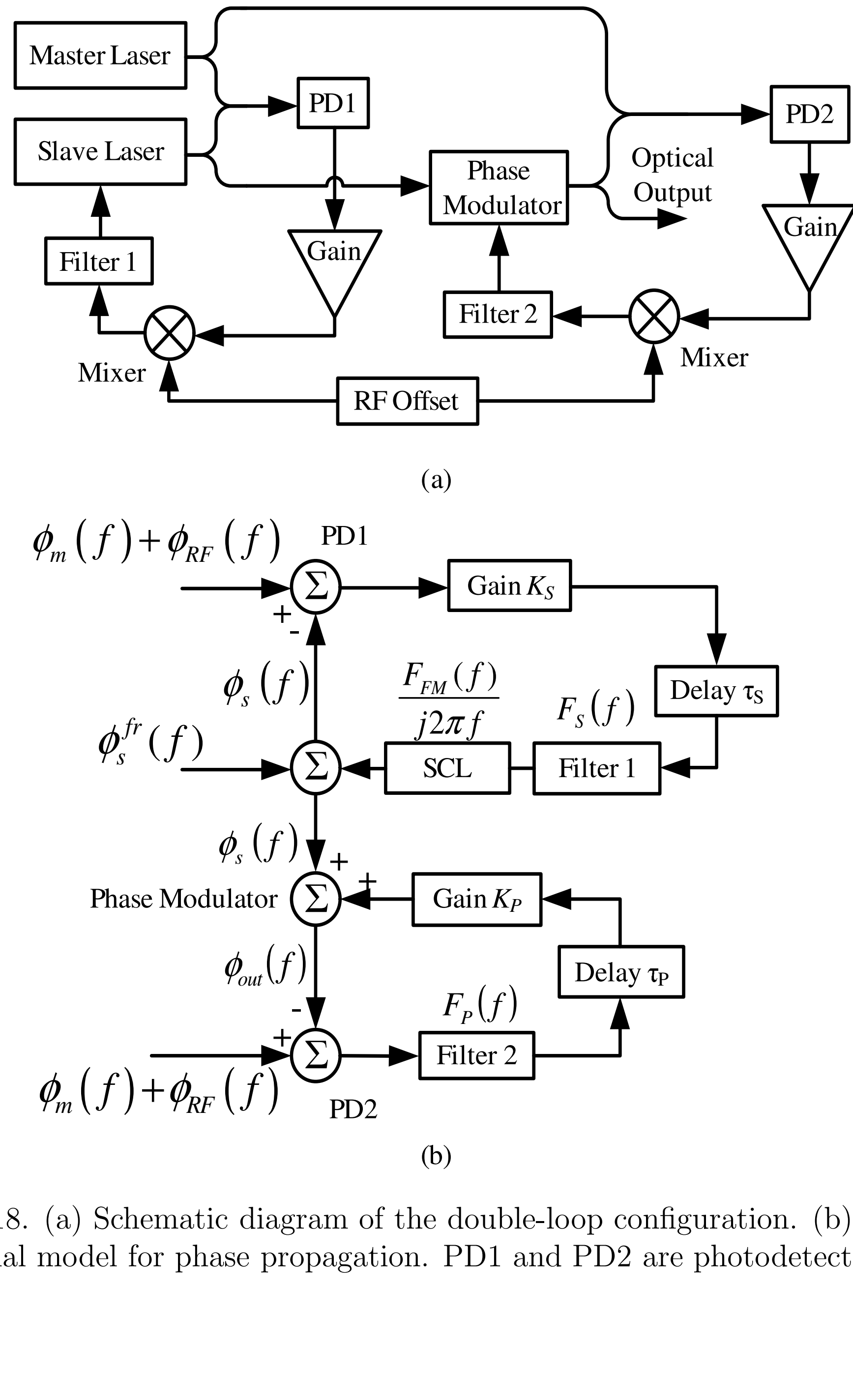

Figure 2.18. (a) Schematic diagram of the double-loop configuration. (b) Linearized small-signal model for phase propagation. PD1 and PD2 are photodetectors.

frequency domain is shown in figure 2.18(b). The DC gain K_P is the product of the gains of the photodetector, mixer, loop amplifier, filter, and the phase modulator. The filter transfer function $F_P(f)$ is assumed to be normalized to unity. For notational simplicity, in this section, we will denote the open-loop transfer function of the simple OPLL (equation (2.10))as $G(f)$ and drop the subscript *op*, and refer to the summed laser linewidth as $\Delta\nu \doteq \Delta\nu_m + \Delta\nu_s$.

This system can simply be analyzed as two separate feedback loops in series. The phase $\phi_s(f)$ of the output of the slave laser locked to the master laser is given by equation(2.12). The open-loop transfer function of the second loop is given by

$$G_P(f) = K_P F_P(f) \exp(-j2\pi f \tau_P). \tag{2.53}$$

The output phase $\phi_{out}(f)$ is related to $\phi_s(f)$ by

$$\phi_{out}(f) = \frac{G_P(f)}{1 + G_P(f)} \left(\phi_m(f) + \phi_{RF}(f)\right) + \frac{1}{1 + G_P(f)} \phi_s(f), \tag{2.54}$$

which, using equation (2.12), reduces to

$$\phi_{out}(f) = \left[\frac{G_P}{1 + G_P} + \frac{G}{(1+G)(1+G_P)}\right] (\phi_m + \phi_{RF}) + \frac{1}{(1+G)(1+G_P)} \phi_s^{fr}, \tag{2.55}$$

where we have omitted the argument f. The spectral density of the residual phase error $\phi_e = \phi_s - \phi_m - \phi_{RF}$ is therefore given by

$$S_\phi^e(f) = \frac{\Delta\nu}{2\pi f^2} \left| \frac{1}{(1 + G(f))(1 + G_P(f))} \right|^2, \tag{2.56}$$

and the variance of the phase error is

$$\sigma_\phi^2 = \int_{-\infty}^{\infty} \frac{\Delta\nu}{2\pi f^2} \left| \frac{1}{(1 + G(f))(1 + G_P(f))} \right|^2 df. \tag{2.57}$$

Comparing equations (2.18) and (2.57), we see that the addition of the second feedback loop causes a reduction in the phase error at frequency f by a factor $|1/(1+$

$G_P(f))|$, and the bandwidth over which the phase noise is reduced can be extended to beyond that of the conventional OPLL, up to the propagation delay limit.

In the preceding analysis, we have made the assumption that the optical path lengths from the master laser and the phase-locked slave laser to the photodetector PD2 are equal, so that the detector is biased at quadrature. (Note that the OPLL forces the two optical fields at PD1 to be in quadrature.) In practice, path length matching may be difficult to achieve without the use of photonic integrated circuits, and this represents a potential drawback of this approach. Further, variations in the relative optical path lengths result in changes in the gain seen by the second feedback loop, resulting in larger residual phase errors. This issue is addressed in the composite OPLL configuration discussed in the next section.

2.7.1.2 Composite PLL

The need for precise optical path length matching is eliminated in the composite PLL architecture shown in figure 2.19(a), where the phase error measurement is performed at a single photodetector PD. This phase error is split into two paths, one of which drives the SCL as in a conventional OPLL, whereas the second path is connected to the input of the optical phase modulator. The output of the phase modulator serves as the useful optical output. The linearized small-signal model for this composite PLL is shown in figure 2.19(b). The gain K_P is again defined here as the product of the DC gains of the photodetector, amplifier, mixer, and Filter 2. This feedback system can be regarded as comprising an integrating path (SCL) and a proportional path (phase modulator). The integral path has large gain only over a limited frequency range, but this is sufficient to track typical frequency drifts of the lasers.

Defining the open-loop transfer functions of the two feedback paths as

$$\begin{aligned} G(f) &= \frac{K_S F_{FM}(f) F_S(f) \exp[-j2\pi f(\tau_1+\tau_2)]}{j2\pi f}, \\ G_P(f) &= K_P F_P(f) \exp(-j2\pi f \tau_2), \end{aligned} \tag{2.58}$$

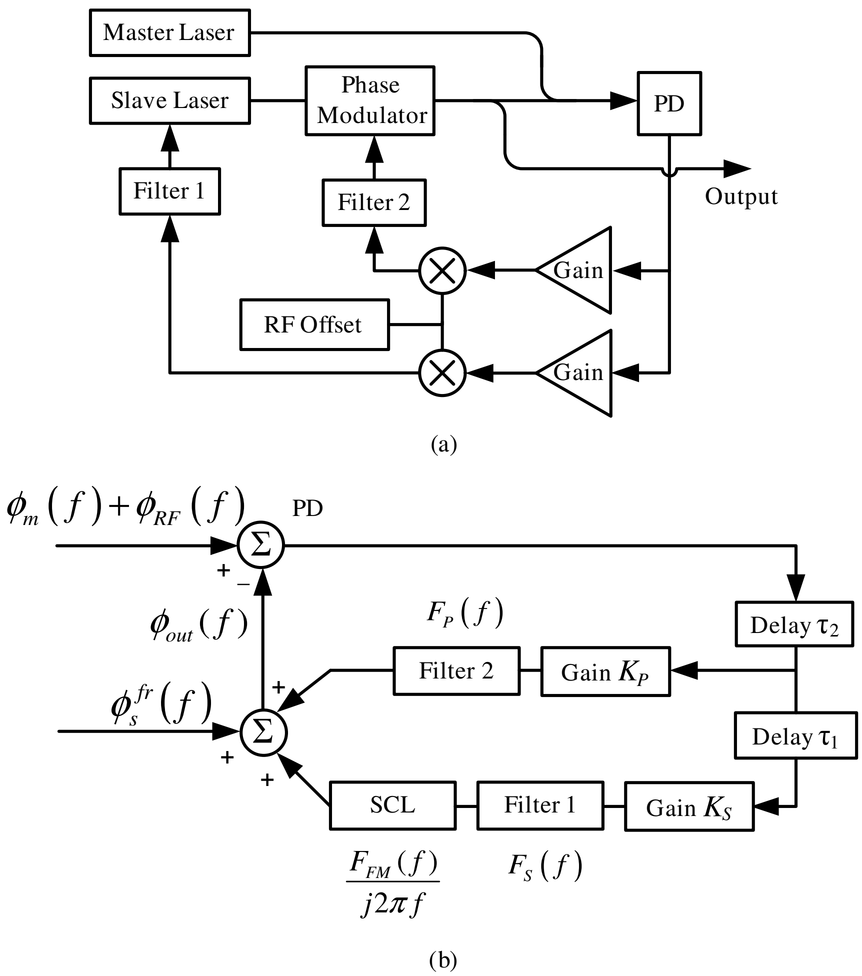

Figure 2.19. (a) Schematic diagram of the composite heterodyne OPLL. (b) Linearized small-signal model for phase propagation. PD: Photodetector.

the output phase is given by

$$\phi_{out}(f) = \frac{G(f)}{1 + G(f) + G_P(f)} \left(\phi_m(f) + \phi_{RF}(f)\right) + \frac{1}{1 + G(f)} \phi_s^{fr}(f), \tag{2.59}$$

and the variance of the residual phase error $\phi_e = \phi_{out} - \phi_m - \phi_{RF}$ is

$$\sigma_\phi^2 = \int_{-\infty}^{\infty} \frac{\Delta\nu}{2\pi f^2} \left| \frac{1}{1 + G(f) + G_P(f)} \right|^2 df. \tag{2.60}$$

The function $G_P(f)$ is chosen so that, at frequencies larger than the FM crossover frequency of the SCL, where the function $G(f)$ exhibits a phase reversal, the gain in the phase modulator arm $G_P(f)$ dominates over the gain in the SCL arm $G(f)$. This ensures phase correction over a larger frequency range, thereby leading to a reduced phase error between the output optical wave and the master laser.

2.7.2 Results

2.7.2.1 Laser Frequency Modulation Response

Two commercial single-mode distributed feedback lasers operating at a wavelength of 1539 nm (JDS-Uniphase) were used in the experimental demonstration. The lasers had a 3 dB linewidth of ~0.5 MHz, and their frequency modulation response exhibited the characteristic phase crossover at a frequency of ~5 MHz as shown in figure 2.20. The FM responses of the two lasers were very similar, and only one curve is shown for clarity. The theoretical fit to the FM response using equation (2.40) is also shown, with fitting parameters $b = 2.7$ and $f_c = 0.76$ MHz.

2.7.2.2 Numerical Calculations

The spectral density of the residual phase error in the loop, and its variance, were numerically calculated for each of the three system configurations shown in figures 2.1, 2.18 and 2.19, using equations (2.18), (2.56) and (2.60) respectively. For the sake of simplicity, the SCL was assumed to have a Lorenzian lineshape (white frequency noise spectrum) with a 3 dB linewidth of 200 kHz, and an FM response as modeled

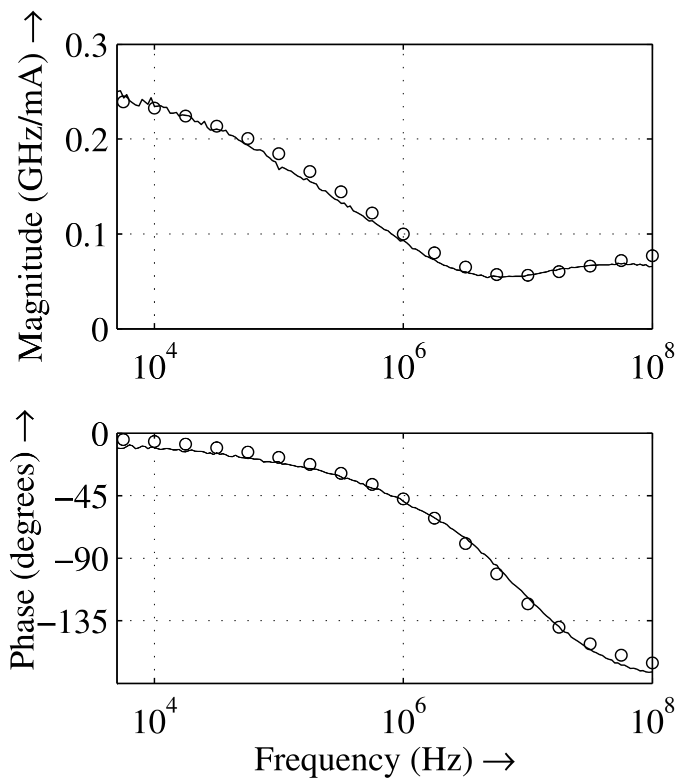

Figure 2.20. Experimentally measured frequency modulation of a single-section distributed feedback semiconductor laser (solid line) and theoretical fit using equation (2.40) (circles).

in the preceding section. The experimentally measured linewidth of the laser is larger than this value, owing to the deviation of the frequency noise spectrum from the ideal white noise assumption (chapter 3, [63]). The propagation delay in each path was assumed to be 8 ns, i.e., $\tau_S = \tau_P = \tau_1 = \tau_2 = 8$ ns. This value was chosen to be a representative value for OPLLs constructed using fiber-optics and discrete electronic components. The parameters of the loop filters were chosen to match the values of the lag filters used in the experiment. The filter transfer functions were given by

$$F_S(f) = \frac{1 + j2\pi f \tau_{Sz}}{1 + j2\pi f \tau_{Sp}}, \tag{2.61}$$

with $\tau_{Sz} = 24$ µs and $\tau_{Sp} = 124$ µs; and

$$F_P(f) = \frac{1 + j2\pi f \tau_{Pz}}{(1 + j2\pi f \tau_{Pp1})(1 + j2\pi f \tau_{Pp2})^2}, \tag{2.62}$$

with $\tau_{Pz} = 15$ ns, $\tau_{Pp1} = 1.3$ µs, and $\tau_{Pp2} = 0.8$ ns. The double-pole at $1/(2\pi\tau_{Pp2}) =$ 200 MHz approximates the finite bandwidth of the op-amp used to construct the filter in the experiment.

With the above parameters, the value of K_S was optimized to result in a minimum residual phase error in the OPLL. With this optimal gain $K_{S,opt}$, the phase modulator gain K_P was optimized to result in a minimum phase error in the double-loop and composite PLL configurations. The calculated spectra of the residual phase error in the loop for the different cases are plotted in figure 2.21. The values of the optimum gain and the residual phase error calculated over an integration bandwidth of ± 50 MHz are tabulated in table 2.2. It can be seen that the standard deviation of the residual phase error is reduced by a factor of 3–4 due to the addition of phase modulator control.

Note that the calculated loop performance is limited by the assumed values of the propagation delay. The values used in the calculations are an order of magnitude larger than the delays that can be achieved using integrated optoelectronic circuits, and therefore the residual phase error achievable in integrated OPLL circuits is ex-

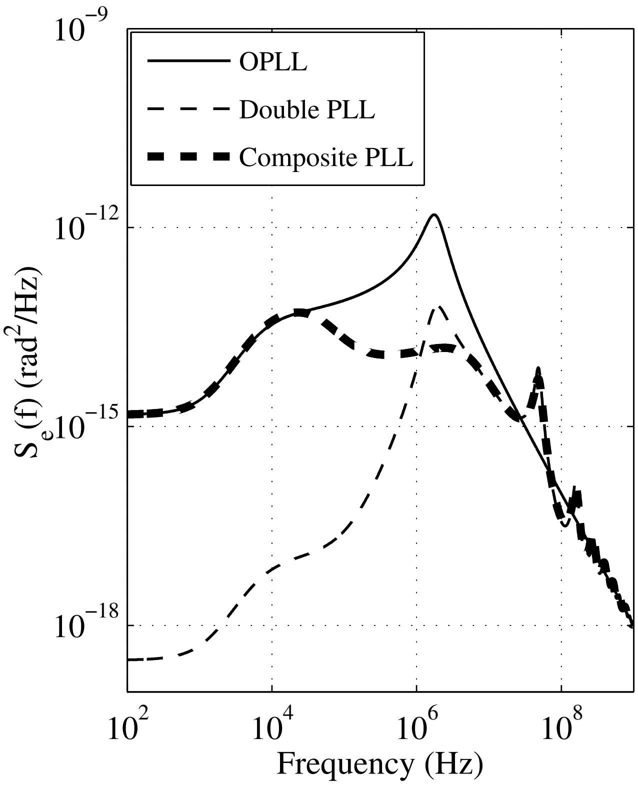

Figure 2.21. Calculated two-sided spectral densities of the residual phase error in the loop, according to equations (2.18), (2.56) and (2.60). The variance of the phase error is the area under the curves. The values of the parameters used in the calculations are listed in the text and in table 2.2.

Table 2.2. Parameters and results of the numerical calculations of the performance of composite OPLLs

System type	Optimal gain	Min. phase error (± 50 MHz BW)
Heterodyne OPLL	$K_{S,opt} = 1.4 \times 10^8$ Hz	$\sigma_\phi = 0.43$ rad
Double-loop	$K_{S,opt} = 1.4 \times 10^8$ Hz $K_{P,opt} = 71.5$	$\sigma_\phi = 0.13$ rad
Composite PLL	$K_{S,opt} = 1.4 \times 10^8$ Hz $K_{P,opt} = 65.8$	$\sigma_\phi = 0.12$ rad

pected to be much smaller. For example, in the composite PLL of figure 2.19, if the delays τ_1 and τ_2 are decreased by one order of magnitude to be equal to 0.8 ns, and if the time constants in the filter $F_P(f)$, viz. τ_{Pz} and τ_{Pp2}, are correspondingly reduced by one order of magnitude, a minimum phase error of $\sigma_\phi = 0.039$ rad over a bandwidth of ± 1 GHz is obtained.

2.7.2.3 Experimental Validation

The reduction in residual phase noise was demonstrated using commercial distributed feedback lasers (JDS-Uniphase) in systems with fiber optical and discrete electronic components (MiniCircuits, Brooklyn, NY). A fiber-coupled $LiNbO_3$ optical phase modulator (EOSpace, Redmond, WA) was used in the experiments, and a narrow-linewidth fiber laser (NP Photonics) was used as the master laser. An RF electronic offset frequency of 1.5 GHz was used in the experiments. The error in the loop was calculated using the (heterodyne) beat signal between the master laser and the phase-locked optical output, and integrating the spectrum.

Double-loop configuration. The double-loop configuration shown in figure 2.18 was constructed with optimized loop filters $F_S(f)$ and $F_P(f)$ as given in equations (2.61) and (2.62), with $\tau_{Sz} = 24$ µs, $\tau_{Sp} = 124$ µs, $\tau_{Pz} = 7.5$ ns and $\tau_{Pp1} = 0.66$ µs. The measured beat signals for (a) the OPLL and (b) the combined double-loop system are shown in figure 2.22. A reduction in the residual phase error (± 50 MHz bandwidth) from 0.31 to 0.16 rad was measured.

Composite PLL. A second, similar SCL was used in the construction of the composite PLL shown in figure 2.19. The loop filter parameters of equations (2.61) and (2.62) were chosen to be $\tau_{Sz} = 24$ µs, $\tau_{Sp} = 124$ µs, $\tau_{Pz} = 15$ ns and $\tau_{Pp1} = 1.3$ µs. The measured spectra of the beat signals corresponding to (a) a conventional heterodyne OPLL using this SCL and (b) the composite PLL are shown in figure 2.23. The residual phase error (± 50 MHz bandwidth) is reduced from 0.28 to 0.13 rad.

The experimentally measured reductions in the phase noise for both the above

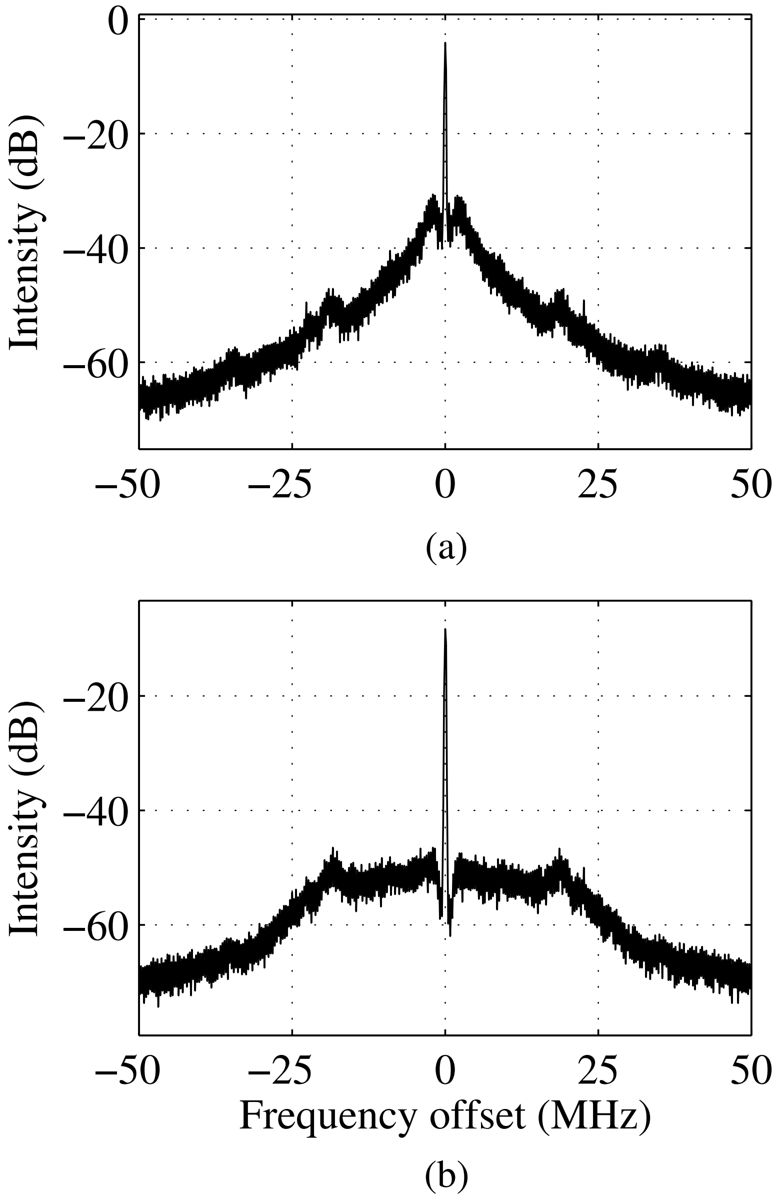

Figure 2.22. Measured spectrum of the beat signal between the optical output and the master laser for an SCL in (a) a heterodyne OPLL, and (b) a double-loop feedback system shown in figure 2.18. Resolution bandwidth = 30 kHz, video bandwidth = 300 Hz.

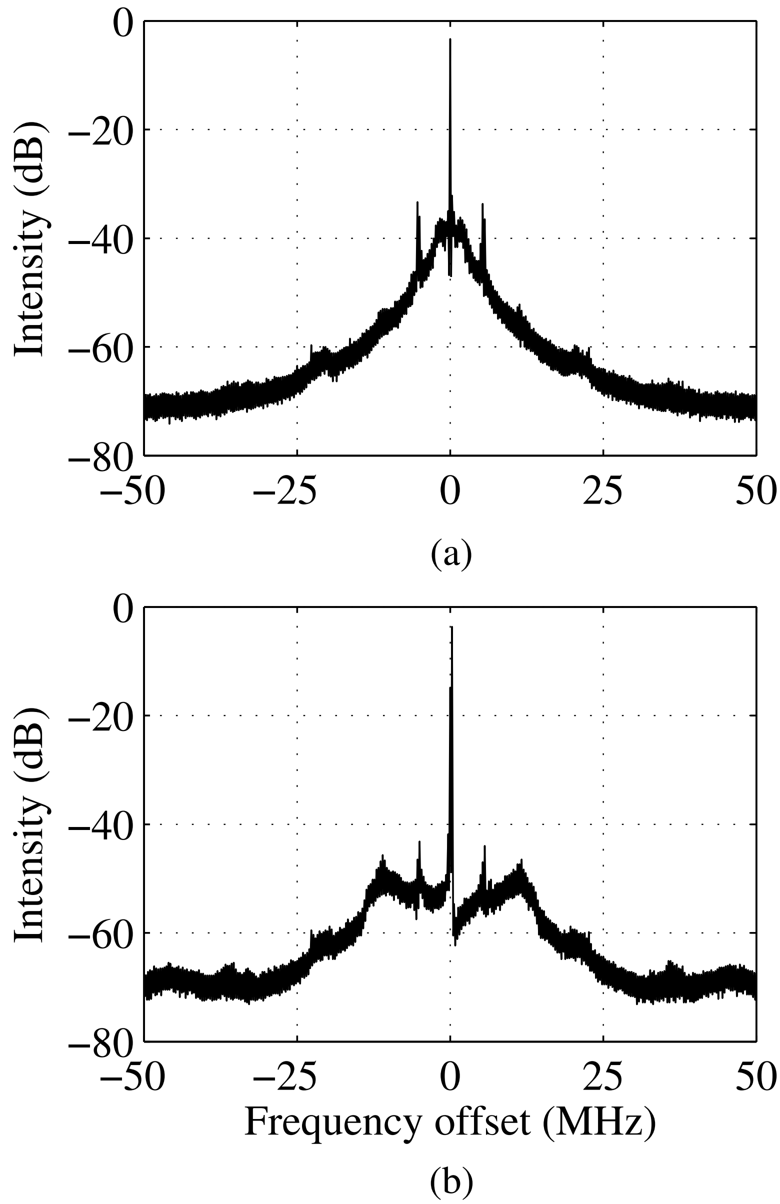

Figure 2.23. Measured spectrum of the beat signal between the optical output and the master laser for an SCL in (a) a heterodyne OPLL, and (b) a composite PLL shown in figure 2.19. Resolution bandwidth = 30 kHz, video bandwidth = 300 Hz.

systems are in fair agreement with the theoretical calculations in table 2.2. The numerical calculations are not exact and are only representative of the expected improvements, since nominal values for the propagation delay and the lineshape of the free-running SCL were assumed. We note that recent independent experiments [38,39] have demonstrated results consistent with figure 2.21 using a feedback system similar to the one developed and analyzed in this work.

2.7.3 Summary

We have proposed and demonstrated experimentally that the residual phase error between the phase-locked optical output of an SCL and the master laser in an OPLL can be further reduced by additional phase correction using an optical phase modulator. *Feedback into the SCL is essential* to compensate for frequency drifts of the SCL due to environmental fluctuations. The use of the additional phase modulator allows large loop bandwidths to be achieved, limited only by propagation delay in the system, as opposed to nonuniformities in the response of the laser. We have demonstrated the phase modulator can be used in two different configurations, both of which yield a considerable reduction in the residual phase error. The experimental demonstrations used fiber optical components and discrete electronic amplifiers and mixers, which caused a large propagation delay and limited the loop bandwidths. The use of integrated photonic circuits in hybrid integrated OPLL systems using these techniques can enable bandwidths of up to a few gigahertz using standard single-section semiconductor lasers and relatively little increase in system complexity.

Chapter 3

Coherence Cloning using SCL-OPLLs

3.1 Introduction

Narrow linewidth fiber lasers and solid state lasers have important applications in the area of fiber-optic sensing, interferometric sensing, LIDAR etc. SCLs are smaller, less expensive and inherently more efficient compared to fiber lasers, dye lasers and solid state lasers. However, they are much noisier due to their small volumes and the low reflectivity of the waveguide facet. The coherence of a high quality master laser, such as a narrow-linewidth fiber laser, can be cloned on to a number of noisy SCLs using OPLLs [81] as shown in figure 3.1. The cloning of the coherence of a single master laser to a number of slave SCLs has important consequences for sensor networks which require a large number of spectrally stabilized laser sources. To appreciate the benefits of this approach, we note that a commercial high-quality fiber laser has a cost of \$10,000–\$25,000, while an SCL typically costs a few hundred dollars, and the OPLL is constructed using inexpensive electronic components. The SCL typically also has a greater output power.

In this chapter, we describe the theoretical and experimental study of coherence cloning of a spectrally stabilized fiber laser to a high power commercial semiconductor DFB laser using an OPLL. We will further analyze the impact of coherence cloning on the observed spectrum in a self heterodyne Mach Zehnder interferometer (MZI).

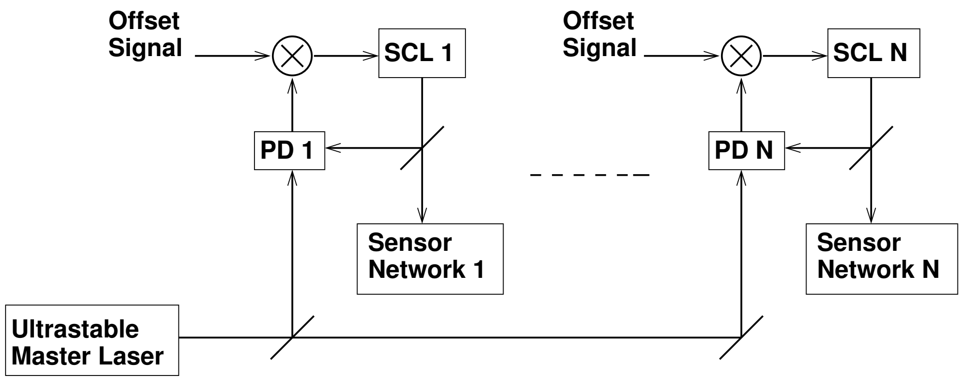

Figure 3.1. Individual SCLs all lock to a common narrow-linewidth master laser, thus forming a coherent array. An offset RF signal is used in each loop for additional control of the optical phase. PD: Photodetector.

Such an experiment is very common and is used for laser lineshape characterization, as well as applications such as interferometric sensing and FMCW LIDAR. We will show that the coherence-cloned slave SCL can act as a substitute for the master laser in the experiment.

3.2 Notation

For any wide sense stationary random process $x(t)$,

- The autocorrelation function is denoted by $R_x(\tau) = \langle x(t)\, x(t-\tau)\rangle$, where $\langle . \rangle$ denotes averaging over the time variable t. It is assumed that time and ensemble averages can be used interchangeably for the random processes considered in this chapter.

- The power spectral density is denoted by $S_x(f)$. From the Wiener-Khintchine theorem, $R_x(\tau)$ and $S_x(f)$ form a Fourier transform pair. In this chapter, we will work with two-sided power spectral densities.

- The variance of $x(t)$ is denoted by σ_x^2. If x is a function of another variable $x(t,\tau)$, we denote its variance by $\sigma_x^2(\tau)$.

3.3 Coherence Cloning in the Frequency Domain

From the small-signal model of the OPLL in figure 2.2(b) and equation (2.12), and ignoring the phase noise of the offset signal, we derive the following expression for the spectral density of the phase of the phase-locked slave SCL:

$$S_\nu^s(f) = S_\nu^m(f)\left|\frac{G_{op}(f)\cos\phi_{e0}}{1+G_{op}(f)\cos\phi_{e0}}\right|^2 + S_\nu^{s,fr}(f)\left|\frac{1}{1+G_{op}(f)\cos\phi_{e0}}\right|^2 \\ +f^2\frac{S_{RIN}^m(f)}{4}\left|\frac{G_{op}(f)\sin\phi_{e0}}{1+G_{op}(f)\cos\phi_{e0}}\right|^2, \qquad (3.1)$$

where $S_\nu^m(f)$, $S_\nu^{s,fr}(f)$ and $S_{RIN}^m(f)$ are the spectral densities of the frequency noise the master laser, the frequency noise of the free-running slave laser, and the RIN of the master laser respectively. From equation (3.1), we find that for frequencies smaller than the loop bandwidth, where $|G_{op}(f)| \gg 1$, the phase noise of the SCL tracks the phase noise of the master laser. For frequencies greater than the loop bandwidth, $|G_{op}(f)| < 1$, and the SCL phase noise reverts to the free-running level. This phenomenon is referred to as coherence cloning.

3.3.1 Experiment

A commercial DFB laser (JDS-Uniphase) is phase-locked to a narrow-linewidth fiber laser (NP Photonics) at an offset of 1.5 GHz using a heterodyne OPLL, as described in chapter 2, and the standard deviation of the residual phase noise is measured to be about 0.32 rad. The phase noise of the master fiber laser and the free-running and phase-locked DFB slave laser are characterized using two measurements. The lineshapes of the lasers are measured using a delayed self heterodyne interferometer with interferometer delay time much larger than the laser coherence time [83]. The frequency noise spectra of the lasers are also directly measured using a fiber MZI as a frequency discriminator [80].

The measured lineshapes of the fiber laser, and the free-running and locked DFB slave laser are plotted on a 50 MHz span in and a 500 kHz span in figure 3.2. The linewidth of the locked DFB laser is the same as that of the fiber laser for frequencies

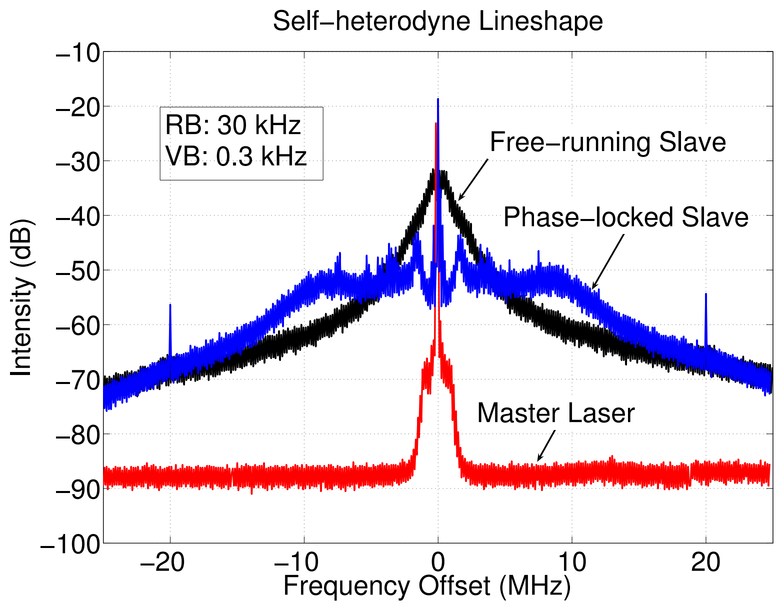

(a)

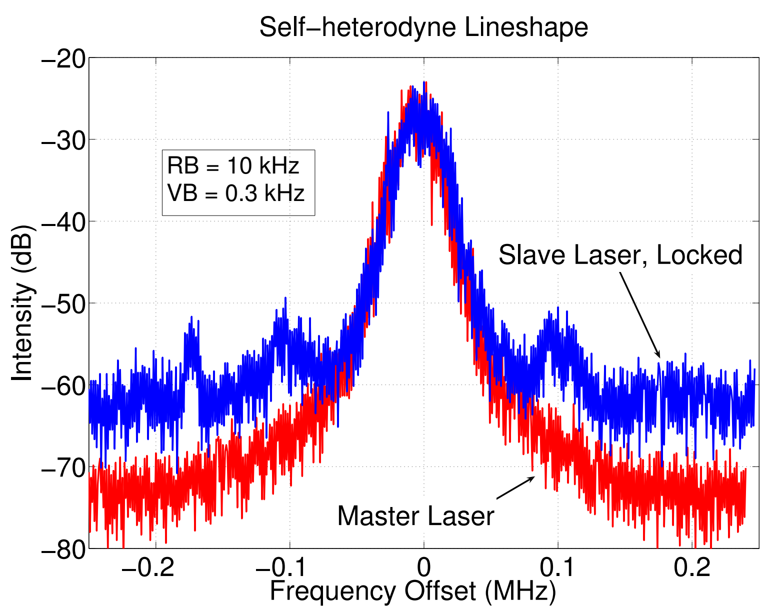

(b)

Figure 3.2. Measured linewidths of the master fiber laser, and the free-running and phase-locked slave SCL.

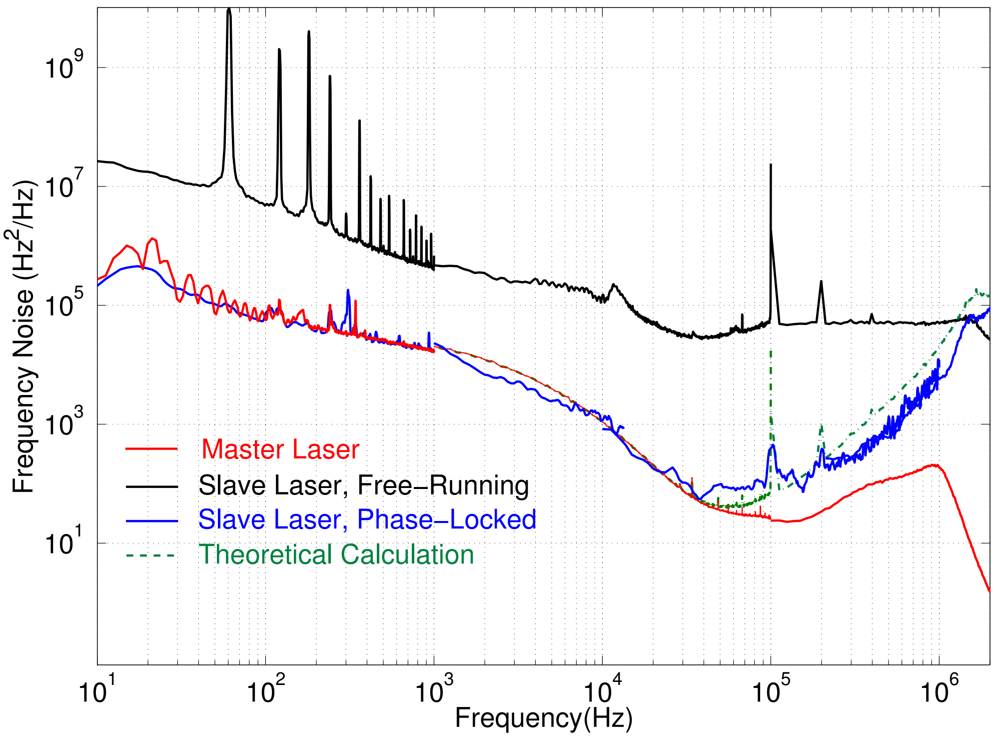

Figure 3.3. Measured frequency noise spectra of the master fiber laser, and the free-running and phase-locked slave DFB semiconductor laser. The green curve is the theoretical calculation of the frequency noise spectrum of the phase-locked slave laser using equation (3.1) and the measured loop parameters.

less than 50 kHz. Above 50 kHz, the linewidth of the locked DFB laser does not completely track the fiber laser due to the limited bandwidth of the OPLL. The 20 dB linewidth of the DFB laser is reduced from 4.5 MHz to 30 kHz.

The measured frequency noise spectra of the master fiber laser and the free-running and locked slave DFB SCL are shown in figure 3.3. The measured frequency noise (blue curve) of the locked DFB laser agrees well with the theoretical calculation (green curve) using equation (3.1). The frequency noise of the locked DFB laser is identical to that of the fiber laser for Fourier frequencies less than 50 kHz, which is consistent with the observation of the lineshapes in figure 3.2(b).

We see, therefore, that the DFB laser inherits the linewidth and frequency noise of the master laser when phase-locked using a heterodyne OPLL. However the coherence cloning is limited to frequencies within the bandwidth of the OPLL.

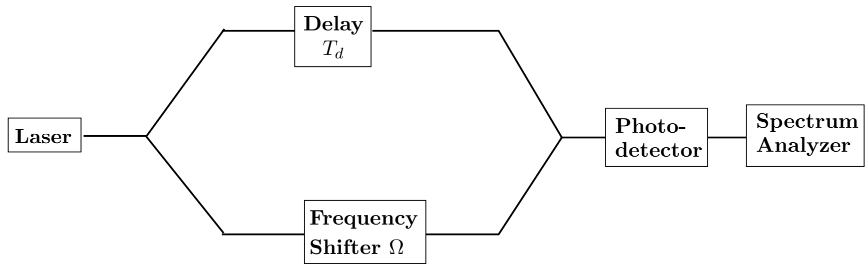

Figure 3.4. Delayed self-heterodyne interferometer experiment

3.3.2 Coherence Cloning and Interferometer Noise

We will now consider the effect of a limited-bandwidth coherence cloning experiment on interferometer noise. In particular, we will consider the Mach Zehnder interferometer (MZI) shown in figure 3.4. The laser output is split into two arms of MZI with a differential delay T_d. One of the arms also has a frequency shifter, such as an electro-optic or acousto-optic modulator that shifts the frequency of the optical field by Ω. This delayed self-heterodyne configuration is very common in a number of applications such as laser lineshape characterization, interferometric sensing and FMCW LIDAR. The laser field is given by $e(t) = a(t)\, e^{j\omega_0 t + \phi(t)}$, where $a(t)$ is the amplitude of the electric field, ω_0 the frequency of the laser, and $\phi(t)$ the laser phase noise. The output of the photodetector in figure 3.4 is given by

$$i(t) = \rho \left| e(t)e^{j\Omega t} + e(t - T_d) \right|^2 . \tag{3.2}$$

The intensity noise of the laser is typically much smaller than the detected phase noise and is neglected in this analysis. Further, without loss of generality, we let $\rho = 1$ and $|a(t)| = 1$ so that the photodetector current (around Ω) is given by

$$\begin{aligned} i(t) &= \Re\left(e^{j[(\omega_0+\Omega)t+\phi(t)]}\, e^{-j[\omega_0(t-T_d)+\phi(t-T_d)]}\right) \\ &= \Re\left(e^{j\omega_0 T_d}\, e^{j\Omega t}\, e^{j\Delta\phi(t,T_d)}\right), \end{aligned} \tag{3.3}$$

where $\Delta\phi(t, T_d) \doteq \phi(t) - \phi(t - T_d)$ is the accumulated phase in the time interval $(t - T_d, t)$. We wish to investigate the effect of coherence cloning on the spectrum of the electric field $e(t)$ and the photocurrent $i(t)$.

3.3.2.1 Coherence Cloning Model

Spontaneous emission in the lasing medium represents the dominant contribution to the phase noise $\phi(t)$ in a free-running semiconductor laser [88]. This gives rise to a frequency noise $\nu(t) = d/dt\,(\phi/2\pi)$ that has a power spectral density

$$S_\nu(f) = \frac{\Delta\nu}{2\pi}, \tag{3.4}$$

which in turn leads to a Lorenzian spectrum for the laser electric field, with full width at half maximum (FWHM) $\Delta\nu$. In practice, there are also other noise sources that give rise to a $1/f$ frequency noise at lower frequencies, as can be seen from figure 3.3. It has been shown [89] that the optical field spectrum of a laser with $1/f$ frequency noise has a Gaussian lineshape as opposed to a Lorenzian lineshape. For simplicity of analysis, we will assume in this chapter that the master and the free-running slave laser have flat frequency noise spectra corresponding to Lorenzian lineshapes with FWHMs $\Delta\nu_m$ and $\Delta\nu_s$ respectively, as shown in figure 3.5. Further, the OPLL is assumed to be an ideal OPLL with bandwidth f_L so that

$$G_{op}(f) = \begin{cases} \infty & \text{if} \quad f \leq f_L, \\ 0 & \text{if} \quad f > f_L. \end{cases} \tag{3.5}$$

Using equation (3.1) and assuming that the effect of the master laser RIN is negligible (as is the case when $\phi_{e0} \ll 1$ even if the RIN is nonnegligible), we obtain

$$S_\nu^{lock}(f) = \begin{cases} \Delta\nu_m/2\pi & \text{if} \quad f \leq f_L, \\ \Delta\nu_s/2\pi & \text{if} \quad f > f_L, \end{cases} \tag{3.6}$$

as shown by the dashed curve in figure 3.5. We denote the reduction in linewidth by β:

$$\beta = \Delta\nu_s - \Delta\nu_m. \tag{3.7}$$

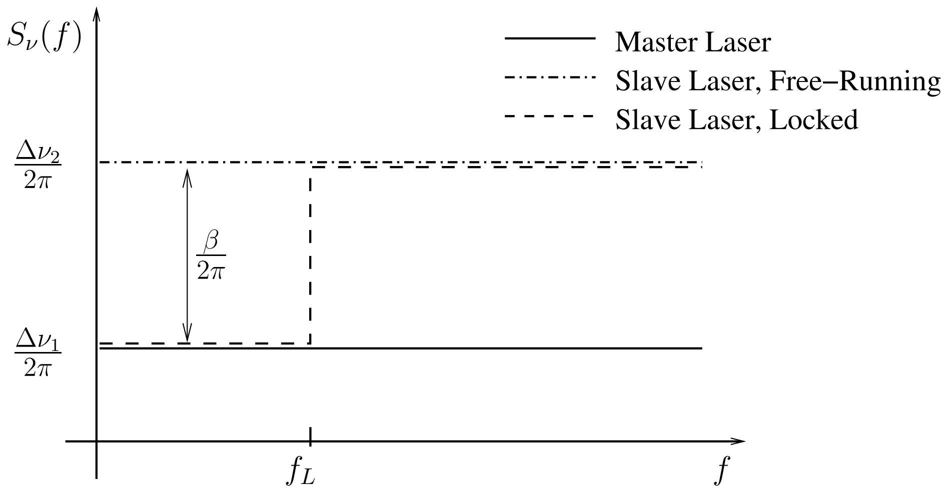

Figure 3.5. Model of the power spectral density of the frequency noise of the master laser and the free-running and locked slave laser. The OPLL is assumed to be "ideal" with a loop bandwidth f_L.

The accumulated phase noise $\Delta\phi\,(t, T_d)$ in equation (3.3) for a free-running laser is the result of a large number of independent spontaneous emission events that occur in the time interval $(t - T_d, t)$, and it follows from the central limit theorem that it is a zero-mean Gaussian random process. In order to simplify the mathematics, it is also assumed that $\Delta\phi\,(t, T_d)$ is a (wide-sense) stationary process. It is a property of Gaussian random variables [90] that the random process obtained by passing a Gaussian random process is passed through a linear time invariant (LTI) filter is also a Gaussian random process.[1] Therefore, the phase noise of a the phase-locked SCL also follows Gaussian statistics. Writing down the autocorrelation of $\Delta\phi\,(t, T_d)$ and taking the Fourier transform, we derive the relation between its spectral density and that of the frequency noise [72, 91]:

$$S_{\Delta\phi(t,T_d)}\,(f) = 4\pi^2\, T_d^2\, S_\nu(f)\,\mathrm{sinc}^2\,(\pi f T_d)\,, \tag{3.8}$$

[1]This follows from the property that a linear combination of Gaussian random process is a Gaussian random process [90, p. 38].

with $\mathrm{sinc}(x) \doteq \dfrac{\sin x}{x}$. The variance of the accumulated phase is therefore given by

$$\sigma^2_{\Delta\phi}\left(T_d\right) = 4\pi T_d \int_{-\infty}^{\infty} S_\nu(f)\, \mathrm{sinc}^2\left(\pi f T_d\right)\, \pi T_d \, df. \tag{3.9}$$

Since $\Delta\phi\left(t, T_d\right)$ is a zero-mean Gaussian process, its statistics (and therefore the statistics of the photocurrent in equation (3.3)) are completely determined by equation (3.9).

We now calculate $\sigma^2_{\Delta\phi}\left(T_d\right)$ for the case of a free-running laser and a phase-locked laser with frequency noise spectra given by equations (3.4) and (3.6) respectively. For a free-running laser, we have from equation (3.9),

$$\begin{aligned}
\sigma^2_{\Delta\phi}\left(T_d\right) &= 2\Delta\nu T_d \int_{-\infty}^{\infty} \mathrm{sinc}^2\left(x\right)\, dx \\
&= 2\pi\Delta\nu T_d \\
&= \frac{2T_d}{t_c}.
\end{aligned} \tag{3.10}$$

Here $t_c = 1/(\pi\Delta\nu)$ is the coherence time of the laser, defined as the time taken for the accumulated phase noise to achieve a root-mean-squared (rms) value of $\sqrt{2}$ radians. This definition of coherence time is a little arbitrary, and other definitions have been used by different authors in literature. The variance of the accumulated phase noise therefore increases linearly with observation time. (Note that $\sigma^2_{\Delta\phi}\left(T_d\right)$ is an even function of T_d.) It is interesting to note that experimental measurements of $\sigma^2_{\Delta\phi}\left(T_d\right)$ show the linear trend of equation (3.10) but have additional damped oscillations at low values of T_d corresponding to the relaxation resonance frequency [92].

For the phase-locked slave laser, we have

$$\begin{aligned}
\sigma^2_{\Delta\phi}\left(T_d\right) &= 4\pi T_d \int_{-\infty}^{\infty} S_\nu^{lock}(f)\, \mathrm{sinc}^2\left(\pi f T_d\right)\, \pi T_d \, df \\
&= 2\Delta\nu_s T_d \int_{-\infty}^{\infty} \mathrm{sinc}^2\left(x\right)\, dx - 2\beta T_d \int_{-\pi f_L T_d}^{\pi f_L T_d} \mathrm{sinc}^2\left(x\right)\, dx \\
&= 2\pi\Delta\nu_2 T_d - 4\beta T_d\, g\left(\pi f_L T_d\right),
\end{aligned} \tag{3.11}$$

where we define the function

$$g(x) \doteq \int_0^x \operatorname{sinc}^2(\alpha)\, d\alpha. \tag{3.12}$$

The second term in equation (3.11) quantifies the improvement in phase noise (or coherence) due to phase-locking. To calculate $g(x)$, we recast equation (3.12) in the form

$$\begin{aligned} g(x) &= \int_0^x \frac{\sin^2\alpha}{\alpha^2}\, d\alpha \\ &= -\left.\frac{\sin^2\alpha}{\alpha}\right|_0^x + \int_0^x \frac{\sin 2\alpha}{\alpha}\, d\alpha \\ &= -\frac{\sin^2 x}{x} + \mathrm{Si}(2x), \end{aligned} \tag{3.13}$$

where $\mathrm{Si}(x)$ is the well-known sine integral [93] $\int_0^x \frac{\sin\alpha}{\alpha}\, d\alpha$, whose values have been numerically computed. The function $g(.)$ has the limits $g(0) = 0$ and $\lim_{x\to\infty} g(x) = \pi/2$.

From equation (3.11), for low values of T_d ($\pi f_L T_d \ll 1$), $\operatorname{sinc}^2(x) \approx 1$, and we have $\sigma^2_{\Delta\phi}(T_d) \approx 2\pi\Delta\nu_s T_d$, whereas for $\pi f_L T_d \gg 1$ we have $g(\pi f_L T_d) \approx \pi/2$ and $\sigma^2_{\Delta\phi}(T_d) \approx 2\pi\Delta\nu_m T_d$. Therefore the variance of the accumulated phase noise follows that of the free-running slave laser for low values of T_d and that of the master laser for large values of T_d. The variation of $\sigma^2_{\Delta\phi}(T_d)$ vs. T_d is numerically calculated and plotted in figure 3.6. The values used in the calculation are $\Delta\nu_1 = 5$ kHz and $\Delta\nu_2 = 500$ kHz. The loop bandwidth f_L is varied between 1 and 100 MHz. It can be seen that $\sigma^2_{\Delta\phi}(T_d)$ follows the free-running slave laser for $T_d \lesssim \frac{1}{10 f_L}$ and is approximately equal to that of the master laser for $T_d \gtrsim \frac{100}{f_L}$.

3.3.2.2 Spectrum of the Laser Field

It is instructive to first calculate the shape of the electric field spectrum, i.e., the spectrum of $e(t) = \cos(\omega_0 t + \phi(t))$ for a free-running and phase-locked laser. To do

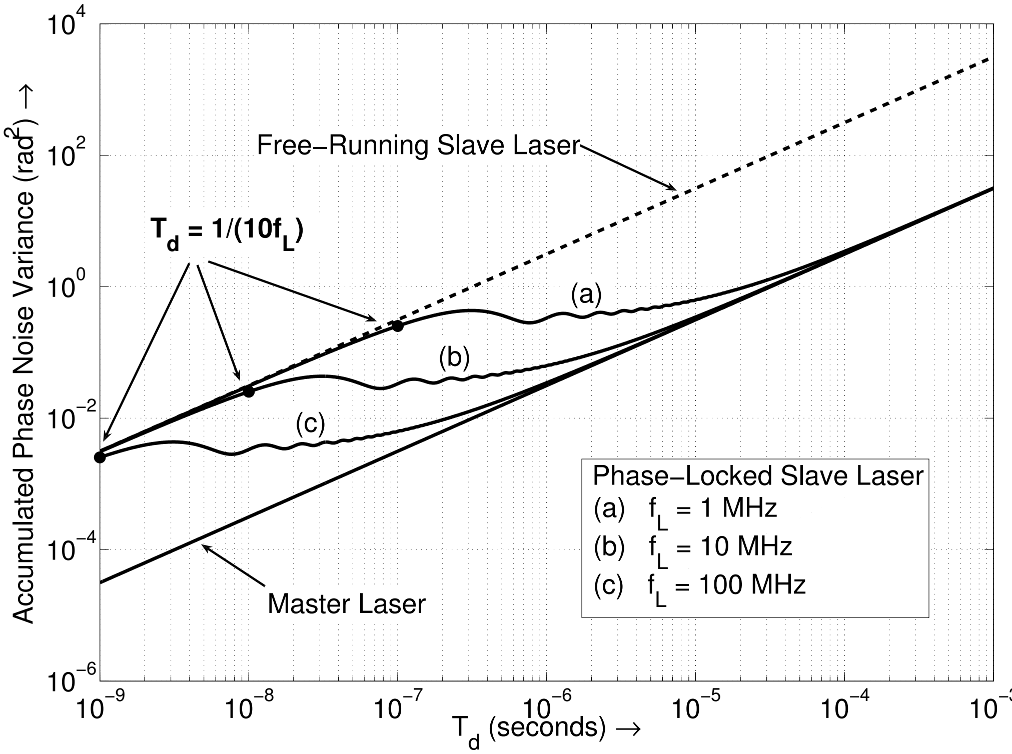

Figure 3.6. Variation of the accumulated phase error variance $\sigma^2_{\Delta\phi}(T_d)$ vs. interferometer delay time T_d for various values of the loop bandwidth f_L. The markers correspond to the delay time $T_d = 1/(10f_L)$. The linewidths of the master laser and the free-running slave laser are assumed to be 5 and 500 kHz respectively.

this, we write down the autocorrelation of the electric field:

$$\begin{aligned}
R_e(\tau) &= \langle e(t)e(t-\tau)\rangle \\
&= \frac{1}{2}\left\langle \cos\left(2\omega_0 t + \omega_0\tau + \phi(t) + \phi(t-\tau)\right) + \cos(\omega_0\tau + \Delta\phi(t,\tau)\right\rangle \\
&= \frac{1}{2}\left\langle \cos(\omega_0\tau)\cos\left(\Delta\phi(t,\tau)\right)\right\rangle \\
&= \frac{\cos(\omega_0\tau)}{2}\exp\left(-\frac{\sigma^2_{\Delta\phi}(\tau)}{2}\right), \qquad (3.14)
\end{aligned}$$

where we have assumed that $\phi(t)$ is constant over one optical cycle and used the result $\langle\cos X\rangle = \exp\left(-\sigma_X^2/2\right)$ for a Gaussian random variable X.[2] From the Wiener-Khintchine theorem, the spectrum of the electric field is given by the Fourier transform of equation (3.14). The $\cos(\omega_0\tau)$ term simply shifts the spectrum of $e^{-\sigma^2_{\Delta\phi}(\tau)/2}$ to the center frequency ω_0. We define the spectrum at baseband by

$$S_{e,b}(f) = \mathcal{F}\left\{\exp\left(-\frac{\sigma^2_{\Delta\phi}(\tau)}{2}\right)\right\}, \qquad (3.15)$$

so that the two-sided spectral density of the field $S_e(f)$ is given by

$$S_e(f) = \frac{1}{4}\left(S_{e,b}\left(f - \frac{\omega_0}{2\pi}\right) + S_{e,b}\left(f + \frac{\omega_0}{2\pi}\right)\right). \qquad (3.16)$$

For a free-running laser, equations (3.10) and (3.15) yields the expected Lorenzian lineshape

$$S_{e,b}(f) = \frac{2}{\pi\Delta\nu}\,\frac{1}{1 + (2f/\Delta\nu)^2}. \qquad (3.17)$$

For the phase-locked laser, the field lineshape is calculated using equations (3.11) and (3.15) and is shown in figure 3.7 for different values of the loop bandwidth f_L. It can be seen that the lineshape of the phase-locked laser follows that of the free-running slave laser for frequencies $f \geq f_L$ and that of the master laser for frequencies $f \lesssim f_L$. This result is in very good agreement with the experimentally measured lineshapes in figure 3.2. We intuitively understand this result by noting that for sufficiently large

[2]This is easily derived by expanding the cosine in terms of complex exponentials and evaluating the expectation by completing squares.

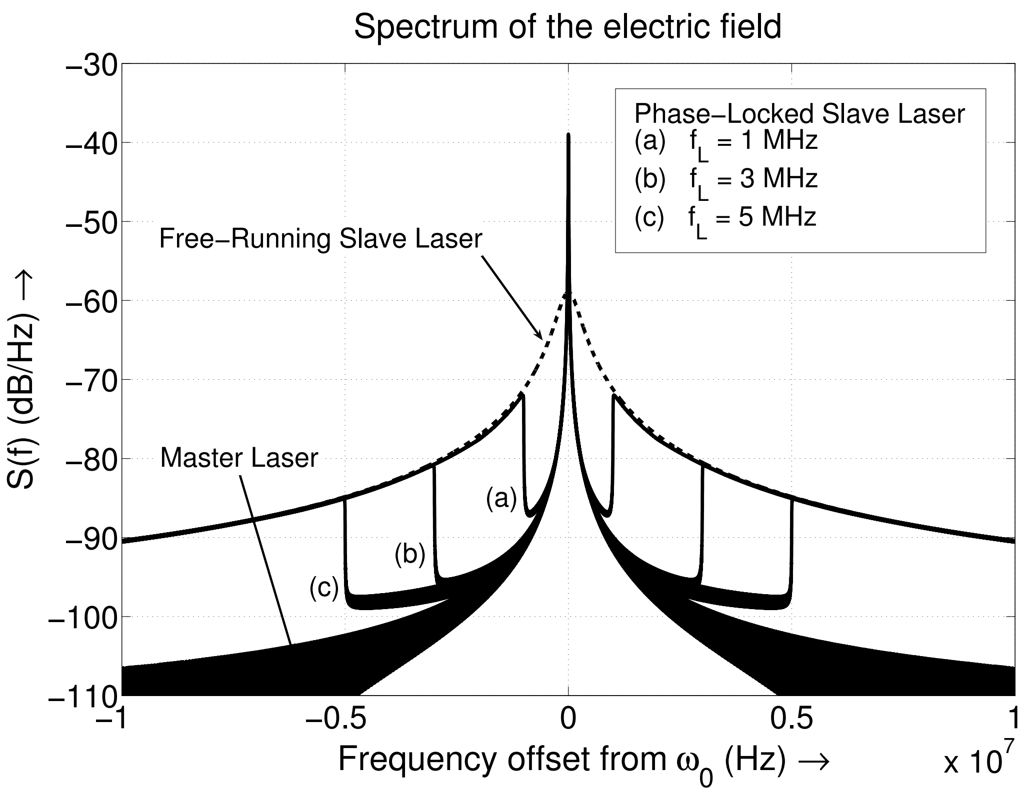

Figure 3.7. Spectral density of the optical field for different values of the loop bandwidth f_L, calculated using equation (3.15). The master laser and the free-running slave laser have Lorenzian lineshapes with FWHM 5 kHz and 500 kHz respectively.

frequencies, the phase noise is much smaller than one radian. We can therefore make the approximation $\cos(\omega_0 t + \phi(t)) \approx \cos(\omega_0 t) + \phi(t)\sin(\omega_0 t)$, and the behavior of the field spectrum in this frequency range is therefore the same as that of the spectrum of the phase noise.

3.3.2.3 Spectrum of the Detected Photocurrent

We now calculate the spectrum of the photocurrent detected in the experimental setup of figure 3.4, i.e., the spectrum of the current $i(t)$ in equation (3.3):

$$i(t) = \cos\left(\omega_0 T_d + \Omega t + \Delta\phi(t, T_d)\right).$$

We begin by deriving the autocorrelation of the photocurrent, similar to equation (3.14)

$$\begin{aligned}
R_i(\tau) &= \langle i(t) i(t-\tau) \rangle \\
&= \langle \cos\left(\omega_0 T_d + \Omega t + \Delta\phi(t, T_d)\right) \cos\left(\omega_0 T_d + \Omega(t-\tau) + \Delta\phi(t-\tau, T_d)\right) \rangle \\
&= \frac{1}{2} \langle \cos\Omega\tau \, \cos\theta(t, T_d, \tau) \rangle \\
&= \frac{\cos\Omega\tau}{2} \exp\left(-\frac{\sigma_\theta^2(T_d, \tau)}{2}\right),
\end{aligned} \tag{3.18}$$

where we define

$$\theta(t, T_d, \tau) \doteq \Delta\phi(t, T_d) - \Delta\phi(t-\tau, T_d). \tag{3.19}$$

In deriving equation (3.18), we have made the assumption that Ω is much larger than the laser linewidth, and used the fact that θ follows Gaussian statistics. The variance of θ is given by

$$\begin{aligned}
\sigma_\theta^2(T_d, \tau) &= \left\langle \theta^2(t, T_d, \tau) \right\rangle \\
&= \left\langle \Delta\phi^2(t, T_d) + \Delta\phi^2(t-\tau, T_d) - 2\Delta\phi(t, T_d)\Delta\phi(t-\tau, T_d) \right\rangle \\
&= 2\sigma_{\Delta\phi}^2(T_d) - 2\langle \Delta\phi(t, T_d)\Delta\phi(t-\tau, T_d) \rangle.
\end{aligned} \tag{3.20}$$

$$
\begin{aligned}
\langle \Delta\phi(t,T_d)\Delta\phi(t-\tau,T_d)\rangle &= \langle (\phi(t)-\phi(t-T_d))\,(\phi(t-\tau)-\phi(t-\tau-T_d))\rangle \\
&= \frac{1}{2}\Big\langle \Delta\phi^2(t,\tau+T_d)+\Delta\phi^2(t-T_d,\tau-T_d) \\
&\qquad - \Delta\phi^2(t,\tau)-\Delta\phi^2(t-T_d,\tau)\Big\rangle \\
&= \frac{1}{2}\sigma^2_{\Delta\phi}\,(\tau+T_d)+\frac{1}{2}\sigma^2_{\Delta\phi}\,(\tau-T_d)-\sigma^2_{\Delta\phi}\,(\tau)\,. \qquad (3.21)
\end{aligned}
$$

Substituting back into equation (3.20), we have

$$
\sigma_\theta^2(T_d,\tau) = 2\sigma^2_{\Delta\phi}\,(T_d)+2\sigma^2_{\Delta\phi}\,(\tau)-\sigma^2_{\Delta\phi}\,(\tau+T_d)-\sigma^2_{\Delta\phi}\,(\tau-T_d)\,. \qquad (3.22)
$$

We again define the baseband current spectrum,

$$
S_{i,b}(f) = \mathcal{F}\left\{\exp\left(-\frac{\sigma_\theta^2(T_d,\tau)}{2}\right)\right\}, \qquad (3.23)
$$

so that the double sided spectral density of the photocurrent is given by

$$
S_i(f) = \frac{1}{4}\left(S_{i,b}\left(f-\frac{\Omega}{2\pi}\right)+S_{i,b}\left(f+\frac{\Omega}{2\pi}\right)\right). \qquad (3.24)
$$

The case of a free-running laser has been studied previously by Richter et al. [83], and will be briefly rederived here. In this case, using $\sigma^2_{\Delta\phi}\,(\tau)=2\pi\Delta\nu|\tau|$ from equation (3.10) in equation (3.22), we obtain

$$
\begin{aligned}
\sigma_\theta^2(T_d,\tau) &= 2\pi\Delta\nu\,(2|\tau|+2T_d-|\tau+T_d|-|\tau-T_d|) \\
&= \begin{cases} 4\pi\Delta\nu|\tau|, & |\tau|\le T_d, \\ 4\pi\Delta\nu T_d, & |\tau|>T_d, \end{cases} \qquad (3.25)
\end{aligned}
$$

which leads to a spectral density

$$
\begin{aligned}
S_{i,b}(f) = e^{-2\pi\Delta\nu T_d}\,\delta(f) &+ \frac{1}{\pi\Delta\nu}\,\frac{1}{1+(f/\Delta\nu)^2} \\
&\times\left[1-e^{-2\pi\Delta\nu T_d}\left(\cos 2\pi f T_d+\pi\Delta\nu\,\frac{\sin 2\pi f T_d}{\pi f}\right)\right]. \qquad (3.26)
\end{aligned}
$$

The resultant spectra for various values of the delay time T_d are shown in figure 3.8, traces (i), (iii). For low values of T_d where $\Delta\nu T_d \ll 1/\pi$, the spectrum is characterized by a sharp delta function accompanied by a pedestal with oscillations. The period of these oscillations corresponds to the delay T_d, or in other words, to the free spectral range of the interferometer. As the value of $\Delta\nu T_d$ increases, the strength of the delta function relative to the pedestal reduces, until we finally obtain a Lorenzian profile for $\Delta\nu T_d \gg 1/\pi$. The FWHM of this Lorenzian is equal to $2\Delta\nu$, as can be expected from beating two identical distinct lasers with linewidths $\Delta\nu$.

For the phase-locked slave laser, we numerically calculate the spectra of the photocurrent using equations (3.23), (3.22) and (3.11). The results of the calculation are shown in figure 3.8. In general, the shape of the spectrum of the photocurrent using the phase-locked slave laser follows that of the master laser with the following important difference. For frequencies larger than the loop bandwidth f_L, the power spectral density of the phase-locked laser increases to the level of the free-running case. However, the features corresponding to the free spectral range of the interferometer are still present. *The improvement in the coherence of the phase-locked SCL manifests itself in the presence of the delta function even at large delay times where the free-running laser results in a Lorenzian output.*

In most practical sensing applications involving lasers, the delay time T_d is much smaller than the coherence time of the laser, in the regime shown in figure 3.8(a). In this case, the presence of a pedestal constitutes a deviation from the "ideal" case of a delta function, and represents unwanted noise in the interferometric sensing measurement. Comparing the spectra of the master laser and the phase-locked laser in figure 3.8(a), we see that the noise level is almost identical for small frequencies, but the phase-locked laser has greater noise for frequencies greater than the OPLL bandwidth. However, this additional noise level is still many orders of magnitude below the delta function, and is outside the signal bandwidth so that it can be filtered out using a narrow bandwidth electrical filter. The coherence-cloned slave SCL can therefore perform well as a substitute for the high-quality master laser.

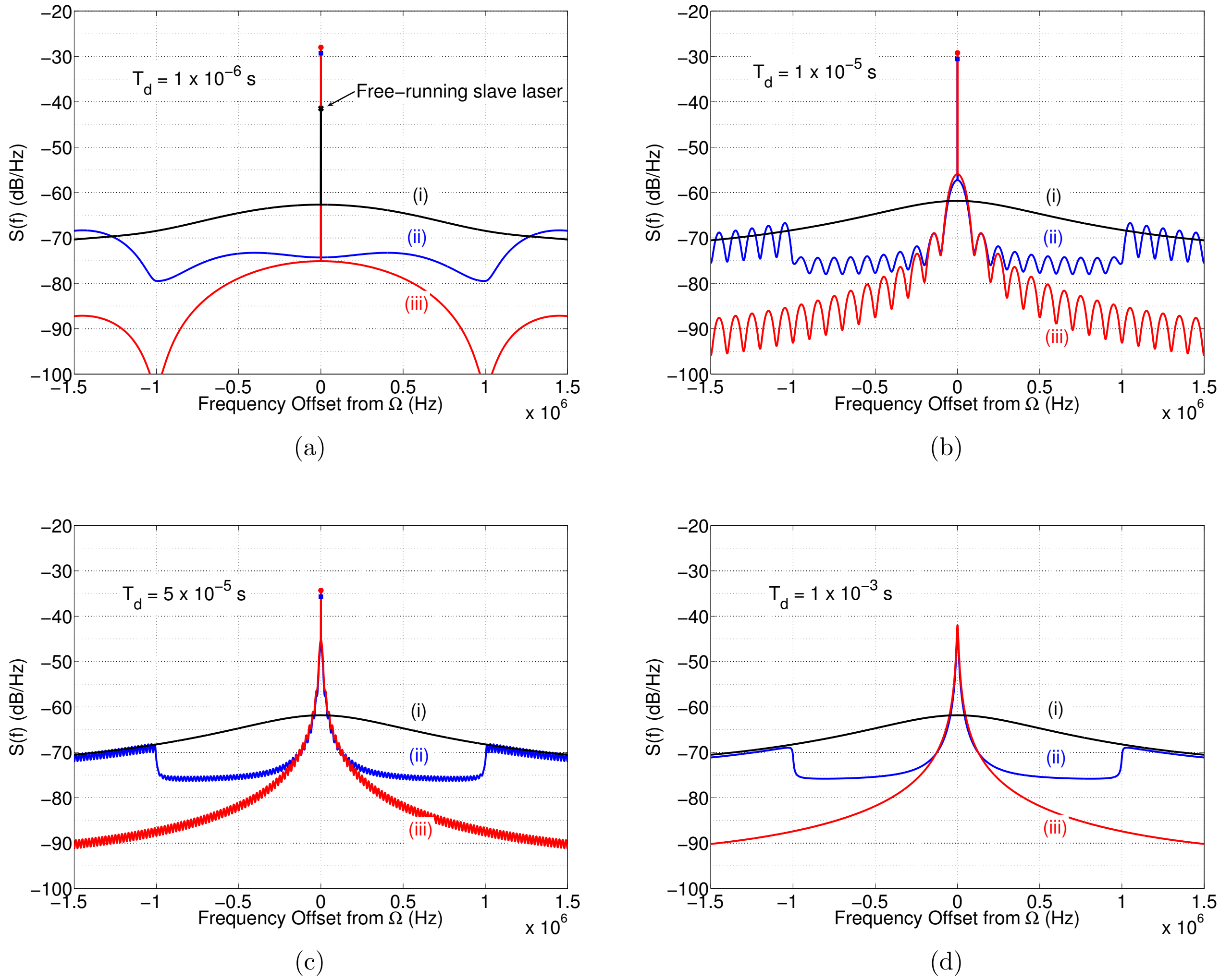

Figure 3.8. Spectral density of the detected photocurrent in a delayed self heterodyne experiment using the free-running slave laser (i), the phase-locked slave laser (ii), and the master laser (iii). The markers denote the height of the delta function. The spectra are calculated using equation (3.23), for different values of the interferometer delay T_d: (a) $T_d = 10^{-6}$ s. (b) $T_d = 10^{-5}$ s. (c)$T_d = 5$ x 10^{-5} s. (d)$T_d = 10^{-3}$ s. The master laser and free-running slave laser linewidths are assumed to be 5 and 500 kHz respectively, and the loop bandwidth is assumed to be $f_L = 1$ MHz.

3.3.3 Summary

In summary, we have demonstrated the concept of "coherence cloning," i.e. the cloning of the spectral properties of a high quality master laser to an inexpensive SCL using an OPLL, and shown that the cloned SCL can act as a substitute for the master laser in interferometric sensing applications. The bandwidth over which the spectrum is cloned is limited by physical factors such as the FM response of the SCL and the OPLL propagation delay. Using a simple model for the coherence cloning, we have investigated the effect of this limited bandwidth on the spectrum of the laser electrical field and on the result of interferometric experiments using the laser, which are common in many sensing applications. We have demonstrated that the spectrum of the field of the locked laser follows the master laser for frequencies lower than the loop bandwidth, and follows the free-running spectrum for higher frequencies. We have further shown that a similar behavior is observed in interferometric experiments. Since the additional noise due to the limited loop bandwidth appears at high frequencies greater than the loop bandwidth, it can be electronically filtered off using a narrow bandwidth filter.

While we have analyzed the effects of a coherence cloning approach using OPLLs, the results are valid for any general feedback-based linewidth narrowing approach, since the bandwidth of linewidth reduction is always finite and limited by the propagation delay in the feedback scheme.

3.4 Time-Domain Characterization of an OPLL

In the previous section, we have described the rigorous characterization of the performance of the OPLL by a measurement of the spectral density of the frequency noise of the lasers. In this section, we investigate the characterization of a heterodyne OPLL in the time domain using a frequency counter. This measurement technique, used widely in the characterization of oscillators [94], is simpler than the frequency-domain measurement of the phase noise, since it eliminates the need for stabilized frequency discriminators. We also show that the measurement can be used to obtain a more accurate measurement of the residual phase error of the OPLL, σ_ϕ.

We will continue to assume that the master and the free-running slave laser have flat frequency noise spectra corresponding to Lorenzian lineshapes with FWHMs $\Delta\nu_m$ and $\Delta\nu_s$ respectively, as shown in figure 3.5, and that the OPLL is ideal with bandwidth f_L as given by equation (3.5):

$$G_{op}(f) = \begin{cases} \infty & \text{if} \quad f \leq f_L, \\ 0 & \text{if} \quad f > f_L. \end{cases}$$

Under these assumptions, equation (2.18) yields

$$\sigma_\phi^2 = \frac{\Delta\nu_m + \Delta\nu_s}{\pi f_L}. \tag{3.27}$$

Whereas a measurement of the spectral density is a thorough characterization of the phase (or frequency) noise of a signal, a simpler measurement, the Allan variance [94], is often used to characterize the stability and phase noise of oscillators. For an oscillator of frequency ν_0 and frequency noise $\nu(t)$, we define the fractional frequency fluctuation $y(t) = \nu(t)/\nu_0$. The Allan variance $\sigma_y^2(\tau)$ is defined as the two-sample variance of the fractional frequency fluctuations [95], i.e.,

$$\sigma_y^2(\tau) = \frac{1}{2}\left\langle (\bar{y}_2 - \bar{y}_1)^2 \right\rangle, \tag{3.28}$$

where $\bar{y}_1$ and $\bar{y}_2$ are consecutive measurements of the average value of $y(t)$, averaged over a gate period τ. As before, $\langle . \rangle$ is the expectation value. There is no “dead time” between the measurements $\bar{y}_1$ and $\bar{y}_2$. In practice, a frequency counter is used to measure the average fractional frequency fluctuation $\bar{y}$.

The Allan variance can be related to the spectral density of the phase noise following a straightforward derivation [95]. From equation (3.28),

$$\begin{aligned}\sigma_y^2(\tau) &= \frac{1}{2}\left\langle\left(\frac{1}{\tau}\int_t^{t+\tau} y(t')\,dt' - \frac{1}{\tau}\int_{t-\tau}^{t} y(t')\,dt'\right)^2\right\rangle \\ &= \left\langle\left(\int_{-\infty}^{\infty} y(t')h_\tau(t-t')\,dt'\right)^2\right\rangle, \end{aligned} \tag{3.29}$$

with

$$h_\tau(t) = \begin{cases} -\dfrac{1}{\sqrt{2}\tau} & \text{for} \quad -\tau < t < 0, \\ +\dfrac{1}{\sqrt{2}\tau} & \text{for} \quad 0 \le t < \tau, \\ 0 & \text{otherwise.} \end{cases} \tag{3.30}$$

In the frequency domain, equation (3.29) can be written as

$$\begin{aligned}\sigma_y^2(\tau) &= \int_{-\infty}^{\infty} |H_\tau(f)|^2\, S_y(f)\,df \\ &= 4\int_0^{\infty} \frac{\sin^4(\pi\tau f)}{(\pi\tau f)^2} S_y(f)\,df, \end{aligned} \tag{3.31}$$

where we have calculated the Fourier transform $H_\tau(f)$ of $h_\tau(t)$. By definition, the spectral density of the fractional frequency fluctuations is

$$S_y(f) = \frac{1}{\nu_0^2} S_\nu(f) = \left(\frac{f}{\nu_0}\right)^2 S_\phi(f). \tag{3.32}$$

The Allan variance can therefore also be written as

$$\sigma_y^2(\tau) = \left(\frac{2}{\pi\tau\nu_0}\right)^2 \int_0^{\infty} \sin^4(\pi\tau f) S_\phi(f)\,df, \tag{3.33}$$

3.4.1 Experiment

The statistics of the relative frequency noise between the slave laser and the master laser were measured in this experiment. The Allan variance of the slave laser is the sum of the Allan variance of the master laser and the measured relative variance. Since the principal idea behind phase-locking is to clone the properties of the slave laser to

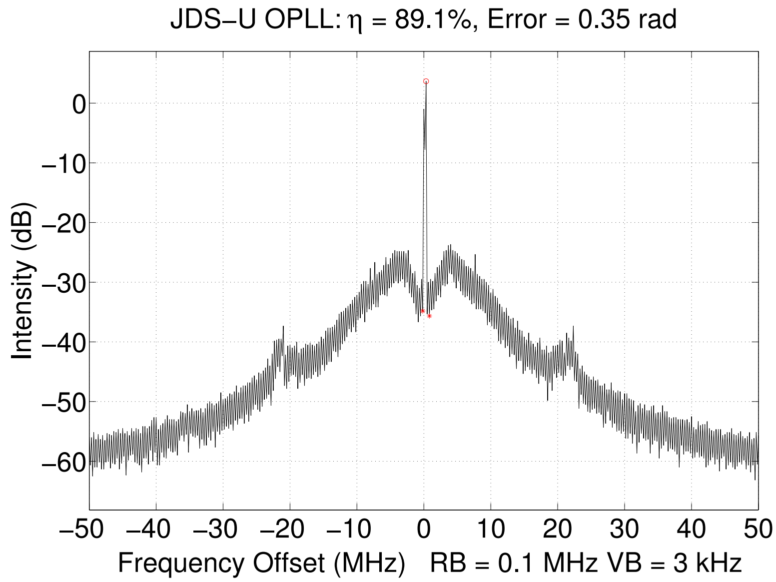

Figure 3.9. Spectrum of the beat signal between the phase-locked slave SCL and the master laser.

the master laser, the measurement of the relative stability sufficiently characterizes the OPLL. A commercial DFB laser (JDS-Uniphase) was phase-locked to a high quality fiber laser (NP Photonics) in a heterodyne OPLL, with an offset frequency $\nu_0 = 800$ MHz. An RF spectrum analyzer and a frequency counter (SR620, Stanford Research Systems, Sunnyvale, CA) were used to characterize the beat signal between the slave and master lasers.

The measured beat spectrum between the phase-locked SCL and the master laser is shown in figure 3.9, and by integrating the noise power over a bandwidth of ± 50 MHz around the offset frequency, we obtain $\eta = 89.1\%$ and $\sigma_\phi = 0.35$ rad. Note that the residual phase error calculated from this measurement is typically a function of the bandwidth over which the noise is integrated, and a large bandwidth has to be chosen in order to achieve accurate results.

3.4.1.1 Allan Variance and Stability

A frequency counter was used to measure the Allan variance of the beat signal between the master laser and the slave laser, for gate times between $\tau = 20$ ns and $\tau = 0.5$ s. The expectation value in equation (3.28) was calculated by averaging over 1000

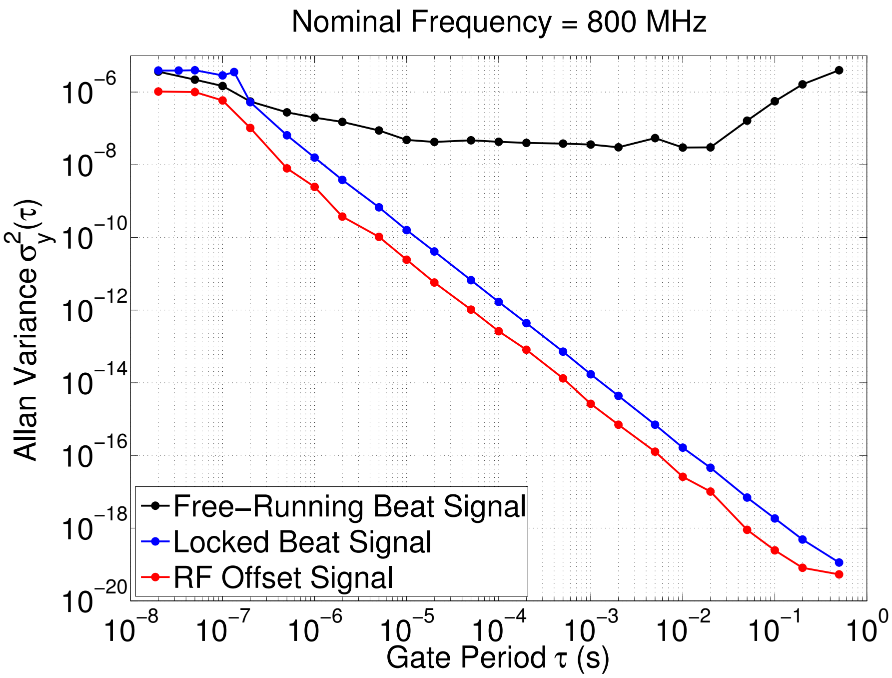

Figure 3.10. Measured Allan variance of the beat signal between the slave and master lasers for the locked and unlocked cases. The variance of the RF offset signal is also shown.

measurements. The results are plotted in figure 3.10. The free-running beat signal displays a large variance, which increases for large gate periods. Such a behavior indicates that the frequency noise spectrum of the slave laser is not flat; rather, the laser displays flicker frequency noise ($S_\nu(f) \sim f^{-1}$) or a random-walk type of frequency noise ($S_\nu(f) \sim f^{-2}$) [95]. This observation is consistent with the measured frequency spectrum of the free-running slave laser (figure 3.3), which shows that the frequency noise spectrum is not flat at low frequencies. The measured Allan variance of the phase-locked laser shows a marked improvement over the free-running case for measurement time scales larger than the inverse of the loop bandwidth (approximately 1–5 MHz), demonstrating the ability of the OPLL to improve the long-term stability of the slave semiconductor laser. The Allan variance of the offset signal is typically an order of magnitude smaller than the variance of the phase-locked beat signal, validating the assumption that the phase noise of the offset signal may be neglected in the analysis.

To understand the behavior of the laser beat signal for the phase-locked case, we consider the simplified model of the OPLL introduced in equation (3.5). Using equations (2.16) and (3.5) in equation (3.33), we obtain

$$\begin{aligned}\sigma_y^2(\tau) &= \left(\frac{2}{\pi\tau\nu_0}\right)^2 \int_0^\infty \sin^4(\pi\tau f) S_\phi^e(f)\,df \\ &= \left(\frac{2}{\pi\tau\nu_0}\right)^2 \int_{f_L}^\infty \sin^4(\pi\tau f) \frac{\Delta\nu_m + \Delta\nu_s}{2\pi f^2}\,df\end{aligned}$$

$$\sigma_y^2(\tau) = \frac{2(\Delta\nu_m + \Delta\nu_s)}{\pi^2\tau\nu_0^2} \int_{\pi\tau f_L}^\infty \frac{\sin^4 x}{x^2}\,dx. \tag{3.34}$$

To evaluate the integral above, we note that

$$\sin^4 x = \frac{3}{8} + \frac{1}{8}\cos 4x - \frac{1}{2}\cos 2x, \tag{3.35}$$

and

$$\begin{aligned}\int_a^\infty \frac{\cos x}{x^2}\,dx &= -\left.\frac{\cos x}{x}\right|_a^\infty - \int_a^\infty \frac{\sin x}{x}\,dx \\ &= \frac{\cos a}{a} - \left(\frac{\pi}{2} - \int_0^a \frac{\sin x}{x}\,dx\right) \\ &= \frac{\cos a}{a} + \mathrm{Si}(a) - \frac{\pi}{2},\end{aligned} \tag{3.36}$$

where $\mathrm{Si}(x)$ is the sine integral [93]. The integral in equation (3.34) is then given by (with $a = \pi\tau f_L$)

$$\begin{aligned}\int_a^\infty \frac{\sin^4 x}{x^2}\,dx &= \int_a^\infty \left(\frac{3}{8x^2} + \frac{\cos 4x}{8x^2} - \frac{\cos 2x}{2x^2}\right) dx \\ &= \frac{1}{a}\left(\frac{3}{8} + \frac{1}{8}\cos 4a - \frac{1}{2}\cos 2a\right) + \frac{\pi}{4} + \frac{1}{2}\mathrm{Si}(4a) - \mathrm{Si}(2a) \\ &= \frac{\sin^4 a}{a} + \frac{\pi}{4} + \frac{1}{2}\mathrm{Si}(4a) - \mathrm{Si}(2a).\end{aligned} \tag{3.37}$$

The Allan variance is therefore given by

$$\sigma_y^2(\tau) = \frac{2(\Delta\nu_m + \Delta\nu_s)}{\pi^2\tau\nu_0^2}\left(\frac{\sin^4 \pi\tau f_L}{\pi\tau f_L} + \frac{\pi}{4} + \frac{1}{2}\mathrm{Si}(4\pi\tau f_L) - \mathrm{Si}(2\pi\tau f_L)\right). \tag{3.38}$$

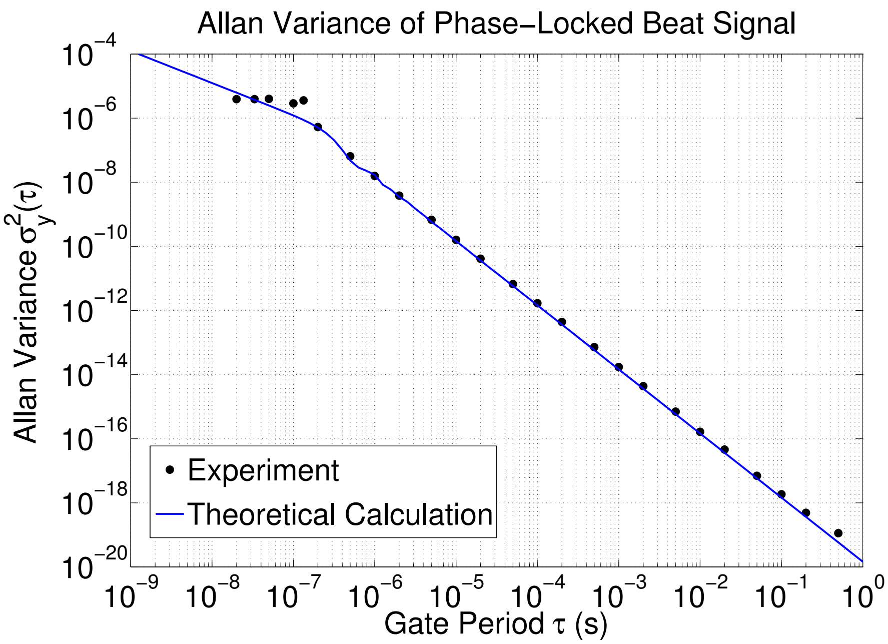

Figure 3.11. Measured Allan variance of the beat signal between the phase-locked slave laser and the master laser, and the theoretical calculation based on equation (3.38). Experimental values of $\sigma_\phi = 0.35$ rad and $\Delta\nu_m + \Delta\nu_s = 0.5$ MHz were used in the calculation.

The measured Allan variance and the theoretical calculation using equation (3.38) are plotted in figure 3.11. The loop bandwidth is calculated from the measured residual phase error $\sigma_\phi = 0.35$ rad and the measured linewidth $\Delta\nu_m + \Delta\nu_s = 0.5$ MHz using equation (3.27). The calculated loop bandwidth is $f_L = 1.3$ MHz. *Note that no freely varying parameters were used to fit the calculation to the data.* The theoretical calculations match the experimental data well, especially at larger gate periods. The discrepancy at lower gate periods (smaller than the inverse of the loop bandwidth) is probably due to a combination of factors: (i) the inaccuracy of the simplified OPLL model (3.5) and (ii) the limitation of the frequency counter in measuring frequencies at very short gate periods. Further investigation is necessary to explain this discrepancy, but the excellent fit at longer gate times suggests that the measurement of the Allan variance is can be an accurate tool to characterize the performance of an OPLL.

3.4.1.2 Residual Phase Error, Revisited

In the previous section, we have considered a particular, simplified, model for the OPLL and calculated the Allan variance of the laser beat signal based on this model. In this section, we will show that the Allan variance measurement can be used to calculate the residual phase error in the OPLL, *irrespective of the shape of the loop transfer function* $G_{op}(f)$. We will only assume that the loop suppresses all the phase noise at frequencies much smaller than the loop bandwidth; this assumption is clearly valid as seen in figure 3.3. The residual phase error in the loop is a key metric in many applications, and its accurate measurement is essential.

We start with equation (3.33):

$$\begin{aligned}\sigma_y^2(\tau) &= \left(\frac{2}{\pi\tau\nu_0}\right)^2 \int_0^\infty \sin^4(\pi\tau f) S_\phi^e(f)\, df \\ &\simeq \left(\frac{2}{\pi\tau\nu_0}\right)^2 \int_{f_1}^\infty \sin^4(\pi\tau f) S_\phi^e(f)\, df \end{aligned} \tag{3.39}$$

for some f_1 much smaller than the loop bandwidth. Let us now choose $\tau \gg 1/f_1$. Then, for frequencies over which the integration is carried out, we have $2\pi\tau f \gg 2\pi$, so that the $\sin^4(.)$ function is rapidly oscillating. The spectral density $S_\phi^e(f)$ does not change appreciably over one period of oscillation, and we can approximate the Allan variance as

$$\begin{aligned}\sigma_y^2(\tau) &\simeq \left(\frac{2}{\pi\tau\nu_0}\right)^2 \left(\frac{1}{\pi}\int_0^\pi \sin^4 x\, dx\right) \int_{f_1}^\infty S_\phi^e(f)\, df \\ &= \left(\frac{3}{2\pi^2\tau^2\nu_0^2}\right) \int_{f_1}^\infty S_\phi^e(f)\, df. \end{aligned} \tag{3.40}$$

From equation (2.15), the integral above is simply half the variance of the residual phase error in the loop, since the spectrum of the phase error is zero at low frequencies. We therefore have a relation between the loop residual phase error and the Allan variance of the laser beat note:

$$\sigma_\phi^2 = \frac{4\pi^2\tau^2\nu_0^2}{3}\sigma_y^2(\tau), \quad \text{for } (1/\tau) \ll \text{ the loop bandwidth.} \tag{3.41}$$

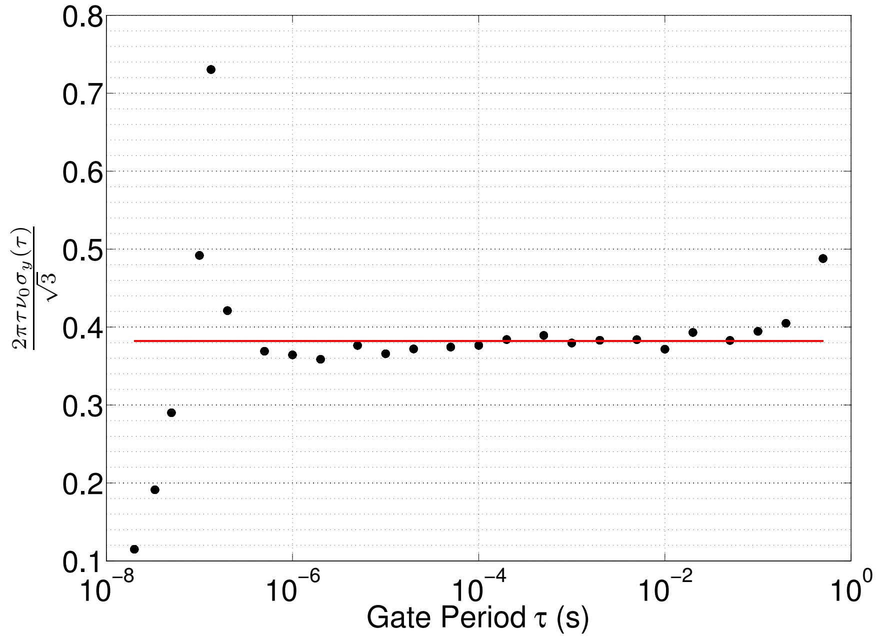

Figure 3.12. Residual phase error calculated from the measured Allan variance using equation (3.41). Using $\tau \gg 10^{-6}$, we obtain $\sigma_\phi = 0.38$ rad.

From the experimental measurement of $\sigma_y(\tau)$, the value $2\pi\tau\nu_0\sigma_y(\tau)/\sqrt{3}$ is calculated and plotted in figure 3.12. It is clear that for large-enough τ, this measurement yields a constant value for the standard deviation of the residual OPLL phase error, here equal to 0.38 rad. This value is about 10% higher than the value calculated from the spectrum in figure 3.9, demonstrating that the spectral method of phase-error calculation tends to underestimate the actual value.

3.4.2 Summary

In this section, we have investigated the use of a frequency counter for the time-domain characterization of the performance of an OPLL. The measured Allan variance of the beat signal between the master laser and the slave SCL clearly shows the improvement in stability and the reduction of the frequency noise of the slave laser by the process of phase-locking. We have shown that theoretical calculations of the Allan variance using a simplified model of an ideal OPLL are in very good agreement with the experimentally measured values. Finally, we have shown that the Allan variance measurement at gate periods much longer than the inverse loop bandwidth of the OPLL can be used to calculate the residual phase error in the loop, which is an important metric in determining loop stability. The residual phase error measured using this method is larger than the value estimated from spectral measurements of the laser by about 10%, a discrepancy attributed to the finite bandwidth of the spectral measurement.

Chapter 4

Phase-Controlled Apertures

When a number of slave SCLs are locked to the same master laser, they all inherit the same coherence properties, as shown in chapter 3. Further, the heterodyne OPLL configuration allows the optical phase to be controlled by varying the electronic phase of the RF offset signal, enabling phase-controlled apertures. In this chapter, we explore applications of such phase-controlled apertures in coherent power-combining and electronic beam-steering.

4.1 Coherent Power-Combining

High power lasers with ideal (diffraction-limited) beam quality are sought after in a multitude of applications including scientific research, materials processing and industrial applications, and research in this direction has been in progress ever since the invention of the laser. While high power (few kilowatts single mode) fiber laser systems have been demonstrated [96, 97], their output powers will ultimately be limited by nonlinear effects in the fiber and material damage. An alternate approach to obtain high power laser radiation with excellent beam quality is by combining a large number of laser emitters with lower power outputs [98–100]. In particular, coherent beam-combining (CBC) is a very promising approach to synthesize high-power optical sources with ideal beam quality. Various coherent beam-combining schemes have been demonstrated by different groups, including evanescent wave-coupling, self-organizing [99], injection locking [100], common resonator [101] and

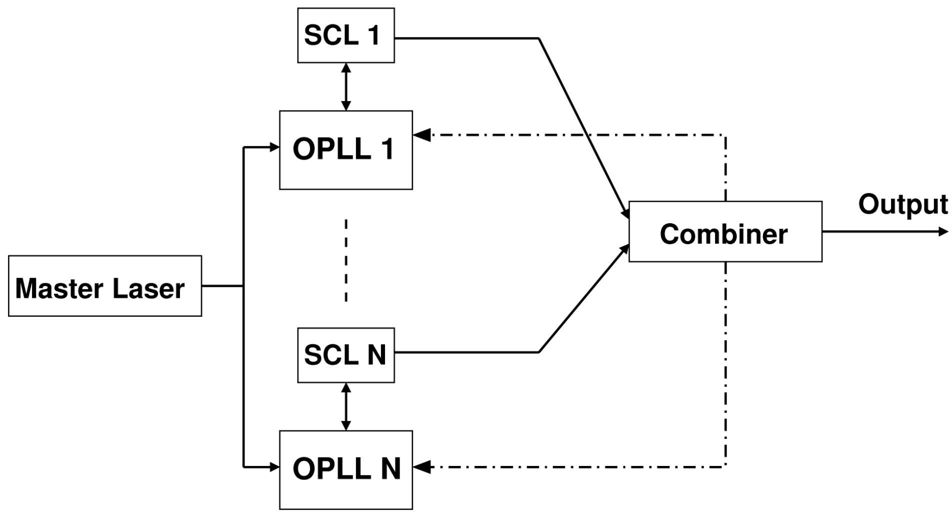

Figure 4.1. Coherent power-combining scheme using heterodyne SCL-OPLLs. Individual SCLs all lock to a common master laser, thus forming a coherent array. The outputs of the individual lasers are coherently combined to obtain a high power single-mode optical beam.

active feedback [102] approaches. While it is desirable to match the relative amplitudes, phases, polarizations and pointing directions of all the component beams to achieve maximum efficiency in a CBC scheme [98], the precise control over the optical phase offers the biggest challenge. Various active feedback approaches for phase control have been demonstrated, where the phase error between the combining beams is fed back to a servo system that includes phase actuators, which could be optical phase modulators [100], acousto-optic modulators [102] or fiber stretchers [103].

In this section, we describe an alternative active feedback approach for CBC where the outputs of an array of SCLs phase-locked to a common master laser are coherently combined to obtain a single high power coherent optical beam as shown in figure 4.1. The use of SCLs has many distinct advantages such as their compactness, high efficiency, low cost and high output power, thereby making them attractive candidates for coherent power combination. The small size and high output powers of SCLs offer the potential for the combination of a number of SCLs on a single chip, leading to extremely compact high power sources. The optical phase of each SCL in a coherent combining scheme can then be controlled *electronically*, which eliminates the need for optical phase or frequency shifters that are bulky, expensive and require the use of large voltages.

Coherent power combination results in optical beams with superior beam quality and larger peak intensities as compared to incoherent power addition. There are two approaches to CBC [98]: (a) the filled-aperture approach where multiple beams are combined into a single beam using a beam-combiner, and (b) the tiled-aperture approach, where the outputs of the individual emitters are adjacent to each other. One of the key aspects in either approach is the control over the relative phases of the individual emitters at the beam combiner. In this section, we concentrate on the filled-aperture approach, while tiled-aperture beam-combining and wavefront control is described in section 4.2.

4.1.1 Experiment

A schematic of the filled-aperture power-combining experiment is shown in figure 4.2(a). Two slave SCLs are locked to a common master laser using fiber-based heterodyne OPLLs as shown in figure 2.1. A common RF offset signal (in the range of ∼0.8–1.7 GHz) is fed to each loop. It is only necessary to use a small fraction of the SCL output in the feedback loop, and the remaining power is used for power combination. The outputs of the two SCLs are combined using a 2×1 fiber combiner, and the output is measured on an oscilloscope. The result of the experiment with high power MOPAs as slave SCLs (QPC Lasers, see table 2.1) is shown in figure 4.2(b). For time <2.5 seconds, one of the lasers is unlocked, and the resultant incoherent addition results in high frequency oscillations on the oscilloscope at the (time-varying) beat frequency between the two SCLs.

When both the loops are in lock (time >2.5 seconds), the result is a "DC" signal that varies very slowly (on the timescale of a few seconds). The combined power is given by

$$P_c = P_0(1 + \cos\theta), \tag{4.1}$$

where θ is the phase difference between the two combining beams. For maximal power-combining efficiency, we need $\theta = 0$. There are two causes of a deviation from

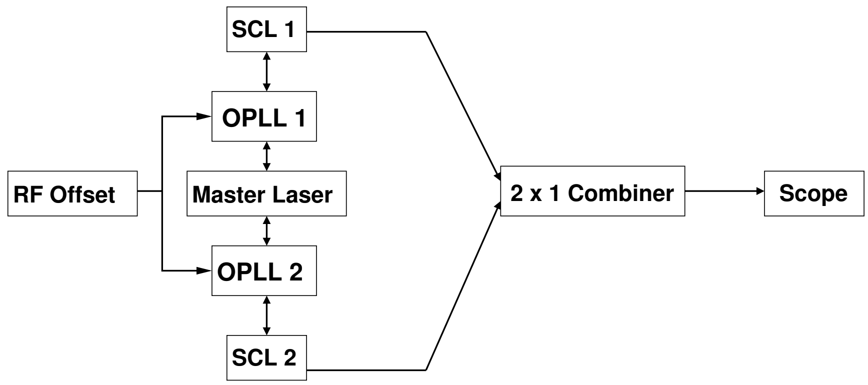

(a)

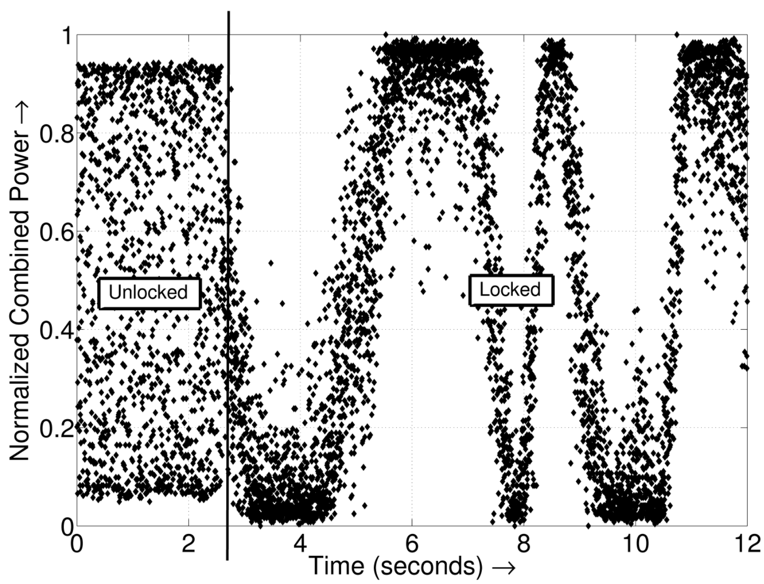

(b)

Figure 4.2. (a) Coherent combination schematic. Two SCLs are locked to a common master laser at a common offset, and the combined output is measured on an oscilloscope. (b) Experimentally measured combined power using two high power MOPAs as slave lasers phase-locked to a common master laser. For $t < 2.5$ seconds, one of the OPLLs is not in lock, and the result is the incoherent power addition of the two lasers.

this ideal value. In fiber-based systems, variations in the differential optical paths of the two combining beams cause a change in phase; this is the cause of the slow drift. The differential phase change may be several full waves, especially if fiber amplifiers are used at the SCL outputs, and a technique to eliminate the effect of this slow drift is described in the next section. In addition to the slow drift, the combined power signal also shows fast variations due to the residual phase noise between the two combined beams. The RMS value of the residual phase error is estimated from the *fast* variations in the measurement in figure 4.2(b) to be about 0.39 radians. This corresponds to a residual phase error of $0.39/\sqrt{2} = 0.28$ radians in each OPLL, which is in excellent agreement with the measured value in table 2.1.

4.1.2 Phase Control Using a VCO

We now describe a novel electronic feedback scheme developed to correct for the slow drift in the relative phase between the optical beams. The variations in the differential optical paths traversed by combining beams is traditionally controlled using a piezoelectric fiber stretcher, an acousto-optic modulator or an optical phase modulator [100, 102, 103]. The phase of the phase-locked SCL in a heterodyne OPLL follows the phase of the RF offset signal, and this allows for the electronic control over the optical phase. The phase of the RF offset signal can be tuned using an RF phase shifter, but this method has the same shortcomings as an optical phase shifter, i.e., insufficient dynamic range to correct for large phase errors [66]. Typical optical or RF phase modulators have a dynamic range of 2π radians, and complicated reset-circuitry is often necessary to increase the dynamic range. In the alternative phase-control scheme described here, the correction signal is provided by an electronic VCO. In addition to acting as an integrating phase shifter with practically infinite dynamic range, the VCO also provides the RF offset signal to the heterodyne OPLL.

A schematic of the power-combining experiment with the VCO correction loop is shown in figure 4.3(a). Two SCLs are phase-locked to a common master laser using heterodyne OPLLs. While an RF source provides a fixed offset signal to one OPLL,

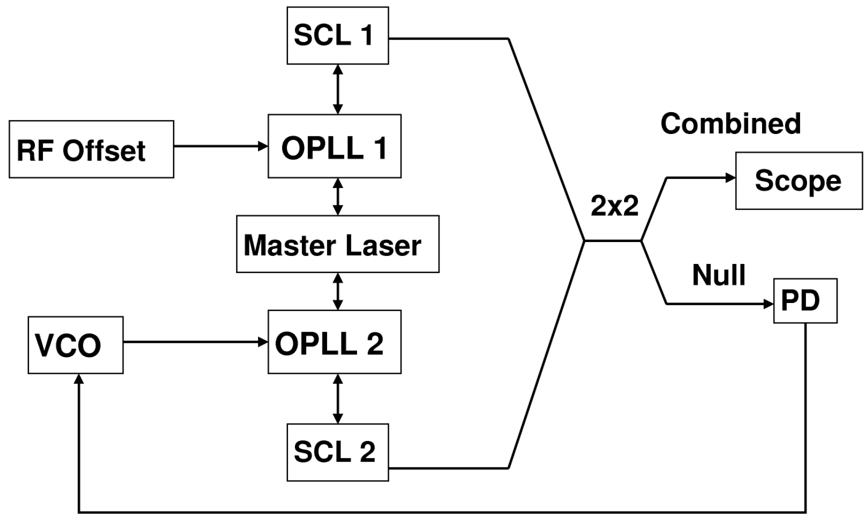

(a)

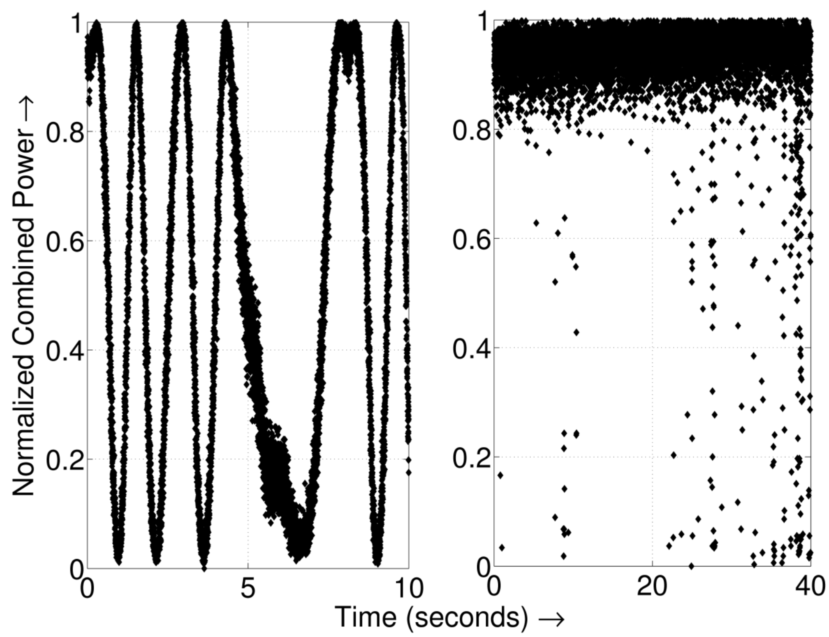

(b)

Figure 4.3. (a) Schematic of the coherent combination experiment with additional electronic phase control. A VCO provides the offset signal to the second OPLL, and also acts as an integrating phase shifter to correct for variations in the differential optical path length. (b) Experimentally measured combined power using external cavity SCLs at 1064 nm, without (left) and with (right) the VCO loop connected. The power-combining efficiency with the VCO loop is 94%.

the offset signal to the other OPLL is provided by a VCO. The nominal free-running frequency of the VCO is chosen to be equal to the frequency of the RF source. The outputs of the two lasers are combined using a 2×2 fiber coupler. One of the outputs of the coupler (the "combined" output) is observed on an oscilloscope, while the other output (the "null" output) is amplified and fed into the control port of the VCO. The measured combined power signal, with and without the VCO control loop, in the power-combining experiment using external cavity lasers (Innovative Photonic Solutions, see table 2.1) is shown in figure 4.3(b). A stable power-combining efficiency of 94% is obtained using the VCO phase-correction loop. This efficiency is mainly limited by the jitter of the free-running frequency of the VCO used in the experiment and not by the residual phase noise in the OPLL, and can therefore be further improved by the use of cleaner VCOs. The VCO frequency jitter is also responsible for the occasional cycle slips seen in figure 4.3(b).

4.1.2.1 Steady-State Analysis

We begin by noting that the behavior of SCL 1 in the system shown in figure 4.3(a) is well understood, both in terms of its steady state and transient performance. Therefore, we will confine ourselves to the analysis of the OPLL with SCL2, and the effects of the power combination feedback on this loop. We first find the steady state operating point of this part of the system. Under steady state, the system can be modeled as in figure 4.4, where the intrinsic phase noise of the lasers, thermal and mechanical fluctuations in the fiber, and the phase noise of the VCO are neglected. The $1-\cos(.)$ term reflects the fact that the output of this detector is out of phase with the combined output in equation (4.1). We assume that the loop filters $G_2(s)$ and $G_v(s)$ have unity gain at DC. We can then write down the equations for the phase "error" signals θ_2 and θ_v at the outputs of the photodetectors:

$$\omega_m t - \left(\omega_{s2}^{fr} t + \int K_2 \sin\theta_2 \, dt\right) + \omega_v^{fr} t + \phi_v = \theta_2, \tag{4.2}$$

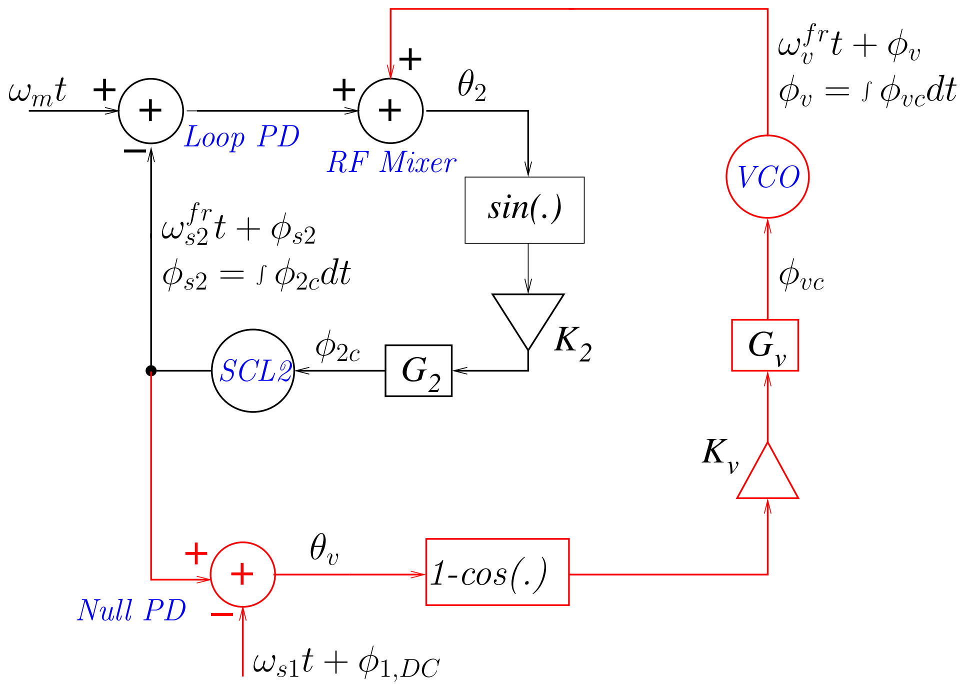

Figure 4.4. Steady-state model for the loop OPLL 2 shown in figure 4.3(a). The frequency of SCL 1 *in its locked state* is denoted by ω_{s1}, and $\phi_{1,DC}$ represents any constant phase difference between the lasers at the "null" photodetector input. The free-running frequencies of Laser 1 and the VCO are ω_{s2}^{fr} and ω_v^{fr} respectively. The frequency of the master laser is ω_m.

so that

$$\dot{\theta}_2 = \left(\omega_m - \omega_{s2}^{fr} + \omega_v^{fr}\right) - K_2 \sin\theta_2 + \dot{\phi}_v. \tag{4.3}$$

Similarly, at the other photodetector,

$$\omega_{s2}^{fr} t + \int K_2 \sin\theta_2 \, dt - \omega_{s1} t - \phi_{1,DC} = \theta_v, \tag{4.4}$$

$$\dot{\theta}_v = \left(\omega_{s2}^{fr} - \omega_{s1}\right) + K_2 \sin\theta_2, \tag{4.5}$$

since $d\phi_{1,DC}/dt = 0$. The VCO phase ϕ_v is given by

$$\phi_v = \int K_v \left(1 - \cos\theta_v\right) \, dt, \tag{4.6}$$

$$\dot{\phi}_v = K_v \left(1 - \cos\theta_v\right). \tag{4.7}$$

The steady state phase errors θ_2 and θ_v are found by setting their time derivatives to zero in equations (4.3) and (4.5), and using the value of $\dot{\phi}_v$ obtained in equation (4.7):

$$\begin{aligned} \theta_{2,s} &= \sin^{-1} \frac{\left(\omega_{s1} - \omega_{s2}^{fr}\right)}{K_2}, \\ \theta_{v,s} &= \cos^{-1} \left(1 - \frac{\left(\omega_{s1} - \omega_m - \omega_v^{fr}\right)}{K_v}\right). \end{aligned} \tag{4.8}$$

Now, we note that ω_{s1} represents the frequency of SCL 1 *when it is locked* to the master laser at a frequency offset of ω_{RF}, so that

$$\omega_{s1} = \omega_m + \omega_{RF}. \tag{4.9}$$

When this is plugged back into equations (4.8), we find the steady state phase errors:

$$\begin{aligned} \theta_{2,s} &= \sin^{-1}\frac{\left(\omega_m + \omega_{RF} - \omega_{s2}^{fr}\right)}{K_2}, \\ \theta_{v,s} &= \cos^{-1}\left(1 - \frac{\left(\omega_{RF} - \omega_v^{fr}\right)}{K_v}\right). \end{aligned} \tag{4.10}$$

Plugging this back into the model in figure 4.4, we find the frequencies of SCL2 and the VCO in lock:

$$\begin{aligned} \omega_{s2} &= \omega_m + \omega_{RF}, \\ \omega_v &= \omega_{RF}. \end{aligned} \tag{4.11}$$

The above results are consistent with the intuitive interpretation that SCL2 is locked to the master laser at the offset frequency ω_v, and ω_v in turn is locked to the frequency reference ω_{RF}.

The steady-state error $\theta_{v,s}$ in equation (4.10) represents the phase difference between the two combining SCLs in equation (4.1), and it is clear that a large K_v is desirable so that $\theta_{v,s}$ is close to zero,[1] and a high efficiency is achieved. Further, $\theta_{v,s}$ can be tuned by varying the free-running VCO frequency ω_v^{fr}.

4.1.2.2 Small-Signal Analysis

We next linearize the phase difference θ_v about the steady state value $\theta_{v,s}$. We drop the subscript v in θ_v. The small-signal model for the VCO control system is shown in figure 4.5. SCL1 is locked to the master laser in OPLL1 and its phase noise ϕ_{s1} is given by equation (2.12):

$$\phi_{s1}(s) = (\phi_m(s) + \phi_{RF}(s))\frac{G_L(s)}{1 + G_L(s)} + \phi_{s1}^{fr}(s)\frac{1}{1 + G_L(s)}, \tag{4.12}$$

where we have substituted $G_L(s)$ for $G_{op}(s)$, and neglected ϕ_{e0}. The free-running phase noise of the VCO and the slave SCL2 are denoted by ϕ_{vn} and ϕ_{s2}^{fr} respectively.

[1]The loop locks stably only for $\theta_{v,s}$ on one side of zero.

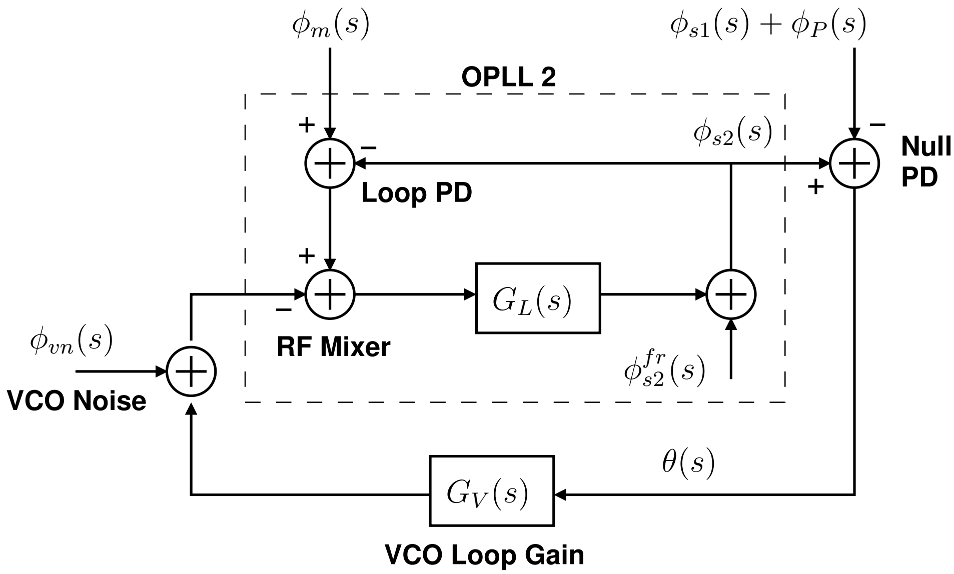

Figure 4.5. Small-signal phase model for the power-combining scheme with the additional VCO loop. SCL1 is locked to the master laser in OPLL1, and is not shown here. PD: Photodetector.

The variation in the differential path lengths traversed by the outputs of SCL1 and SCL2 produces a phase noise at the fiber combiner, and this noise has the Laplace transform $\phi_P(s)$. The OPLL open-loop gain is the same as G_L, and the gain $G_V(s)$ in the VCO branch is

$$G_V(s) = -\frac{K_v \sin\theta_{v,s} e^{-s\tau_v}}{s}, \tag{4.13}$$

where τ_v is the delay in the VCO branch (from the Null photodetector to the RF mixer) and $\theta_{v,s}$ is as in equation (4.10). Note that there is a trade-off in the choice of the value of $\theta_{v,s}$: a smaller $\theta_{v,s}$ results in a higher power combination efficiency, but also results in a lower loop gain. The reduction in loop gain can be compensated by increasing the DC gain K_v.[2]

The model in figure 4.5 can be solved for the variation in the output phase $\theta(s)$ to yield

$$\theta(s) = \frac{1}{1 + G_L + G_L G_V} \left(\begin{array}{l} \phi_{s2}^{fr} + G_L\left(\phi_m - \phi_{vn}\right) \\ \quad - \left(1 + G_L\right)\left(\phi_{s1} + \phi_P\right) \end{array} \right). \tag{4.14}$$

[2]The minus sign in equation (4.13) is present only for bookkeeping; in this case, the system locks with a negative $\theta_{v,s}$.

The argument s has been dropped from all the terms on the right-hand side. We substitute for $\phi_{s1}(s)$ using equation (4.12) to obtain

$$\theta(s) = \frac{1}{1+G_L+G_LG_V}\left(\left(\phi_{s2}^{fr}-\phi_{s1}^{fr}\right)+G_L\left(\phi_{RF}-\phi_{vn}\right)-\left(1+G_L\right)\phi_P\right). \tag{4.15}$$

To obtain some physical insight into the above equation, we note that the delay in the VCO loop τ_v is typically much larger than the OPLL delay. This limits the VCO open-loop gain G_V, so that the approximation $|G_L| \gg |G_V|$ holds at all frequencies. The denominator in equation (4.15) can then be expressed as $(1+G_L)(1+G_V)$, and we can rewrite the equation as

$$\theta(s) \approx \frac{1}{1+G_L}\left(\phi_{s2}^{fr}-\phi_{s1}^{fr}\right)+\frac{1}{1+G_V}\left(\phi_{RF}-\phi_{vn}-\phi_P\right). \tag{4.16}$$

Firstly, the master laser phase noise does not appear in the equation above. This is clear, since each slave SCL is locked to the master, and they beat with each other. Next, the phase noise of the free-running lasers is mainly suppressed by the OPLLs. Further, the VCO noise and phase noise introduced by differential path length delays are suppressed by the loop with transfer function $G_V(s)$. This is consistent with the interpretation that the system is the combination of three phase-locked loops: The slave lasers SCL1 and SCL2 are locked to the master laser using two heterodyne OPLLs at offsets given by ω_{RF} and ω_v respectively; and the VCO (along with other phase noise sources) is then locked to the RF offset frequency ω_{RF} in a third "outer" PLL. The laser phase noise is suppressed by the OPLLs, while the phase jitter of the VCO and the variation ϕ_P in the differential optical path length are suppressed by the third PLL.

4.1.3 Combining Efficiency

The power combination approach presented above can be scaled to a large number of lasers using a binary tree configuration as shown in figure 4.6. Fiber amplifiers can be used at the output of each slave SCL to increase the overall combined power. The

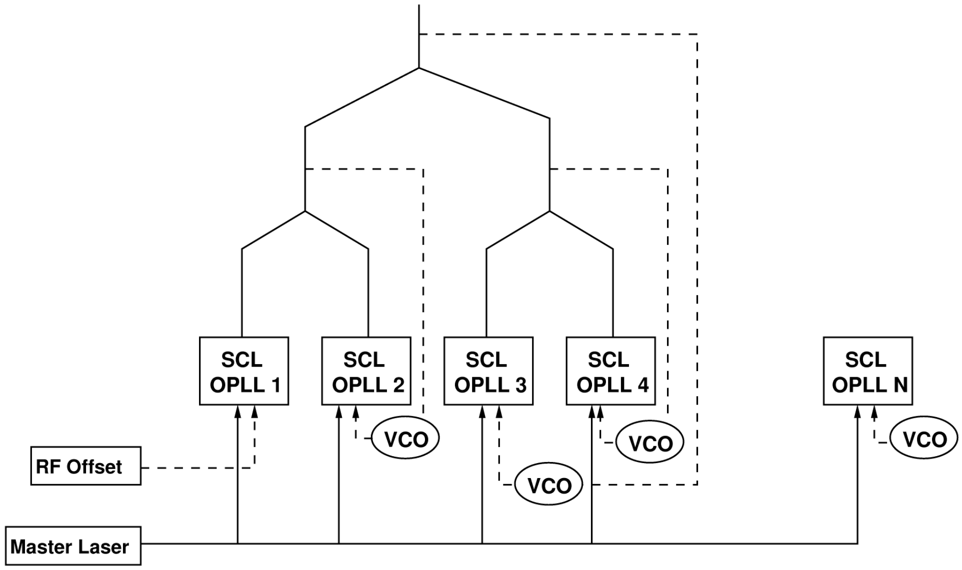

Figure 4.6. Binary tree configuration for the power combination of a number of SCLs locked to a common master laser in the filled-aperture configuration.

addition of fiber amplifiers increases the delay in the outer VCO loop, but the resultant bandwidth is still sufficient to correct for the slow fluctuations in the differential optical path length introduced by the amplifiers. We measured no additional phase noise when fiber amplifiers with output powers of ∼1 W were used at the outputs of the SCLs, and this is consistent with observations by other workers using narrow-linewidth seed lasers [104–106]. Our collaborators at Telaris have demonstrated the coherent combination of 4 fiber-amplified (35–40 W) semiconductor lasers using this approach to achieve a coherent and diffraction limited power output of ∼110 W.

The overall power-combining efficiency for two SCLs is affected by the intensity noise, relative polarizations and relative phase error between the combining beams, but is mainly limited by the phase noise of the combining beams. From equation (4.1), assuming that the deviations of the relative phase about the ideal value of zero are small, the efficiency of combining two optical beams is given by

$$\eta = \frac{P_c}{2P_0} \approx 1 - \frac{\langle \theta^2 \rangle}{4}. \tag{4.17}$$

The mean-squared value of the relative phase, $\langle \theta^2 \rangle$, has two important contributions:

(i) the steady state phase $\theta_{v,s}$ given by equation (4.10), and (ii) the residual phase noise of both the semiconductor lasers and the VCO, given by equation (4.15). The value of $\theta_{v,s}$ can be reduced by the use of cleaner VCOs and by the use of loop filters to increase the DC gain K_v. The residual phase noise of the SCLs can be reduced by increasing the OPLL loop bandwidth.

Let us briefly consider the effect of the residual phase error in the loop on the combination of a large number N of SCLs, e.g., as in figure 4.6. The output of slave SCL i is

$$E_i = \exp(j\omega_0 t + j\phi_0 + j\phi_{i,n}), \tag{4.18}$$

with ω_0 and ϕ_0 denoting the frequency and phase of the master laser (offset by the RF signal), and $\phi_{i,n}$ is the residual phase error in OPLL i. For simplicity, we have normalized the amplitude to unity. The total intensity is given by

$$I = \langle |E|^2 \rangle = \left\langle \left(\sum_{i \neq k}^{N} \exp(j\phi_{i,n} - j\phi_{k,n}) \right) \right\rangle + N. \tag{4.19}$$

For $i \neq k$, $\phi_{i,n}$ and $\phi_{k,n}$ are independent identically distributed random variables, assuming that the OPLLs are identical. Further, we have for a zero-mean Gaussian random variable X with variance σ^2, $\langle \exp(jX) \rangle = \exp(-\sigma^2/2)$. Therefore,

$$I = N + N(N-1)e^{-\sigma_\phi^2} \approx N^2 - N(N-1)\sigma_\phi^2. \tag{4.20}$$

The first term on the RHS is the combined power, and the second term denotes the reduction in efficiency due to residual phase error. The combining efficiency is therefore

$$\eta_c = 1 - \frac{N-1}{N}\sigma_\phi^2. \tag{4.21}$$

We conclude that the combining efficiency due to the residual phase noise in the OPLLs does not degrade with N, and reaches the asymptotic value $1 - \sigma_\phi^2$. Other sources of noise such as the frequency jitter of the VCOs and phase-front deformations caused by the optical elements used for beam-combining are analyzed in detail in reference [66], and it is shown that minimizing these errors is critical to achieve large combining efficiencies.

4.1.4 Summary

We have presented an all-electronic active feedback approach for the coherent power combination of SCLs using OPLLs. Elements of an array of SCLs locked to a common master laser have the same frequency and phase and can be coherently combined. The phase of the combining SCLs is further controlled using an electronic VCO to compensate for differential path length variations of the combining beams. We have demonstrated the coherent combination of various high power SCLs using this approach, and have achieved a stable power-combining efficiency of 94%. The electronic feedback scheme demonstrated eliminates the need for optical phase or frequency shifters. It is possible to obtain coherent and diffraction limited power of tens of kilowatts by the use of fiber amplifiers to amplify the outputs of an array of phase-locked SCLs. When scaled to a large number of SCLs, the overall power combination efficiency is likely to be limited by VCO jitter and phase front deformations.

4.2 Optical Phased Arrays

Phased array antennas have had significant success in the RF domain for beam-forming, steering, communication and three-dimensional imaging applications. Analogous efforts and advances in the optical domain however, have had limited success. Past demonstrations of phased array beam-steering have required injection locking of the individual lasers elements in the array [107], which is inherently unstable and difficult to scale due to complexity and cost. An alternative method utilizing a single laser, which is expanded and passed through an array of phase modulators, results in limited output power [108]. Furthermore, the state-of-the-art for this method utilizes liquid crystal spatial light modulators, which have limited bandwidths.

The CBC approach developed in this chapter provides an alternative technology for optical phased arrays and beam-steering that has the potential to overcome the

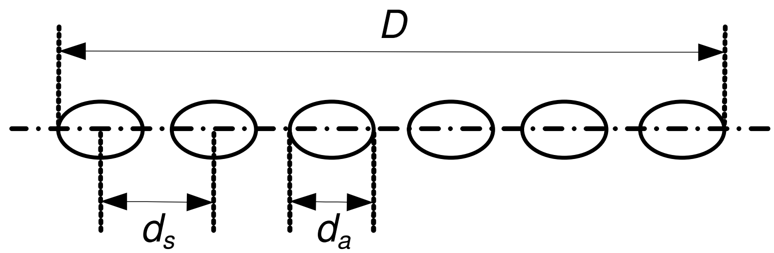

Figure 4.7. A one-dimensional array of coherent optical emitters.

fundamental challenges encountered by previous approaches. An array of SCLs is locked to a common master laser using heterodyne OPLLs, and the individual SCL outputs are placed side by side to form a larger aperture. Electronic phase shifters are utilized to control the phase of the offset signal to each OPLL, hence controlling the phase of each individual laser emitter and enabling electronic control over the optical wavefront. One can foresee a number of potential applications of this approach, including adaptive optics, control over the focusing distance, and fast and robust beam-steering for imaging and free-space data transfer.

4.2.1 Far-Field Distribution

We will limit ourselves to the discussion of a one-dimensional optical phased array, as shown in figure 4.7. A number, N, of coherent optical emitters are arranged along a straight line, with interemitter spacing d_s. The width of each aperture is d_a, and the total width of the optical aperture is D. We are interested in the far-field distribution of the optical intensity, along the axial direction. The far-field angular distribution of the field is simply a Fourier transform of the shape (and phase) of the aperture [109], and can be precisely calculated for the aperture shown in figure 4.7 [68]. Here, we only describe the salient features of the far-field distribution:[3]

- The far-field distribution consists of several lobes or fringes, each of which has an angular width $\theta_{lobe} \sim \lambda/D$, where λ is the wavelength of light. The finite size of the aperture creates "sublobes" around each lobe, and these sublobes

[3] This discussion assumes that $d_s \gg \lambda$. If this is untrue, the inherent approximation that $\tan\theta \approx \theta$, where θ is the angle in the far field, is no longer valid.

can be made smaller by apodizing the aperture.

- The size of each emitter, d_a, defines an overall angular envelope of width $\theta_{steer} \sim \lambda/d_a$, within which the beam may be steered.

- The lobes in the intensity distribution repeat with an angular pitch $\theta_{pitch} = \lambda/d_s$. Since d_s is always larger than d_a, there is always more than one lobe in the far-field distribution pattern. However, by making the ratio d_a/d_s, known as the "fill-factor," close to unity, the optical power can be consolidated into just one central lobe.

- If a linear phase ramp is applied to the aperture, i.e., if the phase of each emitter is offset from its neighbor by $\Delta\phi$, the position of the main-lobe in the far-field (the "beam") is given by $\theta_{beam} = (\Delta\phi/2\pi)(\lambda/d_s)$. This is the basis of beam-steering using an optical phased array. The beam can be steered by a maximum angle of λ/d_s, and an important figure of merit is the number of beamwidths by which the beam can be steered, given by D/d_s.

We use phase-locked SCLs as the coherent emitters in figure 4.7, and the phase of the laser is controlled by changing the phase of the offset signal in the heterodyne OPLL. The maximum speed of tuning is determined by the settling time of the loop, described in equation (2.19).

4.2.2 Experimental Results

The experimental setup for the demonstration of electronic beam-steering using OPLLs is shown in figure 4.8. Two slave DFB SCLs at 1539 nm (JDS-Uniphase, see table 2.1) are phase-locked to a common master laser (NP Photonics) at an offset frequency of 1.7 GHz. An RF phase shifter, used in one of the OPLLs, produces a phase shift of up to π radians. The outputs of the two phase-locked lasers are brought next to each other using a custom 8-channel single-mode fiber array (Oz Optics, Ottawa, Canada) with a channel spacing of 250 µm. The distance between the emitters, d_s, can be varied by choosing different channels of the fiber array. The output of the fiber array

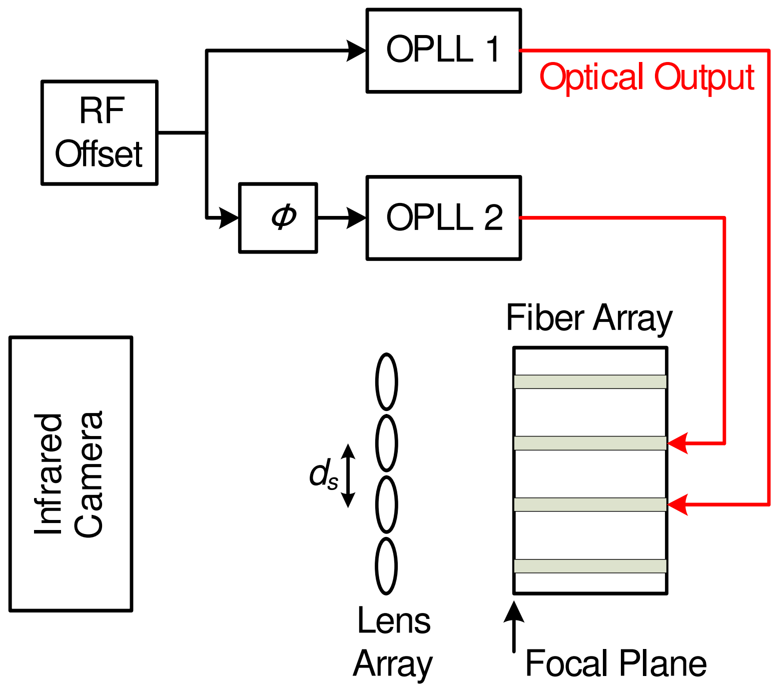

Figure 4.8. Experimental setup for the demonstration of beam-steering using OPLLs. The slave SCLs in the OPLLs are phase-locked to a common master laser. The phase of the RF offset signal into OPLL2 is controlled using an electronic phase shifter.

assembly is placed at the focal plane of a microlens array of the same pitch (Leister Technologies, Itasca, IL), and the resultant far-field distribution is measured using an infrared camera.

The measured intensities on the camera for the incoherent and coherent addition of the beams is shown in figure 4.9, for $d_s = 0.25$ mm.[4] The corresponding horizontal intensity distributions are shown in figure 4.10(a), where two important features should be noted. The coherently added far-field distributions show a peak intensity that is about twice the peak intensity of the incoherent case, and the size of the main lobe is reduced by a factor of two, as expected. Second, a change in the RF phase by π radians causes a steering of the beam by one-half the fringe separation, demonstrating that the change electronic phase results in a change in the optical phase in a one-to-one manner. Similarly, the horizontal intensity distribution for an emitter separation of $d_s = 0.5$ mm is shown in figure 4.10(b), showing that the fringe sepa-

[4]The images in figure 4.9 are not calibrated for the camera's nonlinear response. The calibrated traces are shown in figure 4.10.

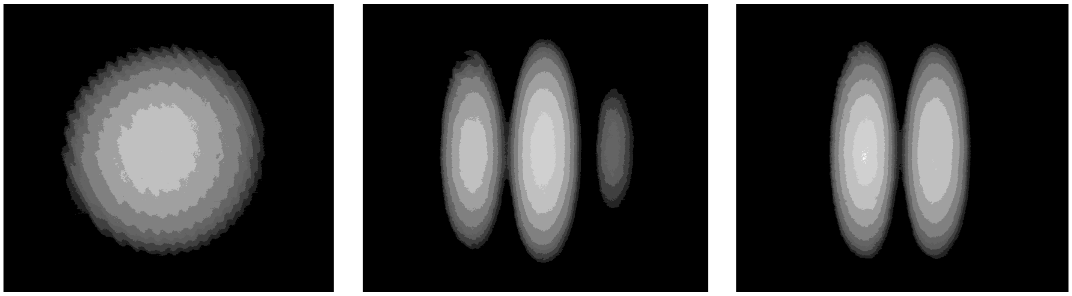

(a) (b) (c)

Figure 4.9. Measured far-field intensities on the infrared camera for $d_s = 0.25$ mm, when (a) one of the OPLLs is unlocked and (b), (c) both OPLLs are locked. The RF phase is varied between (b) and (c), demonstrating electronic steering of the optical beam.

ration reduces by a factor of two within the same envelope of the distribution. The nonideal fringe visibility (the minima do not go down to zero) is mainly a result of poor camera dynamic range, but other factors such as mismatched optical intensities, polarization states and residual phase errors in the OPLLs significantly reduce the visibility.

Modeling the laser outputs as Gaussian beams, the far-field intensity distribution is theoretically calculated [68] and compared to the experimental result in figure 4.11, showing excellent agreement. By choosing different channels of the fiber array, the far-field distributions are measured for different values of the emitter separation d_s. The variation of the experimentally measured fringe separation is plotted against the inverse emitter separation d_s^{-1} in figure 4.12, and the linear dependence is verified.

4.2.3 Effect of Residual Phase Noise on Fringe Visibility

Finally, we consider the effect of the OPLL residual phase noise on optical sidebands in the far field. Consider an optical phased array composed of N individual emitters, labeled $1, 2, \ldots, N$, where each emitter is a SCL phase-locked to the master laser in an OPLL with residual phase error σ_ϕ^2. The effect of a varying steady-state phase error can also be included in this variance. At a point $\vec{r}$ in the far field of the phased

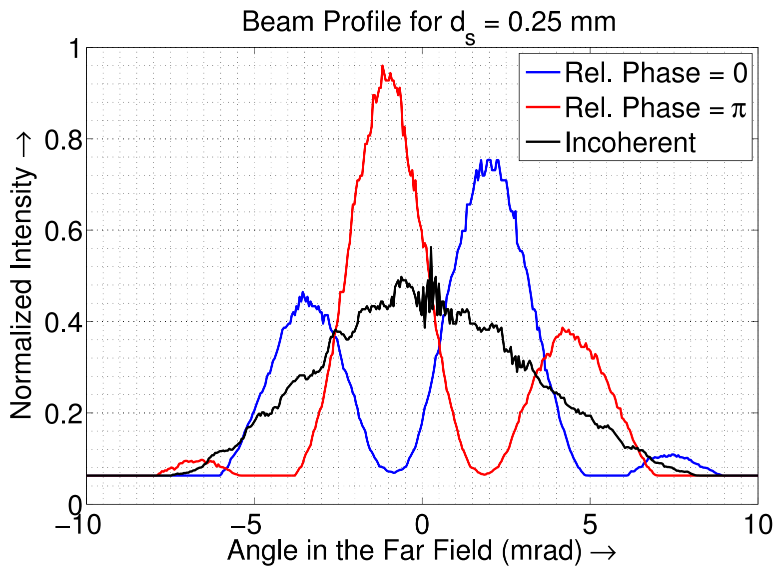

(a)

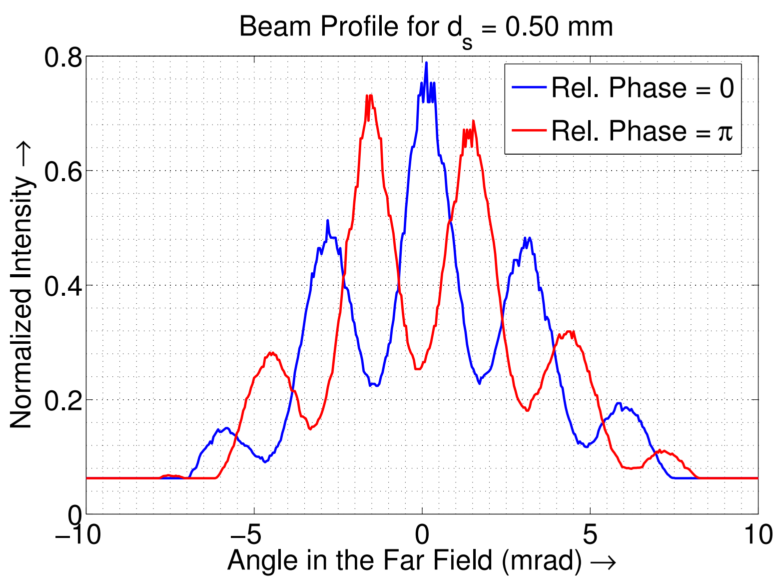

(b)

Figure 4.10. Horizontal far-field intensity distributions demonstrating beam-steering of half a fringe by an RF phase shift of π radians, for emitter spacings of (a) $d_s = 0.25$ mm and (b) $d_s = 0.5$ mm. The incoherently added intensity distribution is also shown in (a).

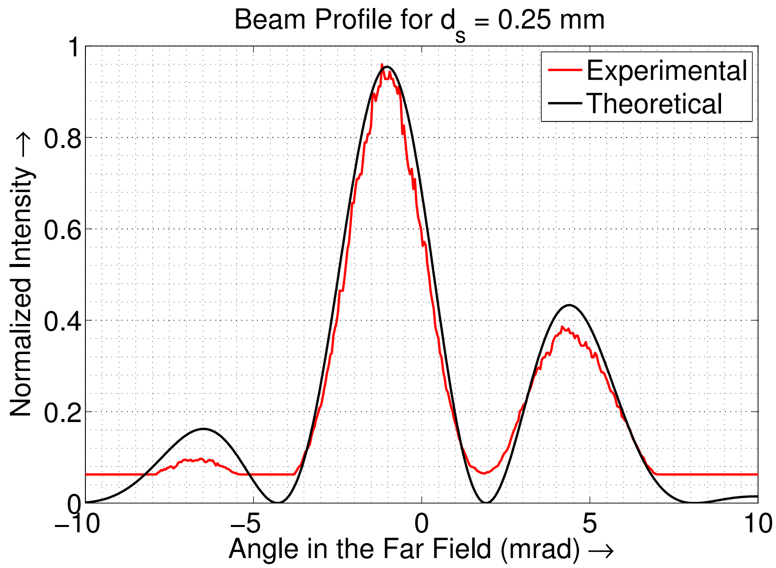

Figure 4.11. Comparison of the experimental far-field intensity distribution with the theoretical calculation.

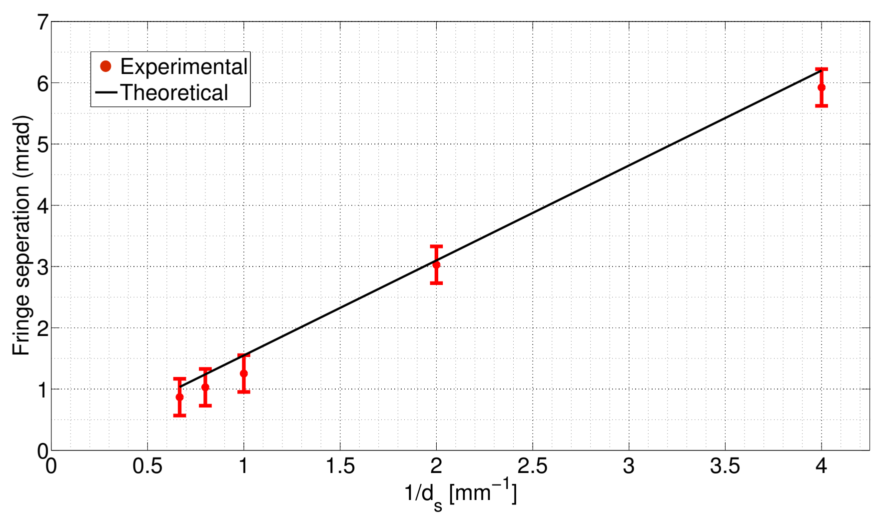

Figure 4.12. Separation between fringes as a function of the inverse beam separation d_s^{-1}, compared to theory.

array aperture, let the field due to emitter i be given by

$$E_i = a_i \exp(j\omega_0 t + j\phi_i + j\phi_{i,n}), \tag{4.22}$$

where a_i and ω_0 denote the amplitude and frequency of emitter i, ϕ_i is the phase of the wave *at the point* $\vec{r}$ (controlled by RF phase shifters), and $\phi_{i,n}$ denotes the phase noise due to emitter i, which is not corrected by the OPLL. $\phi_{i,n}$ is a zero-mean Gaussian random variable with standard deviation σ_ϕ^2. For simplicity, we will assume that the amplitudes a_i are equal to unity; a more general result can easily be derived. The total field at the point $\vec{r}$ is given by $E = \sum_{i=1}^{N} E_i$, and the time averaged intensity is given by

$$I = \left\langle |E|^2 \right\rangle = \left\langle \left(\sum_{i=1}^{N} \exp(j\phi_i + j\phi_{i,n}) \right) \left(\sum_{k=1}^{N} \exp(-j\phi_k - j\phi_{k,n}) \right) \right\rangle . \tag{4.23}$$

The phases ϕ_i are constant over the averaging interval, so that

$$I = \sum_{i \neq k}^{N} \left[\exp(j(\phi_i - \phi_k)) \left\langle \exp(j(\phi_{i,n} - \phi_{k,n})) \right\rangle \right] + N. \tag{4.24}$$

For $i \neq k$, $\phi_{i,n}$ and $\phi_{k,n}$ are independent random variables. Further, we have for a zero-mean Gaussian random variable X with variance σ^2, $\langle \exp(jX) \rangle = \exp(-\sigma^2/2)$. Therefore,

$$I = N + e^{-\sigma_\phi^2} \sum_{i \neq k}^{N} \exp(j(\phi_i - \phi_k)). \tag{4.25}$$

The intensity pattern in the far field consists of maxima and minima according to how the phases in equation (4.25) add up. Let us first assume no phase noise, i.e., $\sigma_\phi = 0$. At a maximum, all the phases add in phase ($\phi_i = \phi_k$) to give

$$I_{max} = N + N(N-1) = N^2. \tag{4.26}$$

At a minimum, we have zero intensity, so that

$$I_{min} = 0 = N + \sum_{i \neq k}^{N} \exp(j(\phi_i - \phi_k)). \tag{4.27}$$

We now consider phase noise. With the addition of phase noise, the intensity at a maximum is

$$\begin{aligned} I_{max,n} &= N + N(N-1)e^{-\sigma_\phi^2} \simeq N + N(N-1)(1-\sigma_\phi^2) \\ &= N^2 - (N^2 - N)\sigma_\phi^2, \end{aligned} \tag{4.28}$$

which is also the result for the CBC efficiency in equation (4.21). At a minimum,

$$\begin{aligned} I_{min,n} &\simeq N + (1-\sigma_\phi^2) \sum_{i \neq k}^{N} \exp(j(\phi_i - \phi_k)) \\ &= N + (1-\sigma_\phi^2)(-N) = N\sigma_\phi^2. \end{aligned} \tag{4.29}$$

We have used equation (4.27) in deriving the above. The ratio of the maximum to the minimum intensity is therefore

$$\frac{I_{max,n}}{I_{min,n}} = \frac{N - (N-1)\sigma_\phi^2}{\sigma_\phi^2}. \tag{4.30}$$

Note that we have made no assumptions about the location of the N emitters in the array. We have only assumed that the interference pattern in the absence of noise produces nulls, an assumption which is valid when the emitters have equal (or symmetric) amplitudes. The ratio derived above sets an upper bound on the maximum achievable sideband suppression ratio. In an aperture with emitters of equal power, the finite size of the aperture creates sidebands. With an apodized aperture, the strength of these sidebands can be reduced until the above limit is reached.

The practical realization of optical phased arrays requires a large number of elements (from tens to hundreds in one dimension), and is a major technological challenge. It will require the fabrication of arrays of narrow-linewidth SCLs. For example, there has been some progress in the fabrication of large-scale independently addressable vertical cavity surface-emitting laser (VCSEL) arrays [110, 111]. Integrated OPLLs have recently been demonstrated by various workers [22, 23, 77]. We believe that it is feasible to use integrated optical waveguides to combine the outputs of many discrete phase-locked SCLs residing on a single chip to form a single coherent aperture with narrow spacing between adjacent emitters and electronic control over the phase of each emitter in the aperture.

Chapter 5

The Optoelectronic Swept-Frequency Laser

5.1 Introduction

In this chapter, we study the application of the feedback techniques developed in the previous chapters to control the frequency of an SCL as it is tuned across a wide frequency range. As described in chapter 1, such broadband sources are important in many upcoming fields such as FMCW imaging and LIDAR, sensing and spectroscopy. The key requirements in these applications are rapid tuning over a broad frequency range, also referred to as the "chirp bandwidth," and the precise control of the frequency chirp profile. The wide gain bandwidth of the semiconductor quantum well media, the narrow linewidth of a single-mode SCL, and the ability to electronically control the lasing frequency using the injection current make the SCL an attractive candidate for a wideband swept-frequency source for FMCW imaging. However, the bandwidth and the speed of demonstrated linear frequency sweeps have been limited by the inherent nonlinearity of the frequency modulation response of the SCL vs. the injection current, especially at high speeds. A feedback system to overcome this nonlinearity using a fiber interferometer and a lock-in technique has been reported [112]; however the rate of the frequency sweep was limited to about 100 GHz in 10 ms.

In this chapter, we report the development of an optoelectronic swept-frequency laser with precise control over the optical frequency sweep. The output frequency of the SCL is a function of its driving current, and is controlled electronically by a combination of two techniques: (i) an open-loop predistortion of the input current into the SCL, and (ii) an optoelectronic feedback loop in which the optical chirp rate is phase-locked to a reference electronic signal. When the system is in lock, the slope and starting frequency of the optical frequency sweep are determined by the frequency and phase of the reference signal, and the laser emits a precise and coherent, predetermined ω vs. t waveform ("chirp"). This chirp is determined by the elements, both optical and electronic, of the feedback circuit and does not depend on the specific laser. The dynamic coherent control of the output frequency of an SCL opens up the field of SCL optics to many important applications such as chirped radar, biometrics, swept source spectroscopy, microwave photonics, and Terahertz imaging and spectroscopy.

Using a high coherence monochromatic reference oscillator in the optoelectronic feedback loop, we demonstrate rapid, highly linear frequency sweeps of up to 500 GHz in 100 µs using DFB SCLs and VCSELs. Further, the frequency of the reference signal can varied dynamically to achieve arbitrary, time-varying optical frequency chirps. We demonstrate quadratic and exponential sweeps of the frequency of the SCL by varying the frequency of the reference signal. We report the results of label-free biomolecular sensing experiments using a precisely controlled SFL and whispering-gallery microtoroid resonators.

5.2 System Description

The feedback system for the generation of linear frequency chirps is shown in figure 5.1. A small part of the output of the fiber-coupled swept SCL is coupled into the feedback loop using a 10/90 fiber coupler. The optical signal is passed through a fiber Mach-Zehnder interferometer (MZI) with a differential time delay τ, and is incident on a photodetector (PD). When the optical frequency is varied with time, the frequency of the generated photocurrent is proportional to the slope of the optical frequency chirp. The output of the PD is mixed down using a reference signal of frequency ω_R,

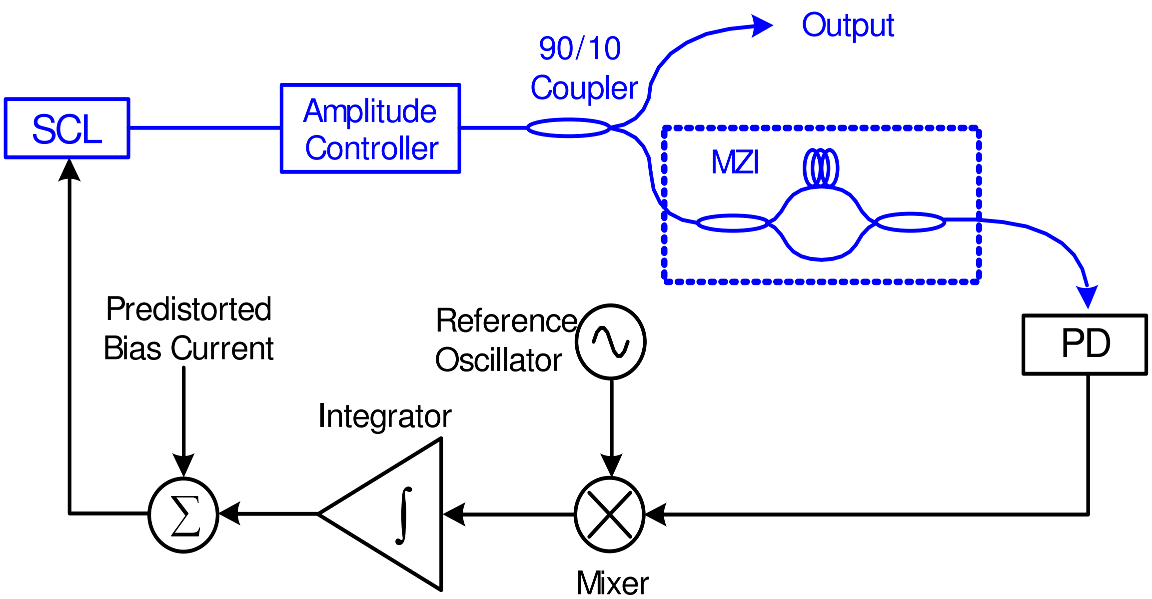

Figure 5.1. Optoelectronic feedback loop for the generation of accurate broadband linear chirps. The optical portion of the loop is shown in blue.

integrated, and injected into the SCL. Since the injection current into the SCL also modulates the optical power, a low-speed amplitude controller is used to maintain a constant output power. A bias current is added to the SCL to set the nominal optical frequency slope, and to provide an open-loop predistortion as described in section 5.2.2. The system is reset so that the chirp repeats every T seconds.

The steady-state solution of the control system is derived below. We start by demonstrating that a linear optical frequency chirp is a self-consistent solution. Let us assume that the laser frequency tuning is perfectly linear, and that there is no predistorted bias current present. Assume that the laser frequency is given by

$$\omega_{SCL}(t) = \omega_0 + \xi t, \tag{5.1}$$

where ξ is the slope of the optical frequency sweep. This corresponds to an optical phase

$$\phi(t) = \phi_0 + \omega_0 t + \frac{1}{2}\xi t^2. \tag{5.2}$$

The output of the photodetector PD is given by

$$i_{PD} = K_P \cos\left(\phi(t) - \phi(t-\tau)\right), \tag{5.3}$$

where the PD gain K_P is the product of the optical power and the PD responsivity, and we have ignored the DC term in the PD output. With the assumed chirp shape in equation (5.2), equation (5.3) describes a sinusoidally varying photocurrent with frequency

$$\omega_{PD} = \xi\tau. \tag{5.4}$$

The output of the mixer is

$$i_M = K_P K_M \cos\left(\phi(t) - \phi(t-\tau) - \omega_R t - \phi_R\right), \tag{5.5}$$

where K_M is the mixer gain, and the reference oscillator has a frequency ω_R and phase ϕ_R. Now let ω_R be chosen so that

$$\omega_R = \omega_{PD} = \xi\tau. \tag{5.6}$$

The mixer output is then a DC signal given by

$$i_M = K_P K_M \cos\left(\omega_0\tau - \frac{1}{2}\xi\tau^2\right). \tag{5.7}$$

This DC current is amplified and integrated to provide a linear (i vs. t) current to the laser, which in turn produces a frequency output as given by equation (5.1), thus providing a self-consistent solution.

More rigorously, the steady-state solution is obtained by requiring that the output current from the mixer in equation (5.5) is a constant, which means that

$$\frac{d}{dt}\left(\phi(t) - \phi(t-\tau)\right) = \omega_R. \tag{5.8}$$

The solution to equation (5.8) is determined by the initial laser frequency chirp, i.e., by the value of the optical frequency over the interval $[-\tau, 0]$. If the MZI delay τ is chosen sufficiently small so that the effect of higher-order derivatives of the optical frequency can be neglected, equation (5.8) reduces to

$$\tau \frac{d\omega_{SCL}}{dt} = \omega_R, \tag{5.9}$$

the solution to which is a linear frequency chirp as given by equation (5.1). Another way to look at the control system is as follows: the combination of the integrator, semiconductor laser, the MZI (which acts as a differentiator) and the PD act as a VCO, since the frequency of the PD output is proportional to the input voltage into the loop integrator. This VCO is locked to the reference oscillator in a typical Type I homodyne phase-locked loop. If we ignore the steady-state phase error in the loop—which is true if the loop gain is high, or the open-loop bias of the laser produces a nearly linear chirp—the slope and starting frequency of the optical chirp are given by

$$\begin{aligned} \xi &= \frac{\omega_R}{\tau}, \\ \omega_0 &= \frac{\phi_R + 2m\pi}{\tau}, \end{aligned} \tag{5.10}$$

where m is an integer. The steady-state solution of the system is therefore a set of linear optical frequency chirps, whose starting frequencies differ by the free-spectral range of the MZI. One of these solutions is picked out by the temperature and bias current of the SCL.

5.2.1 Small-Signal Analysis

The transient response of the system about the steady-state solution described by equation (5.10) is studied in the Fourier domain using the small-signal approximation as shown in figure 5.2. The variable in the loop is (the Fourier transform of) the deviation of the optical phase from its steady-state value in equation (5.10). For frequencies much smaller than its free spectral range, the MZI can be approximated as an ideal frequency discriminator. K denotes the total DC loop gain, given by the

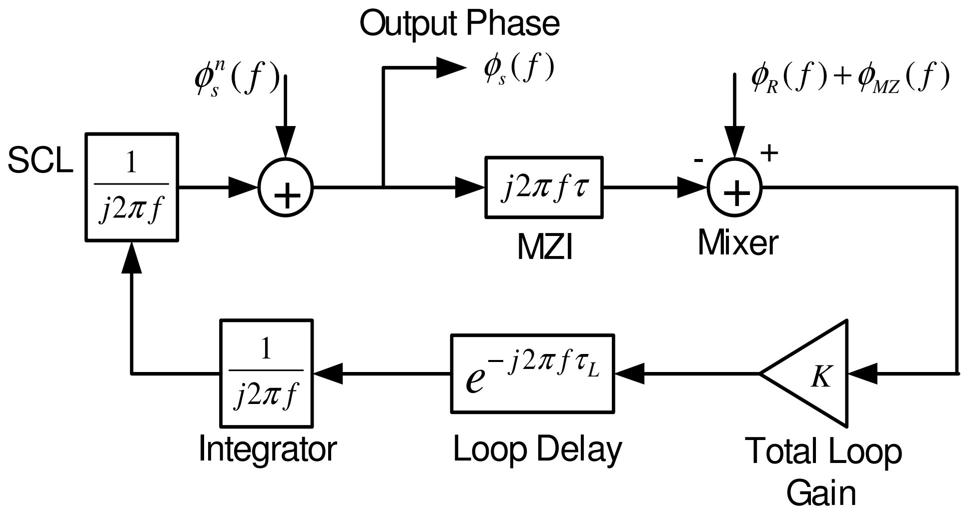

Figure 5.2. Small-signal phase propagation in the optoelectronic SFL feedback loop.

product of the gains of the laser, PD, mixer and the integrator. The phase noise of the laser and the phase excursion due to the nonlinearity of the frequency-vs.-current response of the SCL are lumped together and denoted by $\phi_s^n(f)$. The phase noise of the reference oscillator and the phase noise introduced by environmental fluctuations in the MZI are denoted by $\phi_R(f)$ and $\phi_{MZ}(f)$ respectively. Following a standard small-signal analysis [2], the output phase of the SCL is given by

$$\phi_s(f) = \phi_s^n(f)\frac{j2\pi f}{j2\pi f + K\tau e^{-j2\pi f\tau_L}} + (\phi_R(f) + \phi_{MZ}(f))\frac{K\tau e^{-j2\pi f\tau_L}}{j2\pi f\left(j2\pi f + K\tau e^{-j2\pi f\tau_L}\right)}, \tag{5.11}$$

where τ_L is the loop propagation delay. The nonlinearity and laser phase noise within the loop bandwidth are suppressed by the loop, as seen from the first term in equation (5.11). The frequency components of the nonlinearity are of the order of the repetition frequency of the waveform, and lie within the loop bandwidth. The analysis predicts the reduction in the phase noise of the SCL and an improvement in coherence, leading to a higher signal-to-noise ratio in an FMCW interferometric experiment (as described in chapter 3). From the second term in equation (5.11), we see that the accuracy of the frequency chirp is dependent on the frequency stability of the electronic oscillator used to generate the reference signal, and on the stability of the MZI. It is possible to obtain very accurate linear frequency chirps with the use of ultralow phase noise electronic oscillators and stabilized optical interferometers.

5.2.2 Predistortion of the SCL Bias Current

The small-signal approximation of the preceding section is valid as long as the phase change introduced at the PD output due to nonlinearities in the tuning response of the SCL is small. This condition is satisfied if the differential delay τ in the MZI is small and the SCL nonlinearity is limited. However, the tuning response of the SCL is inherently nonlinear, since the predominant tuning mechanism is a current-induced temperature change which in turn changes the refractive index of the lasing medium. This nonlinearity is especially pronounced at higher sweep rates, and can throw the loop out of lock. The sweep nonlinearity can be reduced by predistorting the open-loop input current to the SCL, as follows. The frequency of the SCL is related to the input sweep current according to

$$\omega_{SCL}(t) = \omega_0 + K_{SCL}(i) \times i(t), \tag{5.12}$$

where the nonlinearity of the modulation response is modeled by a current-dependent gain $K_{SCL}(i)$. From equation (5.3), this generates a photocurrent at the PD which has a (in general, time-varying) frequency

$$\begin{aligned} \omega_{PD}(t) = \tau \frac{d\omega_{SCL}}{dt} &= \frac{di}{dt} \times \left(\tau K_{SCL} + \tau i \frac{dK_{SCL}}{di} \right) \\ &\doteq \frac{di}{dt} \times F_{dist}(i), \end{aligned} \tag{5.13}$$

where we have defined a "distortion function" $F_{dist}(i)$ that is a function of only the laser injection current.

We now develop a predistortion technique based on equation (5.13). A current ramp is applied to the SCL, the resultant PD frequency $\omega_{PD}(t)$ is measured, and the distortion function $F_{dist}(i)$ is extracted from this measurement. Next, this function is used to solve equation (5.13) numerically, and the predistorted current $i_{pre}(t)$ that results in the desired (here, a constant) $\omega_{PD}(t)$ is obtained.

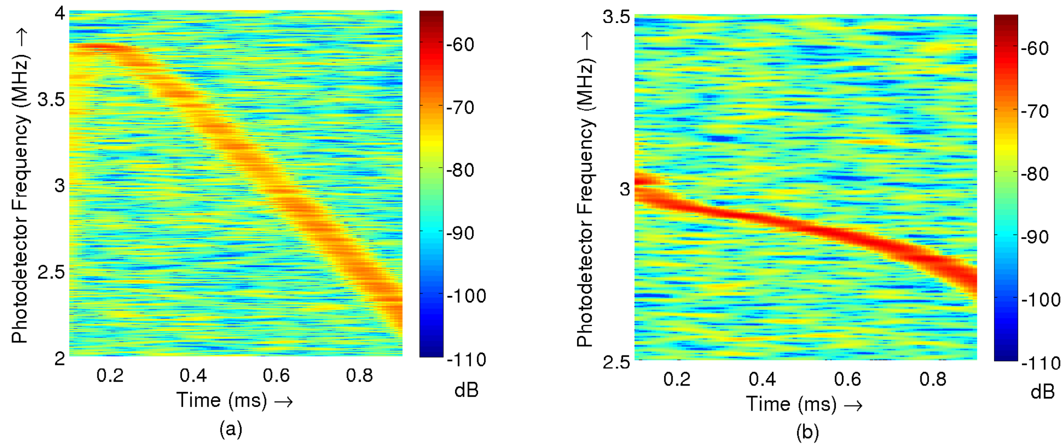

Figure 5.3. Measured spectrograms of the output of the loop photodetector, for the (a) free-running and (b) predistorted cases. The predistortion significantly reduces the SCL nonlinearity. The delay of the MZI is $\tau = 28.6$ ns.

The ability of the predistortion of the input current to significantly reduces the nonlinearity and enable phase-locking over a large frequency range is demonstrated in figure 5.3. The optical frequency chirp is characterized by measuring the frequency of the PD, ω_{PD}, since this is directly proportional to the slope of the frequency chirp as given by equation (5.4).[1] The measurements in figure 5.3 were performed using a DFB SCL (JDS-Uniphase) with an MZI delay of $\tau = 28.6$ ns. Panel (a) shows the spectrogram of the optical chirp slope when a constant current ramp is applied to the SCL, and panel (b) corresponds to the predistorted input. Note that the loop is not closed, i.e. $K = 0$, in these measurements. It is clearly seen that the nonlinearity of the chirp, as characterized by the spread of frequencies in the photocurrent spectrogram, is clearly reduced by the predistortion.

While the predistortion significantly reduces the chirp nonlinearity, it does not eliminate it, as seen in figure 5.3(b). This is due to the fact that the assumed model for the laser nonlinearity (equation (5.12)) is only approximate. The tuning coefficient K_{SCL} is not merely a function of the current i, but also of the rate of change of current, and possibly higher derivatives. Instead of coming up with a more complicated model

[1]The measurements in figure 5.3 are the spectrograms of the photocurrent. A spectrogram is a moving-windowed Fourier transform of the input signal; it effectively measures the variation of the frequency of the signal as a function of time.

of the laser tuning behavior, we simply apply the predistortion technique iteratively, and it is observed that the laser nonlinearity all but vanishes after 3–4 iterations. The success of the iterative approach can be understood by noting that the calculated predistorting current approaches the required predistortion more closely with each iteration, and makes the model in equation (5.12) more and more accurate.

5.3 Experimental Demonstration

Experimental demonstrations of the control system shown in figure 5.1 were performed using various commercially available fiber-coupled SCLs at different wavelengths. We present here results using a DFB SCL (JDS-Uniphase) with an output power of 40 mW at a wavelength of 1539 nm and a VCSEL (RayCan, Daejon, Korea) with an output power of 1 mW at 1550 nm. The delay in the fiber MZI, τ, was chosen to be as large as possible while remaining much smaller than the coherence time of the laser.

5.3.1 Linear Frequency Sweep

5.3.1.1 Distributed Feedback SCL

A perfectly linear chirp of 100 GHz in 1 ms was demonstrated using the DFB SCL, corresponding to a chirp slope of 10^{14} Hz/s. The MZI delay was $\tau = 28.6$ ns, so that the chirp rate of 10^{14} Hz/s corresponded to a photocurrent frequency $\omega_{PD}/2\pi =$ 2.86 MHz. The measured spectrograms of the photocurrent for a ramped current bias and after predistortion are shown in figure 5.3. The predistorted frequency sweep was then locked to a high coherence external reference signal of frequency 2.86 MHz, to obtain a highly linear optical frequency sweep of 100 GHz in 1 ms. The loop gain was adjusted by varying the amplitude of the reference signal. A loop bandwidth of $\pm$200 kHz was achieved. The spectrogram of the PD current when the loop was in lock is plotted in figure 5.4(a), showing that the rate of the optical frequency sweep remains constant with time. The Fourier transform of the PD current, calculated

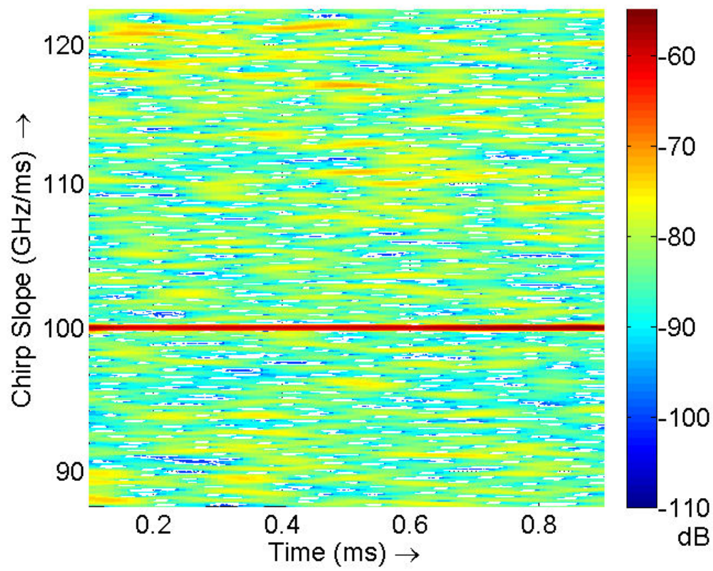

(a)

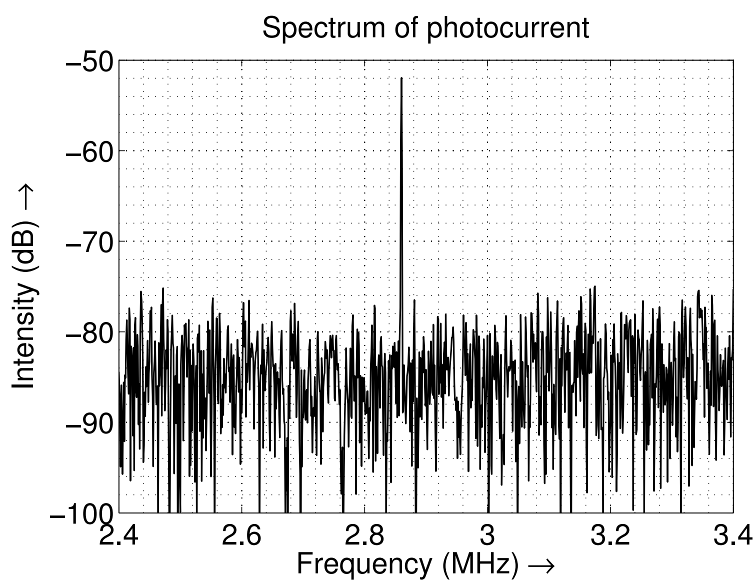

(b)

Figure 5.4. Measured spectrogram of the output of the loop photodetector when the loop is in lock, showing a perfectly linear optical chirp with slope 100 GHz/ms. (b) Fourier transform of the photodetector output measured over a 1 ms duration.

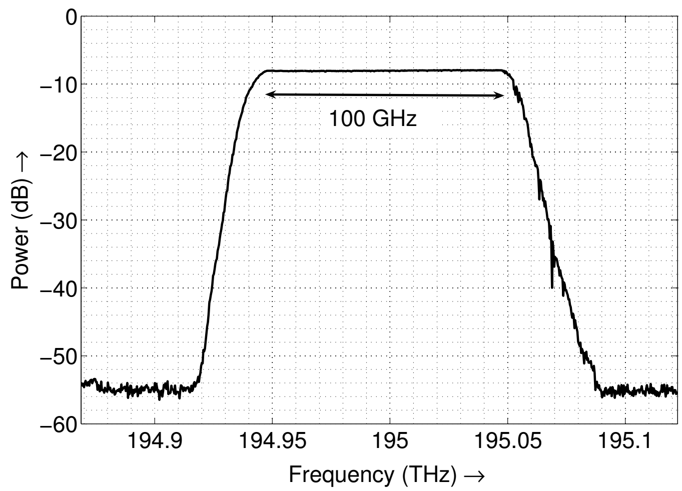

Figure 5.5. Measured optical spectrum of the locked swept-frequency SCL. RBW = 10 GHz.

over 1 ms and shown in Fig 5.4(b), shows a narrow peak at the reference frequency of 2.86 MHz. The width of the peak is transform-limited to 1 kHz. The spectrum of the swept laser measured using an optical spectrum analyzer is shown in figure 5.5.

5.3.1.2 Vertical Cavity Surface-Emitting Laser

The range of the frequency sweep in the experimental demonstration using the DFB SCL was limited by the tuning range of the laser. Single-mode VCSELs have larger tuning ranges, and we therefore performed the same experiment with single-mode VCSELs at 1550 nm. Further, the tuning speed was increased so that the scan time was 0.1 ms. The results of the experiment are summarized in figure 5.6. Panel (a) shows the shape of the optical chirp when a current ramp is applied to the VCSEL, and the tuning is highly nonlinear. The shape of the frequency sweep after four rounds of iterative predistortion is shown in panel (b), and it can be seen that the chirp is already very linear. A transform-limited peak is seen for this case. When the SCL is phase-locked, as in (c), any residual nonlinearities are corrected, and the starting frequency of the optical chirp is locked to the reference oscillator. The spectrum of the swept laser, shown in (d) verifies that the tuning range achieved is equal to 500 GHz.

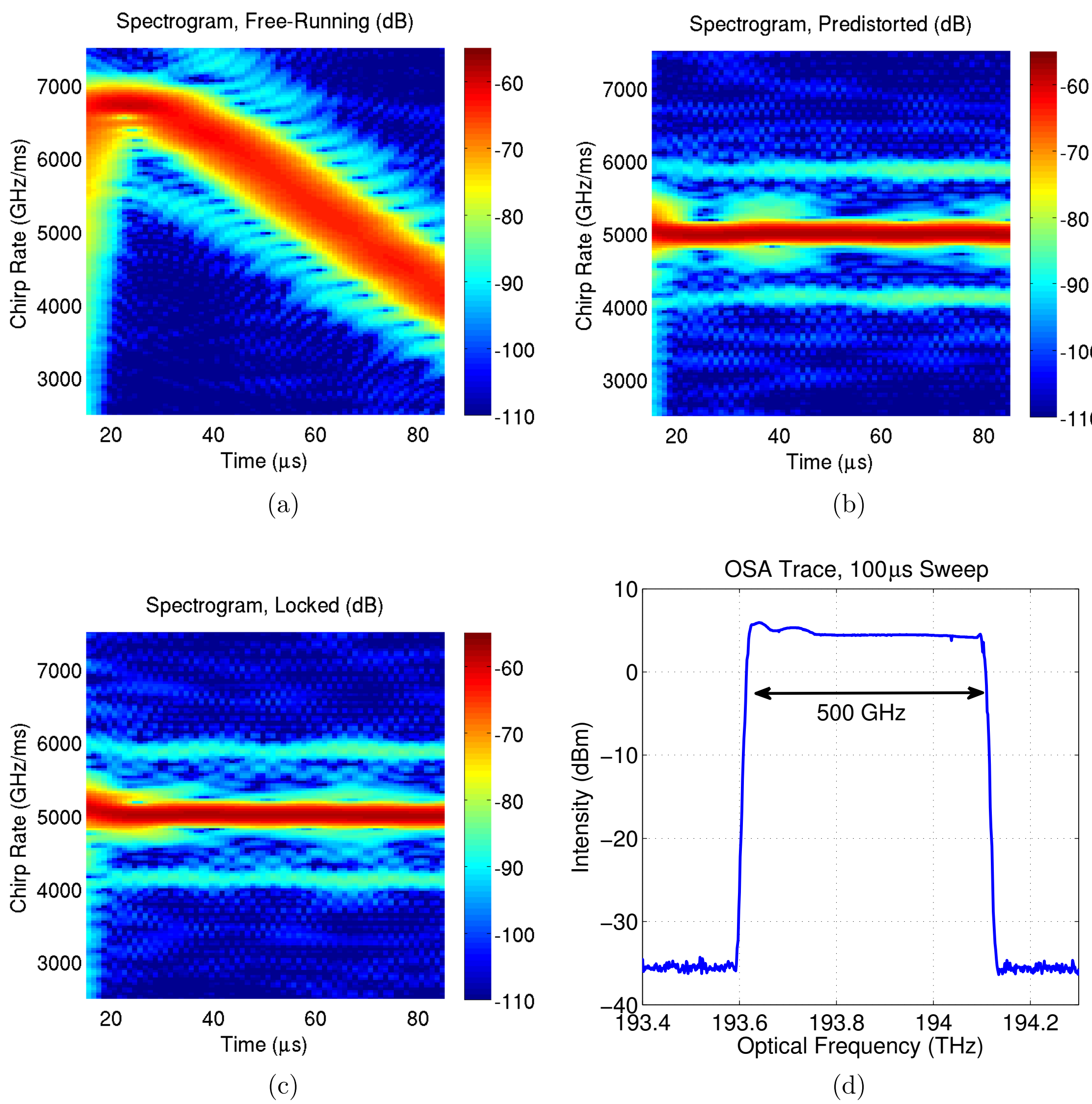

Figure 5.6. Experimental demonstration of generation of a perfectly linear chirp of 500 GHz / 0.1 ms using a VCSEL. (a), (b), and (c) Spectrograms of the optical chirp slope for a ramp input, after iterative predistortion and the phase-locked SFL respectively. (d) Measured optical spectrum.

We have therefore demonstrated the generation of precisely linear and broadband frequency sweeps of up to 5×10^{15} Hz/s and a chirp bandwidth of up to 500 GHz using a combination of laser current predistortion and an optoelectronic feedback loop. The rate of the optical frequency sweep is locked to and determined by the frequency of an external reference signal. The closed loop control system also reduces the inherent phase noise of the SCL within the loop bandwidth, thereby enabling coherent interferometry at larger distances. The chirp bandwidth and rate are mainly limited by the extent and speed of the thermal tuning of the frequency of the SCL.[2] We anticipate that tuning speeds larger than 10^{16} Hz/s are achievable using this technique. Other researchers have very recently demonstrated linearization of frequency chirps of external cavity lasers with a chirp bandwidth of about 5 THz [113], however the speed of the tuning was several orders of magnitude smaller than the frequency chirps demonstrated in this work.

5.3.2 Arbitrary Frequency Sweeps

The optoelectronic feedback technique can be extended to generate arbitrary frequency sweeps by the use of a VCO as the reference signal in figure 5.1. If the reference frequency, ω_R in equation (5.9), is varied with time, the optical frequency is given by

$$\omega_{SCL}(t) = \frac{1}{\tau} \int_0^t \omega_R(t)\, dt. \tag{5.14}$$

This principle was experimentally demonstrated by the generation of quadratic and exponential optical frequency sweeps using the DFB SCL, as shown in figures 5.7(a) and (b) respectively. In the former case, the reference frequency was varied linearly between 1.43 and 4.29 MHz over 1 ms. This corresponds to a linear variation of the optical frequency slope from 50 to 150 GHz/ms, and consequently, a quadratic variation of the optical frequency. In the latter case, the reference frequency was

[2] By "thermal tuning," we mean the tuning due to a change in the device temperature, which is a consequence of a change in the injection current via joule heating.

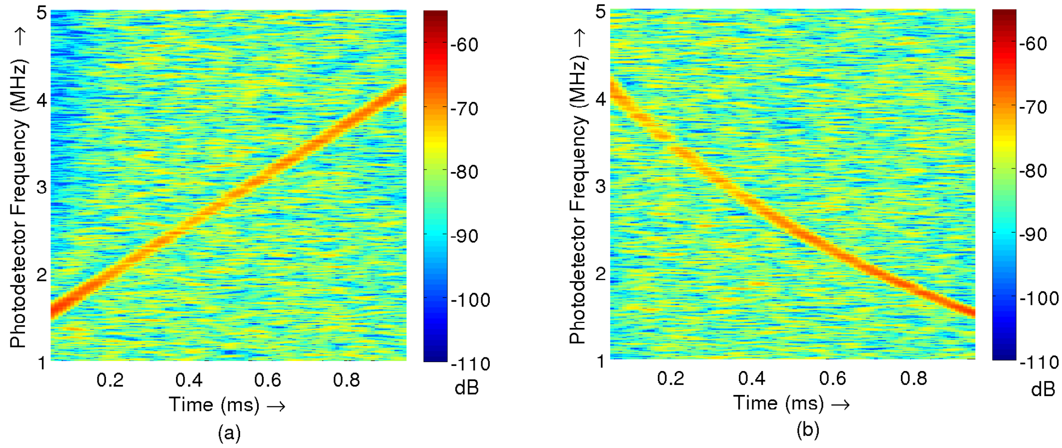

Figure 5.7. Measured spectrograms of the output of the loop photodetector, illustrating arbitrary sweeps of the SCL frequency. (a) The reference signal is swept linearly with time. (b) The reference signal is swept exponentially with time. The laser sweep rate varies between 50 and 150 GHz/ms.

varied exponentially between 4.29 and 1.43 MHz according to the relation

$$\omega_R(t) = 2\pi \times (4.29\text{ MHz}) \times \left(\frac{1.43\text{ MHz}}{4.29\text{ MHz}}\right)^{t/(1\text{ ms})}. \tag{5.15}$$

This corresponds to an exponential decrease of the slope of the optical frequency from 150 to 50 GHz/ms over 1 ms. A predistortion was applied to the integrator input in both cases, as described in section 5.2.2. The measured slope of the optical frequency sweep shown in figure 5.7 is identical to the temporal variation of the frequency of the reference signal. By predistorting the SCL current to produce the nominal output frequency sweep, this locking technique can be applied to generate any desired shape of the optical sweep.

5.4 Range Resolution of the Optoelectronic SFL

One of the most important applications of a linearly swept optical source is in FMCW reflectometry (see figure 1.2). The axial range resolution using a chirped wave with

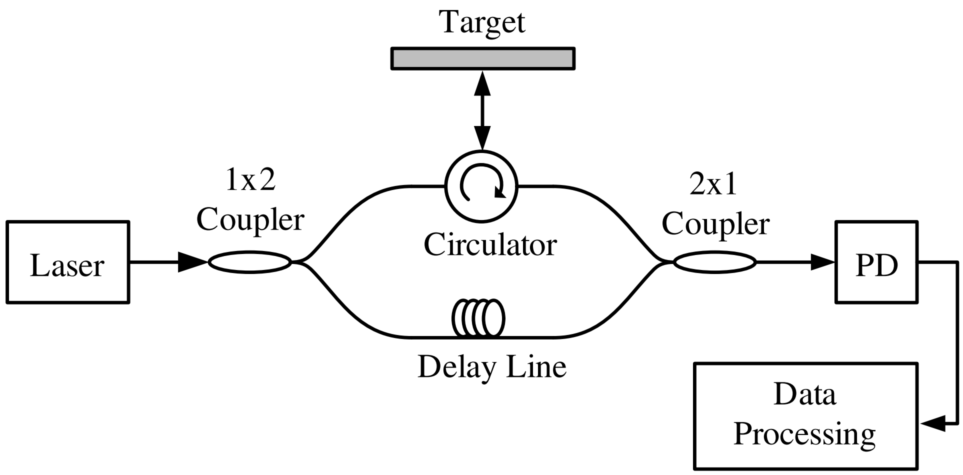

Figure 5.8. Schematic diagram of an FMCW ranging experiment with a linearly chirped optical source.

chirp bandwidth B (rad/s) is given by [54, 55]

$$\Delta d = \frac{\pi c}{B}, \tag{5.16}$$

where c is the speed of light, and a bandwidth of 500 GHz corresponds to a range resolution of 0.3 mm in air. The ability of the chirped VCSEL to resolve closely spaced targets was measured using the FMCW experimental setup shown in figure 5.8. Acrylic sheets of refractive index 1.5 and thicknesses varying from 1 to 6 mm were used as the target, and the reflections from the front and back surfaces were measured. A fiber delay line was used in the other arm of the interferometer to match the path lengths to about 0.5 m. The distance to the target was measured by computing the spectrum of the received photocurrent using a discrete-time Fourier transform.

The results of the measurement are shown in figure 5.9. From equation (5.16), the range resolution of this source is 0.2 mm in acrylic, though the practical resolution limit is 2 to 3 times this theoretical minimum resolution limit [55]. We see that the dual reflections at the smallest spacing of 1 mm are also perfectly resolved by the measurement. Range resolution measurements with smaller separations are discussed in the next chapter.

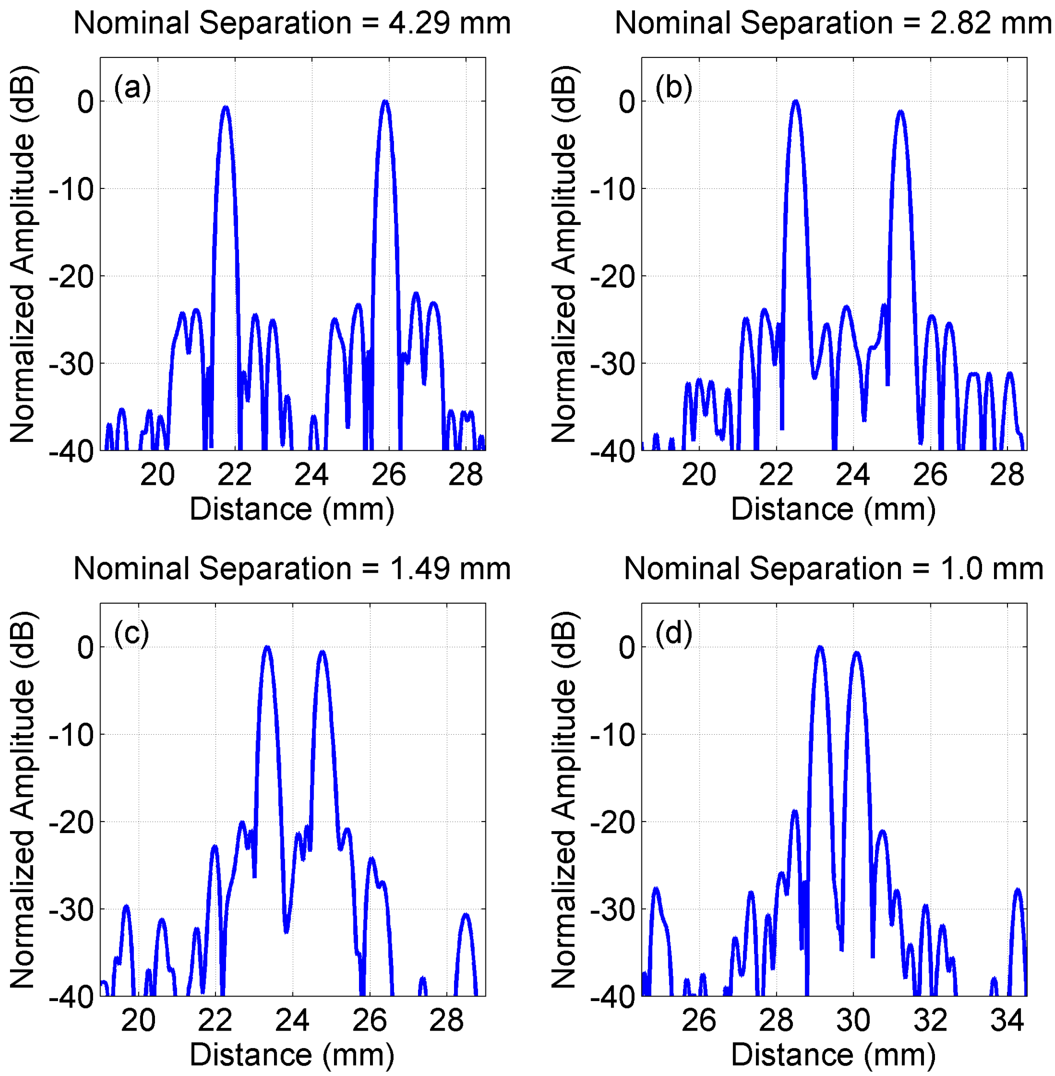

Figure 5.9. Range resolution measurements using the optoelectronic swept-frequency VCSEL. The target was an acrylic sheet of refractive index 1.5 and nominal thickness (a) 4.29 mm, (b) 2.82 mm, (c) 1.49 mm, and (d) 1.0 mm.

5.5 Label-Free Biomolecular Sensing Using an Optoelectronic SFL

Ranging experiments based on a linear swept-frequency optical source make use of the constant slope of the frequency chirp to determine the distance to the target, and the starting frequency of the sweep is not critical.[3] The precise control over the starting frequency of the optical chirps ensures that the frequency profile is repeatable over multiple scans, and enables the use of the SFL in sensing and spectroscopic applications. In this section, we demonstrate the use of the optoelectronic SFL in liquid-phase label-free biomolecular sensing using a whispering gallery mode optical microtoroid resonator. We will limit ourselves to describing the salient features of the experiment and demonstrating that the SFL is particularly suitable for the application—detailed descriptions of sensor fabrication, chemical surface functionalization and the experimental setup are beyond the scope of this thesis.

Biomolecular assays that eliminate the need for labeling target biological molecules are very attractive for medical diagnostics since they can streamline the process and reduce the number of process steps as compared to traditional assays. Systems based on the measurement of surface plasmon resonances are already commercially available and have the ability to detect as little as 10 fg (10^{-14} g) of a target biomolecule material. In this work, we consider an alternative technique which is based on the measurement of the change in resonant frequency of a high-quality factor (Q) optical mode [114], specifically the whispering gallery mode of a silica microtoroid resonator [115]. The resonant frequency[4] of the mode is measured by coupling light into the toroid using a tapered optical fiber [116] and measuring the transmission as a function of frequency. The surface of the resonator is functionalized using a chemical agent that selectively binds the target molecule of interest. The target molecule typically

[3]An exception is in the stitching of multiple swept-frequency sources, described in chapter 6.2

[4]Resonant wavelength shifts are typically reported in literature, whereas the optoelectronic SFL produces a perfectly linear chirp in optical frequency. We will refer to both the resonant wavelength and frequency in this section. The observed changes in the resonant frequency are small enough that they can be considered proportional to the changes in the resonant wavelength.

has a higher refractive index than the medium (water), and it therefore causes a small variation in the effective refractive index of the optical mode when it binds to the surface. The measurement of the resultant shift in the resonant wavelength can be used to quantitatively measure the concentration of the target molecule present in the solution, and sensitivities down to the single molecule level have been reported using this technique [117].

The optical resonant frequency is tracked using a tunable laser, and sensing experiments have almost universally used external-cavity mechanically tuned lasers for this purpose. These lasers suffer from two main drawbacks—their fast tuning range is typically much smaller than the free spectral range of the resonator, making it difficult to locate the resonance of interest; and the chirp is not necessarily linear, which constrains the measurement. The optoelectronic SFL developed in this work can overcome these limitations at a lower price and with improved robustness due to the lack of moving parts. The linewidth of typical DFB SCLs is ∼1 MHz, which corresponds to a Q of $\sim 2 \times 10^8$ at 1550 nm. This implies that if the Q of the resonance is much lesser than 2×10^8, the SFL behaves like a rapidly moving delta function that samples the optical resonance. The wide tuning range of the optoelectronic SFL helps to interrogate a large part of the free spectral range of the mode, making it easier to find the location of the resonance. In our experiments, we used SFLs with a tuning range of 100 GHz and a frequency chirp slope of 10^{14} Hz/s.

The measurement of a high-Q whispering gallery mode of a microtoroid in air at 1539 nm, shown in figure 5.10, demonstrates the ability of the laser to clearly resolve resonances with quality factors of 1.7×10^7 and 3×10^7. The splitting of the resonance in figure 5.10 is attributed to coupling between the two counterpropagating modes of the resonator, which breaks their degeneracy. We note that if a stable resonator can be fabricated sufficiently high-Q, so that the resonance linewidth much smaller than the linewidth of the laser, the resonator can be used to measure the "linewidth" of the laser as its frequency is varied.[5]

[5]The "linewidth" of the chirped laser discussed here is more accurately the frequency resolution of the chirped laser.

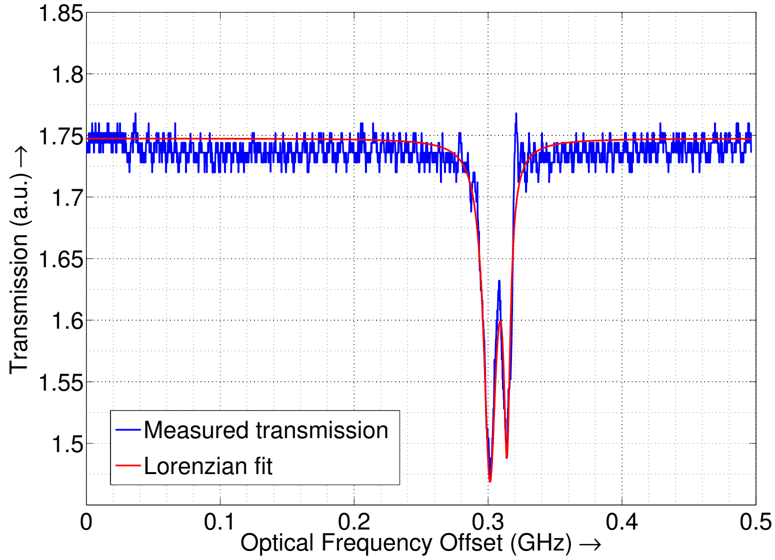

Figure 5.10. High-Q mode of a silica microtoroid in air, measured using an optoelectronic SFL at 1539 nm. The starting frequency of the sweep is subtracted from the x-axis. The splitting of the mode is attributed to scattering that couples degenerate counterpropagating modes and is resolved well by the measurement. From the Lorenzian fits, the quality factors of the modes are given by 1.7×10^7 and 3.3×10^7.

The sensing of biologically relevant molecules requires that the resonator be immersed in water, since these molecules almost always exist in aqueous solution. However, water has a large absorption coefficient at telecom wavelengths, at which our lasers were originally developed. The large absorption in water of the evanescent tail of the optical mode significantly reduces the Q of the resonance. The best quality factors we measured across a large number (hundreds) of microtoroids in water at 1539 nm were limited to $\sim 2 \times 10^4$, as shown in figure 5.11(a), compared to best values of $\sim 2 \times 10^7$ in air. For this reason, liquid-phase sensing using optical resonators is typically performed at lower wavelengths toward the visible region of the optical spectrum. The absorption coefficient of water at 675 nm (4.2×10^{-13}) is much smaller than at 1300 nm (1.1×10^{-10}) and 1550 nm (1.3×10^{-9}) [118]. We therefore developed an optoelectronic SFL based on a DFB laser at 1310 nm, and using this SFL, measured quality factors of up to $\sim 4 \times 10^5$ at this wavelength for microtoroids in water, as shown in figure 5.11(b).[6] Efforts are in progress to develop SFLs at even

[6]It is important to note that the measurements of figure 5.11 (a) and (b) were not performed

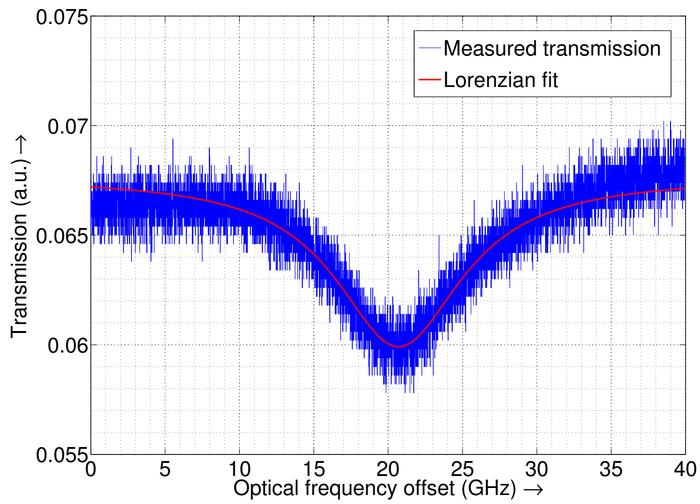

(a)

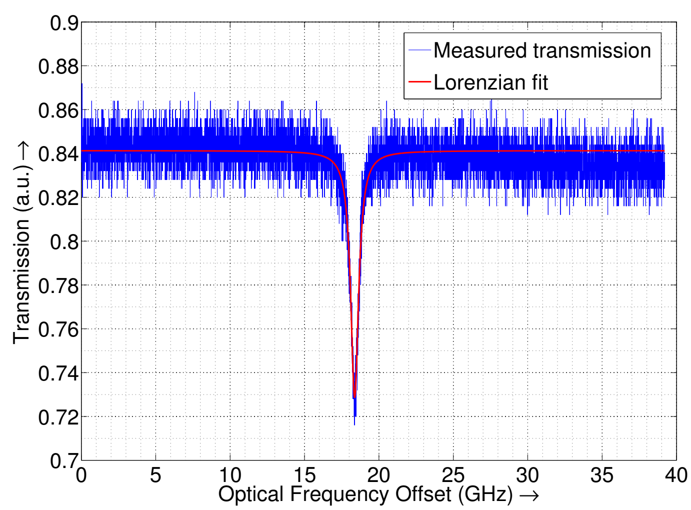

(b)

Figure 5.11. Whispering gallery mode resonances of a microtoroid in water, measured using optoelectronic SFLs at (a) 1539 nm and (b) 1310 nm. The starting frequency of the sweep is subtracted from the x-axis. From Lorenzian fits, the quality factors are measured to be 2.2×10^4 and 3.6×10^5 respectively.

lower wavelengths in the visible region, but the improvement of the quality factor by an order of magnitude to the 10^5 range already enables us to perform high-sensitivity biomolecular sensing experiments at 1310 nm.

We now present results of “specific” sensing of the molecule 8-isoprostane which is a marker for inflammation in exhaled breath. Concentrations of this biomarker are so low that, even when large volumes of breath condensate are collected (requiring a patient to breathe into the collection apparatus for 10 to 20 minutes), measurements remain near the detection limit [119, 120]. Improved sensitivity could reduce sample collection times and improve measurement confidence. The measurement is performed using a whispering gallery mode of a microtoroid resonator with a Q of 4.2×10^5 in water at 1310 nm. The measurement was performed by introducing known concentrations of the following solutions into a “flow cell” (volume $\lesssim$0.1 mL) containing the microtoroid, at a constant flow rate of 50 µL/min maintained using a syringe pump.

1. Protein G solution at 100 nM:[7] This molecule binds to the surface of the silica microtoroid and provides binding sites for the adsorption of the antibody of interest.

2. Anti-8-isoprostane at 67 nM: This antibody binds to the protein G on the microtoroid surface, and provides binding sites for the detection of the target biomolecule.

3. 8-isoprostane, varying concentrations: When a solution containing different biomolecules is introduced into the flow cell, the 8-isoprostane molecules selectively bind to the anti-8-isoprostane on the resonator surface, enabling specific sensing.

---

using the same microtoroid; rather, they correspond to the typical largest quality factors measured among a large number (hundreds) of toroids. Variations in toroid fabrication necessitate the scouting of a large number of devices to find high-Q modes suitable for biosensing.

[7] A solution of concentration 1 M (1 molar) consists of one mole, or 6.023×10^{23} molecules, of the solute in one liter of the solution.

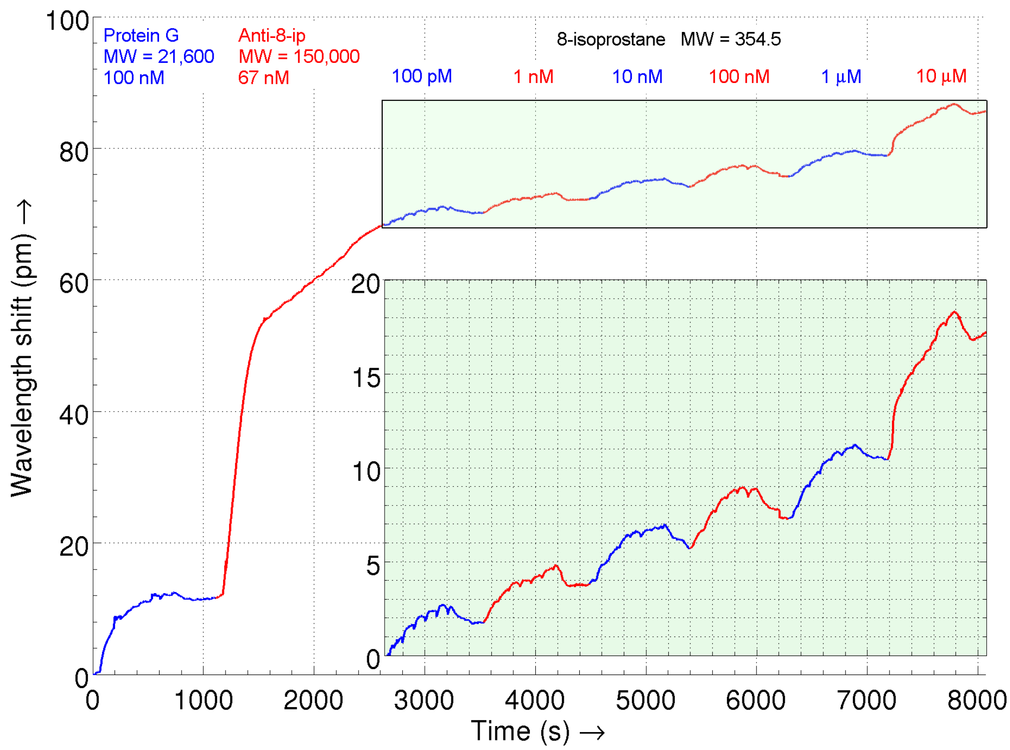

Figure 5.12. Specific sensing of 8-isoprostane using a microtoroid resonator and an optoelectronic SFL at 1310 nm. The quality factor of the resonance was 4.2×10^5, and the flow rate was 50 μL/min.

The resultant shifts in the resonant wavelengths were recorded and are plotted in figure 5.12. Protein G and Anti-8-isoprostane are large molecules (molecular weights of 21,600 and 150,000 respectively, as listed in the figure), and therefore result in large resonant shifts. The introduction of different concentrations of the small target molecule, 8-isoprostane, results in different values of shift in the resonant wavelength. These preliminary experiments demonstrate the ability of this sensor to measure concentrations of the analyte at least as low as 100 pM. The small physical size of the molecule results in very small wavelength shifts, but these can be resolved by the measurement. Further studies are necessary to determine the detection limit and the dynamic range of the sensor. Studies are also in progress to analyze the effects of fluid flow across the toroid and the resultant heat transfer away from the toroid, on the resonant wavelength.

We note that the measurement described above was performed using a resonance with a Q of "only" 4.2×10^5, and does not fully harness the advantages of low scattering losses in a reflown microtoroid resonator [115]. This implies that other, more convenient, resonator configurations can be used to perform measurements with similar sensitivity—in particular, integrated waveguide-resonator configurations lithographically fabricated on a single chip. Such devices will not require the extremely precise alignment of a tapered fiber to couple light into the resonator, and have the potential to enable the sensor to progress from merely a complex laboratory demonstration to a practically feasible and useful device.

Chapter 6

Extending the Bandwidth of SFLs

Frequency-swept optical waveforms with large frequency chirp range (optical bandwidth) have applications in high resolution optical imaging, LIDAR and infrared and Terahertz spectroscopy. The spatial resolution of an imaging system using a chirped laser source is inversely proportional to the chirp bandwidth as per equation (5.16), and the unambiguous range of the distance measurement is governed by the coherence length of the laser. Optical ranging applications therefore benefit from rapidly tunable, wide-bandwidth, and narrow-linewidth swept-frequency optical sources. Rapidly swept laser sources with wide tuning ranges of ∼10–20 THz also find applications in swept-source optical coherence tomography (SS-OCT) [50]. We have demonstrated in chapter 5 the generation of precisely controllable optical frequency sweeps using an SCL in an optoelectronic PLL; however, the chirp bandwidth was limited to about 500 GHz by the tuning range of the single-mode SCLs used. In this chapter, we demonstrate two approaches to increase the chirp bandwidth for high-resolution imaging: (i) chirp multiplication by four-wave mixing (FWM) and (ii) multiple source- (MS-) FMCW reflectometry where measurements using distinct optical chirps are algorithmically stitched to produce a high-resolution image.

6.1 Chirp Multiplication by Four-Wave Mixing

In this section, we propose and demonstrate the doubling of the bandwidth of a chirped optical waveform by the process of FWM in a nonlinear optical medium. It is a well-known observation [121] that the dithering of the pump signal to suppress Stimulated Brillouin Scattering (SBS) in a FWM experiment produces a broadening of the idler signal; this broadening is generally regarded as an undesirable side effect. We theoretically and experimentally demonstrate that the frequency chirp characteristics of the pump signal are faithfully reproduced in the idler, which implies that the chirp-doubled signal can be used for higher-resolution optical imaging. The effect of chromatic dispersion on the maximum achievable output bandwidth is analyzed, and a dispersion compensation technique to reduce the required input power levels is described. We show that this approach can be cascaded to achieve a geometrical increase in the output chirp bandwidth, and that the chirp bandwidth can be tripled using two chirped input fields. Finally, we present the design of a cyclical FWM "engine" to achieve large output chirp bandwidths using a single nonlinear waveguide.

6.1.1 Theory

6.1.1.1 Bandwidth-Doubling by FWM

Consider the experiment shown in figure 6.1. A chirped optical wave and a "reference" monochromatic wave are coupled together, amplified, and fed into a nonlinear optical waveguide with a large third-order nonlinear susceptibility $\chi^{(3)}$, and a relatively low group velocity dispersion (GVD) parameter D_c. Highly nonlinear fibers (HNLF), photonic crystal fibers, higher-order mode (HOM) optical fibers [122], semiconductor optical amplifiers (SOAs) [123] and integrated silicon waveguides [124] can be used to provide the necessary nonlinear susceptibility and control over the GVD. In this work, we will assume that the nonlinear medium is a highly nonlinear optical fiber. An optical filter, typically based on a diffraction grating, is used at the output to select the waveform of interest.

Let the electric fields of the chirped and the reference waves be given by

$$\begin{aligned} E_{ch}(z,t) &= \frac{1}{2}A_{ch}(z)\exp\left(j(\omega_0 t + \phi(t) - \beta_{ch} z)\right) + \text{c.c.}, \\ E_R(z,t) &= \frac{1}{2}A_R(z)\exp\left(j(\omega_R t - \beta_R z)\right) + \text{c.c.}, \end{aligned} \tag{6.1}$$

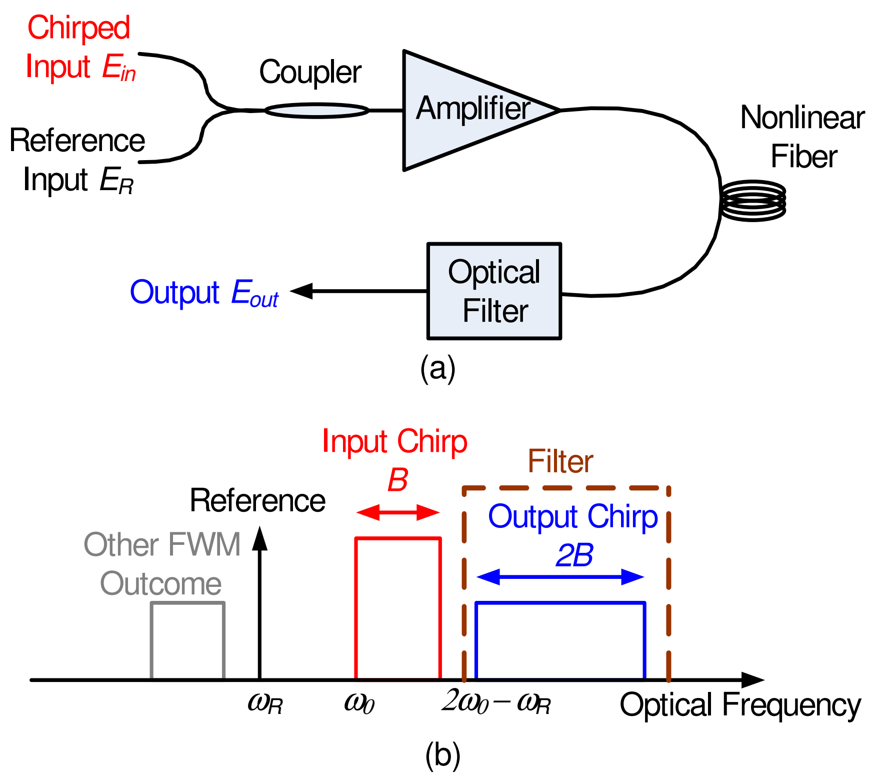

Figure 6.1. (a) Schematic diagram of the four-wave mixing (FWM) experiment for chirp bandwidth-doubling. (b) Spectral components of the input and FWM-generated fields. The chirp-doubled component is optically filtered to obtain the output waveform.

where $\phi(t)$ represents the optical chirp. The fields are assumed to be linearly polarized along the same axis, and z is the direction of propagation. The propagation vectors β are determined by the waveguide. The instantaneous frequency of the chirped wave is given by

$$\omega_{ch}(t) = \omega_0 + \frac{d\phi}{dt}. \tag{6.2}$$

For the particular case of a linearly chirped wave, $\phi(t) = \xi t^2/2$, and $\omega_{ch}(t) = \omega_0 + \xi t$. Typical optical frequency chirps of interest for imaging exceed bandwidths of 100 GHz in a time less than 1 ms, and SBS effects can be neglected in this analysis. The rate of the optical chirp is several orders of magnitude slower than the optical frequency, and the chirped wave can therefore be regarded as a monochromatic wave of frequency $\omega_{ch}(t)$. The chirped and reference waves interact in the nonlinear fiber through the FWM process to give rise to a nonlinear polarization [88]

$$P_{NL} = 4\chi^{(3)}\vdots EEE, \tag{6.3}$$

where E is the vector sum of the electric fields in equation (6.1). Among the various frequency terms which are present in the triple product in equation (6.3) is the term

$$P_{NL}(z,t) \propto A_{ch}^2 A_R^* \exp\left(j\left((2\omega_0 - \omega_R)t + 2\phi(t)\right)\right), \tag{6.4}$$

which radiates a wave of frequency

$$\omega_{out}(t) = 2\omega_0 - \omega_R + 2\frac{d\phi}{dt} = 2\omega_{ch}(t) - \omega_R. \tag{6.5}$$

This process can be described quantum mechanically by the annihilation of two photons of the chirped field to create a photon of the reference field and a photon of the output field. Comparing equations (6.5) and (6.2), we see that the output chirp is twice the input chirp. By the proper selection of the input frequencies ω_0 and ω_R, the output waveform can be separated out by an optical filter, as shown in figure 6.1(b). If the bandwidth of the input chirp is B (radians), the necessary condition for filtering the output waveform is

$$\Delta\omega(t) \doteq \omega_{ch}(t) - \omega_R \geq B. \tag{6.6}$$

Note that the output optical wavelength is in the same region as the input, and the output can therefore be amplified and reused in a cascaded scheme as discussed in section 6.1.3.

The expression for the output optical power can be obtained following a straightforward derivation [125] as outlined below. We restrict ourselves to the output electric field of the form

$$E_{out}(z,t) = \frac{1}{2} A_{out}(z) \exp\left(j(\omega_{out} t - \beta_{out} z)\right) + \text{c.c.}, \tag{6.7}$$

which is generated by plugging the nonlinear polarization in equation (6.3) into the nonlinear wave equation

$$\frac{\partial^2 E}{\partial z^2} = \frac{n^2}{c^2}\frac{\partial^2 E}{\partial t^2} + \frac{\alpha n}{c}\frac{\partial E}{\partial t} + \mu_0 \frac{\partial^2 P_{NL}}{\partial t^2}, \tag{6.8}$$

where n is the refractive index in the fiber and α represents the loss per unit length. The input chirped and reference fields are assumed to be undepleted, i.e.,

$$A_{ch,R}(z) = A_{ch,R}(0) \exp(-\alpha z/2), \tag{6.9}$$

and $A_{out}(z)$ is assumed to be slowly growing along the waveguide, i.e., $\partial^2 A_{out}/\partial z^2 \ll \beta_{out}\, \partial A_{out}/\partial z$. The differential equation for the output field is then given by

$$\frac{dA_{out}}{dz} = -\frac{\alpha}{2} A_{out} - \frac{jnc\epsilon_0 \gamma A_{eff}}{2} A_{ch}^2(0) A_R^*(0) e^{-3\alpha z/2} e^{-j\Delta\beta z}, \tag{6.10}$$

where A_{eff} is the effective area of the mode in the fiber, γ is the nonlinear coefficient of the fiber, given by

$$\gamma = \frac{3\omega\mu_0\chi^{(3)}}{n^2\epsilon_0 A_{eff}}, \tag{6.11}$$

and $\Delta\beta$ is the phase mismatch defined as

$$\Delta\beta \doteq 2\beta_{ch} - \beta_R - \beta_{out}. \tag{6.12}$$

The phase mismatch is a function of the frequency difference between the chirped wave and the reference wave. Ignoring the effect of self phase modulation of the chirped beam (which is valid when the input power is low), equation (6.12) can be written as

$$\Delta\beta = -2\sum_{m=1}^{\infty} \frac{\beta_{2m}}{(2m)!}(\Delta\omega)^{2m}, \tag{6.13}$$

where $\Delta\omega$ is defined in (6.6) and β_m is the mth derivative of $\beta(\omega)$, evaluated at $\omega = \omega_{ch}$. The coefficient β_2 is related to the GVD parameter D_c by $\beta_2 = -\lambda^2 D_c/(2\pi c)$.

6.1.1.2 Bandwidth Limitations due to Dispersion

The power carried by the optical wave is related to its amplitude $A(z)$ by

$$P(z) = \frac{nc\epsilon_0 A_{eff}}{2} \left|A(z)\right|^2. \tag{6.14}$$

Integrating equation (6.10), we derive the output power after propagation through a distance L [125]:

$$P_{out}(L) = \gamma^2 P_{ch}^2 P_R \, e^{-\alpha L}\left(\frac{1-e^{-\alpha L}}{\alpha}\right)^2 \frac{\alpha^2}{\alpha^2 + \Delta\beta^2}\left(1 + \frac{4e^{-\alpha L}\sin^2\frac{\Delta\beta L}{2}}{\left(1-e^{-\alpha L}\right)^2}\right). \tag{6.15}$$

From equations (6.13) and (6.15), the maximum value of the input frequency separation, and hence the output chirp bandwidth, will ultimately be limited by the phase mismatch in the fiber. Consider as an example, a commercially available dispersion-flattened HNLF with a nonlinear coefficient $\gamma = 11.3$ km^{-1}W^{-1}, loss $\alpha = 1$ dB/km, and dispersion parameter $D_c = 0.5$ ps/nm.km. For this dispersion-flattened fiber, higher-order dispersion terms (β_4 and above in equation (6.13)) can be neglected. Let us assume that the chirp and reference powers are equal, i.e., $P_{ch} = P_R$. The output power as a function of the input frequency separation $(\omega_{ch} - \omega_R)$, for various

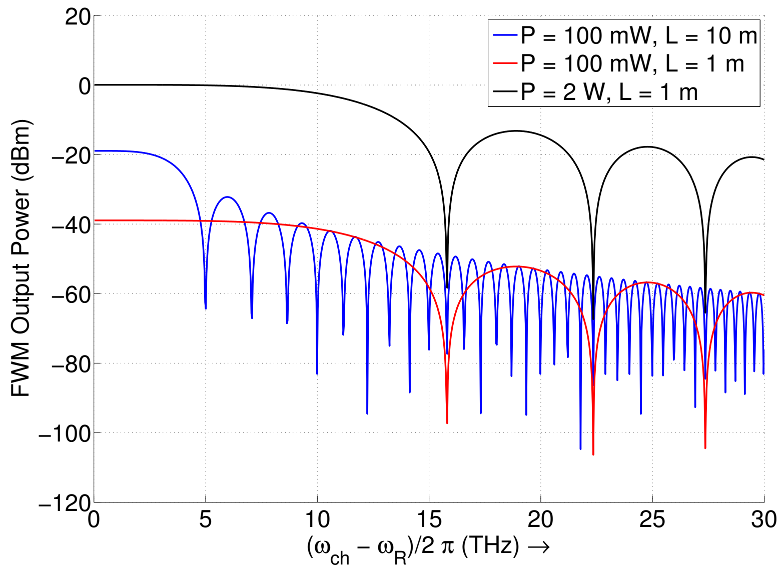

Figure 6.2. Output power as a function of the input frequency difference, for different values of fiber length and input power ($P_{ch} = P_R = P$). The dispersion, loss and nonlinear coefficient of the fiber are described in the text.

values of input power P_{ch} and fiber length L, is calculated using equations (6.13) and (6.15) and plotted in figure 6.2. The FWM bandwidth B_{FWM} can be defined as the maximum input frequency separation over which useful output power is generated, which is here taken to be the -3 dB point. It is important to note that the filtering condition in equation (6.6) implies that B_{FWM} is equal to the maximum possible output bandwidth. The maximum fiber lengths and the input power requirements for different values of output bandwidth and output power are summarized in table 6.1.

It is clear from figure 6.2 and table 6.1 that the maximum output bandwidth is determined by the length of fiber used in the experiment. For a given value of the dispersion parameter, B_{FWM} reduces as L is increased. To obtain larger bandwidths, a fiber with lower dispersion must be used. For a given length of fiber, the output power level depends only on the input power. For example, for a desired output bandwidth of 10 THz and an output power of 0 dBm, the maximum (dispersion-limited) fiber length is 1.1 m, and the input power required is $P_{ch} = P_R = 1.9$ W. This power level can be achieved with high power fiber amplifiers, but is desirable

Table 6.1. Length of HNLF and input power requirements for different output bandwidths and power levels

Output bandwidth (THz)	Maximum fiber length (m)	Input power required $P_{ch} = P_R$ (dBm)	
		$P_{out} = 0$ dBm	$P_{out} = -10$ dBm
1	105	19.5	16.2
5	4.3	29.0	25.4
10	1.1	32.8	29.5
15	0.45	35.2	32.0

that commercially available telecom-grade erbium doped fiber amplifiers (EDFAs) with output powers of approximately +20 dBm be used to reduce the system cost. In the following section, we describe a quasi-phase-matching technique using dispersion compensation to achieve this target.

6.1.1.3 Quasi-Phase-Matching Using Alternating Dispersions

It is desirable to increase the length of the nonlinear fiber used in the experiment, so as to increase the interaction length for the FWM process, thereby reducing input power requirements. However, the length cannot be increased arbitrarily, since the phase mismatch causes a reduction in the overall output power. This limitation can be overcome by using a multisegment HNLF where the sign of the dispersion parameter of a segment is alternatively chosen to be positive or negative, as shown in figure 6.3(a). The dispersion parameter D_c is changed by engineering the waveguide dispersion differently in the alternating segments. We again make the assumption of a dispersion-flattened fiber where β_4 can be neglected. Dispersion-flattened HNLFs with dispersion parameters in the range of -1.0 to +1.5 ps/nm.km at 1550 nm are readily available. An exact expression for the output field is easily obtained by integrating equation (6.10) over the entire structure (see appendix B), but we present below an intuitive explanation of the power buildup in the fiber. For a low loss fiber, we can set $\alpha = 0$

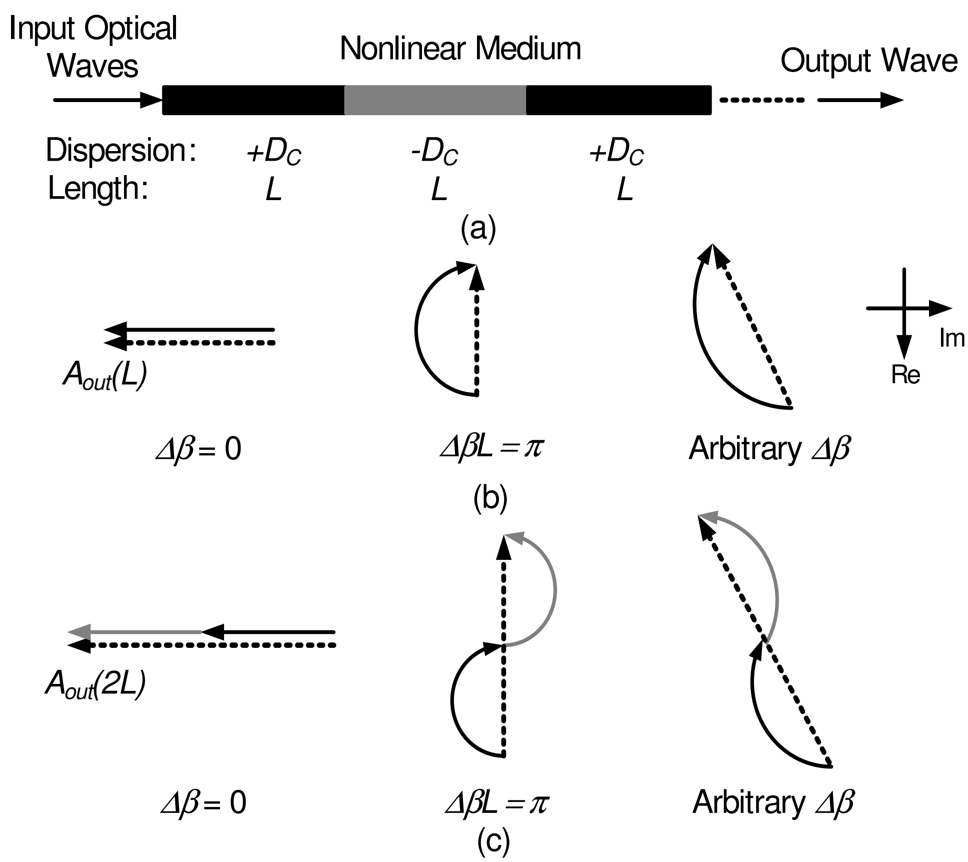

Figure 6.3. (a) Multisegment alternating dispersion waveguide for quasi-phase-matching. The evolutions of the output field $A_{out}(z)$ along the waveguide for one and two segments are shown in (b) and (c) respectively. The dashed lines represent the field at (b) $z = L$ and (c) $z = 2L$.

in equation (6.10) to obtain the simple differential equation

$$\frac{dA_{out}}{dz} = -\frac{jnc\epsilon_0\gamma A_{eff}}{2} A_{ch}^2(0)A_R^*(0)e^{-j\Delta\beta z}. \tag{6.16}$$

The solution to this equation is a phasor that traces out a circle in the complex plane as the distance z is increased, as shown in figure 6.3(b). The maximum value of the field occurs when $z_{max}\Delta\beta = \pi$. As z is increased beyond this value, the magnitude of the field phasor decreases, and the power output decreases. When the sign of the dispersion parameter is reversed, the sign of $\Delta\beta$ is also reversed according to equation (6.13), and the field phasor now traces out a circle of the opposite sense, as depicted in figure 6.3(c). By symmetry considerations, the total output field at the end of the second segment is equal to twice the value of the field at the end of the first segment, *for any arbitrary value of* $\Delta\beta$. For a structure with N alternating segments, the output field scales as N, and the output power scales as N^2. The variation of P_{out} along a structure with three alternating segments of HNLF for an input frequency difference of 10 THz, calculated using equation (B.10), is plotted in figure 6.4, clearly showing the quadratic scaling of the output power with number of segments. Conversely, for a given desired output power, the input power requirement is reduced. For the HNLF example considered in section 6.1.1.2, an output bandwidth of 10 THz and output power of 0 dBm can be achieved using a structure with 30 segments of length L = 1.1 m and alternating dispersions of ±0.5 ps/nm.km, with an input power of only 200 mW, as opposed to an input power requirement of 1.9 W if a single segment were used.

The number of segments that can be used in this technique is limited by the insertion loss due to the fiber splices. Let the ratio of the transmitted to the incident field amplitudes at a fiber splice be given by t, and let $F^{(k)}$ denote the amplitude of the FWM field generated in the kth segment. The fields generated in all the segments add in phase. The chirped and reference fields in the kth segment are given by $A_{ch,R}^{(k)} = t^{k-1}A_{ch,R}^{(1)}$, and the FWM field generated in the kth segment is consequently

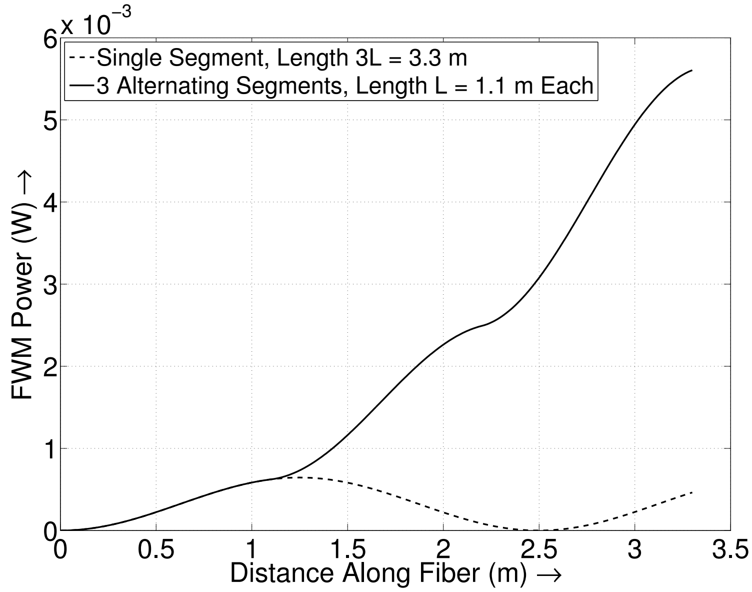

Figure 6.4. Comparison of the generated FWM field in a structure with 3 segments of lengths L each and alternating dispersions of $\pm D_c$, with a single segment of length $3L$ and dispersion $+D_c$. The values used in the calculations were $L = 1.1$ m and $D_c = 0.5$ ps/nm.km.

given by $F^{(k)} = t^{3k-3}F^{(1)}$. The output field after the kth stage is therefore given by

$$A_{out}^{(k)} = tA_{out}^{(k-1)} + t^{3k-3}F^{(1)}, \tag{6.17}$$

which can be solved to yield

$$P_{out}^{(k)} = \left(\frac{t^{k-1}(1-t^{2k})}{1-t^2}\right)^2 P_{out}^{(1)}. \tag{6.18}$$

Under the assumption that $(1-t) \ll 1$, equation (6.18) reduces to

$$\frac{P_{out}^{(k)}}{P_{out}^{(1)}} \approx k^2 t^{2(k-1)}. \tag{6.19}$$

It is therefore crucial to minimize the splice losses in order to increase the FWM interaction length. In the absence of splice losses, the number of segments is limited by material loss in the waveguide, and the total achievable bandwidth is ultimately limited by the gain bandwidth of the amplifiers used in the experiment.

It should be noted that quasi-phase matched FWM using a similar concept has been demonstrated theoretically and experimentally [126, 127], where the phase mismatch accumulated during the FWM process is periodically compensated for using a dispersion-compensating fiber (DCF) or a single-mode fiber (SMF). In the process described in this section, the quasi-phase-matching is achieved using nonlinear fiber. This is an important distinction since the use of SMF or DCF will require two fiber splices per segment of HNLF, which then leads to a lower achievable gain from equation (6.19). Further, the loss per splice is also expected to be higher, since dissimilar fibers have to be spliced together.

We have again neglected the effect of higher-order dispersion terms in the preceding analysis. In the presence of nonnegligible higher-order dispersion terms, perfect quasi-phase-matching can only be achieved by reversing the signs of all the terms β_{2m} in equation (6.13), for $m = 1, 2, \ldots$. However, a degree of quasi-phase-matching can still be achieved by reversing the sign of the dispersion parameter D_c. The modification to the output power due to the effect of higher-order terms can be determined exactly by integrating equation (6.10). A general expression for the power generated due to four-wave mixing in a multisegment nonlinear waveguide is derived in appendix B.

6.1.2 Experiment

6.1.2.1 Chirp Bandwidth-Doubling

A schematic diagram of the proof-of-principle experimental setup is shown in figure 6.5. The input chirped wave was a perfectly linearly chirped waveform that sweeps 100 GHz in 1 ms, generated using a DFB SCL in an optoelectronic feedback loop as described in chapter 5. A tunable laser (Agilent Technologies) was used as the monochromatic reference wave. The two optical waves were coupled using a polarization maintaining coupler, amplified using an EDFA and fed into a commercial dispersion-flattened HNLF. The HNLF had a gain $\gamma = 11.3$ km^{-1}W^{-1}, loss $\alpha =$ 1 dB/km, length $L = 100$ m, and dispersion parameter $D_c = +1.2$ ps/nm.km. The

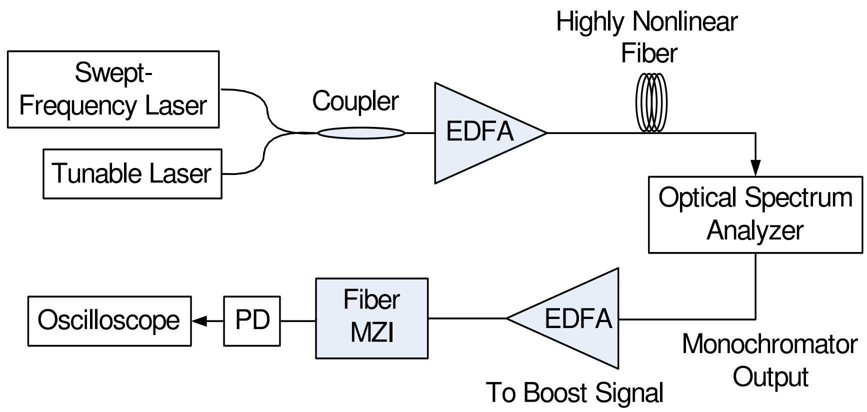

Figure 6.5. Schematic diagram of the experimental setup for the demonstration of chirp bandwidth-doubling by four-wave mixing. EDFA: Erbium doped fiber amplifier, MZI: Mach-Zehnder interferometer, PD: Photodetector. The differential delay in the MZI is approximately 2.7 ns.

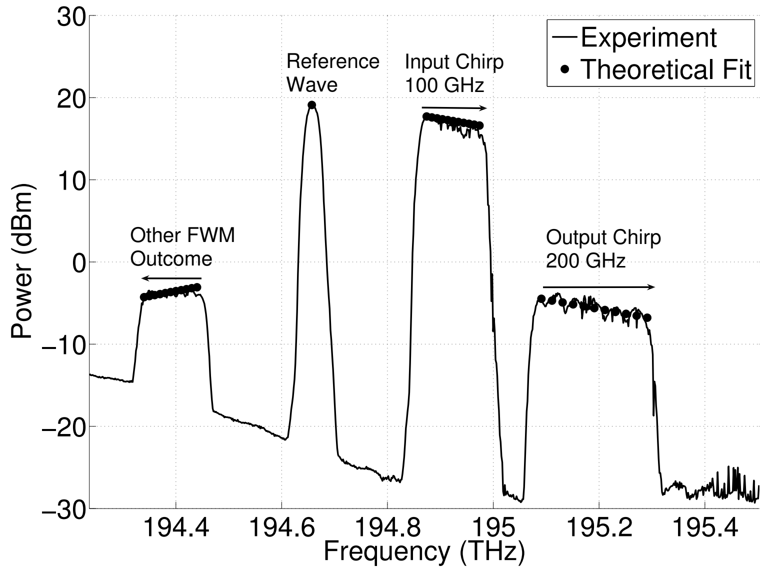

Figure 6.6. Experimental demonstration of bandwidth-doubling by four-wave mixing. The reference wave was monochromatic (resolution limited) and the input chirp bandwidth was 100 GHz. The arrows indicate the direction of the chirp. The second FWM product, generated at the lower frequency, chirps in the opposite direction. The theoretical FWM power was calculated using equations (6.13) and (6.15) using the measured input powers.

output of the HNLF was measured on an optical spectrum analyzer, and is shown in figure 6.6. The figure clearly shows the generation of a frequency doubled FWM output that sweeps over an optical bandwidth of 200 GHz. A second FWM component sweeping over 100 GHz in the reverse direction was generated on the low frequency side, corresponding to the FWM process involving two photons of the reference wave and one photon of the chirped wave. The experimentally measured values of the output fields are in excellent agreement with the theoretical calculation based on the measured input powers and equations (6.13) and (6.15).

The ability of the experiment to reproduce the dynamic characteristics of the input optical frequency chirp at the output was also verified. The output waveform was filtered out using the monochromator output of the optical spectrum analyzer, and amplified using a telecom EDFA. The input and output frequency chirps were characterized by passing them through an MZI with time delay $\tau_{MZI} = 2.7$ ns, as shown in figure 6.5. The frequency of the detected photocurrent is related to the slope ξ of the optical chirp by $\omega = \xi\tau_{MZI}$. The spectrograms of the photocurrents are calculated and plotted in figure 6.7. The results clearly show that the optical chirp rate is doubled by the FWM process from 10^{14} to 2×10^{14} Hz/s, and the transform-limited linearity of the input chirp is maintained at the output, making the output frequency chirped waveform suitable for three-dimensional imaging applications. The FWM technique can also be used to increase the chirp rate of swept frequency optical waveforms.

6.1.2.2 Dispersion Compensation

We also demonstrated improved bandwidth in the FWM process using the dispersion technique for quasi-phase-matching described in figure 6.3. Two segments of dispersion-flattened HNLF with lengths 100 m each, and dispersion coefficients +0.38 ps/nm.km and −0.59 ps/nm.km were spliced together to obtain the dispersion-compensated waveguide. The other parameters of the HNLFs were identical to the one used in the previous section. Single-mode fiber pigtails were used at the input and output ends. The results of bandwidth-doubling experiments using the individual fibers and the

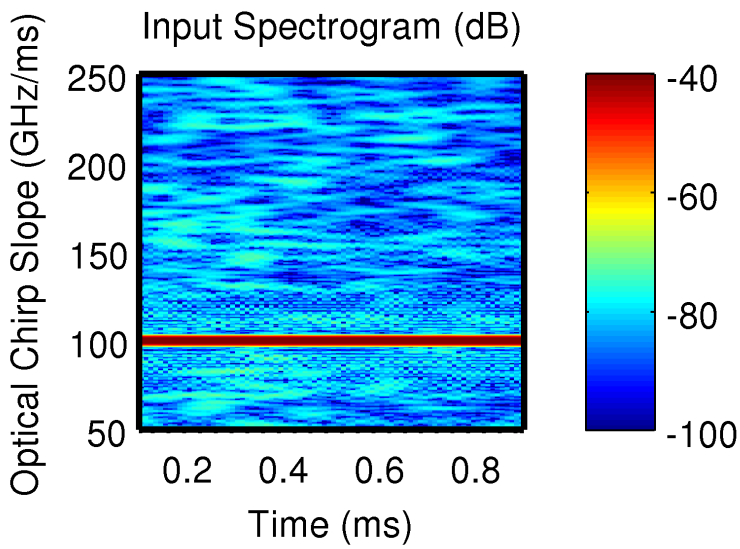

(a)

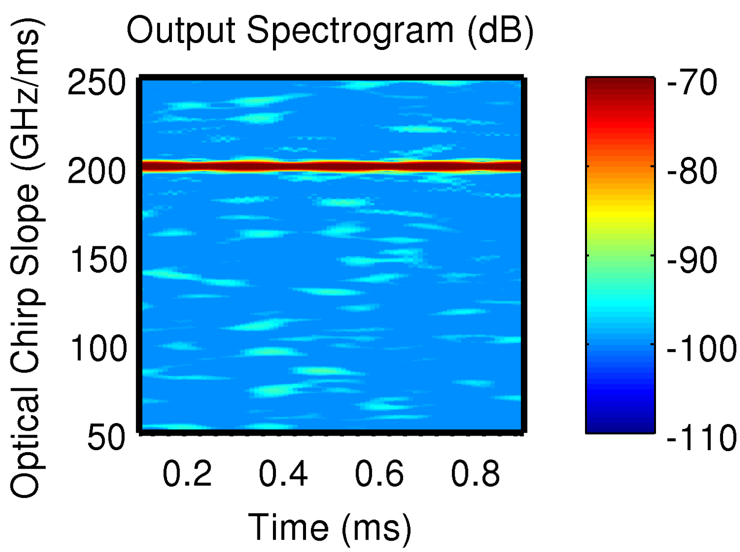

(b)

Figure 6.7. Measured slopes of the (a) input and (b) output optical chirps demonstrating the doubling of the optical chirp slope by FWM.

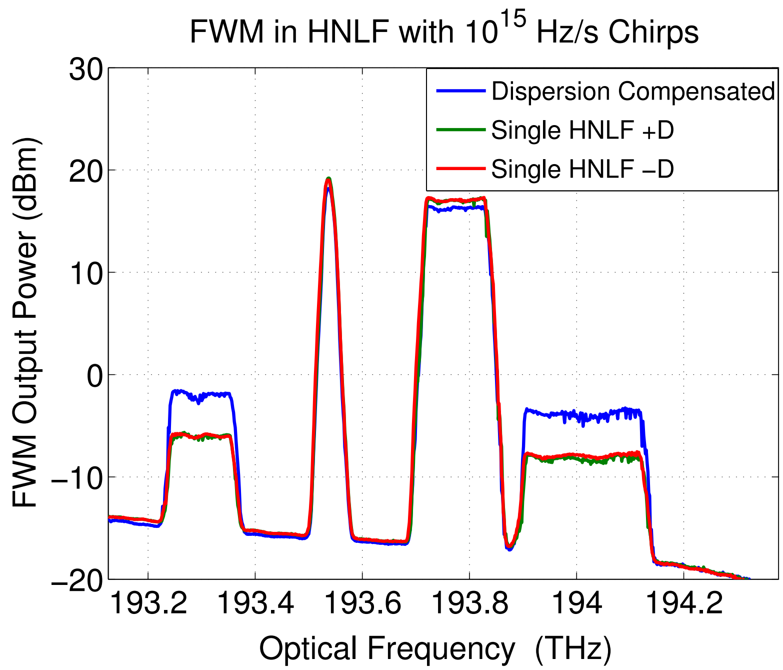

Figure 6.8. Improvement in the power generated by FWM using a two-segment HNLF. The length of each segment was 100 m and the values of the the dispersion parameter in the two segments were +0.38 ps/nm.km (+D) and −0.59 ps/nm.km (-D). The FWM power generated in experiments using the individual 100m HNLF segments is also shown.

dispersion compensated fiber with an input chirp of 100 GHz in 0.1 ms are shown in figure 6.8. An improvement in the conversion efficiency, owing to a longer interaction length for the FWM process, is clearly seen from the figure. If the chirped and reference powers are equal, the theoretical improvement in conversion efficiency is 6 dB; however, the observed improvement is only ∼4 dB, which is due to the slightly lower powers of the chirped and reference waves used.

The output FWM power in this two-segment fiber as a function of the input frequency separation is calculated using equation (B.10) and plotted in figure 6.9. The result is compared to the (hypothetical) case of 200 m of each individual fiber, which results in the same conversion efficiency. The input chirped and reference powers are assumed to be $P_{ch} = P_R = 100$ mW. We note that the bandwidth of the process is improved using the dispersion compensation technique.

As seen from figure 6.9, the low values of the dispersion parameters of the HNLF

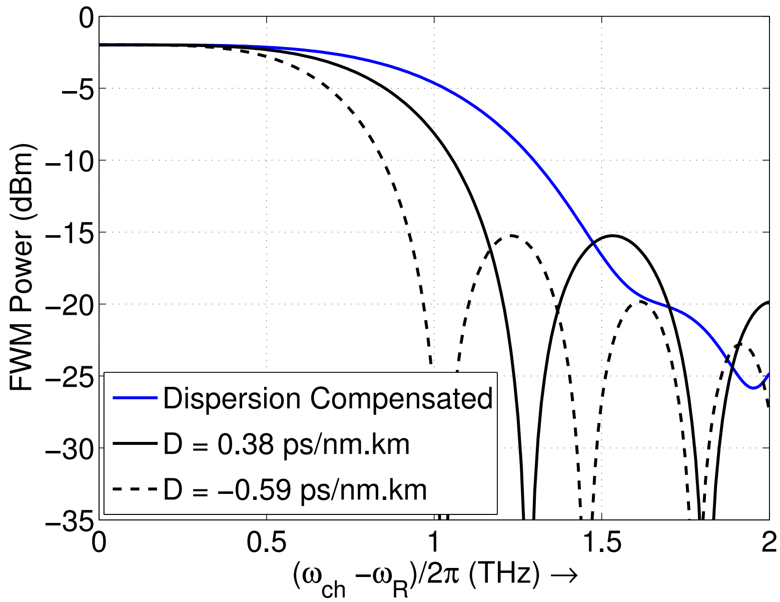

Figure 6.9. Theoretically calculated output power as a function of the input frequency difference for the two-segment dispersion compensated HNLF, compared to the same lengths ($L_{tot} = 200$ m) of individual fibers.

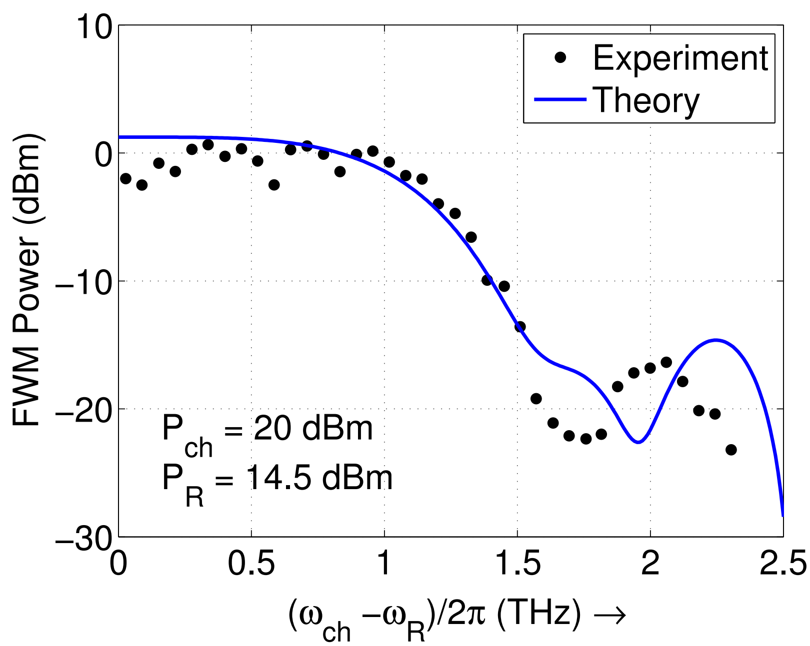

Figure 6.10. Experimentally measured FWM output power as a function of the input frequency difference for a two-segment HNLF, compared to theoretical calculations.

used in the experiment imply that an input frequency separation of the order of 0.5–1 THz is necessary to see a dip in the converted output power. Current implementations of optoelectronic SFLs in our laboratory are limited to bandwidths of $\leq$0.5 THz, and we therefore use a tunable laser (Agilent) as the chirped laser source in the experimental demonstration. The wavelength of the tunable laser is varied over a range of 2.5 THz, and a VCSEL (RayCan) acts as a monochromatic reference wave. The FWM experiment is then performed using a setup similar to figure 6.5. The nominal powers of the "chirped" wave and the reference wave, after amplification at the input stage, are 100 mW and 28 mW respectively. The actual power deviates from the nominal value due to the nonuniform gain spectrum of the EDFA. The experimentally measured output power as a function of the input frequency difference is plotted in figure 6.10, and compared with the theoretical calculation using equation (B.10). We see that there is good agreement between theory and experiment, and the discrepancies are probably due to the fact that we have assumed average and constant values for the dispersion parameters in each fiber segment, and ignored variations in the powers of the chirped and reference waves.

The effect of dispersion compensation can also be understood by comparing the shape of the roll-off of the power generated by FWM, as a function of the input frequency difference, for the individual fiber segments and the two-segment fiber. As seen in figure 6.11, the shape of the roll-off is almost identical for these fibers, corresponding to a dispersion-limited bandwidth of 100 m of fiber. The power generated is, however, larger by a factor of four in the dispersion-compensated fiber, as seen from figure 6.8.[1]

We have demonstrated the improvement in the bandwidth of the FWM process using a two-segment nonlinear fiber. Preliminary results from experiments with a four-segment fiber confirm the expected improvement in bandwidth; these results will be reported elsewhere.

[1]Note that power of the generated FWM wave is normalized in figure 6.11, for low values of $\omega_{ch} - \omega_R$.

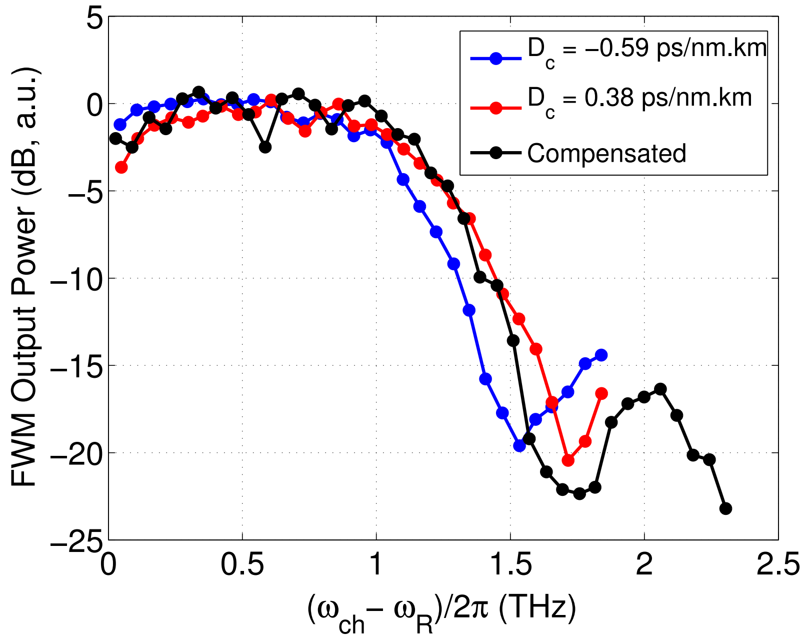

Figure 6.11. Comparison of the normalized experimentally measured FWM power in two individual segments of 100 m each with opposite signs of the dispersion parameter, and the dispersion-compensated two-segment fiber.

6.1.3 Bandwidth Extension

The FWM process demonstrated in this chapter generates a chirp-doubled optical wave in the same wavelength range as the input signal. The frequency spacing between the output chirp and the input chirp is only limited by the sharpness of the optical filter used to filter out the output. Using diffraction grating based filters, this gap can be as small as a few GHz. It has been demonstrated by Ishida and Shibata [128] that the FWM process can be cascaded to geometrically increase the frequency separation between the two input signals. This principle can be extended to chirped signals to achieve geometric increases in the chirp bandwidth. The output chirped signal from the FWM experiment can be filtered, amplified again using an EDFA and mixed with the same reference signal in an HNLF to further double the chirp bandwidth. A cascade of n such stages leads to the geometric scaling of the output bandwidth by a factor 2^n, as shown in figure 6.12. For example, starting with a 200 GHz chirped semiconductor laser at the input, an output bandwidth of 12.8 THz is obtained after

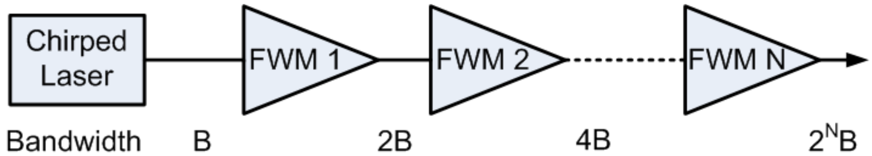

Figure 6.12. Cascaded FWM stages for geometric scaling of the chirp bandwidth. Each stage consists of a coupler, amplifier, HNLF and filter as shown in figure 6.1(a).

$n = 6$ stages. Note that the same reference monochromatic signal can be used for each stage, since the filtering condition (equation (6.6)) is always satisfied if it is satisfied for the first FWM stage. If the dispersion compensation technique for quasi-phase-matching described in section 6.1.1.3 is used, the total output bandwidth is only limited by the gain bandwidth of the amplifiers used in the experiment, and by additional noise introduced by the amplification stages.

The FWM process fundamentally involves the interaction of three input fields to produce the output field. An optimum use of the process for bandwidth multiplication can therefore result in bandwidth tripling, and not just doubling, as described below. Let the monochromatic reference wave of figure 6.1 be replaced by a chirped wave that sweeps in the direction opposite to the original chirp. We now have two input chirped waves which are mirror images of each other, with frequencies given by

$$\begin{aligned} \omega_{in,1} &= \omega_0 - B_0 - \frac{d\phi}{dt}, \\ \omega_{in,2} &= \omega_0 + B_0 + \frac{d\phi}{dt}, \end{aligned} \tag{6.20}$$

where ω_0 and B_0 are constants. The two output fields generated by two distinct FWM processes have frequencies

$$\begin{aligned} \omega_{out,1} &= 2\omega_{in,1} - \omega_{in,2} = \omega_0 - 3B_0 - 3\frac{d\phi}{dt}, \\ \omega_{out,2} &= 2\omega_{in,2} - \omega_{in,1} = \omega_0 + 3B_0 + 3\frac{d\phi}{dt}. \end{aligned} \tag{6.21}$$

The output waveforms have bandwidths that are thrice the bandwidth of the individual input chirps, as shown in figure 6.13. Further, the two output waveforms

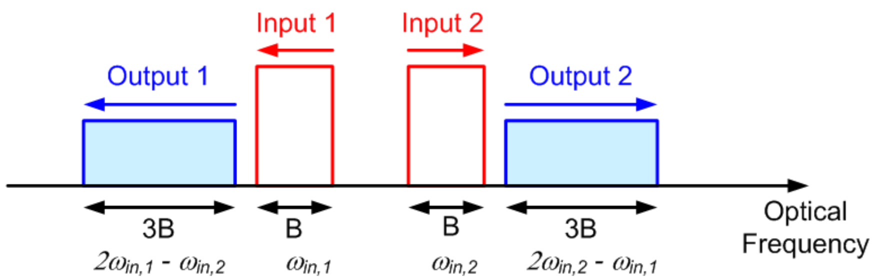

Figure 6.13. Spectral components in a bandwidth tripling FWM experiment using two chirped optical inputs.

can be amplified and used in a cascaded process similar to the one described for the bandwidth-doubling approach, to achieve a geometrical bandwidth scaling of 3^n. Starting with two frequency sweeps of 200 GHz each, a chirp bandwidth of 16.2 THz can now be achieved using $n = 4$ stages.

The geometric enhancement of the chirp bandwidth using a cascade of n stages has the drawback that it requires n amplifiers and n nonlinear waveguides, thereby increasing the overall system cost. This can be overcome by folding back the cascaded process using a FWM "engine" as shown in figure 6.14(a). The input chirped wave sweeps over a bandwidth B during a time T, and is then turned off. A monochromatic reference wave is also coupled into the nonlinear medium. The FWM output of bandwidth $2B$ is selected by the optical filter, delayed by a time T, amplified and fed back into the nonlinear fiber as the chirped input. From time T to $2T$, the optical filter is configured to select the new FWM output of bandwidth $4B$. The combination of optical filter configuration and the delay T therefore ensures that only two optical waves are input into the nonlinear fiber at a given instant of time. The slope of the frequency chirp at the output port then increases geometrically with time, as depicted in figure 6.14(b). The amount of practically achievable delay T imposes a lower bound on the input optical chirp rate, for a given chirp bandwidth. A fiber delay of 20 km provides a delay of 100 μs, which is quite sufficient for sweeping typical semiconductor lasers, and switching the optical filters. This approach can be easily modified to include two chirped inputs.

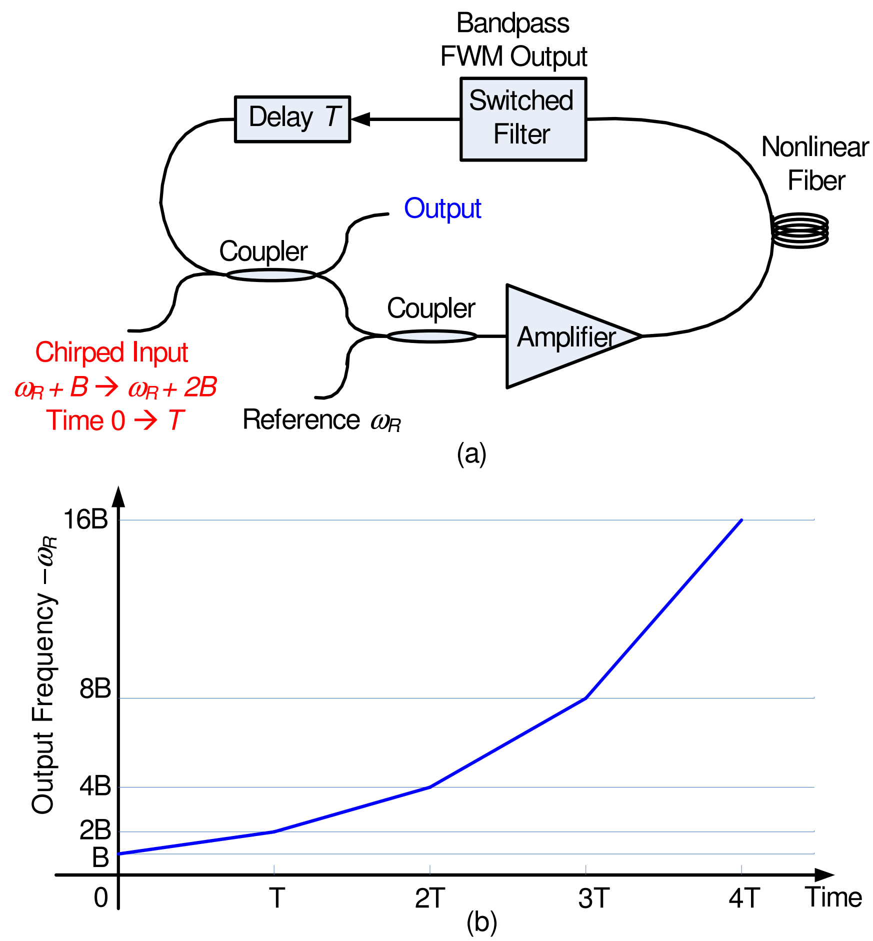

Figure 6.14. (a) FWM "engine" for geometric scaling of the chirp bandwidth. The filter is switched every T seconds so that it passes only the FWM component generated. (b) Output frequency vs. time.

6.2 Multiple Source FMCW Reflectometry

The FWM technique described in section 6.1 relies on a single input chirp and nonlinear optics to achieve bandwidth multiplication. This imposes a rather large power requirement, and the achievable bandwidth can be limited by dispersion in the nonlinear medium. In this section, we present a new approach, multiple source FMCW (MS-FMCW) reflectometry, which combines multiple lasers so that the total chirp bandwidth to the sum of chirp bandwidths of the individual lasers. This leads to a corresponding decrease in the smallest resolvable feature separation (equation (5.16)) while keeping the ranging depth and scan speed unchanged. The key to this technique is sweeping the sources over distinct but adjacent regions of the optical spectrum, so as to approximate a single sweep of greater bandwidth. A related method for improving the range resolution has recently been reported [129], where the chirped sidebands of the discrete frequencies radiated by a mode-locked laser are combined using feedback to create a phase-coherent continuous-frequency wideband chirp. In contrast, our work focuses on an analytical method that can tolerate the presence of discontinuities in the frequency sweep, enabling a much simpler (and cheaper) combination of multiple sources for resolution improvement.

6.2.1 MS-FMCW Analysis

Let us briefly revisit the FMCW experiment with a linearly swept source of bandwidth B (rad/s), as shown in figure 6.15. The target is assumed to consist of multiple reflections with time delays τ_i. The electric field of the source is given by

$$e(t) = \cos\left(\phi_0 + \omega_0 t + \frac{\xi t^2}{2}\right), \tag{6.22}$$

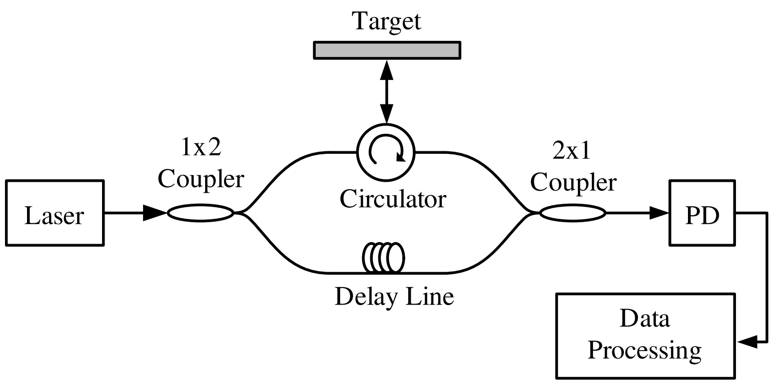

(a)

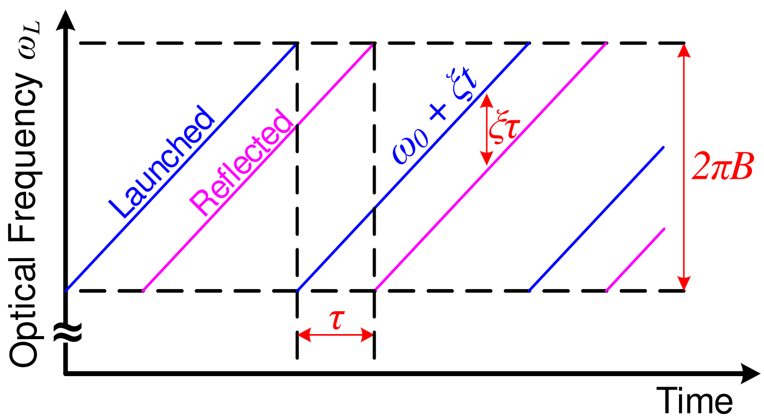

(b)

Figure 6.15. (a) Schematic diagram of an FMCW ranging experiment with a linearly chirped optical source. (b) Variation of the optical frequency with time.

where ϕ_0 denotes the initial optical phase. For a target with a time delay τ, the detected photocurrent is given by

$$\begin{aligned} i(t) &= \left\langle |e(t) + R\, e(t-\tau)|^2 \right\rangle \\ &= R\cos\left[(\xi\tau)t + \omega_0\tau - \frac{\xi\tau^2}{2}\right], \end{aligned} \tag{6.23}$$

where R is the target reflectivity, and the DC terms are neglected. The averaging is done over a time interval that is much longer than an optical cycle, yet much shorter than the period of the cosine in equation (6.23). The term $\xi\tau^2/2$ is typically much smaller than unity, and will be neglected in the rest of this analysis for the sake of simplicity.[2]

We note that time is only a dummy variable in equation (6.23), and can be replaced by the optical frequency, so that the photocurrent is a function only of the optical frequency:

$$i(\omega) = R\,\text{rect}\left(\frac{\omega - \omega_1}{B}\right)\cos(\omega\tau), \tag{6.24}$$

where the rect(.) function denotes that the measurement is done over the optical frequency interval of length B centered around ω_1. This is a consequence of the fact that equation (6.23) is valid only for the time interval $[0, T]$. The delay τ is then calculated by measuring the "frequency" of oscillations of the function $\cos(\omega\tau)$, i.e., we define the conjugate Fourier variable, ζ, of the optical frequency ω and calculate the Fourier transform of equation (6.24):[3]

$$I(\zeta) = \left[\frac{R}{2}\delta(\zeta - \tau)\right] * \left[B\text{sinc}\left(\frac{B\zeta}{2}\right)e^{-j\zeta\omega_1}\right], \tag{6.25}$$

where $*$ is the convolution operator, and we ignore negative "frequencies" ζ, since the photocurrent is real. The value of τ is calculated by measuring the location of the peak of the sinc function. Note that one definition of the resolution of the measurement is given by the location of the first null of the sinc function at $\Delta\zeta =$

[2]The inclusion of the $\xi\tau^2/2$ term does not change the results of the analysis significantly, as shown in [71].

[3]The Fourier transform of $x(\omega)$ is defined by $X(\zeta) = \int_{-\infty}^{\infty} x(\omega)e^{-j\omega\zeta}\, d\omega$. ζ has units of time.

$2\pi/B$, which corresponds to a range resolution $\Delta d = \pi c/B$, as given by equation (5.16).[4] Alternatively, the resolution may be defined by the FWHM of the sinc function.

We now show that the resolution of the measurement can be improved by simply adding measurements performed using several distinct optical windows. Let the N optical windows be centered at ω_k, and have width B each.[5] We further assume that there is a gap between adjacent windows, so that $\omega_{k+1} - \omega_k = B + \delta_k$. For multiple targets, labeled i, imaged using multiple optical windows, the general version of equation (6.25) can be written as

$$\begin{aligned} I(\zeta) &= \left[\sum_i \frac{R_i}{2}\delta(\zeta - \tau_i)\right] * \left[\sum_{k=1}^{N} B\mathrm{sinc}\left(\frac{B\zeta}{2}\right) e^{-j\zeta\omega_k}\right] \\ &\doteq \left[\sum_i \frac{R_i}{2}\delta(\zeta - \tau_i)\right] * A_N(\zeta). \end{aligned} \tag{6.26}$$

$A_N(\zeta)$ can be simplified to yield

$$\begin{aligned} A_N(\zeta) = (\omega_N - \omega_1 + B)\mathrm{sinc}\left(\frac{\omega_N - \omega_1 + B}{2}\zeta\right) e^{-j\zeta\frac{\omega_1+\omega_N}{2}} \\ - \sum_{k=1}^{N-1} \delta_k \mathrm{sinc}\left(\frac{\delta_k\zeta}{2}\right) e^{-j\zeta\left(\omega_k + \frac{B+\delta_k}{2}\right)}. \end{aligned} \tag{6.27}$$

Let us first consider the case $\delta_k = 0$ for all k. This is the case where there are no gaps between the optical windows, and we find that equation (6.27) is identical to equation (6.25) with effective bandwidth $\tilde{B} \doteq \omega_N - \omega_1 + B = NB$. *A resolution improvement by a factor of N can therefore be improved by simply adding measurements taken over N distinct optical windows.*

In the presence of gaps δ_k, the synthesized spectrum in equation (6.27) can be interpreted as the spectrum due to one large window of bandwidth given by *the total frequency extent* $\tilde{B} = \omega_N - \omega_1 + B$, minus the transform of the gaps. In this work,

[4] Note that the range resolution is $\Delta d = c\Delta\zeta/2$ owing to the specular reflection geometry used in the experiment.

[5] In general, it is not necessary that the bandwidths B_k be equal.

we will always assume that the gaps are small, i.e., $\delta_k \ll B$. The resolution of the synthesized spectrum can then be exactly calculated numerically as described in [71], but it is easy to show that the FWHM of the transform is virtually unaffected by the presence of small gaps. This is due to the fact that the magnitude of the sum in equation (6.27) is bounded above by $\sum_k |\delta_k|$, and this is, by assumption, much smaller than the total bandwidth $\tilde{B}$ which determines the maximum value of the spectrum. It can also be shown [71] that an upper bound on the smallest resolvable separation is given by

$$\Delta d_{\mathrm{MS-FMCW}} \leq \frac{\pi c}{NB}. \tag{6.28}$$

To illustrate the effect of the gaps on the synthesized spectrum, we plot in figure 6.16 the transform of a single window of width 5.19 units, compared to the addition of five windows of 1 unit each with interwindow gaps of 0.06, 0.045, 0.03 and 0.055 units respectively. It is clear that the resolution of the synthesized measurement is approximately equal to that using a single frequency sweep of 5 units, and the gaps do not have a significant impact on the resolution of the measurement.

6.2.2 Stitching

We now consider the problem of stitching, i.e., how do we put together multiple measurements using different parts of the optical spectrum to obtain one high-resolution measurement? In the previous section, we have mapped photocurrents from the time domain to the optical frequency domain. Since the optical frequency is linear in time, this mapping involves first scaling the time axis by the chirp slope, and then translating the data to the correct initial frequency. Whereas the rate of each chirp is precisely controlled (chapter 5), the starting sweep frequencies are, in general, not known with sufficient accuracy. To reflect this uncertainty, we omit the translation step—in other words, we translate the ideal measurement back to the origin. In the Fourier domain, this implies that the *measured* spectrum using the kth optical window is related to the ideal value by

$$I_{k,meas}(\zeta) = e^{j\omega_k \zeta} I_k(\zeta). \tag{6.29}$$

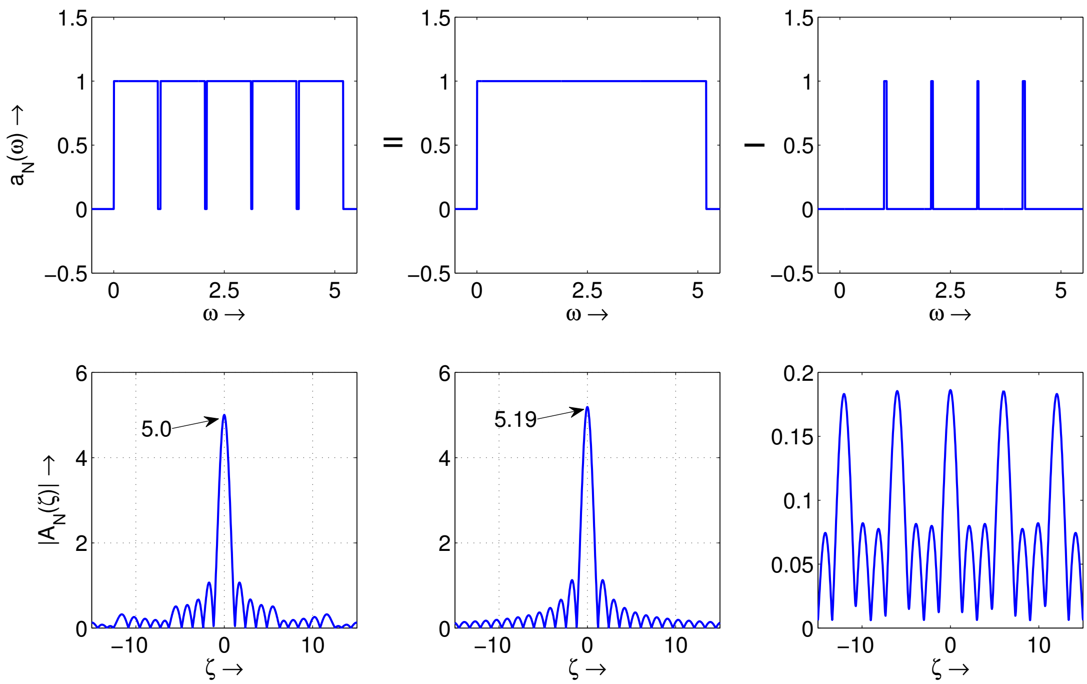

Figure 6.16. Illustration of the MS-FMCW concept. A measurement using five individual optical frequency sweeps of one unit each can be regarded as one large sweep minus the gaps between the optical windows. If the sum of the frequency gaps (here, 0.19 units) is much smaller than the total frequency sweep (5.19 units), the resultant bandwidth of the synthesized measurement is at least equal to the sum of the individual bandwidths (5 units).

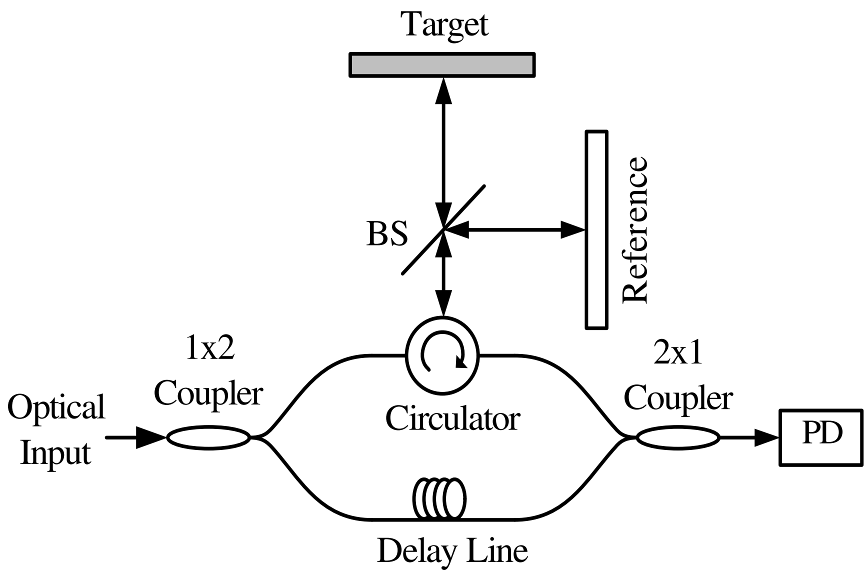

Figure 6.17. Schematic of a multiple source FMCW ranging experiment. A reference target is imaged along with the target of interest, so that the intersweep gaps may be recovered. BS: Beamsplitter. PD: Photodetector.

Using equation (6.25), the measured spectrum is given by

$$\begin{aligned} I_{k,meas}(\zeta) &= e^{j\omega_k\zeta}\left[\sum_i \frac{R_i}{2}\delta(\zeta-\tau_i)\right] * \left[B\text{sinc}\left(\frac{B\zeta}{2}\right)e^{-j\zeta\omega_k}\right] \\ &= \frac{B}{2}\sum_i R_i\,\text{sinc}\left(\frac{B(\zeta-\tau_i)}{2}\right)\exp(j\tau_i\omega_k). \end{aligned} \tag{6.30}$$

The problem of stitching is therefore to determine the phase factors $\exp(-j\zeta\omega_k)$ in order to reconstruct the Fourier transform of equation (6.27) according to

$$I_{stitch}(\zeta) = \sum_{k=1}^{N} e^{-j\omega_k\zeta} I_{k,meas}(\zeta). \tag{6.31}$$

The uncertainty in the starting frequencies manifests itself as an uncertainty in the intersweep gaps. To recover the gaps, we use a known reference target along with the target of interest, as shown in figure 6.17. By analyzing the data collected from the reference target, we extract the parameters δ_k, and stitch together the target of interest measurement, according to equation (6.31). Let us examine a system with two optical sweeps of chirp bandwidth B each, separated by a gap δ. Three and more sweeps can be stitched by considering sweeps in a pairwise manner to calculate the values of the gaps. Suppose the known reference target consists of a single reflector with reflectivity R_a and delay τ_a. We obtain two measurements $I_{1,meas}$ and $I_{2,meas}$ according to equation (6.30). The ratio of these measurements can then be used to obtain the value of the gap δ (note that $\omega_2 - \omega_1 = B + \delta$) according to

$$\delta = \frac{1}{\tau_a} \arg \left[\frac{I_{2,meas}(\tau_a)}{I_{1,meas}(\tau_a)} \exp(-jB\tau_a) \right]. \tag{6.32}$$

The phase of a complex number can only be extracted modulo 2π, so that equation (6.32) can only be used to recover δ with an ambiguity of $2\pi/\tau_a$. Therefore, the nominal gap needs to be known to within $2\pi/\tau_a$ before equation (6.32) may be applied. For example, if the nominal gap is only known to an accuracy of 10 GHz, we need $1/\tau_a > 10$ GHz. However, the use of a very small τ_a is undesirable since it makes the calculation very sensitive to inaccuracies in the measurement of the phase on the right-hand side.

To overcome this issue, we use two known reference reflectors, and express the gap size as a function of the reflector separation. If the two delays are given by τ_a and τ_b, we use equation (6.32) to derive

$$\delta = \frac{1}{\tau_a - \tau_b} \arg \left[\frac{I_{2,meas}(\tau_a) I_{1,meas}(\tau_b)}{I_{1,meas}(\tau_a) I_{2,meas}(\tau_b)} \exp\left(-jB(\tau_a - \tau_b)\right) \right]. \tag{6.33}$$

τ_a and τ_b are chosen so that $1/|\tau_a - \tau_b| > 10$ GHz, and the value of δ is calculated using equation (6.33). The error in this calculation is proportional to $1/|\tau_a - \tau_b|$. The accuracy of the calculation of the gap can now be improved by using equation (6.32), which yields a new value of δ with a lower error proportional to $1/\tau_a$. Depending on system noise levels, more stages of evaluation of δ using more than two reference reflectors may be utilized to achieve better accuracy in the calculations.

A potential system architecture employing the stitching technique for high resolution MS-FMCW is shown in figure 6.18. The optical sources are multiplexed and used to image a target and a reference, as discussed above. The reflected optical signal is

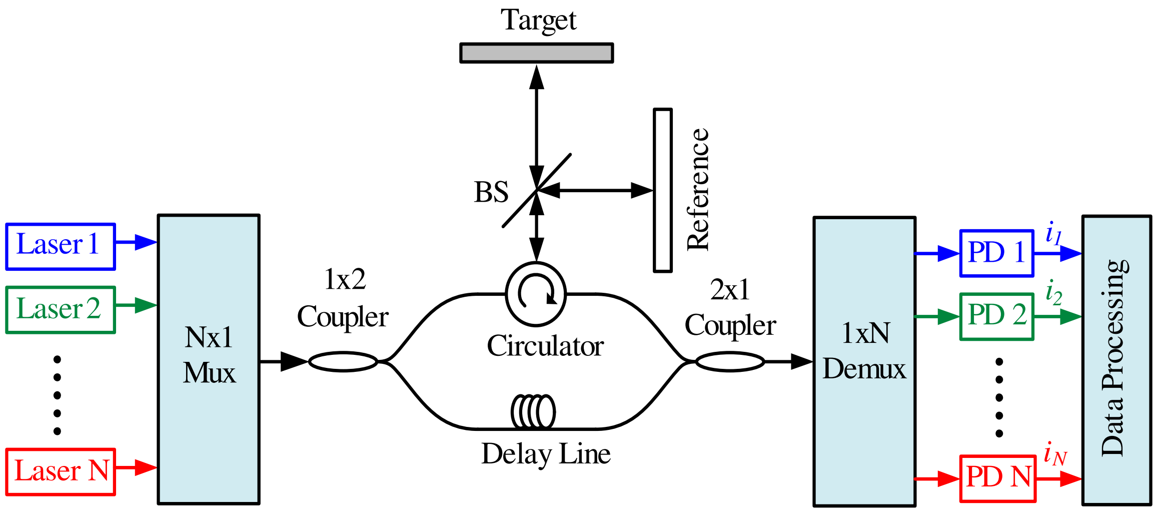

Figure 6.18. Architecture of a potential MS-FMCW imaging system. BS: Beam splitter. PD: Photodetector.

demultiplexed and measured using a set of photodetectors to generate the photocurrents of equation (6.30). The reference data is processed and used to stitch a target measurement of improved resolution. The multiplexing may be performed in time or optical frequency, or a combination of the two. The real power of the MS-FMCW technique then lies in its scalability. We can envision a system that combines cheap off-the-shelf SCLs to generate a swept-frequency ranging measurement that features an excellent combination of range resolution, scan speed, and imaging depth.

6.2.3 Experimental Results

We demonstrated the MS-FMCW technique using a highly linear DFB SCL-based optoelectronic swept-frequency source that chirps 100 GHz around a nominal central wavelength of 1539 nm in a 1 ms long scan (chapter 5). It should be noted that that a specialized source is not necessary for this technique, and chirp nonlinearity may be compensated for by sampling the photocurrent uniformly in optical frequency [51].

We used the configuration of figure 6.17 with a 1.0 mm microscope slide target, and a two reflector reference characterized by $1/|\tau_a - \tau_b| \sim 10$ GHz ($\sim$3 cm free space separation). This reference was chosen to accommodate the accuracy with which the gaps are initially known ($\sim$1 GHz). We tuned the SCL temperature through

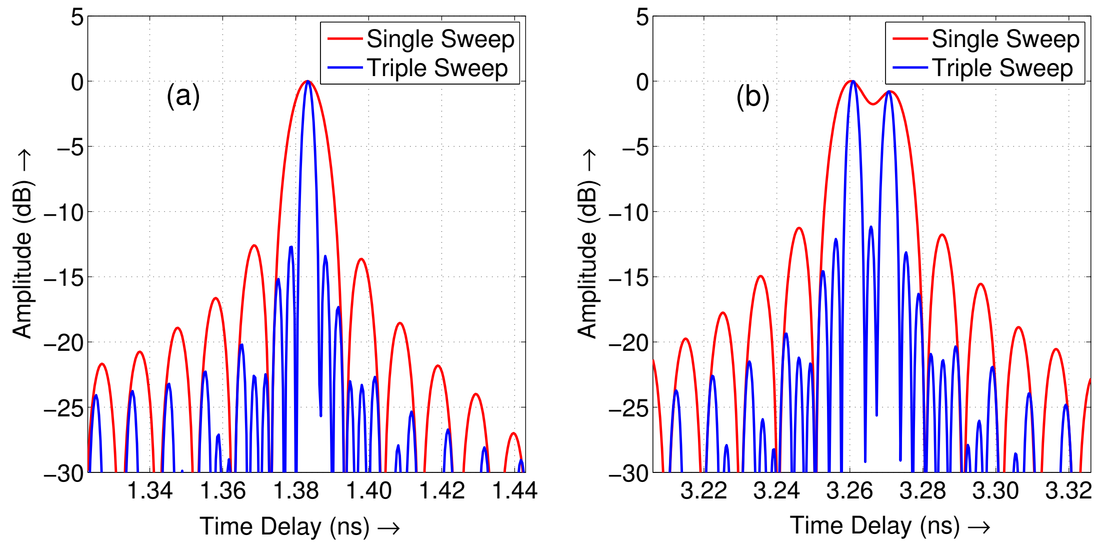

Figure 6.19. Experimental MS-FMCW results using a DFB SCL. The red and blue curves correspond to single-sweep and stitched three-sweep measurements respectively. (a) Single reflector spectrum. (b) Glass slide spectrum. The peaks correspond to reflections from the two air-glass interfaces. The nominal thickness of the glass slide is 1 mm.

three set points to generate three 100 GHz sweeps with different starting frequencies. These sweeps were sequentially launched into the experiment, and the corresponding photocurrents were recorded. Using the two-step procedure described in section 6.2.2, the gaps between the sweeps were calculated to be 1.89 and 0.72 GHz.

These values of the gaps were used in equation (6.31) to stitch the three measured photocurrents, and the results are plotted in figure 6.19. Figure 6.19(a) shows the single sweep and stitched multiple sweep spectra for one of the reference reflectors. The FWHMs are 12.17 and 4.05 ps for the single and multiple source cases respectively. The threefold range resolution enhancement is consistent with equation (6.28). Fig 6.19(b) shows the measurements of the target microscope slide. The two peaks in the single-scan spectrum, corresponding to reflections from the two microscope slide facets, are barely resolved. This is consistent with the theoretical range resolution in glass of 1 mm for a 100 GHz sweep. The stitched curve shows two prominent peaks, demonstrating our improved ability to resolve two closely spaced targets. The measured peak separation of 10 ps is the round-trip delay between the two slide facets, and indeed corresponds to a thickness of 1 mm in glass.

The stitching experiment was also performed using a VCSEL-based optoelectronic SFL with a chirp bandwidth of 500 GHz, corresponding to a range resolution of 200 µm in glass. Two such sweeps were generated by biasing the laser at different temperatures, and the resulting measurements were stitched together to obtain an effective chirp bandwidth of 1 THz and a resolution of 100 µm in glass. The results of imaging measurements of two-reflector targets with different separations is shown in figure 6.20. The results show that a microscope cover-slip of nominal thickness 150 µm, which could not be resolved by a single sweep, is well resolved by the stitched measurement.

6.2.4 Summary

We have analyzed and demonstrated a novel variant of the FMCW optical imaging technique. This method combines multiple lasers that sweep over distinct but adjacent regions of the optical spectrum in order to record a measurement with increased effective optical bandwidth and a corresponding improvement in the range resolution. The MS-FMCW technique is scalable and is a promising approach to realize a wide-bandwidth swept-frequency imaging system that inherits the speed and coherence of the SCL. While we have demonstrated the stitching of three 100 GHz sweeps using DFB SCLs and two 500 GHz sweeps using VCSELs in our proof-of-concept experiments, MS-FMCW reflectometry is not tied to any particular laser type and may be used to combine wideband swept sources to push range resolutions beyond the state of the art.

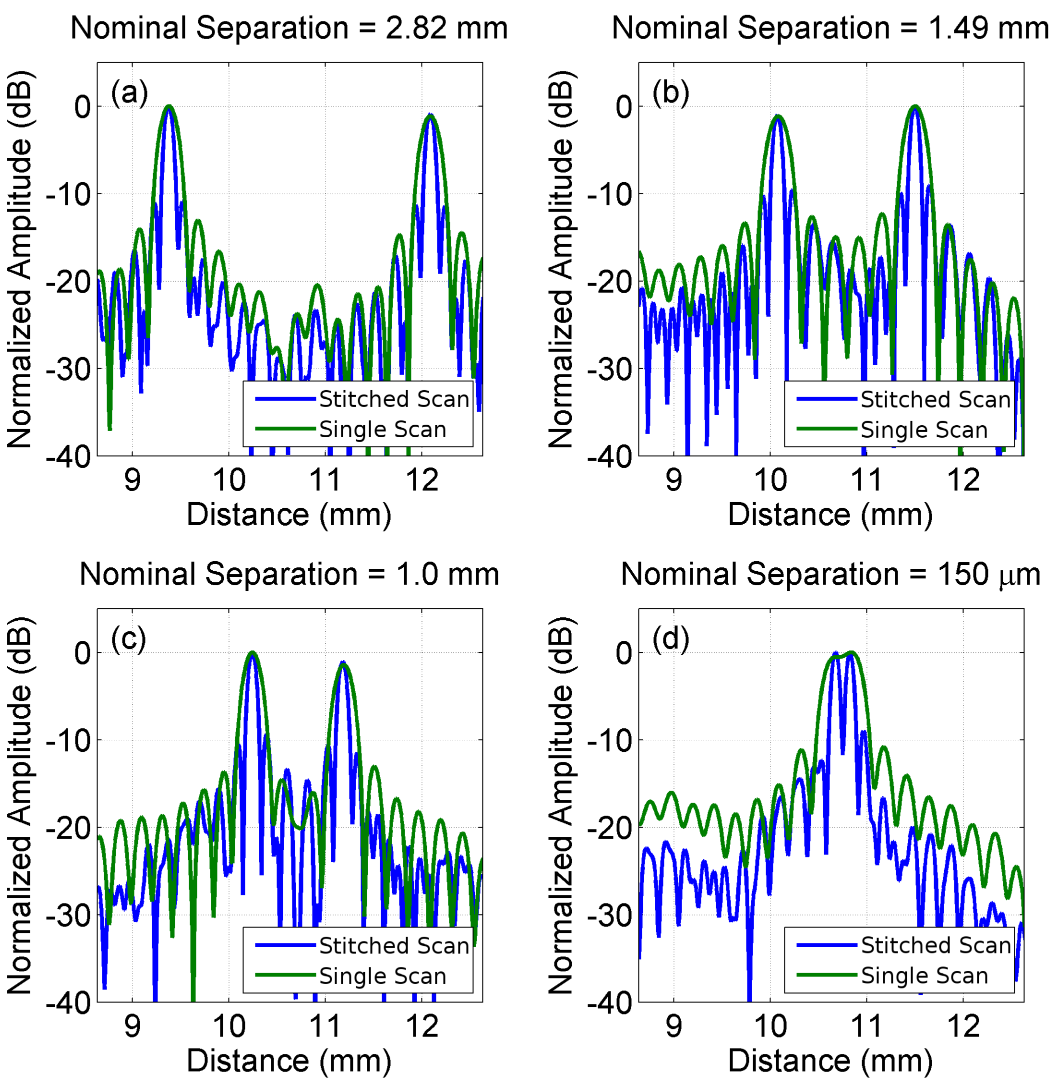

Figure 6.20. Experimental MS-FMCW results using a VCSEL. The green and blue curves correspond to single-sweep and stitched two-sweep measurements respectively.

Chapter 7

Conclusion

7.1 Summary of the Thesis

We have shown that the use of an SCL as a current-controlled oscillator in optoelectronic feedback systems, making use of its direct (frequency vs. current) modulation property, enables precise electronic control of the laser phase and frequency. In particular, electronic control over the SCL phase is achieved using heterodyne OPLLs where a slave SCL is locked to a master laser offset by an RF reference oscillator; and SFL sources using SCLs in PLL-like feedback systems enable precise electronic control of the optical frequency chirp. The unique properties of the SCL such as its small footprint, low cost, high efficiency, robustness etc., and the optoelectronic systems which eliminate the need for any moving parts, precise mechanical alignment, or optical feedback and control, lead to a set of versatile and powerful devices which are attractive for use in many existing and novel applications.

Typical single-section SCLs, studied in this work, are characterized by a nonuniform FM response at low ($<$10 MHz) frequencies. We have theoretically analyzed the performance of SCL-OPLLs in the presence of this FM response, and a loop propagation delay; and experimentally demonstrated OPLLs using different commercial SCLs and optimized loop filters. The linewidth and FM response of an SCL determine the stability of an OPLL, and many lasers with larger linewidths ($\gtrsim$1 MHz) cannot be stably locked. To overcome this limitation, we have developed and demonstrated two novel OPLL architectures, viz. (i) the sideband-locked SCL-OPLL, where the feedback into the SCL was shifted to a higher frequency range where the FM response is uniform, and (ii) composite SCL-OPLL systems, where an external optical phase modulator was used to remove excess phase noise and stabilize the system.

Whereas SCL-OPLLs are typically studied for use as coherent demodulators in optical communication links, we have explored in this work other novel applications of SCL-OPLLs. We have shown theoretically and experimentally, in both the time and frequency domains, that the slave laser inherits the coherence properties of the master; this property is referred to as "coherence cloning." Coherence cloning of a master laser onto an array of slave SCLs, all locked to the same master laser, therefore forms a coherent aperture. We have demonstrated that the optical phase of each emitter in the array could be controlled in a one-to-one manner by varying the phase of an electronic oscillator in the OPLL, thereby forming a phase-controlled aperture with electronic wavefront control. Applications of these phase-controlled apertures in coherent power-combining and all-electronic beam-steering were studied.

We have designed and developed an optoelectronic SFL source based on a modification of the basic OPLL structure, by incorporating an MZI as a frequency discriminator. The output of the SCL was passed through the MZI and phase-locked to an electronic oscillator, to generate an optical wave whose frequency was swept ("chirped") precisely linearly and rapidly over a broad bandwidth (several 100 GHz in 0.1 ms). An iterative predistortion technique was also developed to overcome large nonlinearities in the laser's frequency vs. current tuning curve. The parameters of the frequency chirp were determined solely by the reference oscillator, and arbitrary optical waveforms were generated by tuning the electronic reference oscillator. The precise control over the optical frequency enabled high-sensitivity label-free biomolecular sensing experiments using a high-quality whispering-gallery-mode microresonator.

One of the most widespread use of broadband SFLs is in laser ranging and three-dimensional imaging. The axial resolution in these applications is inversely proportional to the chirp bandwidth, and very large chirp bandwidths ($\gtrsim$10 THz) are necessary for biomedical imaging (OCT). The tuning range of typical single-mode SCLs is, however, limited (typically $<$1 THz). We have demonstrated that FWM between the chirped SFL output and a monochromatic wave generates a chirped wave with twice the chirp bandwidth and the same chirp characteristics. We have also proposed and implemented a quasi-phase-matching scheme to overcome the effects of dispersion in the nonlinear medium. While bandwidth multiplication by FWM is a "physical" effect, we have also developed an algorithmic approach to achieve a larger effective bandwidth for imaging, by "stitching" measurements taken using SFLs chirping over different regions of the optical spectrum, in an experiment analogous to synthetic aperture radar. Using three separate SFL measurements, we have experimentally demonstrated a threefold improvement in the resolution using three SFL measurements.

7.2 Outlook

We have described a set of new optoelectronic devices for the manipulation of the phase and frequency, as opposed to just the intensity, of optical waves. For the most part, we have concentrated on experimentally constructing devices based on discrete, commercially available optical and electronic components. While these are adequate for many applications and for proof-of-principle demonstrations, the major step necessary to harness the full power of these devices is photonic and optoelectronic integration. If the limitations imposed by the SCL FM response are overcome, the minimization of the propagation delay will enable OPLLs with large loop bandwidths to be constructed. OPLLs based on micro-optics have already demonstrated [20] and recent efforts toward integrated OPLLs [22, 23, 77] are beginning to make progress in this direction. Development of integrated OPLLs will be necessary for large-scale integration of OPLL arrays for phase-controlled apertures for free-space optical communication, LIDAR and other applications; however, research into thermal stabilization and prevention of crosstalk in large laser arrays is expected to be necessary to make this a reality.

Integration of optoelectronic SFLs is also an important direction of research: the reduction of the footprint of these devices can enable integration with microresonators

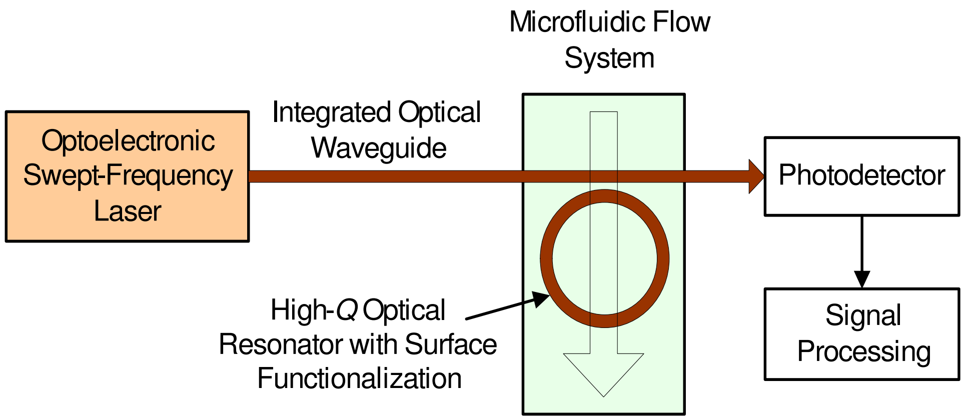

Figure 7.1. Schematic diagram of a potential compact integrated label-free biomolecular sensor. An optoelectronic SFL is coupled to a lithographically defined high-Q resonator with a functionalized surface for biomolecular detection. A microfluidic flow system enables delivery of a small volume of the analyte.

fabricated on chip to yield compact biomolecular sensing platforms (figure 7.1). Integrated optical waveguides on silicon are conducive to chirp multiplication by FWM, since they can have nonlinear coefficients that are up to five orders of magnitude larger than standard single-mode optical fibers [130]. Further, integration of SFLs into optoelectronic circuits enables the stitching of a large number of SFLs for high-resolution imaging (figure 6.18).

OPLLs and wideband SFLs have potential applications in the fields of millimeter-wave and Terahertz photonics. The use of OPLLs for generation and transmission of radio frequency of signals has been studied by various workers [39, 131]. With the development of high speed photodetectors and photomixers that can produce heterodyne output signals in the Terahertz regime [132], the frequency control methods developed in this thesis can be adapted for versatile and wideband Terahertz sources. By photomixing an optoelectronic SFL with a monochromatic laser source, it is possible to generate a narrow-linewidth and tunable "universal" Terahertz source. As faster and faster photomixers are developed, this represents a very promising field of research.

We have demonstrated the coherent combining of phase-locked optical sources for high-power sources. This concept can readily be extended to related fields to achieve improved performance. For example, the output powers of Terahertz photomixers and high-speed photodetectors are typically limited by optical damage thresholds in the small devices (a necessity for high-speed operation). This limitation can possibly be overcome by the coherent combining of the outputs of a number of terahertz detectors illuminated by phase-coherent optical sources. A second application is in the field of high power fiber amplifiers, where the output powers are limited by nonlinear effects in the optical fiber, mainly stimulated Brillouin scattering. It is known that modulating the phase or frequency of the optical wave results in a larger threshold for stimulated Brillouin scattering [133]—this suggests that the use of the optoelectronic SFLs developed in this work as seed sources for an array of high-power fiber amplifiers, and the subsequent coherent combining of the amplified outputs can result in larger output powers than the use of monochromatic seed lasers. Finally, the combining of the outputs of an array of N phase-locked SCLs, where each SCL (k) is locked to its preceding SCL $(k-1)$ at a common RF offset frequency, can generate a comb of optical frequencies with independent control over the amplitude and phase of each frequency component. This *synthesis* approach is fundamentally different from the traditional top-down approach where individual components of a mode-locked laser and filtered and manipulated [134].

In summary, electronic control of the optical phase and frequency can be expected to enable a range of new applications, and vastly-improved performance in existing applications.

Appendix A

Residual Phase Error in an OPLL with Nonuniform FM Response

In this appendix, we calculate the effect of the SCL FM response of the form

$$F_{FM}(f) = \frac{1}{b}\left(\frac{b-\sqrt{jf/f_c}}{1+\sqrt{jf/f_c}}\right), \tag{A.1}$$

where f_c denotes the corner frequency of the thermal response and depends on the device material and structure, and $b = K_{th}/K_{el} - 1$ denotes the relative strength of the thermal and electronic responses, on the minimum residual phase error in a Type I SCL-OPLL. For typical SCLs, $b > 0$, and f_c lies in the range of 0.1–10 MHz. For example, the fit to the experimental data in figure 2.9 was obtained with $b = 1.64$ and $f_c = 1.8$ MHz.

The open loop transfer function of a Type I loop with the nonuniform SCL FM response is therefore given by

$$G_{op}(\bar{f}) = \frac{\bar{K_F}}{jb\bar{f}}\left(\frac{b-\sqrt{j\bar{f}}}{1+\sqrt{j\bar{f}}}\right), \tag{A.2}$$

where the loop gain K_F and the frequency are normalized according to

$$\begin{aligned}\bar{f} &\doteq f/f_c,\\ \bar{K_F} &\doteq K_F/f_c.\end{aligned} \tag{A.3}$$

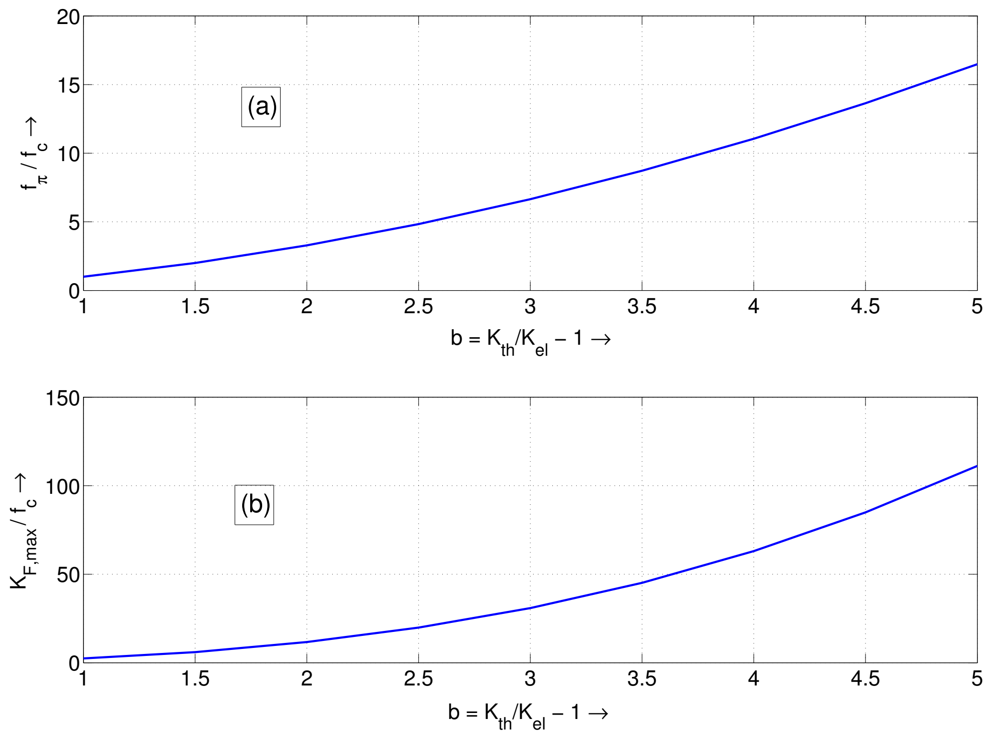

Figure A.1. Variation of (a) the normalized π-crossover frequency and (b) the normalized maximum gain as a function of the parameter b in equation (A.1).

The π-crossover frequency f_π (frequency where the phase of $G_{op}(f)$ goes to π) and the maximum gain (gain at which $|G_{op}(f_\pi)| = 1$ can now be calculated. Setting $\angle G_{op}(f_\pi) = -\pi$ in equation (A.2), we obtain

$$\bar{f}_\pi = 2\left(\frac{b - 1 + \sqrt{b^2 + 6b + 1}}{4}\right)^2. \tag{A.4}$$

Next, setting $|G_{op}(f_\pi)| = 1$, we have

$$\bar{K}_{F,max} = b\bar{f}_\pi\sqrt{\frac{1 + \bar{f}_\pi + \sqrt{2\bar{f}_\pi}}{b^2 + \bar{f}_\pi - b\sqrt{2\bar{f}_\pi}}}. \tag{A.5}$$

The behavior of the normalized π-crossover frequency and the normalized maximum gain as a function of b are shown in figure A.1. $\bar{f}_\pi$ and $\bar{K}_{F,max}$ increase monotonically with b, and larger values of b and f_c therefore lead to higher loop bandwidths.

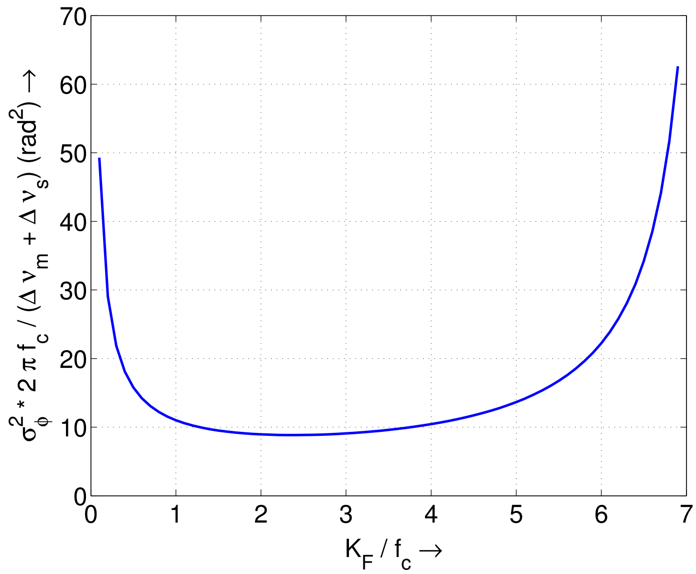

Figure A.2. Variation of the integral $\mathcal{I}(b, \bar{K_F})$ in equation (A.6) as a function of $\bar{K_F}$, for $b = 1.64$.

We now calculate the variance of the residual phase error by using equation (A.2) in equation (2.18), to obtain

$$\begin{aligned}\sigma_\phi^2 &= \frac{\Delta\nu_m + \Delta\nu_s}{2\pi f_c} \int_{-\infty}^{\infty} d\bar{f} \frac{b^2|1+\sqrt{j\bar{f}}|^2}{|K_F(b-\sqrt{j\bar{f}}) + jb\bar{f}(1+\sqrt{j\bar{f}})|^2} \\ &= \frac{\Delta\nu_m + \Delta\nu_s}{2\pi f_c} \mathcal{I}(b, \bar{K_F}). \end{aligned} \tag{A.6}$$

To understand the behavior of the variance of the phase error, we first note that σ_ϕ^2 scales inversely with f_c as expected, since the loop bandwidth increases with f_c. Further, the behavior of the integral $\mathcal{I}(b, \bar{K_F})$ for a given value of b, chosen to be $b = 1.64$ to match the experimental result of figure 2.9, is shown in figure A.2. For this value of b, the maximum stable gain is $\bar{K}_{F,max} = 7.36$. At low gains, the loop has little effect, leading to a high phase error. As the gain approaches the maximum possible value, the phase error again increases since the loop begins to go unstable. Therefore, there is an optimum value of the gain—$\bar{K}_{F,opt} \approx 2.4$ in this case—for which the variance of the phase error is minimized. The ratio of the optimum gain to the maximum stable loop gain lies between 0.25 and 0.35.

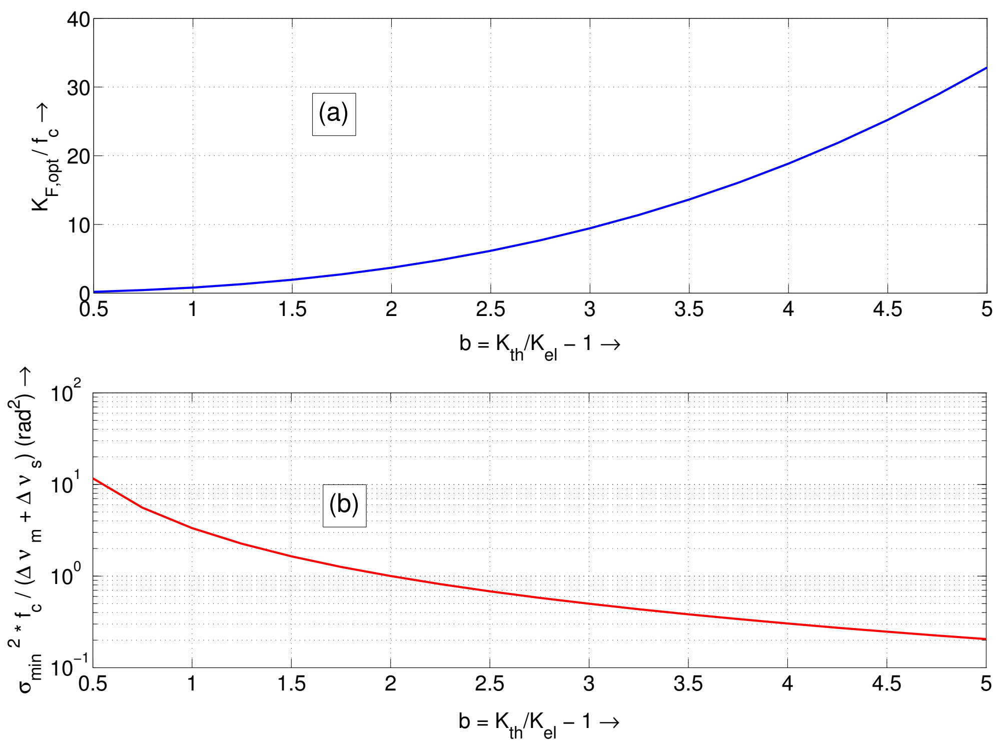

Figure A.3. Variation of the (a) normalized optimum gain $\bar{K}_{F,opt} = K_{F,opt}/f_c$ and (b) the normalized minimum residual phase error $\sigma^2_{min} f_c/(\Delta\nu_m + \Delta\nu_s)$ as a function of the parameter b, for a first-order OPLL with a SCL with nonuniform FM response.

The value of $\bar{K}_{F,opt}$ is a function of b, as is the value of the minimum phase error σ^2_{min}. As b increases, the loop bandwidth is higher, leading to a larger value of $\bar{K}_{F,opt}$ and a smaller value of σ^2_{min}. The values of the (normalized) optimum gain and minimum residual phase error vs. the parameter b are plotted in figure A.3. As a concrete example, consider the experimentally measured FM response of figure 2.9, for which $b = 1.64$ and $f_c = 1.8$ MHz. For these values, we obtain

$$\frac{\sigma^2_{min}}{\Delta\nu_m + \Delta\nu_s} = 8 \times 10^{-7} \text{ rad}^2/\text{Hz}. \tag{A.7}$$

Appendix B

Four-Wave Mixing in a Multisegment Nonlinear Waveguide

In this appendix, we derive a general expression for the power generated by four-wave mixing in the multisegment nonlinear waveguide shown in figure B.1 for arbitrary values of the phase mismatch in each segment.[1] This is important in order to understand practical implementations of the dispersion compensation technique described in section 6.1.1.3, where it is often difficult to precisely control the value of the dispersion parameter D_c. Let the waveguide consist of N segments, labeled $k = 1, 2, \ldots, N$. The length of segment k is given by L_k, and let the propagation constants of the chirped, reference and output fields in this segment be denoted by $\beta_{ch,k}$, $\beta_{R,k}$ and $\beta_{out,k}$ respectively. The phase mismatch in this segment is therefore given by $\Delta\beta_k = 2\beta_{ch,k} - \beta_{R,k} - \beta_{out,k}$, and related to the value of the dispersion parameter in the segment by equation (6.13). For the sake of notational simplicity, we assume that the loss, refractive index, nonlinear susceptibility and the effective mode area of the different segments are equal. Our goal is to calculate the output field and optical power generated by FWM at $z = \sum_{k=1}^{N} L_k$. We ignore splice losses in this calculation.

We begin by describing a separate frame of reference for the kth segment, denoted by the position variable $z_k = \left(z - \sum_{i=1}^{k-1} L_i\right) \in [0, L_k]$. Similar to equation (6.1), the

[1] A similar calculation has been performed by Inoue [135] for the case of a chain of fiber amplifiers with different dispersions.

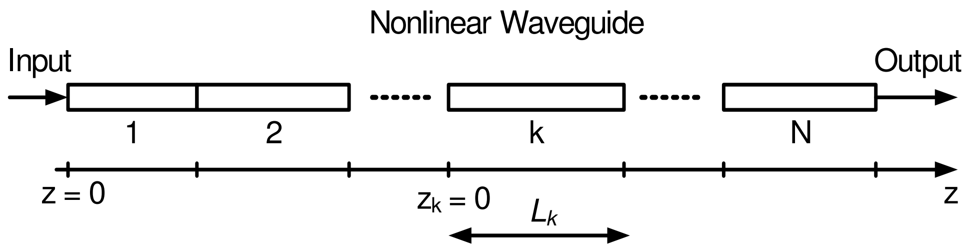

Figure B.1. A multisegment nonlinear waveguide for four-wave mixing.

electric field in this segment is described by its slowly varying complex amplitude as

$$E(z_k, t) = \frac{1}{2} A_k(z_k) \exp\left(j(\omega t - \beta_k z_k)\right) + \text{c.c.} \tag{B.1}$$

The continuity of the electric field at $z_k = 0$ requires that

$$A_k(z_k = 0) = A_{k-1}(z_{k-1} = L_{k-1}) \exp(-j\beta_{k-1} L_{k-1}). \tag{B.2}$$

It is to be understood henceforth that the argument of the function A_k is the variable z_k. We consider the FWM process where the chirped wave of frequency ω_{ch} and the reference wave of frequency ω_R generate an output wave with a frequency $\omega_{out} = 2\omega_{ch} - \omega_R$, and assume that the chirped and reference waves are undepleted by the FWM process. For the chirped wave, we have

$$\begin{aligned} A_{ch,k}(0) &= A_{ch,k-1}(L_{k-1}) \exp(-j\beta_{ch,k-1} L_{k-1}) \\ &= A_{ch,k-1}(0) \exp\left[-(\alpha/2 + j\beta_{ch,k-1}) L_{k-1}\right] \\ &= A_{ch,1}(0) \exp\left(-\frac{\alpha}{2} \sum_{i=1}^{k-1} L_i - j \sum_{i=1}^{k-1} \beta_{ch,i} L_i\right). \end{aligned} \tag{B.3}$$

Similarly, the reference wave at $z_k = 0$ is given by

$$A_{R,k}(0) = A_{R,1}(0) \exp\left(-\frac{\alpha}{2} \sum_{i=1}^{k-1} L_i - j \sum_{i=1}^{k-1} \beta_{R,i} L_i\right). \tag{B.4}$$

In the frame of reference we have set up to describe the kth segment, the equation for the evolution of the output field is identical to equation (6.10):

$$\frac{dA_{out,k}}{dz_k} = -\frac{\alpha}{2}A_{out,k} - jgA_{ch,k}^2(0)A_{R,k}^*(0)e^{-3\alpha z_k/2}e^{-j\Delta\beta_k z_k}, \tag{B.5}$$

where we have defined $g = nc\gamma\epsilon_0 A_{eff}/2$. The solution to this differential equation is

$$A_{out,k}(L_k) = e^{-\alpha L_k/2}\left[A_{out,k}(0) - jgA_{ch,k}^2(0)A_{R,k}^*(0)\left(\frac{1-e^{-(\alpha+j\Delta\beta_k)L_k}}{\alpha+j\Delta\beta_k}\right)\right]. \tag{B.6}$$

Using equations (B.2), (B.3) and (B.4), we obtain

$$\begin{aligned} A_{out,k}(L_k) = & e^{-\alpha L_k/2}\left[A_{out,k-1}(L_{k-1})\exp\left(-j\beta_{out,k-1}L_{k-1}\right) - jg\left(\frac{1-e^{-(\alpha+j\Delta\beta_k)L_k}}{\alpha+j\Delta\beta_k}\right)\right. \\ & \left.\times A_{ch,1}^2(0)A_{R,1}^*(0)\exp\left(-\frac{3\alpha}{2}\sum_{i=1}^{k-1}L_i - j\sum_{i=1}^{k-1}(2\beta_{ch,i}-\beta_{R,i})L_i\right)\right], \end{aligned} \tag{B.7}$$

which can be rewritten as

$$\begin{aligned} A_{out,k}(L_k) = \exp\left(-\frac{\alpha L_k}{2} - j\sum_{i=1}^{k-1}\beta_{out,i}L_i\right)&\left[A_{out,k-1}(L_{k-1})\exp\left(j\sum_{i=1}^{k-2}\beta_{out,i}L_i\right)\right. \\ -jgA_{ch,1}^2(0)A_{R,1}^*(0)\left(\frac{1-e^{-(\alpha+j\Delta\beta_k)L_k}}{\alpha+j\Delta\beta_k}\right)&\left.\exp\left(-\frac{3\alpha}{2}\sum_{i=1}^{k-1}L_i - j\sum_{i=1}^{k-1}\Delta\beta_i L_i\right)\right]. \end{aligned} \tag{B.8}$$

We note that the phase term $\exp\left(-j\sum_{i=1}^{k-1}\beta_{out,i}L_i\right)$ in equation (B.8) has no effect on the power of the output wave, which only depends on the magnitude of $A_{out,k}$ as given by equation (6.14). This term depends on the propagation constants $\beta_{out,i}$ of the output wave, and is difficult to evaluate in general. The physics of the process is mainly determined by the phase-mismatch terms $\Delta\beta_i$. We therefore find it convenient to define a new amplitude

$$\tilde{A}_{out,k}(z_k) = A_{out,k}(z_k)\exp\left(j\sum_{i=1}^{k-1}\beta_{out,i}L_i\right), \tag{B.9}$$

and equation (B.8) can be rewritten in the form

$$\tilde{A}_{out,k}(L_k) = \exp\left(-\frac{\alpha L_k}{2}\right)\Bigg[\tilde{A}_{out,k-1}(L_{k-1}) - jgA^2_{ch,1}(0)A^*_{R,1}(0) \\ \times\left(\frac{1-e^{-(\alpha+j\Delta\beta_k)L_k}}{\alpha+j\Delta\beta_k}\right)\exp\left(-\frac{3\alpha}{2}\sum_{i=1}^{k-1}L_i - j\sum_{i=1}^{k-1}\Delta\beta_i L_i\right)\Bigg]. \tag{B.10}$$

Equation (B.10) is the general solution for the output field generated by FWM in a multiple-segment nonlinear waveguide. The values of the phase mismatch in the various segments is related to the frequency chirp by equation (6.13), and the output power is evaluated using equation (6.14):

$$P_{out}\left(z = \sum_{i=1}^{N} L_i\right) = \frac{nc\epsilon_0 A_{eff}}{2}\left|\tilde{A}_{out,N}(L_N)\right|^2 = \frac{g}{\gamma}\left|\tilde{A}_{out,N}(L_N)\right|^2. \tag{B.11}$$

Bibliography

[1] D. R. Stephens, *Phase-Locked Loops for Wireless Communications: Digital, Analog and Optical Implementations*. Boston, MA: Kluwer Academic Publishers, 2002.

[2] F. M. Gardner, *Phaselock Techniques*. Hoboken, NJ: John Wiley and Sons, 2005.

[3] L. H. Enloe and J. L. Rodda, "Laser phase-locked loop," *Proc. IEEE*, vol. 53, no. 2, pp. 165–166, Feb. 1965.

[4] T. H. Maiman, "Stimulated optical radiation in ruby," *Nature*, vol. 187, pp. 493–494, Aug. 1960.

[5] T. Day, A. D. Farinas, and R. L. Byer, "Demonstration of a low bandwidth 1.06 µm optical phase-locked loop for coherent homodyne communication," *IEEE Photon. Technol. Lett.*, vol. 2, no. 4, pp. 294–296, Apr. 1990.

[6] L. G. Kazovsky and D. A. Atlas, "A 1320-nm experimental optical phase-locked loop: performance investigation and PSK homodyne experiments at 140 Mb/s and 2 Gb/s," *J. Lightw. Technol.*, vol. 8, no. 9, pp. 1414–1425, Sep. 1990.

[7] M. Z. Win, C.-C. Chen, and R. A. Scholtz, "Optical phase-locked loop (OPLL) for an amplitude modulated communications link using solid-state lasers," *IEEE J. Sel. Areas Commun.*, vol. 13, no. 3, pp. 569–576, Apr. 1995.

[8] M. Brunel, F. Bretenaker, S. Blanc, V. Crozatier, J. Brisset, T. Merlet, and A. Poezevara, "High-spectral purity RF beat note generated by a two-frequency

solid-state laser in a dual thermooptic and electrooptic phase-locked loop," *IEEE Photon. Technol. Lett.*, vol. 16, no. 3, pp. 870–872, Mar. 2004.

[9] F. Herzog, K. Kudielka, D. Erni, and W. Bächtold, "Optical phase locked loop for transparent inter-satellite communications," *Opt. Express*, vol. 13, no. 10, pp. 3816–3821, May 2005.

[10] W. R. Leeb, H. K. Philipp, A. L. Scholtz, and E. Bonek, "Frequency synchronization and phase locking of CO_2 lasers," *Appl. Phys. Lett.*, vol. 41, pp. 592–594, Oct. 1982.

[11] R. C. Steele, "Optical phase-locked loop using semiconductor laser diodes," *Electron. Lett.*, vol. 19, no. 2, pp. 69–71, Jan. 1983.

[12] J. Harrison and A. Mooradian, "Linewidth and offset frequency locking of external cavity GaAlAs lasers," *IEEE J. Quantum Electron.*, vol. 25, no. 6, pp. 1152–1155, June 1989.

[13] G. Santarelli, A. Clairon, S. N. Lea, and G. M. Tino, "Heterodyne optical phase-locking of extended-cavity semiconductor lasers at 9 GHz," *Opt. Commun.*, vol. 104, no. 4-6, pp. 339–344, 1994.

[14] F. Z. Fan and M. Dagenais, "Optical generation of a mHz linewidth microwave signal using semiconductor lasers and a discriminator-aided phase-locked loop," *IEEE Trans. Microw. Theory Tech.*, vol. 45, no. 8, pp. 1296–1300, Aug. 1997.

[15] W. Imajuku and A. Takada, "Optical phase-sensitive amplification using two phase-locked light sources," *Electron. Lett.*, vol. 33, no. 16, pp. 1403–1404, July 1997.

[16] O. Ishida, H. Toba, and Y. Tohmori, "0.04 Hz relative optical-frequency stability in a 1.5 µm distributed-Bragg-reflector (DBR) laser," *IEEE Photon. Technol. Lett.*, vol. 1, no. 12, pp. 452–454, Dec. 1989.

[17] J. M. Kahn, "1 Gbit/s PSK homodyne transmission system using phase-locked semiconductor lasers," *IEEE Photon. Technol. Lett.*, vol. 1, no. 10, pp. 340–342, Oct. 1989.

[18] J. M. Kahn, A. H. Gnauck, J. J. Veselka, S. K. Korotky, and B. L. Kasper, "4-Gb/s PSK homodyne transmission system using phase-locked semiconductor lasers," *IEEE Photon. Technol. Lett.*, vol. 2, no. 4, pp. 285–287, Apr. 1990.

[19] U. Gliese, T. N. Nielsen, M. Bruun, E. Lintz Christensen, K. E. Stubkjaer, S. Lindgren, and B. Broberg, "A wideband heterodyne optical phase-locked loop for generation of 3–18 GHz microwave carriers," *IEEE Photon. Technol. Lett.*, vol. 4, no. 8, pp. 936–938, Aug. 1992.

[20] L. N. Langley, M. D. Elkin, C. Edge, M. J. Wale, U. Gliese, X. Huang, and A. J. Seeds, "Packaged semiconductor laser optical phase-locked loop (OPLL) for photonic generation, processing and transmission of microwave signals," *IEEE Trans. Microw. Theory Tech.*, vol. 47, no. 7, pp. 1257–1264, Jul. 1999.

[21] S. Takasaka, Y. Ozeki, S. Namiki, and M. Sakano, "External synchronization of 160-GHz optical beat signal by optical phase-locked loop technique," *IEEE Photon. Technol. Lett.*, vol. 18, no. 23, pp. 2457–2459, Dec. 2006.

[22] S. Ristic, A. Bhardwaj, M. J. Rodwell, L. A. Coldren, and L. A. Johansson, "An optical phase-locked loop photonic integrated circuit," *J. Lightw. Technol.*, vol. 28, no. 4, pp. 526–538, Feb. 2010.

[23] R. J. Steed, L. Ponnampalam, M. J. Fice, C. C. Renaud, D. C. Rogers, D. G. Moodie, G. D. Maxwell, I. F. Lealman, M. J. Robertson, L. Pavlovic, L. Naglic, M. Vidmar, and A. J. Seeds, "Hybrid integrated optical phase-lock loops for photonic terahertz sources," *IEEE J. Sel. Top. Quantum Electron.*, vol. PP, no. 99, pp. 1–8, 2010.

[24] M. Kourogi, C.-H. Shin, and M. Ohtsu, "A 134 MHz bandwidth homodyne optical phase-locked-loop of semiconductor laser diodes," *IEEE Photon. Technol. Lett.*, vol. 3, no. 3, pp. 270–272, Mar. 1991.

[25] C. Henry, "Theory of the linewidth of semiconductor lasers," *IEEE J. Quantum Electron.*, vol. 18, no. 2, pp. 259–264, Feb. 1982.

[26] K. Vahala and A. Yariv, "Semiclassical theory of noise in semiconductor lasers—Part I," *IEEE J. Quantum Electron.*, vol. 19, no. 6, pp. 1096–1101, June 1983.

[27] ——, "Semiclassical theory of noise in semiconductor lasers—Part II," *IEEE J. Quantum Electron.*, vol. 19, no. 6, pp. 1102–1109, June 1983.

[28] C. Harder, K. Vahala, and A. Yariv, "Measurement of the linewidth enhancement factor alpha of semiconductor lasers," *Appl. Phys. Lett.*, vol. 42, pp. 328–330, Feb. 1983.

[29] R. Mears, L. Reekie, I. Jauncey, and D. Payne, "Low-noise erbium-doped fibre amplifier operating at 1.54 µm," *Electron. Lett.*, vol. 23, no. 19, pp. 1026–1028, 1987.

[30] E. Desurvire, J. R. Simpson, and P. C. Becker, "High-gain erbium-doped traveling-wave fiber amplifier," *Opt. Lett.*, vol. 12, no. 11, pp. 888–890, Nov. 1987.

[31] H. Philipp, A. Scholtz, E. Bonek, and W. Leeb, "Costas loop experiments for a 10.6 µm communications receiver," *IEEE T. Commun.*, vol. 31, no. 8, pp. 1000–1002, Aug. 1983.

[32] S. Saito, O. Nilsson, and Y. Yamamoto, "Coherent FSK transmitter using a negative feedback stabilised semiconductor laser," *Electron. Lett.*, vol. 20, no. 17, pp. 703–704, 1984.

[33] L. Kazovsky, “Performance analysis and laser linewidth requirements for optical PSK heterodyne communications systems,” *J. Lightw. Technol.*, vol. 4, no. 4, pp. 415–425, Apr. 1986.

[34] S. Camatel and V. Ferrero, “Homodyne coherent detection of ASK and PSK signals performed by a subcarrier optical phase-locked loop,” *IEEE Photon. Technol. Lett.*, vol. 18, no. 1, pp. 142–144, Jan. 2006.

[35] E. Torrengo, V. Ferrero, and S. Camatel, “A 20-Gb/s quadrature phase-shift-keying real-time coherent system based on a subcarrier optical phase-locked loop,” *IEEE Photon. Technol. Lett.*, vol. 21, no. 18, pp. 1296–1298, Sep. 2009.

[36] K. Kasai, T. Omiya, P. Guan, M. Yoshida, T. Hirooka, and M. Nakazawa, “Single-channel 400-Gb/s OTDM-32 RZ/QAM coherent transmission over 225 km using an optical phase-locked loop technique,” *IEEE Photon. Technol. Lett.*, vol. 22, no. 8, pp. 562–564, Apr. 2010.

[37] L. A. Johansson and A. J. Seeds, “Millimeter-wave modulated optical signal generation with high spectral purity and wide-locking bandwidth using a fiber-integrated optical injection phase-lock loop,” *IEEE Photon. Technol. Lett.*, vol. 12, no. 6, pp. 690–692, June 2000.

[38] J.-F. Cliche, B. Shillue, M. Tetu, and M. Poulin, “A 100-GHz-tunable photonic millimeter wave synthesizer for the Atacama Large Millimeter Array radiotelescope,” in *IEEE/MTT-S International Microwave Symposium, 2007*, June 2007, pp. 349–352.

[39] S. Ayotte, A. Babin, P. Poulin, M. Poulin, A. Jeanneau, M.-J. Picard, D. Poulin, C.-A. Davidson, M. Aubé, I. Alexandre, F. Costin, F. Pelletier, J.-F. Cliche, M. Têtu, and B. Shillue, “Laser synthesizer of the ALMA telescope: Design and performance,” in *2010 IEEE Topical Meeting on Microwave Photonics (MWP)*, Oct. 2010, pp. 249–252.

[40] T. von Lerber, S. Honkanen, A. Tervonen, H. Ludvigsen, and F. Küppers, "Optical clock recovery methods: Review (Invited)," *Opt. Fiber Technol.*, vol. 15, no. 4, pp. 363–372, 2009.

[41] S. A. Diddams, D. J. Jones, J. Ye, S. T. Cundiff, J. L. Hall, J. K. Ranka, R. S. Windeler, R. Holzwarth, T. Udem, and T. W. Hänsch, "Direct link between microwave and optical frequencies with a 300 THz femtosecond laser comb," *Phys. Rev. Lett.*, vol. 84, no. 22, pp. 5102–5105, May 2000.

[42] S. A. Diddams, J. C. Bergquist, S. R. Jefferts, and C. W. Oates, "Standards of time and frequency at the outset of the 21st century," *Science*, vol. 306, no. 5700, pp. 1318–1324, 2004.

[43] L.-S. Ma, Z. Bi, A. Bartels, L. Robertsson, M. Zucco, R. S. Windeler, G. Wilpers, C. Oates, L. Hollberg, and S. A. Diddams, "Optical frequency synthesis and comparison with uncertainty at the 10^{-19} Level," *Science*, vol. 303, no. 5665, pp. 1843–1845, 2004.

[44] R. Slavík, F. Parmigiani, J. Kakande, C. Lundström, M. Sjödin, P. A. Andrekson, R. Weerasuriya, S. Sygletos, A. D. Ellis, L. Grüner-Nielsen, D. Jakobsen, S. Herstrøm, R. Phelan, J. O'Gorman, A. Bogris, D. Syvridis, S. Dasgupta, P. Petropoulos, and D. J. Richardson, "All-optical phase and amplitude regenerator for next-generation telecommunications systems," *Nat. Photonics*, vol. 4, pp. 690–695, Oct. 2010.

[45] M.-C. Amann, T. Bosch, M. Lescure, R. Myllyla, and M. Rioux, "Laser ranging: A critical review of usual techniques for distance measurement," *Opt. Eng.*, vol. 40, no. 1, pp. 10–19, 2001.

[46] G. Beheim and K. Fritsch, "Remote displacement measurements using a laser diode," *Electron. Lett.*, vol. 21, no. 3, pp. 93–94, 1985.

[47] E. M. Strzelecki, D. A. Cohen, and L. A. Coldren, "Investigation of tunable single frequency diode lasers for sensor applications," *J. Lightw. Technol.*, vol. 6, no. 10, pp. 1610–1618, Oct. 1988.

[48] E. C. Burrows and K.-Y. Liou, "High resolution laser LIDAR utilising two-section distributed feedback semiconductor laser as a coherent source," *Electron. Lett.*, vol. 26, no. 9, pp. 577–579, Apr. 1990.

[49] A. Dieckmann, "FMCW-LIDAR with tunable twin-guide laser diode," *Electron. Lett.*, vol. 30, no. 4, pp. 308–309, Feb. 1994.

[50] S. H. Yun, G. J. Tearney, B. J. Vakoc, M. Shishkov, W. Y. Oh, A. E. Desjardins, M. J. Suter, R. C. Chan, J. A. Evans, I.-K. Jang, N. S. Nishioka, J. F. de Boer, and B. E. Bouma, "Comprehensive volumetric optical microscopy in vivo," *Nat. Med.*, vol. 12, pp. 1429–1433, 2007.

[51] M. A. Choma, K. Hsu, and J. A. Izatt, "Swept source optical coherence tomography using an all-fiber 1300-nm ring laser source," *J. Biomed. Opt.*, vol. 10, no. 4, p. 044009, 2005.

[52] C. Ndiaye, T. Hara, and H. Ito, "Profilometry using a frequency-shifted feedback laser," in *Conference on Lasers and Electro-Optics/Quantum Electronics and Laser Science and Photonic Applications Systems Technologies.* Optical Society of America, 2005, p. CThM2.

[53] S. K. Dubey, T. Anna, C. Shakher, and D. S. Mehta, "Fingerprint detection using full-field swept-source optical coherence tomography," *Appl. Phys. Lett.*, vol. 91, no. 18, p. 181106, 2007.

[54] W. S. Burdic, *Radar Signal Analysis.* Englewood Cliffs, NJ: Prentice-Hall, 1968.

[55] I. V. Komarov and S. M. Smolskiy, *Fundamentals of Short-Range FM Radar.* Boston, MA: Artech House, 2003.

[56] S. H. Yun, C. Boudoux, G. J. Tearney, and B. E. Bouma, "High-speed wavelength-swept semiconductor laser with a polygon-scanner-based wavelength filter," *Opt. Lett.*, vol. 28, no. 20, pp. 1981–1983, Oct. 2003.

[57] M. K. K. Leung, A. Mariampillai, B. A. Standish, K. K. C. Lee, N. R. Munce, I. A. Vitkin, and V. X. D. Yang, "High-power wavelength-swept laser in Littman telescope-less polygon filter and dual-amplifier configuration for multichannel optical coherence tomography," *Opt. Lett.*, vol. 34, no. 18, pp. 2814–2816, Sep. 2009.

[58] R. Huber, M. Wojtkowski, and J. G. Fujimoto, "Fourier Domain Mode Locking (FDML): A new laser operating regime and applications for optical coherence tomography," *Opt. Express*, vol. 14, no. 8, pp. 3225–3237, Apr. 2006.

[59] C. Chong, T. Suzuki, A. Morosawa, and T. Sakai, "Spectral narrowing effect by quasi-phase continuous tuning in high-speed wavelength-swept light source," *Opt. Express*, vol. 16, no. 25, pp. 21 105–21 118, Dec. 2008.

[60] C. Wiley, "Synthetic aperture radars," *IEEE Trans. Aerosp. Electron. Syst.*, vol. AES-21, no. 3, pp. 440–443, May 1985.

[61] N. Satyan, A. Vasilyev, W. Liang, G. Rakuljic, and A. Yariv, "Sideband locking of a single-section semiconductor distributed-feedback laser in an optical phase-lock loop," *Opt. Lett.*, vol. 34, no. 21, pp. 3256–3258, Nov. 2009.

[62] N. Satyan, J. Sendowski, A. Vasilyev, G. Rakuljic, and A. Yariv, "Phase noise reduction of a semiconductor laser in a composite optical phase-locked loop," *Opt. Eng.*, vol. 49, no. 12, p. 124301, Dec. 2010.

[63] N. Satyan, W. Liang, and A. Yariv, "Coherence cloning using semiconductor laser optical phase-lock loops," *IEEE J. Quantum Electron.*, vol. 45, no. 7, pp. 755–761, July 2009.

[64] N. Satyan, W. Liang, A. Kewitsch, G. Rakuljic, and A. Yariv, "Coherent power combination of semiconductor lasers Using optical phase-lock loops (Invited),"

IEEE J. Sel. Top. Quantum Electron., vol. 15, no. 2, pp. 240–247, Mar./Apr. 2009.

[65] W. Liang, N. Satyan, A. Yariv, A. Kewitsch, G. Rakuljic, F. Aflatouni, H. Hashemi, and J. Ungar, "Coherent power combination of two Master-oscillator-power-amplifier (MOPA) semiconductor lasers using optical phase lock loops," *Opt. Express*, vol. 15, no. 6, pp. 3201–3205, 2007.

[66] W. Liang, N. Satyan, F. Aflatouni, A. Yariv, A. Kewitsch, G. Rakuljic, and H. Hashemi, "Coherent beam combining with multilevel optical phase-locked loops," *J. Opt. Soc. Am. B: Opt. Phys.*, vol. 24, no. 12, pp. 2930–2939, Dec. 2007.

[67] N. Satyan, W. Liang, F. Aflatouni, A. Yariv, A. Kewitsch, G. Rakuljic, and H. Hashemi, "Phase-controlled apertures using heterodyne optical phase-locked loops," *IEEE Photon. Technol. Lett.*, vol. 20, no. 9-12, pp. 897–899, June 2008.

[68] Y. Vilenchik, B. I. Erkmen, N. Satyan, A. Yariv, W. H. Farr, and J. M. Choi, "Optical phase lock loop based phased array transmitter for optical communications," *The Interplanetary Network Progress Report*, vol. 42-184, Feb. 2011.

[69] N. Satyan, A. Vasilyev, G. Rakuljic, V. Leyva, and A. Yariv, "Precise control of broadband frequency chirps using optoelectronic feedback," *Opt. Express*, vol. 17, no. 18, pp. 15 991–15 999, 2009.

[70] N. Satyan, G. Rakuljic, and A. Yariv, "Chirp multiplication by four wave mixing for wideband swept-frequency sources for high resolution imaging," *J. Lightw. Technol.*, vol. 28, no. 14, pp. 2077–2083, July 2010.

[71] A. Vasilyev, N. Satyan, S. Xu, G. Rakuljic, and A. Yariv, "Multiple source frequency-modulated continuous-wave optical reflectometry: Theory and experiment," *Appl. Opt.*, vol. 49, no. 10, pp. 1932–1937, 2010.

[72] K. Petermann, *Laser Diode Modulation and Noise.* Advances in optoelectronics (ADOP), Dordrecht: Kluwer and Tokyo: KTK Scientific Publishers, 1991.

[73] W. Liang, "Study of optical phase lock loops and the applications in coherent beam combining and coherence cloning," PhD dissertation, California Institute of Technology, Pasadena, CA, 2008.

[74] K. Ogata, *Modern Control Engineering (5th Edition).* Upper Saddle River, NJ: Prentice Hall, 2009.

[75] M. Grant, W. Michie, and M. Fletcher, "The performance of optical phase-locked loops in the presence of nonnegligible loop propagation delay," *J. Lightw. Technol.*, vol. 5, no. 4, pp. 592–597, Apr. 1987.

[76] R. T. Ramos and A. J. Seeds, "Delay, linewidth and bandwidth limitations in optical phase-locked loop design," *Electron. Lett.*, vol. 26, no. 6, pp. 389–391, Mar. 1990.

[77] S. Ristic, A. Bhardwaj, M. J. Rodwell, L. A. Coldren, and L. A. Johansson, "Integrated optical phase-locked loop," in *National Fiber Optic Engineers Conference.* Optical Society of America, 2009, p. PDPB3.

[78] P. Corrc, O. Girad, and I. F. de Faria Jr., "On the thermal contribution to the FM response of DFB lasers: Theory and experiment," *IEEE J. Quantum Electron.*, vol. 30, no. 11, pp. 2485–2490, Nov. 1994.

[79] G. S. Pandian and S. Dilwali, "On the thermal FM response of a semiconductor laser diode," *IEEE Photon. Technol. Lett.*, vol. 4, no. 2, pp. 130–133, Feb. 1992.

[80] W. V. Sorin, K. W. Chang, G. A. Conrad, and P. R. Hernday, "Frequency domain analysis of an optical FM discriminator," *J. Lightw. Technol.*, vol. 10, no. 6, pp. 787–793, June 1992.

[81] A. Yariv, "Dynamic analysis of the semiconductor laser as a current-controlled oscillator in the optical phased-lock loop: applications," *Opt. Lett.*, vol. 30, no. 17, pp. 2191–2193, 2005.

[82] M. Carvalho and A. Seeds, “Simple model for frequency modulation characteristics of semiconductor lasers,” *Electron. Lett.*, vol. 24, no. 7, pp. 428–429, Mar. 1988.

[83] L. Richter, H. Mandelberg, M. Kruger, and P. McGrath, “Linewidth determination from self-heterodyne measurements with subcoherence delay times,” *IEEE J. Quantum Electron.*, vol. 22, no. 11, pp. 2070–2074, Nov. 1986.

[84] F. Aflatouni, O. Momeni, and H. Hashemi, “A heterodyne phase locked loop with GHz acquisition range for coherent locking of semiconductor lasers in 0.13µm CMOS,” *Custom Integrated Circuits Conference, 2007. CICC ’07. IEEE*, pp. 463–466, Sep. 2007.

[85] R. T. Ramos, P. Gallion, D. Erasme, A. J. Seeds, and A. Bordonalli, “Optical injection locking and phase-lock loop combined systems,” *Opt. Lett.*, vol. 19, no. 1, pp. 4–6, Jan. 1994.

[86] A. C. Bordonalli, C. Walton, and A. J. Seeds, “High-performance homodyne optical injection phase-lock loop using wide-linewidth semiconductor lasers,” *IEEE Photon. Technol. Lett.*, vol. 8, no. 9, pp. 1217–1219, Sept. 1996.

[87] ——, “High-performance phase locking of wide linewidth semiconductor lasers by combined use of optical injection locking and optical phase-lock loop,” *J. Lightw. Technol.*, vol. 17, no. 2, pp. 328–342, Feb. 1999.

[88] A. Yariv, *Quantum Electronics (3rd Edition)*. New York, NY: John Wiley and Sons, 1988.

[89] M. J. O’Mahony and I. D. Henning, “Semiconductor laser linewidth broadening due to 1/f carrier noise,” *Electron. Lett.*, vol. 19, no. 23, pp. 1000–1001, Nov. 1983.

[90] J. Goodman, *Statistical Optics*. New York, NY: John Wiley and Sons, 2000.

[91] L. Cutler and C. Searle, "Some aspects of the theory and measurement of frequency fluctuations in frequency standards," *Proc. of the IEEE*, vol. 54, no. 2, pp. 136–154, Feb. 1966.

[92] E. Eichen and P. Melman, "Semiconductor laser lineshape and parameter determination from fringe visibility measurements," *Electron. Lett.*, vol. 20, no. 20, pp. 826–828, Sep. 1984.

[93] E. Weisstein, "Sine Integral." *MathWorld–A Wolfram Web Resource. http://mathworld.wolfram.com/SineIntegral.html*.

[94] D. W. Allan, "Time and frequency (time-domain) characterization, estimation, and prediction of precision clocks and oscillators," *IEEE Trans. Ultrason., Ferroelectr., Freq. Control*, vol. 34, pp. 647–654, Nov. 1987.

[95] F. Riehle, *Frequency Standards: Basics and Applications.* Weinheim: Wiley-VCH, 2005, ch. 3.

[96] Y. Jeong, J. Sahu, D. Payne, and J. Nilsson, "Ytterbium-doped large-core fiber laser with 1.36 kW continuous-wave output power," *Opt. Express*, vol. 12, no. 25, pp. 6088–6092, Dec. 2004.

[97] V. Gapontsev, D. Gapontsev, N. Platonov, O. Shkurikhin, V. Fomin, A. Mashkin, M. Abramov, and S. Ferin, "2 kW CW ytterbium fiber laser with record diffraction-limited brightness," in *Conference on Lasers and Electro-Optics Europe, CLEO/Europe, 2005*, June 2005, p. 508.

[98] T. Y. Fan, "Laser beam combining for high-power, high-radiance sources," *IEEE J. Sel. Top. Quantum Electron.*, vol. 11, no. 3, pp. 567–577, May-June 2005.

[99] A. Shirakawa, T. Saitou, T. Sekiguchi, and K. Ueda, "Coherent addition of fiber lasers by use of a fiber coupler," *Opt. Express*, vol. 10, no. 21, pp. 1167–1172, 2002.

[100] L. Bartelt-Berger, U. Brauch, A. Giesen, H. Huegel, and H. Opower, "Power-scalable system of phase-locked single-mode diode lasers," *Appl. Opt.*, vol. 38, no. 27, pp. 5752–5760, 1999.

[101] Y. Kono, M. Takeoka, K. Uto, A. Uchida, and F. Kannari, "A coherent all-solid-state laser array using the Talbot effect in a three-mirror cavity," *IEEE J. Quantum Electron.*, vol. 36, no. 5, pp. 607–614, May 2000.

[102] S. J. Augst, T. Y. Fan, and A. Sanchez, "Coherent beam combining and phase noise measurements of ytterbium fiber amplifiers," *Opt. Lett.*, vol. 29, no. 5, pp. 474–476, 2004.

[103] C. X. Yu, J. E. Kansky, S. E. J. Shaw, D. V. Murphy, and C. Higgs, "Coherent beam combining of large number of PM fibres in 2-D fibre array," *Electron. Lett.*, vol. 42, no. 18, pp. 1024–1025, 31 2006.

[104] E. Desurvire, *Erbium-Doped Fiber Amplifiers: Principles and Applications.* New York, NY: John Wiley and Sons, 1994.

[105] L. Moller, "Novel aspects of spectral broadening due to fiber amplifier phase noise," *IEEE J. Quantum Electron.*, vol. 34, no. 9, pp. 1554–1558, Sep. 1998.

[106] E. Rochat and R. Dandliker, "New investigations on the effect of fiber amplifier phase noise," *IEEE J. Sel. Top. Quantum Electron.*, vol. 7, no. 1, pp. 49–54, Jan./Feb. 2001.

[107] J. Katz, S. Margalit, and A. Yariv, "Diffraction coupled phase-locked semiconductor laser array," *Appl. Phys. Lett.*, vol. 42, no. 7, pp. 554–556, 1983.

[108] D. P. Resler, D. S. Hobbs, R. C. Sharp, L. J. Friedman, and T. A. Dorschner, "High-efficiency liquid-crystal optical phased-array beam steering," *Opt. Lett.*, vol. 21, no. 9, pp. 689–691, May 1996.

[109] J. W. Goodman, *Introduction to Fourier Optics.* Greenwood Village, CO: Roberts and Company Publishers, 2004.

[110] C. L. Chua, R. L. Thornton, D. W. Treat, and R. M. Donaldson, "Independently addressable VCSEL arrays on 3-µm pitch," *IEEE Photon. Technol. Lett.*, vol. 10, no. 7, pp. 917–919, July 1998.

[111] H.-L. Chen, D. Francis, T. Nguyen, W. Yuem, G. Li, and C. Chang-Hasnian, "Collimating diode laser beams from a large-area VCSEL-array using microlens array," *IEEE Photon. Technol. Lett.*, vol. 11, no. 5, pp. 506–508, May 1999.

[112] K. Iiyama, L.-T. Wang, and K.-I. Hayashi, "Linearizing optical frequency-sweep of a laser diode for FMCW reflectometry," *J. Lightw. Technol.*, vol. 14, no. 2, pp. 173–178, Feb. 1996.

[113] P. A. Roos, R. R. Reibel, T. Berg, B. Kaylor, Z. W. Barber, and W. R. Babbitt, "Ultrabroadband optical chirp linearization for precision metrology applications," *Opt. Lett.*, vol. 34, no. 23, pp. 3692–3694, Dec. 2009.

[114] F. Vollmer, D. Braun, A. Libchaber, M. Khoshsima, I. Teraoka, and S. Arnold, "Protein detection by optical shift of a resonant microcavity," *Appl. Phys. Lett.*, vol. 80, no. 21, pp. 4057–4059, 2002.

[115] D. K. Armani, T. J. Kippenberg, S. M. Spillane, and K. J. Vahala, "Ultra-high-Q toroid microcavity on a chip," *Nature*, vol. 421, pp. 925–928, Feb. 2003.

[116] S. M. Spillane, T. J. Kippenberg, O. J. Painter, and K. J. Vahala, "Ideality in a fiber-taper-coupled microresonator system for application to cavity quantum electrodynamics," *Phys. Rev. Lett.*, vol. 91, no. 4, p. 043902, July 2003.

[117] A. M. Armani, R. P. Kulkarni, S. E. Fraser, R. C. Flagan, and K. J. Vahala, "Label-free, single-molecule detection with optical microcavities," *Science*, vol. 317, no. 5839, pp. 783–787, 2007.

[118] G. M. Hale and M. R. Querry, "Optical constants of water in the 200-nm to 200-µm wavelength region," *Appl. Opt.*, vol. 12, no. 3, pp. 555–563, Mar. 1973.

[119] R. M. Effros, M. B. Dunning, J. Biller, and R. Shaker, "The promise and perils of exhaled breath condensates," *Am. J. Physiol.-Lung C.*, vol. 287, no. 6, pp. L1073–L1080, 2004.

[120] I. Horvath, J. Hunt, and P. J. Barnes, "Exhaled breath condensate: Methodological recommendations and unresolved questions," *Eur. Respir. J.*, vol. 26, no. 3, pp. 523–548, 2005.

[121] F. S. Yang, M. E. Marhic, and L. G. Kazovsky, "CW fibre optical parametric amplifier with net gain and wavelength conversion efficiency >1," *Electron. Lett.*, vol. 32, no. 25, pp. 2336–2338, Dec. 1996.

[122] S. Ramachandran, S. Ghalmi, J. W. Nicholson, M. F. Yan, P. Wisk, E. Monberg, and F. V. Dimarcello, "Anomalous dispersion in a solid, silica-based fiber," *Opt. Lett.*, vol. 31, no. 17, pp. 2532–2534, 2006.

[123] S. Diez, C. Schmidt, R. Ludwig, H. G. Weber, K. Obermann, S. Kindt, I. Koltchanov, and K. Petermann, "Four-wave mixing in semiconductor optical amplifiers for frequency conversion and fast optical switching," *IEEE J. Sel. Top. Quantum Electron.*, vol. 3, no. 5, pp. 1131–1145, Oct. 1997.

[124] W. Mathlouthi, H. Rong, and M. Paniccia, "Characterization of efficient wavelength conversion by four-wave mixing in sub-micron silicon waveguides," *Opt. Express*, vol. 16, no. 21, pp. 16 735–16 745, 2008.

[125] K. O. Hill, D. C. Johnson, B. S. Kawasaki, and R. I. MacDonald, "cw three-wave mixing in single-mode optical fibers," *J. Appl. Phys.*, vol. 49, no. 10, pp. 5098–5106, 1978.

[126] M. E. Marhic and F. S. Yang, "High-nonlinearity fiber optical parametric amplifier with periodic dispersion compensation," *J. Lightw. Technol.*, vol. 17, no. 2, p. 210, 1999.

[127] J. Kim, O. Boyraz, J. H. Lim, and M. N. Islam, "Gain enhancement in cascaded fiber parametric amplifier with quasi-phase matching: Theory and experiment," *J. Lightw. Technol.*, vol. 19, no. 2, p. 247, 2001.

[128] O. Ishida and N. Shibata, "Laser frequency synthesis employing fiber four-wave mixing," *IEEE Photon. Technol. Lett.*, vol. 4, no. 10, pp. 1171–1174, Oct. 1992.

[129] K. W. Holman, D. G. Kocher, and S. Kaushik, "MIT/LL development of broadband linear frequency chirp for high resolution ladar," in *Enabling Photonics Technologies for Defense, Security, and Aerospace Applications III*, vol. 6572, no. 1. SPIE, 2007, p. 65720J.

[130] C. Koos, L. Jacome, C. Poulton, J. Leuthold, and W. Freude, "Nonlinear silicon-on-insulator waveguides for all-optical signal processing," *Opt. Express*, vol. 15, no. 10, pp. 5976–5990, May 2007.

[131] A. J. Seeds, "Microwave photonics," *IEEE Trans. Microw. Theory Tech.*, vol. 50, no. 3, pp. 877–887, Mar. 2002.

[132] S. Matsuura and H. Ito, "Generation of CW Terahertz Radiation with Photomixing," in *Terahertz Optoelectronics*, series Topics in Applied Physics, K. Sakai, editor. Springer Berlin / Heidelberg, 2005, vol. 97, pp. 157–202.

[133] D. Cotter, "Transient stimulated Brillouin scattering in long single-mode fibres," *Electron. Lett.*, vol. 18, no. 12, pp. 504–506, June 1982.

[134] Z. Jiang, D. E. Leaird, and A. M. Weiner, "Optical arbitrary waveform generation and characterization using spectral line-by-line control," in *Conference on Lasers and Electro-Optics, 2006 and 2006 Quantum Electronics and Laser Science Conference. CLEO/QELS 2006.*, May 2006, pp. 1–2.

[135] K. Inoue, "Phase-mismatching characteristic of four-wave mixing in fiber lines with multistage optical amplifiers," *Opt. Lett.*, vol. 17, no. 11, pp. 801–803, June 1992.